

DOCTORAL THESIS

**Variability of head tissues'
conductivities and their impact in
electrical brain activity research**

Hannah McCann

Supervisor

Dr Leandro Beltrachini



Thesis submitted for the degree of
Doctor of Philosophy 2022
01/02/2022

School of Physics & Astronomy
Cardiff University

THESIS SUMMARY

The presented thesis endeavoured to establish the impact that the variability in electrical conductivity of human head tissues has on electrical brain imaging research, particularly transcranial direct current stimulation (tDCS) and electroencephalography (EEG). A systematic meta-analysis was firstly conducted to determine the consistency of reported measurements, revealing significant deviations in electrical conductivity measurements predominantly for the scalp, skull, GM, and WM. Found to be of particular importance was the variability of skull conductivity, which consists of multiple layers and bone compositions, each with differing conductivity. Moreover, the conductivity of the skull was suggested to decline with participant age and hypothesised to correspondingly impact tDCS induced fields. As expected, the propositioned decline in the equivalent (homogeneous) skull conductivity as a function of age resulted in reduced tDCS fields. A further EEG analysis also revealed, neglecting the presence of adult sutures and deviation in proportion of spongiform and compact bone distribution throughout the skull, ensued significant errors in EEG forward and inverse solutions. Thus, incorporating geometrically accurate and precise volume conductors of the skull was considered as essential for EEG forward analysis and source localisation and tDCS application. This was an overarching conclusion of the presented thesis. Individualised head models, particularly of the skull, accounting for participant age, the presence of sutures and deviation in bone composition distribution are imperative for electrical brain imaging. Additionally, it was shown that *in vivo*, individualised measurements of skull conductivity are further required to fully understand the relationship between conductivity and participant demographics, suture closure, bone compositions, skull thickness and additional factors.

TABLE OF CONTENTS

| | |
|---|-------------|
| THESIS SUMMARY | ii |
| LIST OF FIGURES | vii |
| LIST OF TABLES | vii |
| ABBREVIATIONS | viii |
| NOTATION | xi |
| ACKNOWLEDGEMENTS | xiii |
| Publications arising from the Thesis | xiv |
| GENERAL INTRODUCTION | 1 |
| Overview of Thesis | 4 |
| CHAPTER 1: BRAIN ACTIVITY | 6 |
| 1.1. Overview | 6 |
| 1.2. Neurophysiology | 6 |
| 1.3. Electroencephalography | 9 |
| 1.3.1. EEG Interpretation | 12 |
| 1.3.2. EEG Systems | 13 |
| 1.3.3. Strengths and Limitations | 15 |
| 1.4. Transcranial Direct Current Stimulation | 16 |
| 1.4.1. Systems and Protocols | 17 |
| 1.4.2. Mechanism of Action | 20 |
| 1.4.3. Strengths and Limitations | 21 |
| 1.5. EEG and tDCS Reciprocity | 22 |
| 1.6. Basic Head Anatomy | 23 |
| 1.6.1. The Brain and in-skull | 23 |
| 1.6.2. The Skull | 24 |
| 1.6.3. The Scalp | 26 |
| 1.7. Chapter Summary | 27 |
| CHAPTER 2: FORWARD AND INVERSE PROBLEMS | 29 |
| 2.1 Chapter Overview | 29 |
| 2.2. Underlying mechanisms | 29 |
| 2.2.1. From Maxwell to Poisson Equations | 30 |
| 2.2.2. Current Dipole | 32 |
| 2.3. The EEG Forward Problem | 32 |
| 2.3.1. Infinite Homogeneous Medium | 33 |
| 2.3.2. Concentric Spherical Models | 33 |
| 2.3.3. Realistic Head Models | 34 |
| 2.3.3i. Boundary Element Method | 34 |
| 2.3.3ii. Finite Element Method | 36 |
| 2.4. Lead field Matrix | 39 |
| 2.5. The EEG Inverse Problem | 40 |

| | |
|--|-----------|
| 2.5.1. Dipole Fitting Approach | 42 |
| 2.5.2. Pre-defined Dipoles..... | 43 |
| 2.5.3. Distributed Source Models | 44 |
| 2.6. tDCS Induced Fields..... | 46 |
| 2.6.1. tDCS Forward Problem..... | 46 |
| 2.6.2. tDCS Inverse Problem | 47 |
| 2.7. EEG and tDCS Reciprocity | 48 |
| 2.8. Chapter Summary | 49 |
| CHAPTER 3. HEAD TISSUE CONDUCTIVITY VARIATION..... | 51 |
| 3.1 Chapter Overview | 51 |
| 3.2. Motivation | 51 |
| 3.3. Meta-Analysis Methods | 54 |
| 3.3.1. Literature search | 54 |
| 3.3.2. Selection criteria | 54 |
| 3.3.3. Data extraction and Synthesis..... | 55 |
| 3.3.4. Variable Definitions and Classification..... | 55 |
| 3.3.4i. Tissue Types | 55 |
| 3.3.4ii. Measurement Conditions..... | 56 |
| 3.3.4iii. Measurement Methods..... | 56 |
| 3.3.4iv. Frequency | 57 |
| 3.3.4v. Temperature..... | 57 |
| 3.3.4vi. Participant's Age..... | 58 |
| 3.3.4vii. Participant Pathology | 58 |
| 3.3.5. Quality Analysis..... | 58 |
| 3.3.6. Statistical Analysis..... | 59 |
| 3.4. Results | 60 |
| 3.4.1. Search Results | 60 |
| 3.4.2. Included Studies..... | 60 |
| 3.4.3. Scalp..... | 65 |
| 3.4.4. Skull..... | 66 |
| 3.4.4i. Whole-skull..... | 66 |
| 3.4.4ii. Spongiform Bone Skull Layer..... | 67 |
| 3.4.4iii. Compact bone skull layer | 68 |
| 3.4.5. Cerebrospinal Fluid | 69 |
| 3.4.6. Brain..... | 69 |
| 3.4.6i. Grey Matter | 70 |
| 3.4.6ii. White Matter..... | 72 |
| 3.4.7. Brain to Skull Conductivity Ratio (BSCR) | 73 |
| 3.5. Discussion | 74 |
| 3.5.1. Data Exclusions | 75 |
| 3.5.2. Scalp..... | 76 |
| 3.5.3. Skull..... | 77 |
| 3.5.3i. Layered Skull | 78 |
| 3.5.4. Cerebrospinal Fluid | 81 |
| 3.5.5. Whole-Brain | 82 |
| 3.5.5i. Grey Matter | 82 |
| 3.5.5ii. White Matter..... | 84 |
| 3.5.6. Brain-to-skull Conductivity Ratio | 87 |
| 3.6. Chapter Summary | 88 |
| CHAPTER 4. IMPACT OF AGE ON TDCS INDUCED FIELDS | 90 |

| | |
|---|------------|
| 4.1. Chapter Overview | 90 |
| 4.2. Motivation | 90 |
| 4.3. Materials and Methods | 93 |
| 4.3.1. Head Models | 93 |
| 4.3.2. Conductivity Assignment | 94 |
| 4.3.3. Experiments | 97 |
| 4.3.4. Analysis | 99 |
| 4.4. Results | 101 |
| 4.4.1. Head models | 101 |
| 4.4.2. Peak fields | 104 |
| 4.4.3. Focality | 108 |
| 4.5. Discussion | 110 |
| 4.5.1. Atlas Justification | 110 |
| 4.5.2. Age and peak induced fields | 111 |
| 4.5.3. Age and focality..... | 115 |
| 4.5.4. Limitations | 116 |
| 4.6. Chapter Summary | 119 |
| CHAPTER 5: SKULL CONDUCTIVITY AND EEG | 120 |
| 5.1 Chapter Overview | 120 |
| 5.2. Motivation | 120 |
| 5.3. Methods | 124 |
| 5.3.1. Head model construction..... | 124 |
| 5.3.2. Experiments | 126 |
| 5.3.3. Model computation methodology..... | 129 |
| 5.3.3i Ground truth model | 129 |
| 5.3.3ii. EIT protocol | 130 |
| 5.3.3iii. Age-appropriate models..... | 131 |
| 5.3.4. EEG forward and inverse problems..... | 133 |
| 5.4. RESULTS | 135 |
| 5.4.1. Impact of sutures and bone composition | 135 |
| 5.4.2. Homogeneous skull models | 137 |
| 5.4.3. Age-appropriate models | 141 |
| 5.5. DISCUSSION | 143 |
| 5.5.1. Impact of sutures and bone composition | 144 |
| 5.5.2. Impact of a homogeneous skull | 148 |
| 5.5.3. Influence of age..... | 150 |
| 5.5.4. Research and clinical applications..... | 151 |
| 5.6. Chapter Summary | 152 |
| CHAPTER 6. GENERAL DISCUSSION..... | 154 |
| 6.1. Thesis Overview | 154 |
| 6.2. Summary of Findings..... | 155 |
| 6.3. Future Directions | 160 |
| 6.4. Overall Conclusion | 165 |
| REFERENCES | 167 |
| APPENDIX..... | 204 |

| | |
|--|------------|
| Appendix A: Prisma Flow Diagram | 204 |
| Appendix B: Keywords for Literature Search | 205 |
| Appendix C: Quality Assessment Protocol for All Studies | 205 |

LIST OF FIGURES

| | |
|--|-----|
| <i>Figure 0.1: Representation of brain imaging modalities.</i> | 2 |
| <i>Figure 1.1: Schematic diagram of a neuron and it's synapse.</i> | 8 |
| <i>Figure 1.2: Schematic diagram of pyramidal neurons.</i> | 11 |
| <i>Figure 1.3: EEG oscillation examples during wakefulness and sleep.</i> | 12 |
| <i>Figure 1.4: Schematic representation of an EEG system.</i> | 15 |
| <i>Figure 1.5: Schematic representation of a tDCS system.</i> | 19 |
| <i>Figure 1.6: Schematic diagram of the main skull bones and sutures.</i> | 25 |
| <i>Figure 1.7: Diagram of head tissue compartments.</i> | 27 |
| <i>Figure 2.1: Example of head model discretisation.</i> | 39 |
| <i>Figure 2.2: Illustration of the EEG forward and inverse problem with relevant equations.</i> | 41 |
| <i>Figure 3.1: Variation in electrical conductivity for all head tissues.</i> | 64 |
| <i>Figure 3.2: Assigned weights for each meta-analysis study.</i> | 65 |
| <i>Figure 3.3: Variation in scalp conductivity according to method.</i> | 66 |
| <i>Figure 3.4: Variation in skull conductivity according to method.</i> | 67 |
| <i>Figure 3.5: Variation in spongiform bone conductivity according to condition.</i> | 68 |
| <i>Figure 3.6: Variation in compact bone conductivity according to condition.</i> | 69 |
| <i>Figure 3.7: Variation in whole-brain conductivity according to method.</i> | 70 |
| <i>Figure 3.8: Variation in grey matter conductivity according to method.</i> | 71 |
| <i>Figure 3.9: Variation in grey matter conductivity according to pathology.</i> | 71 |
| <i>Figure 3.10: Variation in white matter conductivity according to method.</i> | 72 |
| <i>Figure 3.11: Brain-to-skull conductivity ratio according to method.</i> | 73 |
| <i>Figure 3.12: Brain-to-skull conductivity ratio according to age.</i> | 74 |
| <i>Figure 4.1: Skull conductivity according to age from three datasets.</i> | 99 |
| <i>Figure 4.2: Base MRI for each tDCS age atlas.</i> | 102 |
| <i>Figure 4.3: Finite element head meshes for each tDCS age atlas.</i> | 103 |
| <i>Figure 4.4: Variation in peak electric fields dependent on tDCS intensity and age.</i> | 105 |
| <i>Figure 4.5: Peak electric fields at 1 mA tDCS for varying age, datasets and conductivity.</i> | 107 |
| <i>Figure 4.6: Global derivative-based sensitivity coefficients of 1 mA tDCS.</i> | 108 |
| <i>Figure 4.7: Focality of 1 mA tDCS for different ages and conductivity.</i> | 109 |
| <i>Figure 5.1: Schematic diagram of adult skull sutures.</i> | 122 |
| <i>Figure 5.2: Head mesh and skull conductivity distribution for EEG simulations.</i> | 125 |
| <i>Figure 5.3: Suture conductivities as a function of age.</i> | 133 |
| <i>Figure 5.4: Error distribution when neglecting the sutures and bone composition.</i> | 136 |
| <i>Figure 5.5: FP MAG and RDM when neglecting the sutures and bone composition.</i> | 137 |
| <i>Figure 5.6: Error distribution for homogeneous skull conductivities.</i> | 139 |
| <i>Figure 5.7: FP MAG and RDM for homogeneous skull conductivities.</i> | 140 |
| <i>Figure 5.8: Probability histogram for homogeneous skull conductivities.</i> | 141 |
| <i>Figure 5.9: Error distribution when omitting sutures for age-appropriate models.</i> | 142 |
| <i>Figure 5.10: FP MAG and RDM when omitting sutures for age-appropriate models.</i> | 143 |

LIST OF TABLES

| | |
|---|-----|
| <i>Table 3.1: Strengths and weaknesses of imaging methods.</i> | 53 |
| <i>Table 3.2: Summary of papers included in meta-analysis.</i> | 62 |
| <i>Table 3.3: Summary of the electrical conductivity values for each tissue.</i> | 63 |
| <i>Table 4.1: Summary of the tissue volumes and conductivity for EEG analysis.</i> | 98 |
| <i>Table 5.1: Summary of head model conductivity distribution for EEG analysis.</i> | 128 |

ABBREVIATIONS

A

| | |
|-------|--|
| ADHD | Attention deficit hyperactivity disorder |
| AE | Absolute error |
| ANOVA | Analysis of Variance |

B

| | |
|------|--|
| bEIT | Boundary electrical impedance tomography |
| BEM | Boundary Element Method |
| BSCR | Brain-to-skull conductivity ratio |
| BOLD | blood oxygenation level dependent |

C

| | |
|-----------------|---------------------|
| CG | Centre of gravity |
| Cl ⁻ | Chloride ion |
| CSF | Cerebrospinal fluid |
| CT | Computed Tomography |

D

| | |
|--------|---|
| DAC | Directly applied current |
| DLPFC | Dorsolateral prefrontal cortex |
| DSM | Distributed Source Model |
| DTI | Diffusion tensor imaging |
| DV | Dependent variable |
| DW-MRI | Diffusion weighted Magnetic Resonance Imaging |
| DWI | Diffusion weighted imaging |

E

| | |
|------------|---|
| ECoG | Electrocorticography |
| ECT | Electroconvulsive therapy |
| EEG | Electroencephalography |
| EEG-FP | Electroencephalography forward problem |
| EEG-IP | Electroencephalography inverse problem |
| EIT | Electrical impedance tomography |
| EIT-FP | Electrical impedance tomography forward problem |
| EIT-IP | Electrical impedance tomography inverse problem |
| EMA | Effective medium approximation |
| EPSP | Excitatory post-synaptic potential |
| ExSo-MUSIC | Extended sources Multiple Signal Classification |
| EZ | Epileptogenic zone |

F

| | |
|--------|--|
| FDR | False discovery rate |
| FE | Finite Element |
| FEM | Finite Element Method |
| fMRI | Functional Magnetic Resonance Imaging |
| FOCUSS | Focal Under-determined System Solver |
| FP | Forward problem |
| FSL | FMRIB [John Radcliffe Hospital] Software Library |

G

| | |
|------|------------------------------|
| GABA | Gamma-Aminobutyric acid |
| GLM | General Linear Model |
| GM | Grey matter |
| gPC | Generalised polynomial chaos |

I

| | |
|------|------------------------------------|
| IP | Inverse problem |
| IPSP | Inhibitory post-synaptic potential |
| IV | Independent Variable |

K

| | |
|----------------|---------------|
| K ⁺ | Potassium ion |
|----------------|---------------|

L

| | |
|--------|---|
| LCMV | Linearly constrained minimum variance |
| LFP | Local field potentials |
| LORETA | Low Resolution Electromagnetic Tomography |
| LSEE | Least-squares estimator |
| LTD | Long term depression |
| LTP | Long term potentiation |
| LU | Lower-upper (factorisation) |

M

| | |
|-------|--------------------------------|
| MCI | Mild cognitive impairment |
| MEG | Magnetoencephalography |
| MLE | Maximum likelihood estimation |
| MNE | Minimum norm estimates |
| MR | Magnetic Resonance |
| MRI | Magnetic Resonance Imaging |
| MSP | Multiple sparse priors |
| MUSIC | MUltiple SIgnal Classification |

N

| | |
|-----------------|----------------------|
| Na ⁺ | Sodium ion |
| NMDA | N-methyl-d-aspartate |

O

| | |
|-----|-----------------------------|
| ONS | Occipital nerve stimulation |
|-----|-----------------------------|

P

| | |
|-----------|--|
| PCG | Preconditioned conjugated gradient |
| PNS | Peripheral nerve stimulation |
| POP-MUSIC | Proper orthogonal projection MUltiple SIgnal Classification |
| PRISMA | Preferred Reporting Items for Systematic reviews and Meta-Analyses |
| PSP | Post-synaptic potential |

Q

| | |
|--------|---|
| QAS | Quality Assessment Score |
| QUADAS | Quality Assessment of Diagnostic Accuracy Studies |

R

| | |
|-----------|--|
| RAP-MUSIC | Recursively Applied Multiple Signal Classification |
| RE | Relative error |
| ROAST | Realistic vOlumetric-Approach to Simulate Transcranial electric simulation |
| ROI | Region of interest |

S

| | |
|---------|--|
| SimNIBS | Simulation of Non-invasive Brain Stimulation |
| sLORETA | Standard Low Resolution Electromagnetic Tomography |
| SPM | Statistical parametric mapping |

T

| | |
|------------|--|
| T-PBM | Transcranial photobiomodulation simulation |
| tACS | Transcranial alternating current stimulation |
| tDCS | Transcranial direct current stimulation |
| TENS | Transcutaneous electrical nerve stimulation |
| TMS | Transcranial magnetic stimulation |
| TRAP-MUSIC | Truncated Recursively Applied Multiple Signal Classification |

U

| | |
|----|----------------------------|
| UQ | Uncertainty quantification |
|----|----------------------------|

V

| | |
|-----|-------------------------|
| VNS | Vagus nerve stimulation |
|-----|-------------------------|

W

| | |
|---------|-------------------------------------|
| WM | White matter |
| WM_par | parallel oriented white matter |
| WM_perp | perpendicular oriented white matter |

NOTATION

Throughout the thesis (and unless otherwise stated), scalars are denoted by uppercase/lowercase letters, 1-D vectors as bold-face lowercase letters, and matrices (or multidimensional arrays) as bold-face uppercase letters.

| | |
|----------------------|---|
| \mathbf{j} | current density |
| \mathbf{j}^p | primary current |
| \mathbf{j}^R | return (secondary) current |
| σ | conductivity |
| $\underline{\sigma}$ | rank-2 conductivity tensor |
| I | current |
| V | voltage |
| R | resistance |
| ρ | charge density |
| t | time |
| \mathbf{e} | electric field |
| \mathbf{b} | magnetic field |
| μ | tissue permeability |
| ϵ_0 | electric constant |
| u | electric potential |
| u^∞ | singularity potential |
| u^{corr} | correction potential |
| \mathbf{r} | position |
| \mathbf{q} | moment |
| δ | Dirac delta distribution |
| Ω | head domain |
| Γ | head boundary (i.e., scalp surface) |
| $\hat{\mathbf{n}}$ | unitary vector normal to head boundary |
| f | abstract source term (dependent on source model) |
| φ | test function |
| K | suitable space in EEG-FP variational formulation |
| n | number of mesh nodes |
| \mathbf{A} | stiffness matrix |
| \mathbf{u} | vector of potential values on mesh nodes |
| \mathbf{c} | column (load) vector of source terms |
| x_r | reference electrode |
| \mathbf{L} | lead field matrix |
| \mathbf{S} | selection matrix |
| N_E | number of EEG electrodes |
| N_S | number of source dipoles |
| \mathbf{y} | forward model vector measurement |
| \mathbf{d} | additive noise |
| \mathbf{Y} | signal matrix containing superposition of dipole signals for potential data |
| \mathbf{X} | matrix representation of EEG data |
| F | data fidelity term |
| M | regularisation function |
| λ | minimising regularisation parameter |
| \mathbf{I} | identity matrix |

| | |
|-----|---------------------------------------|
| T | transpose |
| W | depth weighting matrix |
| R | resolution matrix |
| w | tDCS current injection pattern vector |
| Q | head volume tessellation element |
| h | injected electric current |

ACKNOWLEDGEMENTS

I would like to express my sincere appreciation to all those who have supported and helped me throughout the course of my PhD. Firstly, I am considerably grateful to my primary supervisor Dr Leandro Beltrachini for their continuous support, guidance, advice, and endless patience. Their gentle encouragement, reassurance and optimism has been essential for the completion of my PhD, especially when at times, I saw no end in sight. Leo has been incredibly understanding and kind when things have been difficult, but also directed and encouraged an expansion of my own knowledge and confidence in myself. I am incredibly thankful and consider myself lucky to have had Leo as my supervisor.

Secondly, I would like to thank my secondary supervisor Professor Giampaolo Pisano, who has since moved on to a different university, but was filled with eager enthusiasm and always willing to help in any way possible. I am also appreciative to Dr James Avery from Imperial College who provided equipment and training, fundamental for this PhD. He was constantly supportive, answering my relentless emails and questions and helping with any problems that arose. Thank you also to Dr Yi-Jhong Hang who equally offered equipment and necessary training. I am also very grateful for the Knowledge Economy Skills Scholarships (KESS 2) initiative and Magstim for their financial support, training opportunities and experiences. In particular, thank you to Anna Hodges and Dr Lothar Krinke who welcomed me to the company.

Finally, I would like to thank my friends and family for their unconditional support over the many years. Thank you to my closest friends, Rachel, Anna, Jake, and Bee for providing much needed encouragement, laughter, advice, fun, distractions, understanding, and long-lasting friendship. An important thank you to my Nan, although she may not always understand she was there with tears of joy and infinite encouragement and love. Equally as important, a thank you to my stepdad who, more of a father, has been wonderful, always there at the end of the phone and supporting me through the last few years. Lastly, but most importantly, I would like to thank my Mum, who was my best friend, my biggest supporter and most important person in my life. Sadly, she passed away toward the end of my PhD, but I know she would be proud of me, and I would not be where I am if it were not for her unconditional love. This is for you Mum, I love you.

Publications arising from the Thesis

- **The work from Chapter 3 has been published in Brain Topography (Springer):**

McCann, H., Pisano, G., & Beltrachini, L. (2019). Variation in reported human head tissue electrical conductivity values. *Brain topography*, 32(5), 825-858. Doi: 10.1007/s10548-019-00710-2.

- **Chapter 4 has been published in Biomedical Physics & Engineering Express (IOP):**

McCann, H. M., & Beltrachini, L. (2021). Does participant's age impact on tDCS induced fields? Insights from computational simulations. *Biomedical Physics & Engineering Express*. Doi: 10.1088/2057-1976/ac0547.

- **The work from Chapter 5 has been published in the Journal of Neural Engineering (IOP):**

McCann, H. M., & Beltrachini, L. (2021). Impact of skull sutures, spongiform bone distribution, and aging skull conductivities on the EEG forward and inverse problems. *Journal of Neural Engineering* (in press). Doi: 10.1088/1741-2552/ac43.

GENERAL INTRODUCTION

The human brain is one of the most complex systems we know of. Neuroimaging techniques allow us to explore the brain anatomy and physiology and their relationship to biological processes. Of these, structural neuroimaging such as Magnetic Resonance Imaging (MRI; Dale et al., 2015), and computed tomography (CT; Cervantes, 2016) enable visualisation of specific head structures. Furthermore, electrical impedance tomography (EIT) can be utilised to infer the electrical conductivity field within the head (Holder, 2004). Contrastingly, functional neuroimaging measures a particular brain function to ascertain their relationship with behaviour or disease. This includes functional MRI (fMRI), which measures the blood oxygenation level dependent (BOLD) effect, and electro/magneto-encephalography (E/MEG) which is sensitive to the electromagnetic activity of the brain (Hari & Puce, 2017). Neuromodulation techniques, such as transcranial direct current stimulation (tDCS) and transcranial magnetic stimulation (TMS), on the other hand, aim to alter brain activity through delivery of an electric or magnetic stimulus (Knotkova & Rasche, 2014).

Each technique has varying spatial and temporal resolution, as depicted in Figure 0.1.

Notably, electromagnetic methodologies (as E/MEG and TMS/tDCS) have high temporal resolution (1 – 5 ms) but particularly low spatial resolution (limited to brain regions, i.e., on the order of cm; Darvas et al., 2004). These modalities are therefore able to capture rapid activity, such as electrical impulses between neurons that are essential for communication throughout the brain, executive and automatic functioning, stimuli response and features of cognition, emotion, and perception. Understanding the electrical signals within the brain, through measurement (i.e., E/MEG) and modulation (i.e., tDCS/TMS), provides insight into these processes for both research and clinical applications.

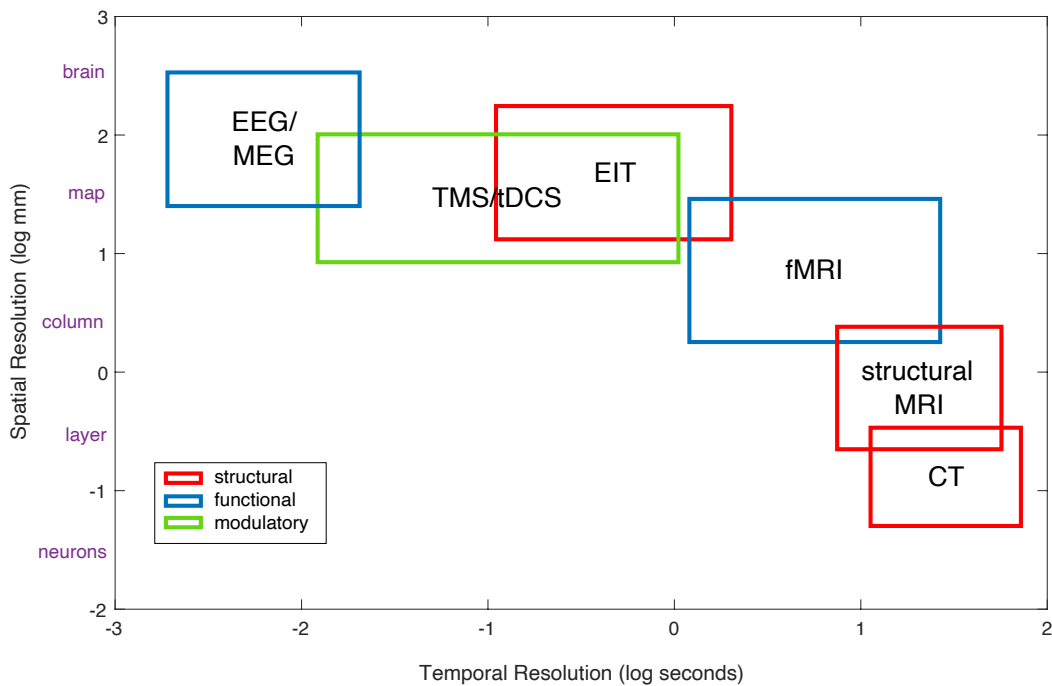


Figure 0.1: Representation of brain imaging modalities and their respective temporal (in log seconds) and spatial (in log mm) resolutions for techniques most frequently referred to as structural (red), functional (blue) or modulatory (green) acquisition.

Determining the spatial localisation of E/MEG activity and the TMS/tDCS stimulation, however, is dependent on many parameters and requires additional computational techniques. This includes the *forward problem (FP)* which determines the observable electromagnetic measurements from a known current source and assumes the domain as perfectly known. In EEG, the *inverse problem (IP)* then consists of reconstructing the activity from a given electromagnetic signal, whilst in EIT the objective is to estimate electrical conductivity from the given FP. The IP in tDCS comprises determining the optimal current injection pattern on the scalp that produces the most ideal estimate of the desired current density at the location. The EEG-FP computes the electric potential generated from a known source in the conductor, relying on an accurate head domain (geometry of the tissues of the head, such as the scalp, skull, and brain) and electrical conductivity field. These parameters, both of which vary throughout participants, are essential for determining the propagation of current from the source to the scalp. Correct tissue conductivity knowledge is particularly essential where, for example, the electrical current will travel more readily through the highly conductive cerebrospinal fluid (CSF) than the highly resistive skull.

Given the computationally modelled current from a known source, the IP then aims to localise the electrical activity by determining the best fit between the modelled (FP solution) and the observed data (i.e., that measured with EEG). The IP, however, does not have a unique solution and is therefore known as an ill-posed problem (Hämäläinen et al., 1993). This is due to the fact a sole solution does not exist to explain the observable data. As an illustration, posed by Keller (1976), when asking the question “what is the question to which the answer is 4?”, there are many possible solutions. These include mathematical options such as “what is $2 + 2$?”, “what is 1×4 ?” etc., whereas the true question may have been “how many legs does a giraffe have?”. Without further information, it is impossible to determine the question being asked. This is true when generating the source of electrical activity within the brain, as infinite source combinations allow to explain identical measurements (Gylys-Colwell, 1996). Without an accurate FP solution, which is dependent on precise and accurate knowledge of head anatomy and tissue conductivity, an accurate IP solution and therefore source localisation is impossible.

The presented thesis thus chose to focus on spatial localisation of electrical activity within the brain, particularly as modulated with tDCS (i.e., exogenous) and measured with EEG (i.e., endogenous). The contribution of relevant parameters, specifically head anatomy, and tissue conductivity, to tDCS stimulation propagation and EEG source analysis was explored. The importance of accounting for variation in head tissue conductivity and geometry according to participant demographics was highlighted. This was undertaken through simulation studies with particular emphasis on conductivity variation of the skull, the most highly resistive tissue, as a function of age.

Overview of Thesis

Chapter 1. Brain Activity.

This chapter introduces the neurophysiological basis of brain activity and the neuroscientific origins of EEG and tDCS. The fundamental understanding of neuronal activity is described, including the production of electric and magnetic activity and thus how these are measurable and modulated by the discussed techniques. The basic protocols for EEG and tDCS are also described. Finally, the anatomy of the human head is discussed to understand the relevance of head geometry.

Chapter 2. Forward and Inverse Problems.

Mathematical formulation of the forward and inverse solutions relevant for EEG and tDCS are provided in this chapter. This begins with the fundamental equations describing electromagnetic fields preceding forward problem construction. Head and source modelling techniques are also discussed in detail, with various methods described. This leads to defining the lead field matrix – mapping cortical activity to electromagnetic measurements. The basic principles of the inverse solution are discussed, and various dipole fitting methods mentioned. The formulae are finally related to tDCS current propagation.

Chapter 3. Head Tissue Conductivity Variation.

Chapter 3 outlines the importance of accurate conductivity values for electromagnetic techniques. A systematic meta-analysis is provided to assess the significant and important factors effecting conductivity variation in 15 different head tissue types (ranging from different skull to brain tissues). This variation included those as a result of measurement technique (such as direct measurements, E/MEG, diffusion tensor imaging (DTI) and EIT), other methodology parameters (e.g., temperature, frequency, etc.) and participant demographics (such as age and pathology). The results highlight significant variation in electrical conductivity of the scalp, whole-skull, the layered-skull, grey matter (GM), and white matter (WM), which could be attributed to a combination of differences in methodology and demographics.

Chapter 4. Impact of Age on tDCS Induced Fields.

The previous three chapters highlighted the role tissue conductivity plays in electromagnetic distribution within the head and how these values vary throughout the literature, employed methodology and participant demographics. An important contributing factor was revealed to be the relationship between skull conductivity and participant age, which remains unclear. This chapter explored the impact that changing skull conductivity as a proposed function of age effected tDCS induced fields via a simulation study. The motivation for the research is first explained and the methodology outlined. This includes generation of the head models and proposed homogeneous, age-dependent conductivity values and the resultant tDCS induced field calculations and additional parameters. The results emphasised significant deviations in electric fields as a function of age and provided suggestions for adjusted tDCS dose across the lifespan. Further research for individualised head anatomy and *in vivo* skull conductivity were recommended.

Chapter 5: Skull Conductivity and EEG Source Localisation

The first two chapters outlined the necessity for accurate head geometry and tissue conductivity in electromagnetic source analysis. Following from this, Chapter 3 indicated how such conductivity values, particularly that of the skull, vary throughout participants and the literature. Proposed skull conductivity deviation as a function of age was revealed to impact tDCS induced electric fields in Chapter 4. Uncertain skull conductivity and head geometry was therefore hypothesised to additionally impact EEG forward and inverse solutions. Chapter 5 compares inhomogeneous skull conductivity models, accounting for bone composition differences and the presence of adult sutures against homogeneous models neglecting such details for EEG-FP and IP solutions. The presented simulation study aimed to determine the impact of adult sutures and varying proportion of spongiform bone on EEG source localisation, particularly when also accounting for age.

Chapter 6. General Discussion

The final chapter concludes the main contribution of the presented thesis. Firstly, a thesis overview is provided summarising the previous chapters and the respective important findings. Propose future research is also outlined and final conclusions as well as a take-home message are discussed.

CHAPTER 1: BRAIN ACTIVITY

1.1. Overview

This chapter introduces the neurophysiology underlying EEG and tDCS methodologies. The fundamental characteristics of neuronal activity are discussed, including the structure and function of neurons, the electrochemical processes involved in signal generation and transmission and the resultant electromagnetic activity. These are related to the origins of EEG measurements and the typical protocols and parameters are considered. The mechanisms underlying the neuromodulation of electric activity via tDCS are further discussed. Finally, the importance and relevance of accurate head geometry for EEG source localisation and tDCS optimisation are mentioned and the basic anatomy explored.

1.2. Neurophysiology

The average human brain contains approximately 86 billion neurons and as many glial cells (necessary for maintaining ion concentration, structure support and transporting nutrients; Azevedo et al., 2009). Information-processing neurons comprise a cell body, dendrites, and an axon. The cell body, or soma, is where the cell nucleus resides and is responsible for synthesising vital proteins. The dendrites are long filaments extending from the cell body that receive inputs from connecting neurons. The axon (a longer branched cellular filament) attaches to other neurons or organs and is covered with a myelin sheath, formed from oligodendrocytes, that insulates the nerves fibres, and accelerates signal transmission. An axon terminal occurs at the end of the axon, farthest from the soma, and contains the synapses where neurotransmission occurs (Debanne et al., 2011). An example of a neuron can be seen in Figure 1.1. Each neuron is connected to thousands of others, with trillions of synaptic connections.

Neurotransmission is the fundamental force for information transfer across the brain, regulating inhibitory and excitatory processes and underlying sensory and executive, automatic functions. Efficient neurotransmission occurs from a repetitive cycle of transfer and retrieval across synaptic regions (Bean, 2006). Differences between intra- and extracellular ion concentrations (sodium $[Na^+]$, potassium $[K^+]$ and chloride $[Cl^-]$) maintain

voltage gradients across neuron membranes (approximately -60 to -70 mV). Ionic pumps and selective membrane permeability stabilise the unequal distribution of these electrically charged ions (particularly Na^+ and K^+). Stimuli can cause specific ion-channels within the cell membrane to open. This results in an influx of ions changing the membrane potential and ‘exciting’ the cell. If the voltage change reaches a certain threshold, an action potential (electrical impulse) is fired, travelling from the neuron’s soma, along the axon, to the dendrites. The speed of conduction depends upon the presence of the myelin sheath and ranges from 1 to 100 m/s. Nodes of Ranvier interrupt the insulated sheath and allow the action potential to be regenerated (Miller et al., 2017). The action potential amplitude remains constant at 100 mV due to the so-called all-or-none principle, which states that, – if a neuron responds at all, it responds completely (Lucas, 1909). The synapse, near the end of the axon allows electrical impulses to pass from the presynaptic cell via diffusion of transporter molecules (neurotransmitters) across the synaptic cleft (physical space between two neurons). Some molecules then bind to receptor proteins on the postsynaptic cell membrane (Figure 1.1). Molecule binding in turn opens specific ion channels, allowing the resultant charge flow to alter the membrane potential in the receiving cell – termed the post-synaptic potential (PSP). This causes an electrical field and current to flow either into the cell, depolarising it and hence producing an excitatory PSP (EPSP). Conversely the current can flow out of the cell, hyperpolarising and therefore inhibiting it (IPSP). These extracellular field potentials are frequently referred to as local field potentials (LFPs; Miller et al., 2017; Hari & Puce, 2017).

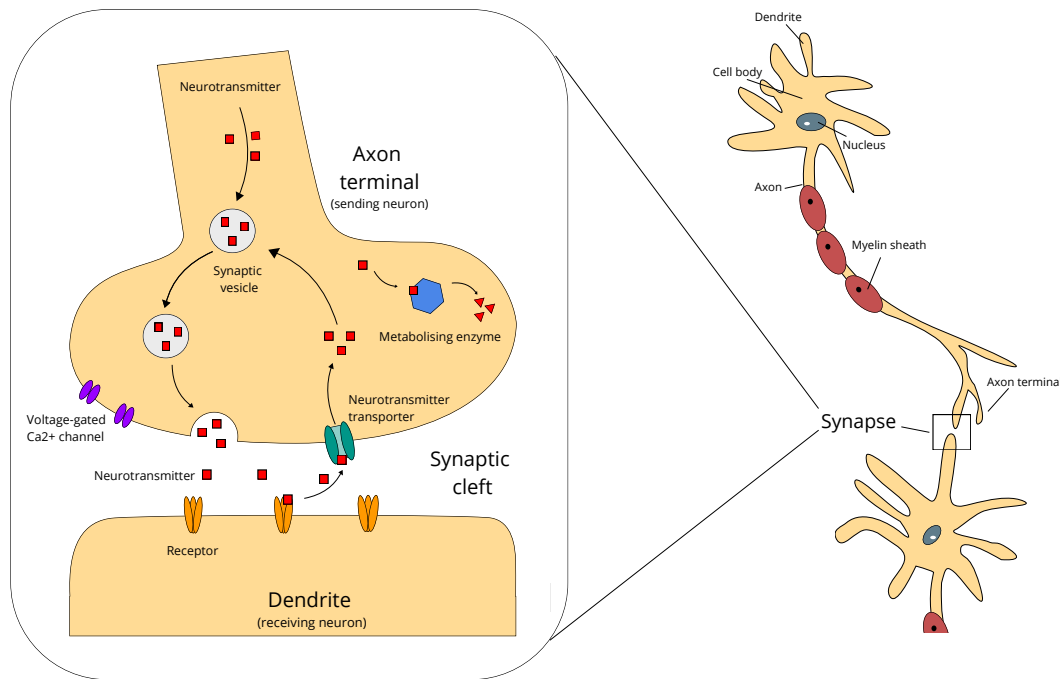


Figure 1.1: Schematic diagram of a neuron and its synapse. The figure depicts neurotransmission from an axon terminal of one neuron to the dendrite of the receiving neuron, across what is termed the synapse. Following application of stimuli and if changes in cell voltage reach a certain threshold, an action potential is released and travels from the neurons soma along the axon, accelerated due to the myelin sheath, to the axon terminal (depicted to the right). At the axon terminal, neurotransmitter transporters allow electrical impulses to pass from the presynaptic to postsynaptic cell dendrites via diffusion across the synaptic cleft. Here, molecules can then bind to receptor proteins and open specific ion channels, in turn altering the membrane potential of the receiving cell (depicted to the left). This either hyper- or de-polarises the cell and contributes to the extracellular field. Adapted from Pickel & Segal (2013).

All excitable membranes contribute to the extracellular field, which is the superposition of all ionic processes. The largest involvement, however, comes from synaptic activity of PSPs. The local de- or hyperpolarisation of the postsynaptic membrane following neurotransmitter release creates a potential cell membrane gradient and current. EPSPs generate an active sink at the extracellular synapse and a passive source along the cell. IPSPs on the other hand generate an active source at the synaptic level (non-excited cell body membrane) and a passive sink along the cell (at the dendritic membrane; Henry, 2006). A current flow between the source and sink is thus produced by the difference in potential. Due to the LFP sink-source derivation, the electric field surrounding one neuron is usually modelled as a current

dipole oriented along the dendrite (de Munck & Peters, 1993; Hämäläinen et al., 1993). A mathematical dipole consists of two adjacent oppositely charged sites, where positive current (i.e., sodium and calcium) flows from one end (the sink) to the other (the source). Although dendritic current can flow in both directions (producing a quadrupole source), the majority of the current flows toward the postsynaptic cell body and due to the asymmetric geometry of the cortical layer one component is dominant and thus considered a current dipole, not quadrupole (Brette & Destexhe, 2012). However, quadrupoles can arise from two dipoles located close together, or from specific folding of the cortex (Beltrachini, 2018). The current through the synapse can be calculated from the voltage change. This equivalent pointwise current dipole may therefore be used to approximate the electrical activity generated from the centre of an active area. The electrical potential change triggered by the intra- and extracellular ion flow induces the electromagnetic field propagation within the tissue (an example of potential field generation and corresponding dipole is depicted in Figure 1.2). Following the electric charge conservation law, this produces a primary current that predominantly travels within the neuron (and are thus intracellular) due to the high resistance of the cell membrane. Some primary current, however, continuously flows out of the cell to produce secondary (a.k.a. return or Ohmic) currents in the opposite direction that close the current path in extracellular space (Hämäläinen et al, 1993; Rutecki, 1992).

1.3. Electroencephalography

Electroencephalography is a non-invasive electrophysiological modality that records electrical activity on the scalp stemming from the macroscopic brain activity beneath the signals. It has the advantage of being relatively low in cost and easily transferable and thus is used worldwide. Alongside this, EEG has high temporal resolution (of several milliseconds), allowing invaluable insights into dynamic cognitive processes. EEG exploits the current voltage changes in synapses to measure the electrical activity in brain neural cell assemblies (de Munck & Peters, 1993; Hämäläinen et al, 1993).

EEG employs a distribution of multiple scalp electrodes to passively and non-invasively measure the voltage fluctuations (the secondary current flow) arising from ionic current flow of thousands of synchronously active neurons. Typically, between 2 and 512 (as used in Ryyänen et al., 2004) electrodes are placed along the scalp boundary, at least 2 cm from

brain tissue. The volume conduction of ionic current flow generates a wave of ions which can reach electrodes distributed on the scalp and effect electrons on the metal in the electrodes. Differences in this effect, and thus the electrical potential, between any two electrodes can be measured using a voltmeter (usually in μV). The product of these recorded voltages over time results in the observable EEG measurements (Tatum, 2021).

Scalp electrodes cannot detect the small electric field generated by one neuron alone. This is particularly considering that the electric field additionally travels from brain tissue, through the CSF, skull and scalp and thus impeding the current, the amplitude of which would be generated by a single neuron. Hence, thousands of synchronously active neurons are required, generating synchronous extracellular PSPs, resulting in a detectable extracellular potential field (Nunez & Srinivasan, 2006). The potential field travels from the source of activity, within the brain, through the layers of the head (depicted in Figure 1.2) to reach the scalp, where the signal is then perceived. Most of these signals are thought to be generated from pyramidal neurons due to their spatially aligned and unique orientation. Their dendrites are perpendicular to the surface and parallel to one another. This amplifies their extracellular potential and thus electric field surrounding the neuron, frequently represented as a current dipole (Figure 1.2; de Munck et al., 1988). The electrical field surrounding a pyramidal cell corresponds to a dipole as the long-elongated axis results in evident membrane potential differences at either end. The resultant activity represents the sum of all EPSPs and IPSPs of cortical pyramidal neurons to typically produce a vertical dipole perpendicular to the scalp, due to their orientation, and thus measurable through EEG (Da Silva, 2009).

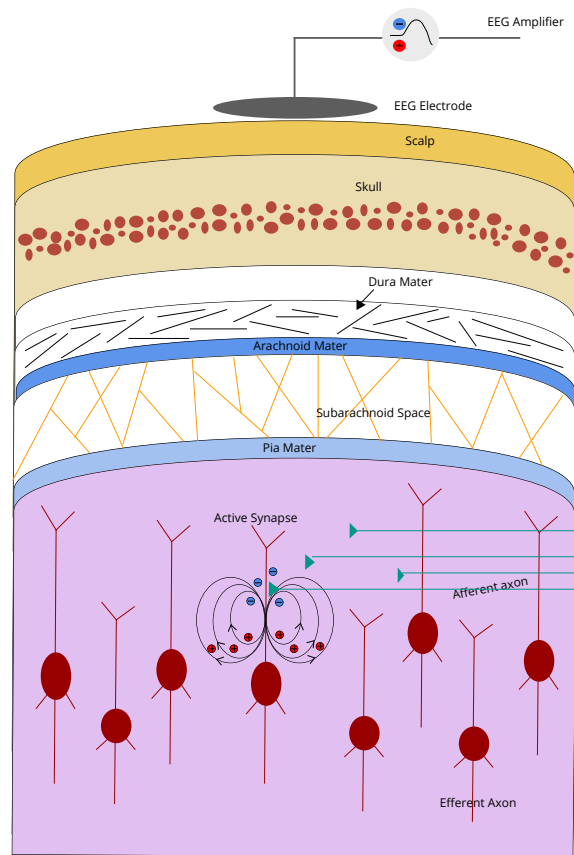


Figure 1.2: Schematic diagram of pyramidal neurons generating a potential field. The EEG electrode resides on the surface on the scalp and is attached to an EEG amplifier, detecting changing electric fields within the brain (purple layer). The positive and negative potential field is generated from thousands of active synapses across spatially aligned pyramidal neurons (red diagrams) within the brain. This electric field travels from the brain across various layers of the head, including the pia mater (light blue), subarachnoid space (white with orange lines), arachnoid mater (dark blue), dura mater (white with black lines), skull (beige, representing two compact bone layers and a sandwiched layer with red circles indicating spongiform bone) to reach the scalp (yellow layer) electrode. See section 1.6 for further descriptions of each head layer. Note that the size and relative width of each layer is not proportional and is for illustration purposes only. Figure adapted from Bear et al., (2001).

1.3.1. EEG Interpretation

The polarity of surface EEG recordings depend upon synaptic activity location within the cortex. Upward deflections, as recorded in EEG, are a result of EPSPs in superficial cortical layers or IPSPs in deeper layers. Whereas downward deflections are a consequence of deep layered EPSPs or superficial layered IPSPs (Kirschstein & Köhling, 2009). This produces a graphical waveform of rhythmic activity and transients, representing neurotransmission signal variations within the brain. The measured EEG oscillations illustrate synchronised neuronal activity at varying frequencies and is described as the rhythmic activity. Many of these frequencies are characteristic selections with spatial ranges associated with different brain functions and diseases (e.g., sleep stages, epilepsy, schizophrenia, among many others; Figure 1.3).

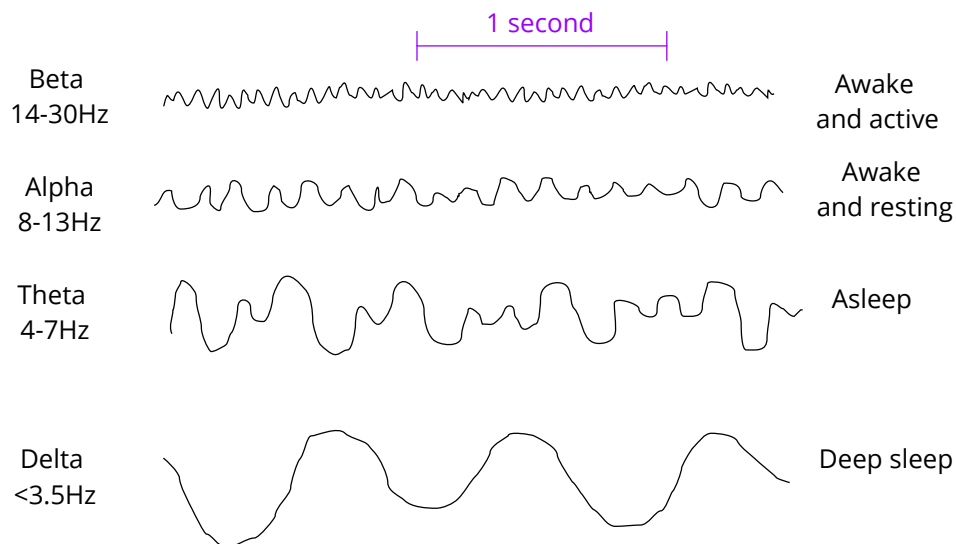


Figure 1.3: EEG oscillation examples during wakefulness and sleep. The waveforms represent synchronised neuronal activity of four different frequency ranges over approximately 2.5 seconds. The frequencies, beta, alpha, theta, and delta coincide with awake and active, awake and resting, asleep and deep sleep states, respectively.

EEG, in a clinical setting, is most commonly employed to diagnose epilepsy. Focal epileptiform activity is signified by rapid, synchronous potentials in hundreds of neurons in a distinct brain area. Dispersed epileptic activity can also be synchronously distributed throughout the entire brain, with a localised epicentre, termed generalised epilepsy. Epilepsy can thus be diagnosed with an EEG, when other potential causes, such as syncope or drugs and alcohol are ruled out. Ictal EEG recordings can also be obtained during a seizure (as opposed to inter-ictal – between seizures) when further information is required for diagnosis

or treatment. EEG can additionally aid in treatment by localising the source of epileptogenic activity when resection or surgery is required (Engel, 2013). Methodologies with higher spatial resolution, however, are typically employed due to the low spatial resolution of scalp EEG (source localisation is discussed in detail in Chapter 2). For example, stereo EEG, where depth electrodes are implanted by neurosurgeons and allow lower voltage (due to the current not being shielded by the high resistivity of the skull) and faster brain activity components to be detected (Henry, 2006). Aside from epilepsy, EEG can also be beneficial for diagnosing and treating stroke, sleep disorders, brain tumours, damage or dysfunction and brain death, among others.

Additionally, EEG is extensively used within a research setting, for example for exploring memory, language, motor function, sleep, emotional processing and regulation, perception, spatial awareness etc. It is further utilised as a tool for research and treatment of multiple psychological, developmental, and physiological disorders, such as autism, attention deficit hyperactivity disorder (ADHD), Parkinson's Disease, and mood, anxiety, and psychotic disorders.

1.3.2. EEG Systems

A typical EEG measurement system comprises of electrodes, a multichannel amplifier (to reinforce weak signals) and a data acquisition system (to record, display and store data). Each EEG electrode recording represents a spatially smoothed form of the LFP.

EEG electrodes attach to the scalp using conducting electrode gel, traditionally in the standard 10-20 position scheme and embedded within a head cap. Dry electrodes also exist which do not require application of a conductive gel and therefore have a faster preparation time and can be efficiently applied by non-experts (Fiedler et al., 2014). The international 10-20 system denotes the distances between neighbouring electrodes. This is either 10 or 20% of the total nasion (on the bridge of the nose, between the two eyebrows) toinion (at the centre of the base of the skull, the tip of the occipital bone) to right to left skull dimension (left and right preauricular). The traditional 10-20 system has a total of 21 electrodes (Towle et al., 1993). When a higher number of EEG electrodes are employed, extra electrodes are placed according to the 10% division, halfway between the existing 10-20 electrodes. These additional electrode placement systems include, for example the 10-10 system (with 81

electrodes based on 10% fractions of the nasion-inion and interauricular lines) and the 10-5 system (with 345 electrodes, based upon 5% fractions; Oostenveld & Praamstra, 2001). Variations on these three placements also exist, for example including 32, 64 and 164 electrodes in total, this is also dependent on the specific EEG cap manufacturer (Hari & Puce, 2017). Each electrode is connected to an input of a differential amplifier (one amplifier per pair of electrodes), which amplifies the corresponding voltages between the active electrode and the reference (discussed below).

Voltages recorded at each electrode in EEG are relative to measurements at other electrodes. Consequently, a reference electrode that acts as a ‘baseline’ for the remaining channels is essential. The reference electrode should ideally be placed where no neural activity contributes to the measurement, however no place in the human body is electrically silent. The reference is thus popularly placed in areas farthest from the region of interest (ROI), such as the nose, earlobe, or mastoid. Often, EEG caps have pre-defined reference positions, frequently in the right frontal region (termed Fz) and the top centre of the scalp (Cz), which do not amplify the signal in one hemisphere versus the other (Hari & Puce, 2017). An average reference montage can additionally be used, where the output of all the amplifiers is totalled and averaged and provided as the collective reference. A Laplacian montage, on the other hand, uses the difference between one electrode and the weighted mean of its surrounding electrodes (Nunez & Pilgreen, 1991).

Classically, EEG is acquired in regular research or clinical rooms. However, measurements inside Faraday cages, or MEG shielded rooms (made of aluminium and mu-metal, to reduce high and low-frequency noise, respectively [Burgess, 2020]), to avoid external electrical interference, can be performed. Transportable EEG devices also exist (Usakli, 2010).

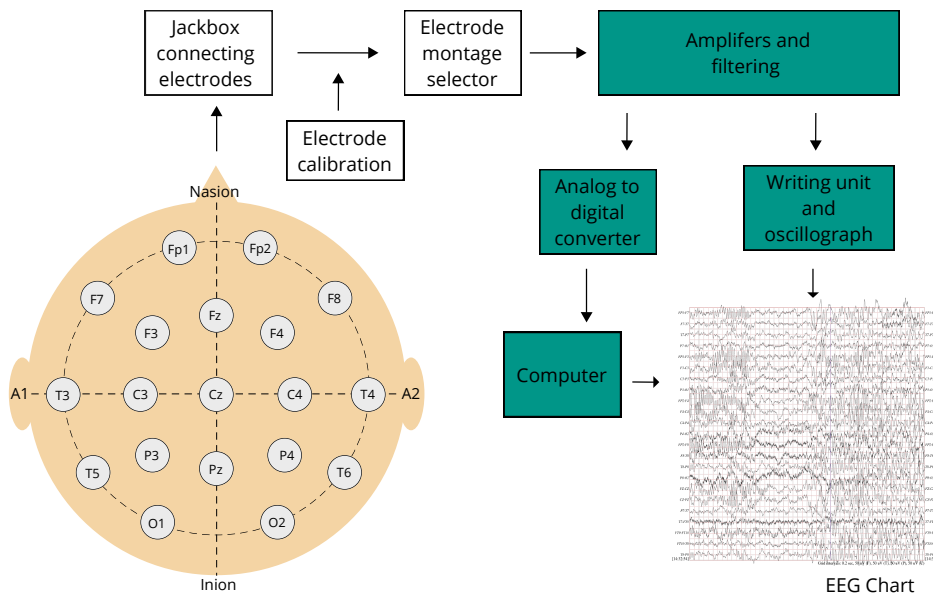


Figure 1.4: Schematic representation of an EEG system. The 10-20 electrode position system is displayed on a human scalp, using the appropriate typical naming system to indicate the pre-frontal (Fp), frontal (F), temporal (T), parietal (P) occipital (O) and central (C) regions. The nasion, inion left (A1) and right (A2) preauricular is also displayed on the scalp for reference. The electrodes are connected to a jackbox and the electrode montage selected, this includes calibration of the electrodes. The acquired signals are amplified, filtered, and converted from analog to digital. The oscillograph records the EEG oscillations and a computer programme allows representation of EEG signals, as displayed in the example EEG chart. The EEG data example is taken from the openly available database described in Shoeb (2009).

1.3.3. Strengths and Limitations

As briefly discussed, an advantage of EEG, particularly over other imaging methods, is the significantly lower hardware and administration costs. Alongside the base apparatus, a specialist environment is not necessary, unlike MEG and MRI, and can be carried out in a quiet room. EEG is also portable and relatively small in size, allowing it to be easily transferred between use. Taken together, this allows EEG equipment to be easily accessible and applied in clinical and research settings worldwide. Another main advantage is that EEG has relatively high temporal resolution (on the order of milliseconds) and can thus capture rapid information such as stimuli response and epileptic seizures. Some characteristics of EEG also allow for specific analysis such as recording activity in participants with no or

limited motor response (Secco et al., 2021), relative stability to participant movement, distinguishing covert processing (where a response is unnecessary) and detecting activity to inattentive stimuli. It also provides benefits for auditory processing (due to EEG being relatively silent), and for determining processing stages (as opposed to the final response; Lochy et al., 2015) and life stages (for example specific characteristic of brain development through sleep analysis [Campbell et al., 2012]). There also exist fundamental advantages of EEG compared to other imaging modalities, including its non-invasive nature (e.g., compared to stereo EEG), non-exposure to radiation and high-intensity magnetic fields and non-augmentation of claustrophobia (for example compared to most CT and MRI systems).

Despite these benefits, EEG has several limitations. A significant disadvantage is its relatively low spatial resolution (see Figure 0.1). As discussed within the General Introduction (and throughout the thesis), determination of a unique current source for a given EEG signal (i.e., the EEG inverse problem solution) is highly dependent on accurate forward problem simulations. This is computationally expensive and relies on correct and precise head volume conductors (and, consequently, complimentary structural imaging data). Furthermore, EEG is less sensitive to deep sources, such as dendrites residing within the sulci or those emitting tangential currents to the skull and is instead most perceptive to superficial layers (in the cortex) and radial currents (Ahlfors et al., 2010; Haueisen et al., 2012; Srinivasan, 1999). EEG is additionally limited to capturing dendritic currents and non-axonal action potentials. Following this, due to the preference for pyramidal neuron activity, the contribution of other neuronal populations to EEG signals is restricted (Murakami & Okada, 2006). EEG additionally has relatively low signal-to-noise ratio, meaning advanced data analysis is necessary and, for research purposes, a large number of participants is required to enable meaningful conclusions.

1.4. Transcranial Direct Current Stimulation

Non-invasive neurostimulation modulates nervous system activity by exploiting electromagnetic approaches. Typical non-invasive methods include TMS and tDCS which stimulate brain areas through magnetic fields or electric currents respectively. Other techniques exist such as transcranial alternating current stimulation (tACS), electroconvulsive therapy (ECT), transcutaneous electrical nerve stimulation (TENS) and invasive procedures,

such as deep brain stimulation (DBS) and vagus, peripheral or occipital nerve stimulation (VNS, PNS and ONS respectively) but the focus remains on tDCS for the presented thesis.

For tDCS, a fixed, low direct current (approximately 0.5 – 2 mA) is delivered using a battery-powered device via an electrode encased in a relatively large (25 – 35 cm²) saline-soaked sponge. The current is ramped up to the desired intensity, over a specified time period (on the order of seconds). A positively charged electrode (so-called anode) is placed over the desired stimulation region on the scalp to induce intracerebral current flow. A negatively charged electrode (termed cathode) sponge is placed elsewhere (typically bihemispherically). This completes the circuit and allows current to flow from the anode, through the conductive head tissue, to the cathode. The electrical current penetrates the scalp and skull to modulate spontaneous neural activity by changing the neural resting membrane potentials and hence neuronal excitability (Nitsche et al., 2008). Positive ions within the head flow toward the cathode, whilst negative ions flow toward the anode. This modulation can alter brain function and can thus be utilised to provide information regarding brain activity or for various therapies (Nitsche et al., 2008). Typically, anodal stimulation increases the neuronal excitability, whereas cathodal decreases the excitability of the target region. Alongside the standard setup equipment, control software can be employed to automate the stimulation protocol.

1.4.1. Systems and Protocols

The electrode positions determine the targeted brain region, most frequently compiled with the 10-20 EEG system (Nitsche et al., 2008). For this, the participants head is firstly measured (i.e., from the inion to the nasion and from the left to right pre-auricular) and used in conjunction with the 10-20 system to determine the ROI. Accurately placing the electrodes within the desired region is essential for effective tDCS stimulation. Placement can be enhanced by employing complementary structural imaging data (such as MRI) to determine the location of interest beforehand (Nitsche et al., 2008). This can be done with the support of a neuronavigational software. The target electrode is placed on the scalp over the ROI, guided by the 10-20 system or neuronavigational methods. The reference is typically located opposite to the anode, where a larger distance between them (suggested as greater than 8 cm) is expected to increase cortical modulation (Wagner et al., 2007). Placing the two electrodes too close together may result in current being shunted through the highly conducted CSF, or

across the scalp, rather than through the cortex (Moliadze et al., 2010). The reference can alternatively be placed extracephalically (i.e., not on the scalp) which limits the effect the cathode has on cortical modulation (Nitsche & Paulus, 2011). Differences in electrode placements (extra or intracephalically) can alter the current direction. Consequently, determining their positions based on the research hypothesis or clinical goal beforehand is imperative. Dual stimulation can also be obtained where the location of both electrodes is essential to excite one region (anodal current) and inhibit another (cathodal current).

The size of electrodes typically varies between 25 (5 x 5) – 35 (5 x 7) cm², where smaller electrodes result in a more focal target site. The most appropriate size can depend on the ROI for stimulation. To ensure limited stimulation of the reference electrode, a small focal stimulation and a larger reference electrode can be employed (Thair et al., 2017). The anatomy of the head is an additional factor which influences stimulation site and optimum electrode size. For example, using the same electrode size on an adult versus an infant (who have notably smaller head geometries) may result in a larger current spread and reduced focality in infants compared to adults.

As with electrode position, the stimulation intensity and duration vary depending on the clinical or research goals. The majority of applications range between 5 – 30 minutes at 1 – 2 mA (Thair et al., 2017), intensities above and below this have additionally been utilised, for example in stroke patients. The stimulation duration regulates the return of cortical excitability to baseline, i.e., the after-effects (a longer duration increases the after-effect time). The relationship between duration and intensity, however, is not necessarily linear. For example, high intensity or high duration can induce an inhibitory (as opposed to excitatory) effect for anodal stimulation and vice versa for cathodal stimulation (Batsikadze et al., 2013). Furthermore, although it is generally assumed higher intensities translate to an increased effect, this trend is also not necessarily linear and can be influenced by many factors such as head anatomy and size, electrode size, participant demographics, etc. Brain stimulation simulation tools such as Simulation of Non-invasive Brain Stimulation (SimNIBS; Thielscher et al., 2015) allow for exploration of specific tDCS parameters and quantification of how factors influence current flow and hence induced electric fields. SimNIBS for example produces realistic calculations of the electric field induced by TMS and tDCS. This software employs and integrates with MRI segmentation tools FreeSurfer (Fischl, 2012) and FSL (FMRIB [John Radcliffe Hospital] Software Library; Jenkinson et al., 2012) as well as open-

1.4.2. Mechanism of Action

tDCS is a neuromodulatory interaction, working by altering membrane potentials, rather than directly inducing targeted neuronal action potentials (as with TMS). When a negative stimulation (cathodal tDCS) is delivered, a weak, constant, electrical current flows from the anodal to cathodal electrode polarising brain tissue. An electron pool gathers around the cathodal electrode, increasing negative charge and in turn hyperpolarising (inhibiting) the cathodal targeted area. This decreases neuron excitability and decreases spontaneous cell firing. Conversely, the opposite occurs during positive (anodal) stimulation, which depolarises (excites) the anodal targeted area and increases spontaneous cell firing (Nitsche et al., 2008). The intensity (mA), electrode size (cm²), density (mA/cm²), position and stimulation duration effect the cortical excitability and magnitude and is therefore altered dependent on research/clinical treatment aims.

Although the mechanisms behind tDCS stimulation are widely attributed to membrane-potential polarity shift, a complete understanding is unknown. For example, research has revealed tDCS modifies synaptic microenvironments such as N-methyl-d-aspartate (NMDA; excitatory) receptors, and gamma-Aminobutyric acid (GABA)-ergic (an inhibitory neurotransmitter) activity (Liebetanz et al., 2002). Further to this, tDCS is proposed to promote cortex meta-plasticity, indicated by a build-up of Ca²⁺ within the cortex following tDCS stimulation, which increases the pH environment. Generation of OH⁻ and H⁺ alongside this, alters the intracellular environment, both contributing to the induced plasticity (Monai et al., 2016). Furthermore, tDCS can achieve cortical changes long after the stimulation has ceased. These effects are thought to be dependent on protein synthesis and associated intracellular calcium concentration alterations. Thus, tDCS has also been suggested to promote long term potentiation (LTP) and long-term depression (LTD), a persistent strengthening or weakening, respectively, of synapses and thus synaptic activity and PSPs (Nitsche et al., 2008). This phenomenon also underlies synaptic plasticity.

The neuromodulatory tDCS technique has demonstrated beneficial effects for a range of psychological and neurological disorders, such as depression (Nitsche et al., 2009), addiction (Lapenta et al., 2018) and schizophrenia (Agarwal et al., 2013), Alzheimer's disease, stroke, chronic and movement disorders (Flöel, 2014) as well as cognitive enhancement for healthy and clinical populations (Hsu et al., 2015). Further to this, tDCS is also extensively utilised

within research, for example, in memory and learning, particularly involving plasticity (Ridding & Ziemann, 2010).

1.4.3. Strengths and Limitations

One advantage of tDCS is its cost effectiveness, requiring limited equipment and no specialist environment. This also allows the modality to be easily transportable between settings and accessible worldwide. Alongside this, tDCS is relatively simple to utilise, meaning, highly specialist training is unnecessary. These strengths also allow tDCS to be carried out within participants' homes, particularly beneficial for treatment purposes. The advantages are particularly evident when compared to other neuromodulatory techniques, such as TMS. Furthermore, tDCS is generally considered safer than TMS as it is less likely to induce seizures and has no serious adverse effects (Stagg & Nitsche, 2011). For research purposes, sham tDCS, compared to sham TMS is also more indistinguishable than the respective control and is thus superior when exposing placebo effects. Another main advantage of tDCS is the potential for treatment of several disorders non-invasively, without the need for drug intervention. This is particularly attractive when the use of pharmaceuticals is limited, for example due to cost, allergies, or drug interactions. Similarly, tDCS allows for temporary and reversible cortical modulation, as opposed to the potentially long-term effect of drugs and surgery. In a research setting, tDCS can therefore be employed to determine brain-behaviour relationships through modulation without invasive procedures or expensive and time-consuming equipment.

Conversely, although there are many advantages of tDCS, it is also subject to multiple disadvantages. Due to its low cost and ease-of-use tDCS does have the potential to be misused, for example if unsupervised medically and for recreational or unethical use (i.e., enhancing memory or learning when studying). Furthermore, although tDCS is widely recognised as being a relatively safe brain stimulation methodology, detrimental effects can still occur. For example, tDCS can increase the skin temperature and induce chemical reactions following stimulation that cause skin lesions. These can occur due to changes in skin impedance as a function of stimulation intensity and duration. To avoid this, the applied voltage should therefore be regulated to preserve the required current across variable impedances (Frank et al., 2009). Mild adverse effects have also been associated with tDCS such as tingling, fatigue, itching, headache, nausea, and transient redness (Poreisz et al.,

2007). However, these effects are safe and generally well tolerated by most participants (Nitsche et al., 2008).

A major limitation of tDCS is the relatively low spatial resolution (see Figure 0.1 in the General Introduction). The resolution is generally dependent on electrode size (which are relatively large as a proportion of whole head volume) and the prerequisite of including a reference electrode. A large region of brain, outside the ROI is consequently stimulated. Alongside this, many factors influence tDCS induced current propagation. These include the anatomy and size of the head, skull and scalp thickness and the electrical conductivity of the various head tissues. These factors are further discussed in Chapter 3 (variation in head conductivity) and Chapter 4 (tDCS induced fields as a function of age). One way to optimise the current injection pattern to deliver the required current within a target region is to model the tDCS induced fields from the scalp. Such computations involve solving the tDCS forward problem to predict the electric field strength and distribution induced by tDCS (Datta et al., 2013). The precise geometry of participant head volumes can be obtained via a structural imaging method such as MRI and the residing tissues assigned variable conductivity values to model an accurate representation on an individual basis. Precise head geometry and tissue conductivity are essential as current follows a path of least resistance and is thus highly influenced by, for example, hard bone and CSF distribution. Individualisation of tDCS protocols and computational modelling are discussed in Chapter 4. The methodology involved in solving the forward problem and calculating tDCS induced fields is further discussed in Chapter 2.

1.5. EEG and tDCS Reciprocity

The electric potential at the scalp from a known dipolar current source within the brain is complementarily related to the electric field at the position of the aforementioned source, generated by an applied current on the scalp. This is known as the reciprocity principle. The principle represents a duality between EEG and tDCS and their forward problems, which can be efficiently combined for source analysis. An analogous duality exists between MEG and TMS (Malmivuo & Plonsey, 1995). As such, the reciprocity principle can be utilised to determine optimal current injections when EEG-FP solutions are available. For an array of electrodes that can both measure electric potentials and stimulate electrical currents, the potentials are a linear superposition of multiple current sources, whilst the stimulation current

generates an electric field. The reciprocity principle states a relationship between these associations – i.e., the electrical flow is parallel from electrode-to-source as from source-to-electrode (Fernández-Corazza et al., 2016). This relationship can be operationalised to generate a strong electric field at active sources and therefore tune tDCS stimulation at appropriate targets. The duality involves applying a minimum-norm least squares estimation, where the electric field produced by multiple return currents is proportional to the minimum-norm source estimate of the cortical activity. This mathematical formulation and its application is further discussed in Chapter 2, Section 2.7.

1.6. Basic Head Anatomy

Understanding the complex anatomy of the human head is essential for brain stimulation parameters and protocols, as well as for localising the source of generated EEG activity. Electrical current penetrates through the many layers of the head, with varying compositions, to or from the brain. Understanding the path this takes is imperative for determining the location of brain activity from EEG and tDCS induced fields and stimulated area. The anatomy of the human head is therefore discussed in detail in this section. In one of its simplest forms, the head is typically composed of the scalp, skull, and brain. These three layers can be further segmented into a more refined head model, allowing realistic and personalised representations of electric current propagation from the brain to the scalp surface.

1.6.1. The Brain and in-skull

The brain is enclosed within the skull and consists of the cerebrum, cerebellum, and brainstem. The brainstem is the distal part of the brain connecting it with the spinal cord and regulates essential functions such as heart rate, temperature and breathing (Arnould-Taylor, 1998). The cerebellum is at the base of the brain and is responsible for coordinating voluntary movements as well as balance and posture. The cerebrum is the largest uppermost section and contains two hemispheres, separated by a central fissure, and processes all higher order executive functioning. The cerebral cortex is the outermost layer of the cerebrum, consisting of GM, which contains neuronal cell bodies and dendrites. The neuronal axons connecting multiple GM areas with one another, and the WM resides beneath the GM (Arnould-Taylor, 1998). The cortical layers of neurons comprise the majority of cerebral GM, whilst the WM

consists of deeper subcortical areas of myelinated axons. For maximum size within a confined volume, the cerebral cortex is a folded surface (gyri) with many grooves (sulci), which aid into the division of four lobes: the frontal, parietal, occipital, and temporal. These are classified as such based on their overlying neurocranial bones (Arnould-Taylor, 1998). The cortex is further mapped into approximately 50 functional regions, termed Brodmann's areas, such as the primary motor and sensory cortex, visual and auditory cortex (Garey, 1999). Blood vessels lie within the brain, where oxygenated blood is supplied to its front via carotid arteries and the back via vertebral arteries. They join between the midbrain and pons (located within the brainstem) and branch throughout the whole brain (Hirsch, 2009).

Surrounding the brain and spinal cord, attached to the inner wall of the skull, is the dura mater, a thick membrane of dense irregular connective tissue that helps protect the brain from trauma. The arachnoid (less dense meninge) and pia mater (delicate inner layer meninge) are the remaining two meninges, located beneath the dura layer, between which lies the subarachnoid space (Gagan et al., 2007). Here, CSF circulates to support the brain, deliver nutrients, and perform waste removal. CSF is produced in the ventricles, areas of interconnected cavities within the brain. See Figure 1.7 for a schematic representation.

1.6.2. The Skull

The skull is the primary focus of the current thesis and is thus described and referred to in the most detail. The skull is a bone structure consisting of two key segments: the neurocranium and viscerocranium. The main skull bones and skull sutures can be seen in Figure 1.6. The viscerocranium, or facial skeleton, houses several sensory structures such as the eyes, nose, mouth, and ears and include the lacrimal, mandible, maxilla, nasal and zygomatic bones. The neurocranium encases the brain and CSF and is composed of two portions: the membranous flat bone structures for the upper part (cranial vault) and the cartilaginous part (chondrocranium) forming the lower base of the skull. The four major flat bones of cranial vault that surround the brain include the frontal, two parietal bones and the upper most part of the temporal and occipital bones. The chondrocranium, which grows to envelop the rapidly developing embryonic brain, consists of the two sphenoidal bones, the ethmoid bone, and the lower part of the occipital bone (Sadler, 2018). Bones are fused together across the suture lines, rigid joints formed by ossification (direct laying down of new bone material; Tang et al., 2008). Initially, in the early stages of human development, upper skull bones are

separated by fontanelles, dense connective soft tissue, to allow for skull growth and remodelling. During progression through childhood, the fontanelles close and are replaced by bone to create the adult sutures. This occurs at different stages, for example, the frontal fontanelle typically fuses between 3-9 months old (Vu et al., 2001), whilst the sphenosquamosal usually closes by 6 years, but can take as long as 10 (Idriz et al., 2015). The adult sutures also fully close at different ages across the lifespan, for example, the coronal, sagittal, lambdoid and squamosal sutures do not close until approximately 45, 50, 55 and 70 years of age, respectively (Russell & Russell, 2018; Idriz et al., 2015; Singh et al., 2004; Nakahara et al., 2006).

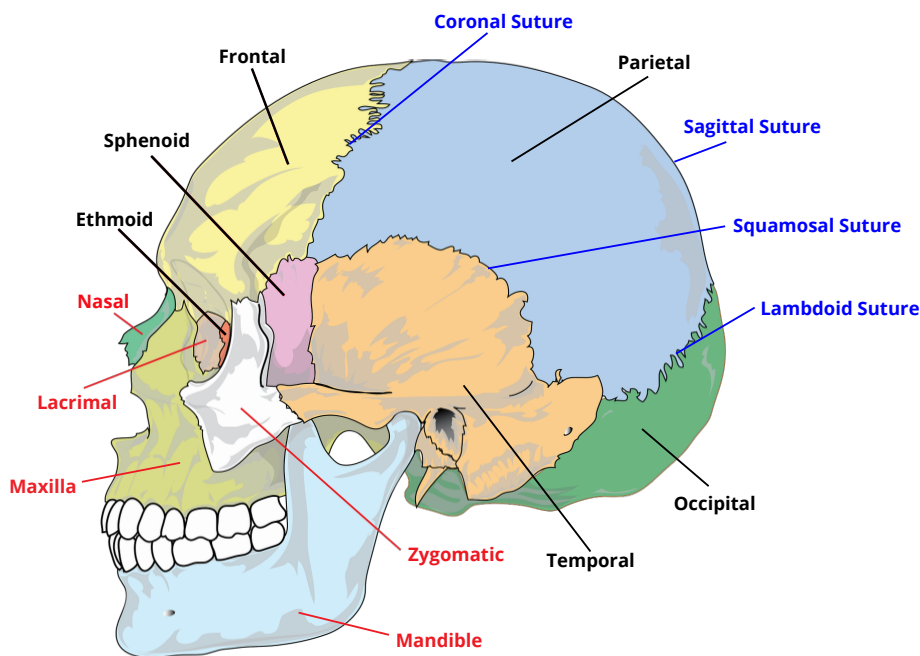


Figure 1.6: Schematic diagram of the main skull bones, the neurocranium (black labels) and viscerocranium (red labels), as well as the main skull sutures (blue labels). The sagittal suture is visible as occurring across the top of the parietal bone. The coloured skull diagram is publicly available under the Pixabay License.

The composition of the bone itself includes three layers; two outer compact bone layers with a spongiform layer sandwiched in between, both of which vary in thickness at different points (Akhtari et al., 2002; Tang et al., 2008). The compact layers are much denser than spongiform bone and form a hard external layer consisting of osteons, a linear matrix aligned parallel to the long axis of the bone. Blood vessels are distributed along the compact bone to supply blood to the various areas. Unlike spongiform bone, this is present across the cranium

(Akhtari et al., 2002). Spongiform (or cancellous) bone, on the other hand, is an open cell porous network not containing osteons, but instead consisting of trabeculae aligned as plates or rods. This reduces the density and allows for compression and growth.

Alongside differences in skull structure due to the presence of fontanelles (in infants) and sutures (in adolescents and adulthood), which vary throughout development and between participants, skull morphology changes throughout the lifespan. The skull continues to undergo microstructural, density and histological changes until death. For example, an increase in calcium content, and thus ‘hardening’ of the bone, with age has been revealed (Peyman et al., 2001; 2007). The majority of foetal bones also contain red marrow (with active haemocyto blasts – capable of producing blood cells) which has a higher water content than the yellow bone marrow (haemocyto blasts replaced with fat cells) commonly present in adult bones. Furthermore, skull thickness has been suggested to deviate with participant age – from 2-3 mm at birth to 3-6 mm during early adulthood (Hansman et al., 1966; Despotovic et al., 2013). This increase however is non-linear, slowing down towards 3 years of age, and is non-uniformly distributed throughout the skull, with higher thickness in occipital than frontal and parietal regions (Li et al., 2015). Total cranial thickness in adults has further been discovered to increase with age (Todd, 1924; Ross et al., 1998), notably related to an increase in spongiform thickness (Hatipoglu et al., 2008; Sabancıoğulları et al., 2012; Delye et al., 2015). One study accompanied this with inner and outer compact thinning (Skrzat et al., 2004). However, other results have been inconsistent, finding no such relationship between skull thickness and age (Pensler & McCarthy, 1985; Ishida & Dodo, 1990; Lynnerup, 2001; Lynnerup et al., 2005). The relationship between age and the skulls’ structure, morphology and, importantly, electrical conductivity is not yet fully understood throughout the literature. A main focus of the presented thesis is to disentangle this relationship and the impact it has on tDCS (Chapter 4) and EEG (Chapter 5).

1.6.3. The Scalp

The scalp is an anatomical boundary covering the head which consists of five layers; the skin, connective tissue (dense layer of fat and fibrous tissue), epicranial aponeurosis (dense fibrous layer), loose areolar connective tissue (collagen containing matrix) and the pericranium (membrane covering outer surface of bones). Blood vessels are also positioned throughout the scalp to allow for blood supply distribution.

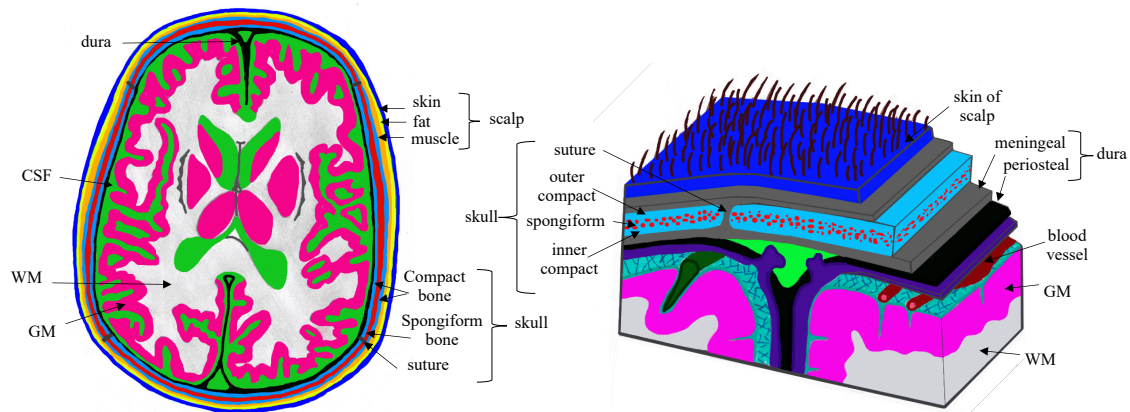


Figure 1.7: Figure displaying the various tissue compartments of the head and a subfigure of the detailed layers of the scalp, skull, and brain, labelled accordingly.

The importance of accounting for a realistic and accurate head model, with particular focus on electrical conductivity values of the tissue layers and composition of the skull is discussed throughout the remainder of the thesis. The contribution to the underlying physics is addressed in Chapter 2 (particularly section 2.3), whilst an exploration of tissue conductivity is presented in Chapter 3 and corresponding influence on tDCS and EEG in Chapters 4 and 5, respectively.

1.7. Chapter Summary

Chapter 1 introduced the basic neurophysiology underlying brain activity, notably that which contributes to electromagnetic brain imaging methods. The principal neurological origins and application protocols of these methods, EEG and tDCS, were described. The importance of human head anatomy was additionally highlighted. In summary:

- Postsynaptic synchronous activity of thousands of spatially aligned pyramidal neurons within the cortex produces an observable electrical current within the brain.
- EEG is a non-invasive modality that measures the electrical activity stemming from current voltage changes in synapses. This electrical activity is frequently modelled as a dipole. EEG enables diagnosis of neurological disorders, such as epilepsy, and can inform understanding of several brain processes, including sleep, memory, and vision.

- EEG is cost-effective, portable, easily accessible and has high temporal resolution, however, has relatively low spatial resolution (on the order of cm) and requires computationally expensive forward and inverse solutions for source localisation.
- Non-invasive tDCS modulates the neuronal activity within the brain by applying a low direct electrical current, to the scalp via two electrodes – anodal (positive current) and cathodal (negative current). It can be used for many clinical treatments such as depression, anxiety, stroke rehabilitation and Parkinson’s Disease.
- tDCS, as with EEG, is inexpensive, easily transportable, and administrable making application within homes and hospitals possible worldwide. However, tDCS has low spatial resolution, similarly to EEG and accurate determination of the target site requires forward modelling and precise head geometries and conductivities.
- tDCS target site optimisation can benefit from the EEG and tDCS reciprocity principle which states that the electrical flow from electrode-to-source (i.e., following tDCS stimulation) is equivalent to that from source-to-electrode (i.e., EEG signals).
- Accurate representation of human head geometry is essential for understanding propagation of electric current and magnetic fields, necessary for EEG source localisation and tDCS optimisation.
- Important features of head anatomy involve, but are not limited to, inclusion of the brain (consisting of GM and WM), CSF, the skull (compact bone, spongiform bone, and sutures) and the scalp.

CHAPTER 2: FORWARD AND INVERSE PROBLEMS

2.1 Chapter Overview

The previous chapter introduced the neurophysiological basis and mechanisms behind EEG and tDCS. This chapter focuses on the essential mathematical modelling of these processes in more detail, needed to understand the importance of the parameters involved. The governing equation is firstly derived from the general Maxwell equations. The forward problem is then discussed in detail and analytical and numerical methods comprising different head models are briefly reviewed. The forward operator, the lead field, is then provided and multiple solutions to the ill-posed inverse problem to reconstruct EEG sources are explored. Finally, the mathematical processes involved in tDCS are outlined and the reciprocity theorem, linking EEG and tDCS electric fields, and its use for optimising tDCS electrode placement is discussed.

2.2. Underlying mechanisms

Localising the source of electrical activity generated from EEG provides valuable knowledge for brain function origin and diagnosis of neurological disorders, such as epilepsy (Georgopoulos et al., 2007; Michel et al., 2004; Rowley & Roberts, 1995). Alongside this, understanding electrical current propagation from tDCS brain stimulation informs its application and treatment parameters. Estimating the neural generators of an acquired EEG signal and electrical propagation – the so-called *inverse problem* – however, has no unique solution (discussed in the general introduction). Moreover, the search for a solution requires knowledge of the many parameters of the head, such as its geometry and tissues' electrical conductivities. Current travels from a source, within the brain, through the head's many tissue compartments (as described in Section 1.6), typically following a path of least resistance. This is highly dependent on the tissues' electrical conductivities. For example, current will transmit more readily through the CSF, a liquid, than the hard compact bone of the skull. Hence, accurate and precise *a priori* knowledge of head geometry and conductivity is essential for electromagnetic neuroimaging methods.

To solve the inverse problem, the measured current (associated with variation in electric fields) must first be computationally modelled from known current dipole generators inside

the head, known as *the forward problem*. The best fit between the modelled and measured data is then determined, intending to localise the source of electrical activity; this is the *inverse problem* solution (Sanei & Chambers, 2013).

2.2.1. From Maxwell to Poisson Equations

The complete electric current inside the head, i.e., the current density \mathbf{j} , can be described as the sum of the primary current \mathbf{j}^p , and the return (or secondary) current \mathbf{j}^R (Hämäläinen et al., 1993). The primary current is the electrical current that flows through and across neurons and is embedded within the conductive medium (i.e., brain tissue). The return current is the current distribution outside of the source and is the product of the medium's conductivity, $\underline{\sigma}$ (a rank-2 tensor), and electric field vector, \mathbf{e} . This is described in the microscopic version of Ohm's law $\mathbf{j} = \underline{\sigma}\mathbf{e}$. Thus, the total current, where the extracellular (passive) current satisfies Ohm's law, can be written as:

$$\mathbf{j} = \mathbf{j}^p + \underline{\sigma}\mathbf{e}. \quad (1)$$

Electric current follows the principle of “charge conservation”, stating that the total (net) electric charge in a system remains unchanged and is represented by the continuity equation (Purcell & Morin, 2013). This states that the electric charge quantity within a volume only fluctuates by the electric current extent flowing out of or into the space via its boundaries. Applying Gauss's Law, where the divergence of the current density \mathbf{j} is equal to the negative rate of change of the charge density ρ , with time t , this can be written in differential form as

$$\nabla \cdot \mathbf{j} + \frac{\partial \rho}{\partial t} = 0. \quad (2)$$

When the conductivity and current source are known, the continuity equation and the following Maxwell Equations can be employed. These equations relate the electric field \mathbf{e} , with magnetic field \mathbf{b} and the current density \mathbf{j} , over time t (Nunez & Srinivasan 2006):

$$\text{Gauss's Law} \quad \nabla \cdot \mathbf{e} = \frac{\rho}{\epsilon_0} \quad (3)$$

$$\text{Gauss's Law for Magnetism} \quad \nabla \cdot \mathbf{b} = 0 \quad (4)$$

$$\text{Maxwell-Faraday equation} \quad \nabla \times \mathbf{e} = -\frac{\partial \mathbf{b}}{\partial t} \quad (5)$$

$$\text{Ampere-Maxwell Law} \quad \nabla \times \mathbf{b} = \mu_0 \mathbf{j} + \mu_0 \epsilon_0 \frac{\partial \mathbf{e}}{\partial t}. \quad (6)$$

The Maxwell equations are first reduced by observing that head tissue permeability equals permeability of free space ($\mu = \mu_0$). The quasistatic approximation can also be used, where, when computing the electric (\mathbf{e}) and magnetic field (\mathbf{b}), the time derivatives $\frac{\partial \mathbf{e}}{\partial t}$ and $\frac{\partial \mathbf{b}}{\partial t}$ are overlooked (Baillet et al., 2001). As sources change sufficiently slowly it can be assumed the structure is constantly at equilibrium because the temporal scale is considerably smaller than information propagation velocity. Time derivatives must also be small compared to ohmic current for the quasistatic approximation to be valid. Considering the human head diameter is small (<1 m) and the majority of neuronal frequencies are <100 Hz, the time derivative of \mathbf{b} to the electric field intensity is insignificant, meaning the quasistatic equation is valid. Hence, $\nabla \times \mathbf{e} = 0$, from equation 5.

The electric field can be further expressed as a function of a scalar potential, u , at position \mathbf{r} since its curl is zero and thus irrotational, i.e.,

$$\mathbf{e} = -\nabla u(\mathbf{r}). \quad (7)$$

Employing equations 1 and 7, the current density becomes:

$$\mathbf{j} = \mathbf{j}^p - \underline{\sigma} \nabla u(\mathbf{r}). \quad (8)$$

The current flowing into an infinitely small volume equals that leaving the volume as current cannot accumulate in the extracellular space (except for the primary source). Hence, once applying the divergence operator to both sides and since the current density is divergent-free in the quasistatic approximation, we get:

$$\nabla \cdot \mathbf{j} = 0, \quad (9)$$

where the unit of $\nabla \cdot \mathbf{j}$ is A/m^3 . This relates the electric potential and primary current by a Poisson equation, a generalisation of Laplace's equation that describes general electrical

activity at a given point in time. Under the assumption that each EEG electrode is a passive point in the head, the point electrode model can be employed and the EEG-FP reduces to finding $u(\mathbf{r})$ satisfying

$$\nabla \cdot (\underline{\sigma} \nabla u(\mathbf{r})) = \nabla \cdot \mathbf{j}^p(\mathbf{u}). \quad (10)$$

2.2.2. Current Dipole

As mentioned in Section 1.2, the generation of electrical activity within the brain can be approximated as an equivalent current dipole (Brette & Destexhe, 2012; de Munck et al., 1988). This represents a source of oriented current situated at a specific location, \mathbf{r}_0 with dipolar moment \mathbf{q} (a unit vector with magnitude and orientation). Mathematically, it takes the form

$$\mathbf{j}^p(\mathbf{u}) = \mathbf{q} \delta(\mathbf{r} - \mathbf{r}_0), \quad (11)$$

where, δ , is a Dirac delta distribution, a generalised function mapping every function to its value at zero (Hosseini et al., 2016).

2.3. The EEG Forward Problem

For any primary current distribution $\mathbf{j}^p(u)$, the electric potential on and outside the head can be obtained, a problem coined as the EEG *forward problem*. The EEG-FP computes the generated electric potential at the scalp for the head domain Ω (geometry of several head tissues), where the primary current, $\mathbf{j}^p(\mathbf{r})$, and conductivity field, $\underline{\sigma}$, are provided

To solve for the electric potential at the scalp, a numerical solution thus requires knowledge of the conductivity, geometries, and the current generator, modelled as single (or multiple) current dipoles. Analytical solutions can be employed when the head geometry is simple. The simplest utilises an infinite homogeneous model, where conductivity is assumed as constant across the whole medium. More realistic models, such as with layered spherical geometries, represent the electrical conductivity as homogeneous and isotropic within each tissue layer of the head. A range of approximations also exist, where conductivity can be represented as inhomogeneous and anisotropic (de Munck & Peters, 1993).

2.3.1. Infinite Homogeneous Medium

Within a homogeneous volume with a unique homogeneous conductivity value, approximating the primary current as a current dipole becomes a Poisson equation:

$$\Delta u(\mathbf{r}) = \frac{1}{\sigma} \mathbf{q} \cdot \nabla \delta(\mathbf{r} - \rho). \quad (12)$$

For a homogeneous, unbounded medium, $u(\mathbf{r})$ can be computed by utilising the fundamental solution of the Poisson equation:

$$u(\mathbf{r}) = \int G_L(\mathbf{r}) \nabla \cdot \mathbf{j}^p(\mathbf{r}') d\mathbf{r}', \quad (13)$$

where $G_L(\mathbf{r}) = -\frac{1}{4\pi\|\mathbf{r}\|}$ (Wolters et al., 2007).

However, air does not conduct electricity, therefore an infinite conductor field is impractical for EEG measurements. A boundary condition stating current does not flow externally from the head, should therefore constrain the forward solution. The EEG-FP is thus mathematically stated by (Hallez et al., 2007):

$$\begin{cases} \underline{\sigma} \frac{\partial u(\mathbf{r})}{\partial \hat{\mathbf{n}}} = \underline{\sigma} \nabla u(\mathbf{r}) \cdot \hat{\mathbf{n}} = 0 & \text{on } \partial\Omega \\ \nabla \cdot (\underline{\sigma} \nabla u(\mathbf{r})) = f = \nabla \cdot \mathbf{j}^p(\mathbf{r}) & \text{in } \Omega. \end{cases} \quad (14)$$

Here, $\hat{\mathbf{n}}$ is the unitary vector normal to the head's boundary and f is an abstract source term that depends on the source model (see section 2.3.2).

2.3.2. Concentric Spherical Models

The human head cannot be accurately represented as a homogeneous sphere and consists of many layers of differing conductivities (see section 1.6 for detailed description of typical head geometry). An analytical solution can still be utilised, proposed by de Munck (1988), where head tissues are represented by concentric spherical surfaces, each with different and anisotropic conductivities. For a three-shell model, an inner sphere represents the brain, an intermediate layer signifies the skull, and an engulfing layer embodies the scalp. The

diameter of the outermost sphere can either be matched with the diameter of a human head (Rush & Driscoll, 1968) or fixed (Clerc et al., 2012).

For a layered concentric volume conductor, a semi-analytical solution of Poisson's equation is applied. In EEG, the dipole thus has a potential u as a function of the position, radial and tangential component, outer, inner, and intermediate layer radius, scalp and brain conductivity, ratio between the skull and soft tissue, distance between dipole and centre, and polar angle of surface point (Mosher et al., 1999).

Despite this inclusion, spherical models deviate from a realistic head shape and can result in substantial forward problem errors (Cuffin & Cohen, 1977). Non-spherical models have been proposed, such as the use of ellipsoids in place of spherical shells (i.e., in Fieseler, 1999 and Kariotou, 2004), for which analytical solutions can still be derived. Eccentric spheres or differently shaped spheroids can additionally be employed (Meijs & Peters, 1987; Vatta et al., 2005). Independent spherical volume conductors have alternatively been utilised for each sensor, which can be locally fitted to each surface neighbouring the corresponding sensor (Ilmoniemi, 1985).

2.3.3. Realistic Head Models

Realistic models aim to describe the head tissues in greater detail, accounting for additional layers than a three-layer spherical model and variants in geometry, i.e., not assuming spherical or ellipsoidal layers. Solutions to the forward problem using realistic models require numerical, rather than analytical methods, such as the Boundary Element Method (BEM) and FEM.

2.3.3i. Boundary Element Method

The BEM computes the surface potentials based on the discretisation of the equivalent integral equations on the surfaces separating volumes with different electrical parameters (Kybic et al., 2005). Of a piecewise homogeneous isotropic volume conductor interfaces separate compartments of differing conductivities, whilst the boundary separates the outer surface and non-conductive air. Surface meshes for the interfaces are generated and each region between interfaces is assumed to be isotropic. The solution is bounded by the Cauchy

boundary conditions ensuring that the potential and perpendicular component of the current is continuous across each interface. For the outermost boundary, the perpendicular component is zero, and the original boundary condition is imposed. The potential is approximated on realistic compartment boundaries, the simplest being a three-shell model including the brain, skull, and scalp (Stenroos et al., 2014; Stenroos & Nummenmaa, 2016). These 2D interface layers are discretised into small elements, most commonly, triangles. For example, the interfaces are digitised with triangles and the potentials within each triangle calculated. The integral over the triangles is then calculated of that surface (Kybic et al., 2005; Stenroos & Nenonen, 2012).

The forward problem can be solved iteratively or directly, with finer grids requiring iterative solvers due to memory limitations. Solutions are still computationally expensive as they involve all mesh nodes. Boundary discretisation is also important when constructing BEM models, where mesh refinement can increase localisation precision. For example, it has been shown for deep sources at least 0.5 triangles/cm² is required, whereas for shallow dipoles 2-6 triangles/cm² is necessary for comparable results (Yvert et al., 1997). Additionally, Haueisen and colleagues (1997) revealed triangular size should be <10 mm or below the distance between boundary and source.

Following this, a limitation of the BEM is as the triangle size becomes comparable to the distance from source to boundary, the localisation accuracy decreases. A symmetric formulation (Kybic et al., 2005) reduces this error by classifying functions on the equivalent of a smooth bounded surface with discontinuous conductivity. Furthermore, for inhomogeneous and non-symmetric or non-linear problems, wholly populated system of equations will often occur in BEM, making it increasingly computationally expensive. Additionally, including the CSF requires representation of the cortex surface with 15-20 K nodes, substantially increasing BEM computation time and making the inclusion difficult (Vorwerk et al., 2012). Distinguishing between compact and spongiform skull bone is also relatively challenging as the compartments are not nested. Most importantly, BEM is incapable of considering anisotropy for general conductivity fields of the head. The electrical conductivity of some brain tissue regions, particularly WM, is accepted as anisotropic, and conduct electrical current preferentially in directions according to tissue structure (Geddes & Baker, 1967; Haueisen et al., 1996; Wolters et al., 2006). Exclusion of tissue anisotropy significantly effects forward potential computation (Haueisen et al., 2002; Wolters et al.,

2006). Generally, BEM is more frequently used for MEG source modelling, for which tissue conductivities are assumed to have less of an impact than EEG (Cuffin, 1990; Koulouri, 2014).

2.3.3ii. Finite Element Method

The FEM is a further numerical method for solving partial differential equations (PDE). It consists of discretising the PDE into finite elements and approximating the solution within each of them by employing a basis function set (generally polynomial). Such a discretisation, in this case, will consist of a set of elements spanning the entire head geometry, each with its corresponding conductivity tensor. As such, the FEM can incorporate anisotropy of the head volume, not achievable with other methods, such as the BEM. The FEM is generally preferred to other techniques due to its ability to incorporate arbitrary geometries and anisotropic and heterogeneous conductivity fields (Beltrachini, 2019) as well as including non-layered and complex structures such as the CSF and differing bone composition. Within each element a 3D parameterised (Ansatz) function defines the electrical potential as a function of the solutions at the surrounding nodes. By further considering the boundary condition (equation 14) and accounting for numerical singularities, a system of sparse high-dimensional linear equations is reached. Such sparsity allows for an efficient computation, despite its size. The current is thus calculated from numerical derivation of the potential and the magnetic flux density computed using the Biot-Savart Law. FEM is employed for the current thesis; thus, this is formulaically described in more detail below.

As discussed, the EEG-FP involves finding the electric potential $u(\mathbf{r})$ due to a current dipole (or multipole) source defined over the head domain Ω with boundary Γ (i.e., the scalp surface). Assuming sources in EEG volume conductor modelling as dipoles (or multipoles), however, causes a singularity, where the standard finite element (FE) methods cannot be applied when the Dirac delta functions are involved. This prevents a guarantee for the existence and uniqueness of the solution. Different approaches for representing source dipoles have thus been suggested. The simplest is to epitomise a dipole as a pair of stable voltages with opposite polarity on two neighbouring nodes (Schimpf et al., 2002). A further approach represents a current dipole as a summation of many current monopoles across adjacent nodes, a variant of the St-Venant principle and referred to as the blurred dipole model (Wolters et al., 2002). The subtraction approach, however, is generally applied as the

most numerically sound method (Beltrachini, 2018; 2019; Wolters et al., 2007). Here the field is separated into two parts. First, the analytically known singularity potential (u^∞), a standard field produced by an ideal dipole in an infinite homogeneous domain with constant conductivity across the whole head domain ($\underline{\sigma}^\infty$). This is calculated in equation 13 (Wolters et al., 2007). Second, a solution in the closed source-less domain under boundary conditions that corrects for current movement across boundaries with different conductivity regions (the singularity-free correction, u^{corr}). This can be numerically approximated using an FE approach, where $\underline{\sigma}^{corr}$ is zero in the subdomain. Combining both parts and accounting for the Neumann boundary conditions means the solution is then singularity free due to the homogeneity condition stating $\underline{\sigma}^{corr} = \underline{\sigma}^\infty - \underline{\sigma} = 0$ within the head domain (Beltrachini, 2019; Bashar, 2011; Wolters et al., 2003; 2007). The electric potential is thus expressed as the sum of the two terms: $u = u^{corr} + u^\infty$. The problem then consists of approximating the correction potential using a numerical method for which u^∞ is subsequently added.

Each approach has advantages and disadvantages, the subtraction approach has been revealed to perform best for both radial and transverse dipoles, followed by the Laplace method for radial dipoles (Schimpf et al., 2002), whilst the Saint-Venant representation has been deemed the most appropriate in other studies (Hauelsen et al., 1995; Wolters et al., 2007). The subtraction approach is considered the most rigorous method, as it exhibits existence and uniqueness of the solution with standard basis functions (Beltrachini, 2019; Wolters et al., 2007). However, it is more computationally expensive compared to other methods such as the St. Venant's approach. Iterative solvers are thus often used, with varying techniques and algorithms proposed to reduce time and increase efficiency. For example, the preconditioned conjugated gradient (PCG) algorithm is frequently employed which is an iterative algorithm using LU (lower-upper) factorisation as preconditioners. The analytical subtraction approach, a variation of the subtraction method minimising the numerical integration errors in tetrahedral domains, is utilised for solving the EEG forward problem in the current thesis. A more detailed description of its derivation is provided in Beltrachini (2019), where a MATLAB implementation is also publicly available through the provided FEMEG GitHub toolbox.

To approximate the EEG-FP solution the variational formulation of the subtraction version is firstly found. Here, the corresponding differential equation (a continuous operator problem) is

converted to a discrete problem by applying linear constraints, determined by finite sets of basis (test) functions. Briefly, the differential equation is multiplied with a test function φ , belonging to a suitable space (K) and then integrated over the domain Ω (Beltrachini, 2019). The divergence (integral form of Gauss's) theorem, which connects the current flux of a closed surface to divergence over its volume, is then applied and the boundary conditions utilised.

The variational formulation results in finding $u(\mathbf{r}) \in K$, so, for all $\varphi(\mathbf{r}) \in K$, satisfies $a(u, \varphi) = l(\varphi)$, where $a : K \times K \rightarrow \mathbb{R}$ is the bilinear form defined as

$$a(u, \varphi) = \int_{\Omega} \langle \underline{\sigma}(\mathbf{r}) \nabla u(\mathbf{r}), \nabla \varphi(\mathbf{r}) \rangle dr, \quad (15)$$

(the stiffness matrix) and $l : K \rightarrow \mathbb{R}$ is the linear form given by

$$l(\varphi) = - \int_{\Omega} \langle \underline{\sigma}^{corr}(\mathbf{r}) \nabla u^{\infty}(\mathbf{r}), \nabla \varphi(\mathbf{r}) \rangle dr, \\ - \int_{\Gamma} \varphi(\mathbf{r}) \langle \underline{\sigma}^{\infty} \nabla u^{\infty}(\mathbf{r}), \hat{\mathbf{n}}(\mathbf{r}) \rangle dr. \quad (16)$$

The unknown potential function $u(\mathbf{r})$ can thus be expressed as a linear combination of the basis functions multiplied by the value of the solution at the corresponding node. This can be described as:

$$u(\mathbf{r}) = \sum_{j=1}^n u_j \varphi_j(\mathbf{r}), \quad (17)$$

where, $\{\varphi_i\}_{i=1}^n$ is the set of test functions, generally chosen as piecewise polynomial functions, with n number of mesh nodes. Each function is equivalent to unity at each computational point and zero at all other points. This leads to solving the discretised system of equations

$$\mathbf{A} \cdot \mathbf{u}^{corr} = \mathbf{c}. \quad (18)$$

Here, $\mathbf{A} \in \mathbb{R}^{n \times n}$ is the stiffness matrix with elements $\mathbf{A}_{ij} = a(\varphi_i(\mathbf{r}), \varphi_j(\mathbf{r}))$, that incorporates the conductivity and geometry of the volume. $\mathbf{c} \in \mathbb{R}^{n \times 1}$ is the column (load)

vector of the source terms and vector $\mathbf{u}^{corr} \in \mathbb{R}^n$ represents the potential values at n mesh nodes (Beltrachini et al., 2018; Haueisen et al., 1995; Wolters, 2003). Quadratic shape functions can be employed (second-order FEM), however linear functions are most frequently used (first-order FEM).

For FEM, the volume conductor is generally discretised into tetrahedral or hexahedral elements (an example of a head model is provided in Figure 2.1). Hexahedral elements are advantageous as they completely match imaging voxel shapes, whilst tetrahedral elements are versatile to represent arbitrary shapes. Elements can also vary in size depending on tissue segmentation or be represented as uniform elements (e.g., 1 mm³ voxels).

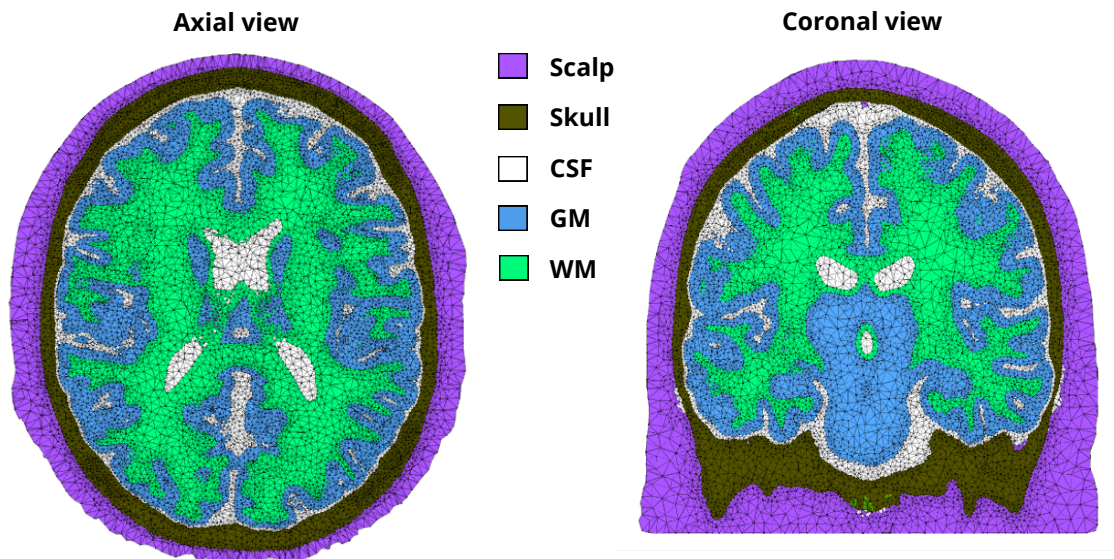


Figure 2.1: Example of head model discretisation (mesh) with in 6.8M elements and 1.1M nodes, displayed five layers; scalp (purple), skull (dark green), CSF (white), GM (blue) and WM (green). The axial (left) and coronal (right) views are shown.

2.4. Lead field Matrix

The lead field matrix (\mathbf{L}) is a collection of solutions for dipolar sources distributed within the brain, with unitary amplitude. It is a linear operator that maps potentials on a surface from the activation within sources and is thus the solution at the electrodes. For the FEM, each row consists of solving a system of equations as in equation 18. Each unit norm source on the EEG electrodes supplies to the equivalent column on the lead field matrix. The $N_E \times N_S$

(number of EEG electrodes \times number of source dipoles) lead field matrix can thus be represented as

$$\mathbf{L}_{ee\mathit{g}} = \mathbf{S}_{ee\mathit{g}} \mathbf{A}_{\underline{\sigma}}^+ \mathbf{c}_{\underline{\sigma}}. \quad (19)$$

Here $\mathbf{A}_{\underline{\sigma}}^+$ denotes the pseudoinverse of the stiffness matrix (computed once the head geometry, conductivity values and element basis functions are fixed), which is solved iteratively, and $\mathbf{c}_{\underline{\sigma}}$ represents the source vector, expressed as a linear combination of conductivity independent matrices. $\mathbf{S}_{ee\mathit{g}}$ is the selection matrix which selects or interpolates the potentials only at electrode positions.

2.5. The EEG Inverse Problem

The inverse problem in EEG utilises measured electric potentials to reconstruct the source of the generated current that best explains such measured values. The inverse source estimation problem, however, does not have a unique solution and is not well-posed. As discussed in the general introduction, the solution is ill-posed as, firstly, results can be unstable due to increased noise compared to the power of the acquired signals. This means that it is possible that no current distribution explains the data. Secondly, multiple source distributions can explain identical EEG measurements (Gyllys-Colwell, 1996). For example, some current distributions within a conductor generate no external electric potentials (i.e., are electrically silent). Hence, accurate reconstruction is not possible solely from the external measurements. Thirdly, small changes in measurements can drastically change the solution, i.e., large changes in currents from sources far from surface measurements can result in much smaller surface changes (Grech et al., 2008). Solutions therefore require a detailed head volume conductor model as well as a source model with distribution constraints. This allows computation of meaningful solutions by approximating a well-posed problem.

Following from lead field calculations, the forward model with assumed known and fixed source orientations can also be written as

$$\mathbf{y} = \sum_i \mathbf{L}_i \mathbf{u}_i + \mathbf{d} = \mathbf{L} \mathbf{u} + \mathbf{d} \quad (20)$$

Here, $\mathbf{y} \in \mathbb{R}^{N_E}$ is a vector measurement with additive noise $\mathbf{d} \in \mathbb{R}^{N_E}$, $\mathbf{u}_i \in \mathbb{R}^{N_S}$ is a source amplitude vector for the i -th source, and \mathbf{L} is the lead field matrix, as $N_E \times N_S$. Thus, the inverse problem then consists of finding the best estimate for dipole magnitude and position that best explains the vector measurements with additional noise, modelled as Gaussian (Beltrachini et al., 2013). Noise can include external electrical, environmental sources that convert to EEG measurements such as that from power lines and electronic equipment. Further contributions to noise include physiological measurements such as cardiac signals, movement artifacts and ocular signals (for a review on noise removal see Chatterjee et al., 2020).

An overview of both the EEG-FP and IP is provided in Figure 2.2. Here, the signal matrix, $\mathbf{Y} \in \mathbb{R}^{N_S}$, contains the superposition of all source dipole signals (for N_S sources) of the electric potential data, recorded at N_E electrodes of an EEG sensor array. The lead field matrix (forward operator), $\mathbf{L} \in \mathbb{R}^{N_E \times N_S}$, characterises the propagation of the signals in the head volume conductor, dependent on Ω and $\underline{\sigma}$. The EEG-IP in turn, aims to estimate the unknown sources, \mathbf{Y} , from the measurements \mathbf{X} .

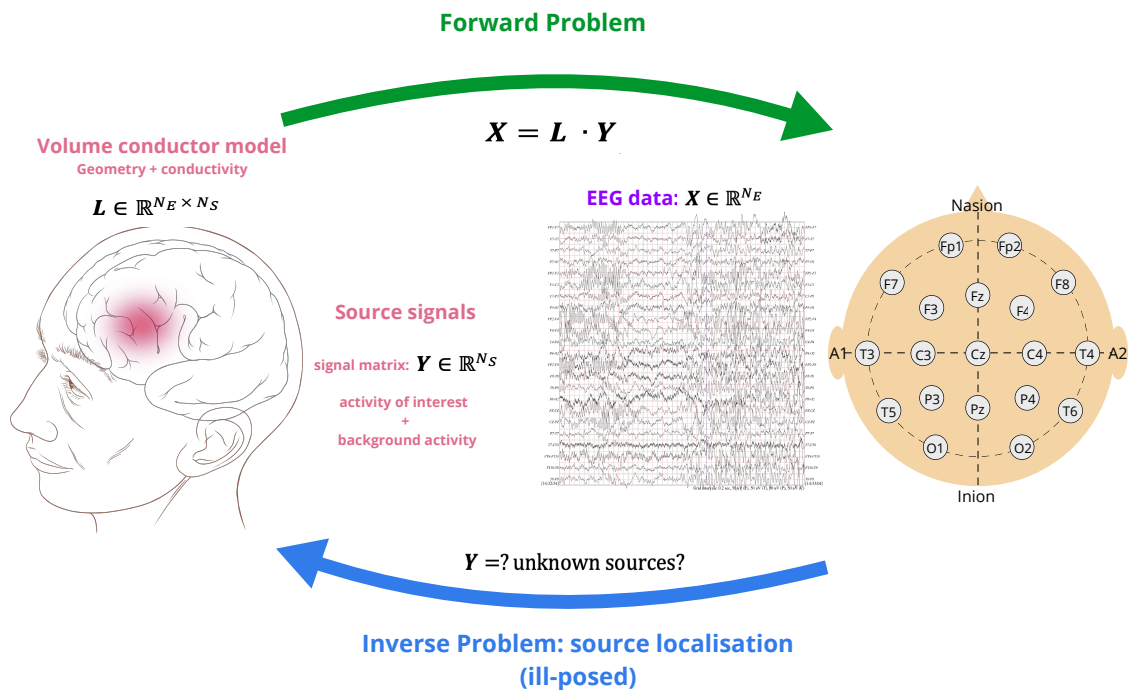


Figure 2.2: Illustration of the EEG forward and inverse problems with relevant equations. In the forward problem (green arrow), the propagation of the signals in the head volume conductor (\mathbf{L}) associates the source signals (\mathbf{Y}) to the EEG measurement data (\mathbf{X}), for N_E electrodes and N_S

sources. The ill-posed inverse problem (blue arrow) then maps the modelled data (FP solution) with the observed EEG data to estimate the source of activity. The head diagram is publicly available from medical illustrator Patrick J. Lynch under the copyright Attribution 2.5 License 2006. The EEG data example is taken from the openly available database described in Shoeb (2009).

Solutions describe neuronal currents as known source terms in many ways, which can be divided into two main categories. The first estimates a best fit of the dipoles to the measurements using a small number of dipoles, which have unknown locations and orientations, and then solving with least squares, i.e., the Dipole Fit Model (Scherg & Ebersole, 1993; Oostendorp & van Oosterom, 1991). The second, i.e., the Distributed Source Model (DSM), employs a larger number of sources, with fixed locations and sometimes fixed orientations, which are distributed across a larger area and calculates a distribution of dipole moments at each point (Ding & Yuan, 2012). These methods are described in more detail below.

2.5.1. Dipole Fitting Approach

This approach assumes that measurements can be explained by the activity generated by a single dipole source with unknown position and moment (magnitude and orientation). This provides an optimal dipole for the given location and can be solved for a fixed source. Several active dipoles can be fitted through generalisation to this method, where the solution non-linearly determines the optimal dipoles by altering the position parameters. A large limitation of this approach, however, is that it is exponentially complex and hence can only assume a small number of dipoles. Additionally, the number of sources needs to be predefined and if this number is incorrect, localisation can fail. Typically, a maximum of two dipoles can be utilised for this approach and results become more accurate when the dipoles are spatially separated (Grech et al., 2008). When sources have overlapping fields (most often the case), this technique also fails. For this reason, it is often only employed when the source of brain activity is concentrated to a small volume. Alternatively, the addition of temporal information can provide better determination of the solution (Ou et al., 2009; Koulouri, 2014).

2.5.2. Pre-defined Dipoles

When the location of the dipole(s) is pre-defined, for example when the cortex area of a particular brain function has been extensively pre-assessed, so-called scanning methods can be used.

Beamforming is one such approach that uses a sensor array to combine measurements at all locations to increase the signal-to-noise ratio (and resolution) and focus the array on a specific pre-defined area. Most frequently, beamforming algorithms scan ROIs voxel by voxel (Van Veen et al., 1997; Robinson & Vrba, 1999). Alternatively, they can apply anatomical constraints, for example, restricting sources to cortical GM with perpendicular to the surface orientation (Fuchs, 2002; Hillebrand & Barnes, 2003). One example of beamforming employs linearly constrained minimum variance (LCMV) and spatial filtering to minimise the estimated variance using an optimisation solution. It is assumed that sources are uncorrelated with one another and noise and source amplitudes are a random variable. A downside of this method is that multiple time samples are required, and noise and signal covariance matrices are pre-requisites, estimated from the available data. Additional beamforming techniques can be found in Sekihara and Nagarajan, (2015).

A similar method, Multiple Signal Classification (MUSIC) separates all measurement space into two mutually orthogonal spaces: the signal and the noise space. A single dipole is scanned within the source volume (3D head) and the forward problem for a dipole at each location is estimated against the signal subspace. Positions where the source model represents the optimal prediction to the signal subspace corresponds to the dipole site (Schmidt, 1979). Contrasting to beamformers, MUSIC does not require sources to be uncorrelated, nor the inversion of the signal covariance matrix and it also has improved endurance for interconnected time sources (although it does require a sufficient number of time samples; Mosher et al., 1992). Additions to MUSIC have been proposed, for example Recursively Applied MUSIC (RAP-MUSIC), which avoids multiple dipoles describing equivalent signals by extracting a single maximum and subtracting the signal involvement of this source from the data (Mosher & Leahy, 1998). A development, Truncated RAP-MUSIC (TRAP-MUSIC) remedies the concealed limitation that prevents precise estimation of the correct number of sources. For more specific applications, synchronous activity can be located using source

clustering (POP-MUSIC; Liu & Schimpf, 2006) and ExSo-MUSIC locates extended sources (Biro et al., 2011).

2.5.3. Distributed Source Models

For DSMs, dipoles can be positioned on the cortex surface mesh. Solutions to DSM inverse problems apply different *a priori* assumptions and constraints to ensure reliability and accurately reflect brain activity properties. The current thesis utilised a DSM method (specifically sLORETA, see below) and is thus discussed in more detail.

The variational regularisation method determines two different functionals. One which measures the distance between the vector measurements and the lead field matrix, termed the data fidelity term ($F(\mathbf{r})$) and the second, a regularisation function ($M(\mathbf{r})$), where \mathbf{r} denotes the volume coordinates in the brain. This appropriately minimises resolutions with non-optimal assemblies (Benning & Burger, 2018). Hence:

$$\hat{\mathbf{r}} = \underset{\mathbf{r}}{\operatorname{argmin}} F(\mathbf{r}) + M(\mathbf{r}) . \quad (21)$$

A Euclidean norm is often used to denote $F(\mathbf{r})$ as Gaussian noise is most frequently used for actual EEG measurements.

Tikhonov regularisation (Hämäläinen & Ilmoniemi, 1994), based upon Euclidean norm regularisation, is the most universally employed method. MNE evaluates the dipole distribution to meet the potential values with the smallest complete power. A minimising regularisation parameter λ is commonly used to regulate the contribution of both the data fidelity term and regularisation function (the higher λ , the more regularised the solution is) so

$$\hat{\mathbf{r}}_{\lambda} = \underset{\mathbf{r}}{\operatorname{argmin}} \|\mathbf{y} - \mathbf{L}\mathbf{r}\|_2^2 + \lambda \|\mathbf{r}\|_2^2. \quad (22)$$

Here, $\|\mathbf{y} - \mathbf{L}\mathbf{r}\|_2^2$ is the fidelity term assuming Gaussian noise and $R(\mathbf{r}) = \|\mathbf{r}\|_2^2$ is the regularisation of the Euclidean norm. This has a unique closed form solution

$$\hat{\mathbf{r}}_{\lambda} = \mathbf{L}^T (\mathbf{L}\mathbf{L}^T + \lambda \mathbf{I})^{-1} \mathbf{y}, \quad (23)$$

where \mathbf{I} is the identity matrix and the superscript T indicates the transpose of the corresponding matrix. \mathbf{L} can also be represented as its singular value decomposition (factorisation of the matrix) $\mathbf{L} = \mathbf{U}\mathbf{S}\mathbf{V}^T$, and the identity matrix as $\mathbf{I} = \mathbf{U}\mathbf{U}^T$. Thus, $\hat{\mathbf{r}}_\lambda = \mathbf{L}^T \mathbf{U} \mathbf{S}_\lambda^{-1} \mathbf{U}^T \mathbf{y}$, where \mathbf{S}_λ^{-1} is a diagonal matrix with i^{th} diagonal element $\frac{1}{\sigma_i^2 + \lambda}$, $\{\sigma_i\}_i$. From this, with i^{th} element of a vector or column of a matrix,

$$\hat{\mathbf{r}}_\lambda = \sum_i \frac{1}{\sigma_i^2 + \lambda} [\mathbf{U}^T \mathbf{y}]_i \mathbf{u}_i. \quad (24)$$

Hence, the solution can be calculated as the weighted sum of singular vectors \mathbf{u}_i .

MNE, however, frequently locates deep sources as residing on the surface of the cortex. Instead of the source amplitude, the linear transform, $\mathbf{W}\mathbf{r}$, can be regularised, for example to reduce the predisposition to superficial sources. This can be represented as a depth weighting matrix (Lin et al., 2006) $\hat{\mathbf{r}}_\lambda = \underset{\mathbf{r}}{\operatorname{argmin}} \|\mathbf{y} - \mathbf{L}\mathbf{r}\|_2^2 + \lambda \|\mathbf{W}\mathbf{r}\|_2^2$. Low Resolution

Electromagnetic Tomography (LORETA) is one such method that calculates the smoothly distributed electric activity whilst assuming synchronous and simultaneous neuronal firing of adjacent neurons (Pascual-Marqui, 2002), using \mathbf{W} as a discrete spatial Laplacian operator. A limitation of this method, however, is that it results in superficial sources to be near zero.

A similar formulation, the standardised LORETA (sLORETA; Pascual-Marqui, 2002), assumes no noise and computes the source position as the maximum measurements of the standardised power and utilises diagonal elements of a resolution matrix \mathbf{R} (a source covariance matrix), where $\mathbf{W} = \mathbf{R}^{-1/2}$. The diagonal elements of the resolution matrix relate the sensitivity of each estimated source to itself, whilst the off-diagonal elements indicate the sensitivity to the remainder of brain sources. For EEG, inverse solutions for off-diagonal elements typically incur leakage (Farahibozorg et al., 2018) and can result in false positives and imaging artifacts (Matsuura & Okabe, 1995), especially for focalised sources. Additional methods have been introduced to reduce this effect, such as the Focal Under-determined System Solver (FOCUSS) which estimates focal sources using interactions of the weighting matrix (Gorodnitsky & Rao, 1997; Gorodnitsky et al., 1995) and *a priori* thresholding (Maksymenko et al., 2017). However, non-linear solutions that use the sparse l_1 norm

regularisation are more often employed. The current thesis utilised sLORETA for EEG inverse calculations due to the assumption of no noise and it being a widely used application.

2.6. *tDCS Induced Fields*

As with EEG, bioelectromagnetism underlies the tDCS stimulated induced electric field. The quasi-static approximations can be applied, to simplify the field solutions, as the electric permittivity and magnetic permeability for biological tissues is relatively low (Wagner et al., 2007). An electric field \mathbf{e} , is related to the current density vector \mathbf{j} , with conductivity $\underline{\sigma}$, by Ohm's law, as in equation 1. Following the quasistatic condition, \mathbf{e} is the negative gradient of the scalar potential $u(\mathbf{r})$ (equation 7) which in combination results in a Poisson partial differential equation (equation 10). Hence, this describes the field distribution within the head after tDCS stimulation. The connection between the external stimulation and estimated potentials is defined by the Neumann boundary conditions (equation 14). As with EEG, the electric field can then be attained through numerical methods in a realistic head model using, e.g., FEM.

2.6.1. tDCS Forward Problem

More specifically, the tDCS forward solution solves for the electric potential distribution on the scalp as a result of the current injection pattern, where the electrical conductivities are assumed as known. The current injection on the scalp can thus be structured as the linear combination of a complete array of independent current injection patterns, with N_E number of electrodes and $N_E - 1$ patterns. This is a quasistatic problem with Neumann boundary conditions (Fernández-Corazza et al., 2013)

$$\begin{cases} \nabla \cdot (\underline{\sigma}(\mathbf{r})\nabla u(\mathbf{r})) = 0 & \text{in } \Omega \\ \underline{\sigma}(\mathbf{r})(\nabla u(\mathbf{r})) \cdot \hat{\mathbf{n}} = \mathbf{j}(\mathbf{r}) & \text{in } \partial\Omega. \end{cases} \quad (25)$$

Here, \mathbf{j} represents the normal component of the current density on the boundary, which is 0 everywhere except for the current injection sites. As with EEG, this problem is thus reduced to a linear system of equations (equation 18, $\mathbf{A} \cdot \mathbf{u} = \mathbf{c}$). Here, \mathbf{c} contains the current injection information, \mathbf{A} is the stiffness matrix $\mathbf{A} \in \mathbb{R}^{n \times n}$, incorporating the conductivity, geometry of the volume and impedance and \mathbf{u} is the unknown electric potential at each mesh node. The

FEM with first order tetrahedral elements and the point electrode model can thus be utilised. For every head volume tessellation element (Q), the electric field can be computed for each injection pattern, \mathbf{w} to form \mathbf{Q} , a $3Q \times (N_E - 1)$ transfer matrix. The tDCS FP is therefore solved for a complete set of $N_E - 1$ forward solutions with an N_E electrode montage (Dmochowski et al., 2017; Saturnino et al., 2019). For a standard tDCS application (one anode/cathode), the input current density at the anode/cathode on the boundary of the head is selected and zero current flow perpendicular to the scalp at all other regions imposed.

2.6.2. tDCS Inverse Problem

The application of tDCS can be optimised for scalp location and current intensity by employing the so-called tDCS inverse solution. This can also be reframed to maximise the desired directional current density at the target whilst minimising its effect elsewhere in the brain and in other directions. Similar to the EEG inverse solution (section 2.5.3, equations 21 and 22, without the regularisation function), the vector of individual current injection currents, \mathbf{w}_c , in each electrode generating the electric field spatial profile \mathbf{e} , can be analytically represented as

$$\mathbf{w}_c = \underset{\mathbf{w}_c}{\operatorname{argmin}} \|\mathbf{T}\mathbf{w}_c - \mathbf{e}\|^2 = (\mathbf{Q}^Q \mathbf{Q})^{-1} \mathbf{Q}^Q \mathbf{e}. \quad (26)$$

For the EEG inverse solution, the number of unknowns is greater than the number of electrodes (equations) and is underdetermined, hence the problem is ill-posed and requires regularisation. On the other hand, the number of unknowns for tDCS is less than the number of electrodes (dependent on simulation region area) and is thus overdetermined, resulting in a solution not requiring regularisation (Sekihara & Nagarajan, 2008).

Solutions to the presented tDCS inverse problem thus determine optimum electrode placement. Methods for solving this analytical problem include Least Squares, weighted Least Squares and Linearly constrained minimum variance, among others (more detailed derivation of these methods are summarised in Dmochowski et al., 2011). These are discussed briefly. Firstly, the least squares optimisation method assigns a comparatively large electric field close to the target and zero at unaffected areas. The squared error between the required electric field and the attainable field computed as the linear superposition of the

induced electric fields across the electrodes is thus aimed to be minimised. For this formulation, the number of total nodes is considerably high (so as to accurately compute FEM solutions), whereas the number of target nodes is comparatively small. To regulate the balance between reaching the desired intensity within a minimal (focal) field, the weighted sum of squares can be employed to both (weighted least squares method). Here, a scalar constant can control the compromise, where a low constant accentuates a zero field at non-target areas and a high constant prioritises achieving the required intensity at the ROI. The current must also be constrained to a maximum value within the safety range (typically 2 – 2.5 mA). This either involves limiting the sum of all positive currents, or restricting the current at each individual electrode, utilised in a weighted least squares with individual constraint approach. This method is particularly useful when the electrodes are considerably far apart or when two electrodes reside on one side of the head (which may increase the local current). It is necessary to iteratively adjust the applied constant (as used in standard weighted least squares) until the required intensity is reached, which can be computationally expensive. A further method, linearly constrained minimum variance, lessens this cost by employing a hard linear constraint (i.e., to accomplish a precise electric field at a single node). The current distribution satisfying this restraint with the lowest total electric field across the volume can then be specified. A limitation of this, however, is that the maximum field cannot be demonstrated at the ROI with certainty and high fields at non-target regions can occur. Furthermore, if the target intensity is too high, the applied current safety criteria may be violated, thus a lower target intensity can be specified. A complete outline of tDCS inverse solutions is unnecessary for the current thesis, thus a more detailed formulation of the discussed schemes is provided in Dmochowski and colleagues (2011).

2.7. EEG and tDCS Reciprocity

As discussed in section 1.5 and outlined by Malmivuo and Plonsey (1995), the reciprocity coupling EEG and tDCS theories that for a dipole at \mathbf{r} , with dipolar moment \mathbf{q} , the difference between the electric potential u , between two points on the scalp (a and b) is:

$$u(a) - u(b) = \frac{\vec{\nabla}u_{ab}(\mathbf{r}) \cdot \mathbf{q}}{h_{ab}}. \quad (27)$$

Here, the injected electric current h_{ab} , between a and b results in the electric potential $u_{ab}(\mathbf{r})$, at location \mathbf{r} . This is greatest at \mathbf{r} and thus the imposed potential gradient at \mathbf{r} and the dot product of \mathbf{q} are also maximal, when the two points are the poles of the scalp forward potential generated by a dipole \mathbf{q} . The desired current injection h_{ab} into the EEG poles thus also maximises the directional current density \mathbf{j} on the position \mathbf{r} :

$$\begin{aligned} a, b &= \operatorname{argmax}_{a,b} \{u(a) - u(b)\} \\ &= \operatorname{argmax}_{a,b} \left\{ \frac{\nabla u_{ab}(\mathbf{r})}{h_{ab}} \cdot \mathbf{q} \right\} \Leftrightarrow \mathbf{q} \cdot \nabla u_{ab}(\mathbf{r}) \cdot \mathbf{q} \text{ is maximal} \end{aligned} \quad (28)$$

The solution, point pair a, b on the scalp, maximises the potential gradient u at location \mathbf{r} , along the required orientation \mathbf{q} , and thus based on the reciprocity theorem are the ideal points for tDCS application. More details on this formulation can be found in Malmivuo and Plonsey (1995), Wagner et al. (2016) and Fernández-Corazza and colleagues (2016). This duality has been employed to reduce computation time in EEG lead field calculations (Wolters et al., 2004; Hallez et al., 2007), but less so for tDCS optimisation. Such application is beyond the scope of the current thesis, however is discussed more thoroughly in Salman and others (2015) and multiple methodologies for optimum tDCS placement based on the reciprocity principle are provided in Fernández-Corazza et al. (2016).

2.8. Chapter Summary

Chapter 2 provides an overview of the underlying mathematical mechanisms involved in EEG source localisation and tDCS field propagation. Several forward and inverse solution methods were reviewed, and a summary of important points are discussed below:

- The Maxwell equations can be employed to calculate the electric field within the head. This requires accurate and precise knowledge of the head domain (geometry) and electrical conductivity of the head tissues.
- Realistic head models are the most appropriate and accurate representation which require numerical methods to solve the EEG forward problem. The Finite Element Method (FEM) is generally preferred by discretising the head volume and solving a system of linear equations.

- The lead field matrix, a linear forward operator mapping electrical potential on a surface from the activation source, is subsequently computed in the EEG forward problem.
- The inverse problem is ill-posed and can have an infinite number of solutions. There exist many solutions, each of which are based on specific *a priori* hypotheses.
- Of these, minimum norm estimates are the most widely utilised methods which evaluate the distribution of a dipole to account for the potential values with the smallest complete power. An example is standardised Resolution Electromagnetic Tomography (sLORETA) which is utilised in the current thesis.
- The field distribution within the head after tDCS stimulation is described as a Poisson partial differential equation, as with EEG, and the association between the estimated potentials and external stimulation is defined by boundary conditions.
- The reciprocity principle, linking the EEG electric potential and tDCS induced fields allows computation for optimum tDCS electrode placement based on a provided desired current intensity and target region.

CHAPTER 3. HEAD TISSUE CONDUCTIVITY VARIATION

3.1 Chapter Overview

The previous two chapters highlighted the importance of accurate and precise head geometry and tissue electrical conductivity for EEG source localisation and tDCS induced fields. This chapter focuses on how the electrical conductivity of head tissues varies throughout the literature and thus has the potential to effect electrical source characterisation and field propagation. A meta-analysis was conducted to determine significant variation and any influential factors. This included measurement methodology such as technique, condition, frequency and temperature and participant demographics such as age and pathology.

3.2. Motivation

As discussed in Chapters 1 and 2, necessary parameters for determining electrical source localisation and induced fields are accurate and precise head tissue electrical conductivity values. Electrical conductivity of biological tissues predominantly results from the movement of hydrated ions, constrained, and impeded by anatomical microstructure. The differences in extracellular ion concentration, tissue cell size, orientation, membranes, and channels contribute to the variability in electrical conductivity between biological tissues. CSF, a liquid with high free movement of ions, for example, has a higher electrical conductivity than brain tissue, consisting of 70-80% water which in turn is more conductive than hard skull bone (Plonsey & Barr, 2007).

As mentioned in the previous chapters, erroneous head tissue conductivities can impact significantly in electric surface potential estimations as well as magnetic field strength (Cohen & Cuffin, 1983a; Haueisen et al., 1995; Okada et al., 1999). This, in turn, can introduce systemic errors for both EEG and MEG forward problems (Gonçalves, et al., 2003a; Gonçalves et al., 2003b) and thus inaccurate source localisation (Akhtari et al., 2002; Haueisen et al., 2002; Pohlmeier et al., 1997; Vatta et al., 2002). Furthermore, inappropriate conclusions inferred from EEG data for brain function, pathology and disease treatments can stem from tissue conductivity misspecification (Wendel et al., 2006). This includes, for example, insights into psychiatric and neurological disorders (Frantseva et al., 2014; Park et

al., 2002; Schlosser et al., 2007) and epilepsy treatment implications (Akhtari et al., 2006; Fabrizi et al., 2006).

Head tissue conductivity values, however, are frequently assumed from previous literature, which vary and are inconsistent, as shown below. Considerable differences in conductivity have been revealed within and between reports (Faes et al., 1999; Gabriel et al., 1996a; Geddes, & Baker, 1967). Such variation can be dependent on participant demographics, such as age and pathology, as well as measurement condition (i.e., *in vivo*, *ex vivo* or *in vitro*), applied frequency, tissue temperature and employed methodology. Differing methodologies, such as directly applied current (DAC), EIT, E/MEG and DTI, can produce diverse conductivity values. DAC refers to any invasive method where current is directly applied to the medium and electrical conductivity is determined from the resulting potential difference between a pair of electrodes. For EIT, alternating current at single or multiple frequencies is applied to the scalp via two or more conducting surface electrodes. The electrical conductivity can then be inferred from the resulting potential difference between the remaining electrodes, not involved in current injection (Holder, 2004). E/MEG data can also be used to iteratively estimate the optimum equivalent electrical conductivities given the acquired E/MEG measurements (Baysal & Haueisen, 2004). DTI, on the other hand, transforms diffusion tensor eigenvalues, measured using diffusion-weighted MRI, to electrical conductivity tensor eigenvalues with various estimation methods (further discussed in Section 3.5.5i).

Methods are often chosen due to their respective strengths and weaknesses for determining different tissue (i.e., soft tissues vs bone) conductivities (summarised in Table 3.1). Advantages for DAC methods are that they can analyse conductivity of all tissue types, are relatively cost effective, with a low acquisition time, easily portable and without requiring a computational head model. Simplified assumptions regarding the neurobiology and dynamics of the human head, however, are consequently often introduced. Furthermore, DAC is invasive and may depend on post-mortem samples or excised tissues which are subsequently not often under natural biophysical conditions. For example, post-mortem tissues undergo biochemical processes initiated by death, such as changes in cell membrane polarisation and ion mobility, which consequently effect conductivity (Opitz et al., 2017). Opitz and colleagues (2017) validated differences between post-mortem and live intracranial electrical fields, despite controlling for confounding variables (i.e., temperature). Comparably, excised

tissues endure numerous extracting and preservation procedures (i.e., saline soaked, time since excision, etc.). Such practices can change the electrolyte concentration (Akhtari et al., 2002) and hence influence conductivity. Conversely, EIT, E/MEG and DTI methods are non-invasive and occur *in vivo*, and thus advantageously remain under natural conditions. EIT and E/MEG are cost effective with low acquisition times and portable, compared to DTI methods which are more expensive with high acquisition times, and which are non-portable. EIT and E/MEG, however, have lower spatial resolution than DTI and require the use of a computational head model (detailed strengths and weakness of EEG specifically are provided in section 1.3.3.). DTI, however, employs MRI, making skull conductivity non-accessible due to weak MR signal towards bone layers. A further advantage of DTI is the ability to classify anisotropic and heterogenous conductivity values of soft tissues (Johansen-Berg & Behrens, 2013). Conversion from diffusion measurements to conductivity, however, also depends upon basic assumptions and can differ throughout applications (Rullmann et al., 2009; see also Section 3.5.5ii).

| Method | Strengths | Limitations |
|--------|---|--|
| DAC | <ul style="list-style-type: none"> - no need of head model - can classify all tissues - portable - cost effective - low acquisition time | <ul style="list-style-type: none"> - invasive - unnatural conditions if not <i>in vivo</i> - homogeneous |
| EIT | <ul style="list-style-type: none"> - non-invasive - <i>in vivo</i> - portable - cost effective - low acquisition time | <ul style="list-style-type: none"> - head model required - low spatial resolution - low signal-to-noise - homogeneous |
| E/MEG | <ul style="list-style-type: none"> - non-invasive - <i>in vivo</i> - portable - cost effective | <ul style="list-style-type: none"> - head model required - low spatial resolution - homogeneous |
| DTI | <ul style="list-style-type: none"> - non-invasive - <i>in vivo</i> - high spatial resolution - anisotropic - heterogeneous | <ul style="list-style-type: none"> - non-portable - relatively expensive - weak MR signal in skull - high acquisition time |

Table 3.1. Summary of the strengths and limitations for the four included methods; direct applied current (DAC), electrical impedance tomography (EIT), electro/magnetoencephalography (E/MEG) and diffusion tensor imaging (DTI).

Assuming conductivity from previous literature is insufficient when accurate and precise values are required. Significant and important factors affecting this variation, however, are currently unknown. Knowledge of influential variables, such as tissue segmentation, methodology employed, sample temperature or participant pathology can provide insights into the stability of tissue conductivity values and methodology, as well as suggest areas for future research. This chapter therefore systematically and extensively investigated all published reports of human head tissue electrical conductivity to i) evidence any significant variations in conductivity values of different head tissue types and ii) determine any significant factors contributing to variation. Chapter 3 thus outlines a systematic meta-analysis, restricted to human head tissue, to identify relevant papers and reveal significant factor variables via a multiple regression.

3.3. Meta-Analysis Methods

3.3.1. Literature search

Preferred Reporting Items for Systematic reviews and Meta-Analyses (PRISMA) statement guidelines (Moher et al., 2009) were followed and a PRISMA checklist and flow diagram completed (Appendix A.) An extensive literature search, spanning three databases (PubMed, Scopus, and Web of Knowledge), was conducted to retrieve published and peer-reviewed studies exploring electrical conductivity (or equivalent) of the human head (or equivalent). The keywords utilised for the systematic literature search are provided in Appendix B. Article titles were systematically searched using relevant and/or equivalent keywords, unrestricted by year of publication, language, or design. Reference lists of included papers were hand-searched to identify additional papers. Duplicates following the initial literature search were removed.

3.3.2. Selection criteria

Papers met the inclusion criteria if they i) provided at least one defined conductivity measure (or equivalent from which conductivity could be calculated), of the ii) human iii) head, where both iv) employed methodology and v) tissue type were available. Reviews were only included as an information source to the original reference, where data was thus extracted. Exclusions were made if any of the five inclusion criteria were absent or ambiguous, or if an English version was unavailable after extensive search. In addition to conductivity value,

methodology and tissue type, reports were collected on measurement condition (i.e., *in vivo*, *ex vivo*, or *in vitro*), applied frequency to determine the conductivity, tissue temperature, as well as participant's age, gender, and pathology. Missing information for one or more of these variables did not result in exclusion. Studies applying frequencies above approximately 1 kHz were excluded from analysis on the grounds this frequency is besides the scope of typical brain activity recorded in EEG and enhanced in tDCS.

All identified titles resulting from the literature search, following removal of duplicates, were initially screened for applicability and/or immediate exclusion. Remaining abstracts were further assessed, and full texts of potentially relevant papers were obtained to determine if they consequently met the inclusion criteria. The papers and respective analysis comprised in this chapter include studies conducted before publication of the associated research paper in 2019. Studies reporting conductivity values, and meeting inclusion criteria, published after this meta-analysis are presented in a GitHub Repository (see Section 3.4.2.).

3.3.3. Data extraction and Synthesis

All conductivity, resistivity or impedance values were extracted from each paper and converted to S/m for standardisation. The sample mean and standard deviation were subsequently calculated for every differentiation in methodology within each paper and characterised according to the aforementioned variables.

3.3.4. Variable Definitions and Classification

3.3.4i. Tissue Types

Tissues were separated into four major compartments, each comprised of sub-compartments: the scalp (*skin, fat, muscle*), the skull (*spongiform, inner, and outer compact bone and sutures*), CSF and the brain (*GM, WM, the dura layer, blood, epileptogenic zone [EZ]*). Conductivity values were assigned according to tissue type as reported. Tissues were classified as *whole-scalp*, *whole-skull*, or *whole-brain* (assumed as GM and WM) when no conductivity values for their sub-compartments were reported, similarly *whole-compact bone* was assigned if no values for the inner and outer compact bone were provided. If given, WM was further segmented into WM oriented in parallel (*WM_{par}*) or perpendicular (*WM_{perp}*) to the applied current. See Figure 1.6 for a detailed representation of all tissue compartments.

Additionally, when available, the brain to skull conductivity ratio (*BSCR*) was reported as a nominal ratio without units. *BSCR* was included as multiple existing studies involving E/MEG source localisation have employed a piecewise homogeneous head model, consisting of three compartments (the brain, skull, and scalp). For neural source localisation utilising these models, where the brain and scalp have additionally been assumed to have the same conductivities, the relative strength of the source only has commonly been of interest. Thus, the ratio between the scalp (and brain) and skull conductivities is essential for BEM calculations (Clerc et al., 2005; Oostendorp et al., 2000; Zhang et al., 2006).

3.3.4ii. Measurement Conditions

Conditions were separated into three main categories:

In vivo – “within the living”; experiment conducted on or in whole living organisms/cells. Electrical conductivity values obtained within a living head were considered *in vivo*.

Ex vivo – “out of the living”; experiment in or on tissue from an organism in an external environment, but with minimal alteration of natural conditions, e.g., cultured cells derived from biopsies. Experiments where tissue was excised but kept within conditions similar to the human head were characterised as *ex vivo*.

In vitro – “within the glass”; experiment within a controlled artificial environment outside of a living organism, isolated from their usual biological surroundings e.g., in a test tube/dish. Measurements where tissue was excised and stored in environments unlike the human head were classified as *in vitro*.

3.3.4iii. Measurement Methods

Data acquisition techniques were categorised into four groups:

DAC - invasive method of determining electrical conductivity, where a current was directly applied to the tissue, either via implanted electrodes in the head, or onto excised samples. The resulting electric potential difference from the applied current is measured via additional (implanted or applied to excised tissue) electrodes to calculate the electrical conductivity.

Studies where electrical current was directly and invasively applied to the head tissue were characterised as DAC.

EIT – a non-invasive medical imaging technique where alternating current at single or multiple frequencies is applied to the skin through two or more conducting surface electrodes. The resulting potential difference between the remaining measuring electrodes is then recorded. From this the electrical conductivity, permittivity and impedance can be inferred to create a tomographic image (Barber & Brown, 1984; Henderson & Webster, 1978). Papers indicating an applied current of less than 1 kHz, injected through any number of electrodes and the resulting voltage were classified as EIT.

E/MEG – electromagnetic data recorded from E/MEG employed to iteratively estimate the equivalent electrical conductivity that best matches the computed source localisation given the obtained E/MEG data (Baysal & Haueisen, 2004). Articles estimating conductivity by employing data from E/MEG (of any set up) were characterised as E/MEG.

DTI – diffusion-weighted MR images of the brain are acquired to measure the diffusion tensor eigenvalues, from which the electrical conductivity tensor eigenvalues are directly calculated (Sekino et al., 2005; Tuch et al., 1999; Tuch et al., 2001). Transformation from diffusion to conductivity was conducted manually for papers which did not explicitly mention conductivity values. Texts using diffusion imaging (of any protocol) to explicitly estimate the electrical conductivity tensor map were considered as employing DTI methodology. This included any method for estimating conductivity from the diffusion tensor.

3.3.4iv. Frequency

Frequency of applied or injected current (if applicable). Frequency was not extracted from papers where this was not specified.

3.3.4v. Temperature

Classified according to whether the tissue sample was measured at/near *body* temperature (37°C) or *room* temperature (18-25°C). Unknown values were not reported for analysis.

3.3.4vi. Participant's Age

When available, mean, and standard deviation of participant's age were calculated for each paper. Age at time of death was recorded for deceased participants. If specific age was unavailable, age was characterised as *adult* (all participants were over the age of 18), *paediatric* (all participants were under the age of 18), or *both* (participants were a mixture of over and under the age of 18).

3.3.4vii. Participant Pathology

Participants were characterised as *healthy* if they had no neurological, developmental, or psychological deficits, as reported in the research paper. Pathology was categorised as *epilepsy* for studies recruiting patients that presented with any classification of epileptic seizure. Similarly, *tumour* was assigned to papers where patients displayed any type of tumour in the tissue under question, and *neuro* to patients with any type of neurological disorder that was not otherwise classifiable. Further pathologies included *Parkinson's Disease*, and *stroke*. All conductivity values were assumed to originate from healthy tissue, within the classified pathology, unless otherwise stated. Pathology was reported as unknown if not available in the literature.

3.3.5. Quality Analysis

Drawing robust conclusions from systematic reviews and meta-analyses requires consideration of the systematic and random errors introduced in each included study. "Assessing the methodological quality" must be carried out in order to estimate "risk of bias" (Moher et al., 1996; Verhagen et al., 2001). Various tools are available for assessing study quality and addressing the systematic errors in each study. None, however, specifically assess the quality of studies measuring the electrical conductivity of the human head. This meta-analysis, therefore, made use of the Cochrane Collaboration recommended Quality Assessment of Diagnostic Accuracy Studies (QUADAS) checklist (Whiting et al., 2003). Each item was adjusted for relevance, and any additional applicable items were added. A scaled numerical value was further assigned according to the studies compliance with each item; any irrelevant items were ignored. The sum, divided by the number of items, was subsequently calculated to provide a final Quality Assessment Score (QAS), with an absolute maximum value of one (the closer the score is to one, the more reliable the study was

considered). To ensure reliability of the QAS's, papers were chosen at random and QAS's calculated by two researchers, any discrepancies were discussed and if not resolved the mean QAS was assigned. The employed Quality Assessment Protocol and three examples are provided in Appendix C.

In addition to accounting for systematic errors within each study, random errors produced from inherently unpredictable variation in methodology were accounted for. This was adapted from the guidelines provided by Rosenthal (1991) and Borenstein and colleagues (2011) for meta-analysis weighting. Confidence values for each measurement were calculated to indicate the confidence each value of conductivity was 100% accurate. Firstly, the relative error was calculated for each conductivity value. This was taken as the standard deviation percentage of a multitude of values for a single tissue type for each participant. If the method is 100% precise, each value for the same tissue should be the same. Alternatively, if unavailable, the error attributed to the measurement protocol was employed – both described as a decimal. If both the standard deviation and measurement error were provided, the standard deviation was used to calculate the relative error. The relative error was then subtracted from one (where one indicates complete confidence the conductivity value is 100% accurate) to obtain a final confidence value. The maximum value is one. For example, a reported conductivity value with an associated standard deviation percentage of 8% will receive a confidence value of 0.92. Alternatively, when the standard deviation was not provided, the experimental error was utilised instead, e.g., a study with a methodological error of 0.05 would receive a confidence value of 0.95.

To incorporate both the systematic and random errors associated with each study, the Quality Assessment Score of each study and the confidence values of each conductivity value were combined to provide a “weight”. This weight was calculated by multiplying the QAS by the confidence value (both with a maximum of one). The maximum associated weight each value has towards the analysis is therefore one. Values assigned weights closer to one were therefore regarded as being more accurate.

3.3.6. Statistical Analysis

Data was pooled and grouped according to tissue type, in order to determine i) the variation in conductivity for each tissue, ii) which significant variables account for differences in

conductivity, iii) whether mean conductivity values for each tissue type are statistically different depending on employed methodology and participant demographics, and iv) reveal any statistical relationship between conductivity and reported variables.

Boxplot diagrams, presenting the range, median and mean of conductivity measurements for each tissue type were created to demonstrate variation in conductivity within different tissues. For each tissue with more than three results in at least two variables, a weighted multiple regression was carried out using SPSS (Corp, 2013). The dependent variable (DV; i.e., conductivity) was regressed against every independent variable (IV; i.e., measurement condition, method, frequency, temperature, age, and pathology). This was done collectively, to determine the proportion of variance accounted for by all factors, and individually to discover significant factors predicting variation in conductivity. Weights for each conductivity value were assigned according to the QAS described above (section 3.2.5). A two-tailed t-test (when comparing two independent variables) or a one-way Analysis of Variance (ANOVA, when comparing more than two independent variables) was conducted to reveal differences in conductivity for each tissue according to categorical IV's. A Pearson correlation analysis was alternatively conducted for continuous IV's accounting for significant variation to reveal any statistical relationships.

3.4. Results

3.4.1. Search Results

Following removal of duplicates, 3121 studies were identified through the literature and reference list search, of which 382 abstracts were screened for relevance and 211 full text articles were obtained and assessed for eligibility. A total of 170 papers were excluded (see Appendix A).

3.4.2. Included Studies

A total of 41 studies (342 participants) were included in the quantitative synthesis (Table 3.2). Seventeen different tissue types were identified (in addition to BSCR), using 4 methodologies and 3 measurement conditions. Conductivity was measured *in vivo* in 27, *in vitro* in 7 and *ex vivo* in 8 research papers. Measurements were obtained using DAC in 14 studies, EIT in 11, E/MEG in 8 and DTI in 9 papers. Conductivity was acquired at

frequencies varying between 0 Hz and 1005 Hz, and tissue temperatures between 18.5 and 37.5°C. Of the 20 articles that specified, total participant age ranged from 4 months to 87 years old. The remainder classified subjects into adults or children. Twenty-nine papers reported on healthy participants, participants from 10 studies were diagnosed with epilepsy, whilst separate papers included patients with various neurological disorders, Parkinson's Disease, and stroke. A summary of all included papers is presented in Table 3.2. Descriptive statistics for each tissue type are provided in Table 3.3, in addition to a boxplot displaying variation in conductivity values for different tissue types (Figure 3.1). A GitHub Repository was created to provide continual updates, for any measurements of human head electrical conductivity values (<https://github.com/Head-Conductivity/Human-Head-Conductivity.git>). This resource provides information on all values from the current literature mentioned in this chapter as well as further results since publication in 2019.

The average mean was calculated for each tissue type, where all conductivity values contributed equally to the mean. A weighted average mean was additionally calculated to take into consideration the quality of each study and provide a recommended value that was obtained under suitable and realistic conditions. The weighted average mean and standard deviation (in S/m) for the main tissue types were: scalp = 0.4137 ± 0.176 , whole skull = 0.016 ± 0.019 , spongiform skull layer = 0.048 ± 0.0735 , whole compact skull layer = 0.0046 ± 0.0016 , outer compact = 0.0049 ± 0.0029 , inner compact = 0.0068 ± 0.0036 CSF = 1.7358 ± 0.17 , GM = 0.3787 ± 0.16 , WM = 0.1462 ± 0.11 , BSCR = 50.4 ± 39 . A boxplot evidencing the average weights assigned to each study according to the employed methodology is further demonstrated (Figure 3.2). Average study weights were revealed to be significantly different depending on methodology [$F(3, 41) = 3.121, p=.022$].

| Author | Method | Design | Freq. | Part. N. | Age | Path. | Weight |
|----------------------------------|-------------|-------------------|-----------|-----------|------------|-------------|------------|
| (Burger & van Milaan, 1943) | DAC | ex vivo | 0 | 1 | adult | healthy | 0.8 |
| (Rosenthal & Tobias, 1948) | DAC | ex vivo | 1000 | 1 | adult | healthy | 0.36 |
| (Burger & Van Dongen, 1961) | DAC | ex vivo | 1000 | 1 | adult | healthy | 0.44 |
| (Rush & Driscoll, 1968) | DAC | ex vivo | | 1 | adult | healthy | 0.83 |
| (Cohen & Cuffin, 1983b) | E/MEG | in vivo | 0.3-300 | 2 (m) | adult | healthy | 0.71 |
| (Eriksen, 1990) | E/MEG | in vivo | 40 | 4 | adult | healthy | 0.22 |
| (Law, 1993) | DAC | in vitro | 100 | 1 | adult | healthy | 0.87 |
| (Pierpaoli et al., 1996) | DTI | in vivo | | 8 | adult | healthy | 0.34 |
| (Baumann et al., 1997) | DAC | in vitro | 10 – 1000 | 7 (3m) | 6.6 | neuro | 0.69±0.05 |
| (Sorensen et al., 1999) | DTI | in vivo | | 1 | adult | stroke | 0.81 |
| (Uluğ and Van Zijl, 1999) | DTI | in vivo | | 5 | adult | healthy | 0.36 |
| (Oostendorp et al., 2000) | DAC | in vitro | 10-100 | 1, 2 (1m) | adult | healthy | 0.77 |
| (Akhtari et al., 2000) | DAC | in vitro | 20 | 1 | adult | healthy | 0.86 |
| (Akhtari et al., 2002) | DAC | ex vivo | 10, 90 | 4 (2m) | 56±26.7 | epilepsy | 0.93 |
| (Hoekema et al., 2003) | DAC | in vitro, ex vivo | 10 | 1 (f), 5 | 68, 34±1 | healthy | 0.86 |
| (Gonçalves et al., 2003b) | EIT | in vivo | 60 | 6 (3 m) | 32.3±7 | healthy | 0.62 |
| (Gonçalves et al., 2003a) | EIT & E/MEG | in vivo | 60 | 6 (3 m) | adult | healthy | 0.5 ±0.01 |
| (Baysal & Haueisen, 2004) | E/MEG | in vivo | 4 | 10 (5m) | 30±13 | healthy | 0.37±0.37 |
| (Gutiérrez et al., 2004) | E/MEG | in vivo | 2 | 2 (1m) | 32.5±10.6 | healthy | 0.52±0.08 |
| (Clerc et al., 2005) | EIT | In vivo | 110 | 1 | adult | healthy | 0.64±0.009 |
| (Sekino et al., 2005) | DTI | in vivo | | 5 | adult | healthy | 0.67±0.02 |
| (Lai et al., 2005) | EIT | in vivo | 50 | 5 (4m) | 10±2 | epilepsy | 0.54 |
| (Zhang et al., 2006) | EIT | in vivo | 50 | 2 | paediatric | epilepsy | 0.66 |
| (Akhtari et al., 2006) | DAC | ex vivo | 5-1005 | 21 (12m) | 13.5±15.1 | epilepsy | 0.95 |
| (Tang et al., 2008) | DAC | in vitro | 1000 | 48 (38m) | 47.6 | healthy | 0.999 |
| (Gattellaro et al., 2009) | DTI | in vivo | | 20 (10m) | 61±12 | healthy, PD | 0.34 |
| (Rullmann et al., 2009) | DTI | in vivo | | 1 | 0.916 | epilepsy | 0.98 |
| (Akhtari et al., 2010) | DAC | ex vivo | 6 - 1005 | 15 (8m) | 7.93±6.04 | epilepsy | 0.95 |
| (Gullmar et al., 2010) | DTI | in vivo | | 1 (m) | 30 | healthy | 0.41 |
| (Wang et al., 2010) | DTI | in vivo | | 71(39m) | 41.8±14.5 | healthy | 0.36 |
| (Dannhauer et al., 2011) | E/MEG | in vivo | | 4 | 25±4.6 | healthy | 0.34 |
| (Aydin et al., 2014) | E/MEG | in vivo | | 1 (f) | 17 | epilepsy | 0.86 |
| (Ouypornkochagorn et al., 2014) | EIT | in vivo | | 1 | adult | healthy | 0.77±0.01 |
| (Dabek et al., 2016) | EIT | in vivo | 2 | 9 (4m) | 32.5±10 | healthy | 0.63±0.04 |
| (Akhtari et al., 2016) | DAC | in vitro | 10 | 24 | paediatric | epilepsy | 0.7±0.2 |
| (Acar et al., 2016) | E/MEG | in vivo | | 2 (m) | 21.5±2.12 | healthy | 0.72±0.02 |
| (Koessler et al., 2017) | EIT | in vivo | 50 | 15 (10m) | 38±10 | epilepsy | 0.64±0.048 |
| (Huang et al., 2017) | EIT | in vivo | 1 - 100 | 10 | adult | epilepsy | 0.61 |
| (Fernández-Corazza et al., 2017) | EIT | in vivo | 27 | 4 (m) | 49±4.8 | healthy | 0.59±0.08 |
| (Arumugam, 2017) | EIT | in vivo | 27 | 10 | adult | healthy | 0.3 |
| (Chauhan et al., 2018) | DTI | in vivo | 10 | 2 (m) | adult | healthy | 0.94 |

Table 3.2. Summary of papers included in the meta-analysis. This includes the authors name(s), employed methodology (direct applied current (DAC), electrical impedance tomography (EIT), electro- or magneto-encephalography (E/MEG), diffusion tensor imaging (DTI)) and measurement condition. As well as, frequency (Hz), number of participants (number, including gender (m=male)), age (years, either as mean \pm standard deviation or classified into adult/paediatric), pathology (where neuro = neurological disorder and PD = Parkinson's Disease) and average assigned weight (\pm standard deviation) according to the QAS described in section 3.3.5.

| Tissues | Min | Max | Mean | Weighted mean | St. Dev. | n. of values | n. of studies | Part. n. |
|---------------|--------|--------|--------|---------------|----------|--------------|---------------|----------|
| Scalp | 0.137 | 2.1 | 0.5345 | 0.4137 | 0.1760 | 44 | 10 | 44 |
| Muscle | 0.1482 | 0.4167 | 0.3243 | 0.3243 | 0.1526 | 3 | 1 | 1 |
| Whole skull | 0.0018 | 1.718 | 0.0708 | 0.0160 | 0.019 | 99 | 20 | 121 |
| Spongy | 0.0012 | 0.2890 | 0.0559 | 0.048 | 0.0735 | 16 | 4 | 10 |
| Compact | 0.0024 | 0.0079 | 0.0045 | 0.0046 | 0.0016 | 8 | 4 | 54 |
| Outer Compact | 0.0008 | 0.0078 | 0.0047 | 0.0049 | 0.0029 | 10 | 2 | 5 |
| Inner Compact | 0.0028 | 0.0129 | 0.0067 | 0.0068 | 0.0036 | 10 | 2 | 5 |
| Sutures | 0.0078 | 0.0735 | 0.0273 | 0.0266 | 0.0239 | 6 | 2 | 49 |
| CSF | 1.39 | 1.799 | 1.611 | 1.7358 | 0.1731 | 20 | 3 | 11 |
| Whole Brain | 0.054 | 13.75 | 1.3519 | 0.3841 | 0.1017 | 44 | 6 | 30 |
| GM | 0.06 | 1.13 | 0.4083 | 0.3787 | 0.1549 | 46 | 11 | 140 |
| WM | 0.0646 | 0.6412 | 0.1455 | 0.1462 | 0.1054 | 71 | 8 | 71 |
| WM perp | 0.0620 | 0.4390 | 0.1216 | 0.1175 | 0.0495 | 41 | 3 | 49 |
| WM par | 0.0543 | 0.9150 | 0.1352 | 0.1226 | 0.0929 | 41 | 3 | 49 |
| Blood | 0.433 | 0.7622 | 0.5799 | 0.5737 | 0.106 | 14 | 3 | 3 |
| EZ | 0.2320 | 0.5278 | 0.2994 | 0.2949 | 0.0737 | 15 | 1 | 15 |
| Dura | | | 0.461 | | | 1 | 1 | 2 |
| BSCR | 11 | 290 | 58.69 | 50.4 | 38.93 | 51 | 10 | 47 |

Table 3.3. Summary of the electrical conductivity values for each tissue. From the literature, the minimum, maximum, mean, weighted mean (according to the QAS described in section 3.3.5), standard deviation (st. dev.), number of values, number of studies and number of participants for each tissue type is provided.

Variation in Conductivity Values for all tissues

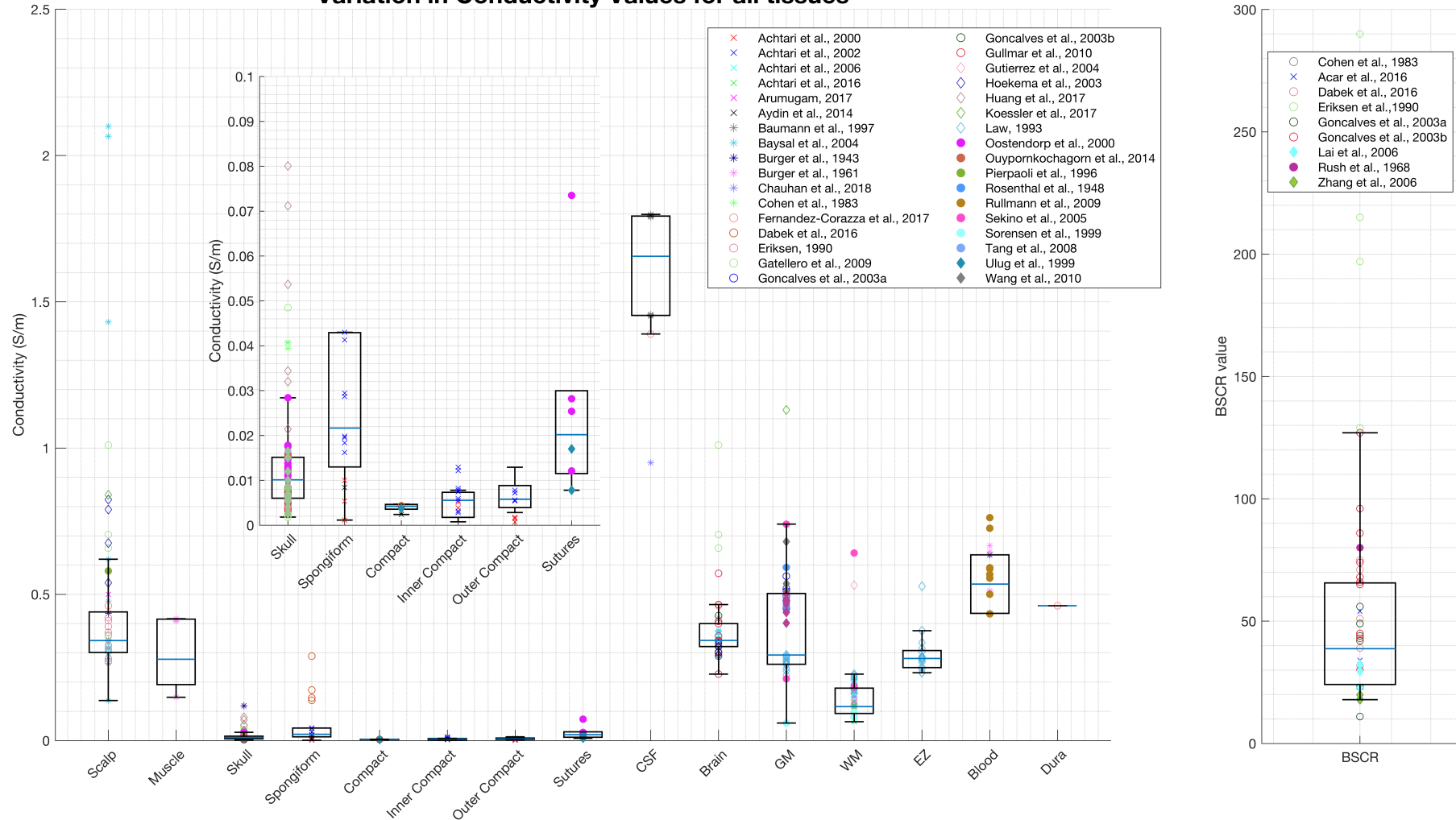


Figure 3.1. Boxplot displaying the inter-quartile range (first to third quartile as solid box), the median (solid blue line), minimum and maximum (solid whiskers) of all available conductivity values (S/m) for all tissues and BSCR, corresponding to the respective paper

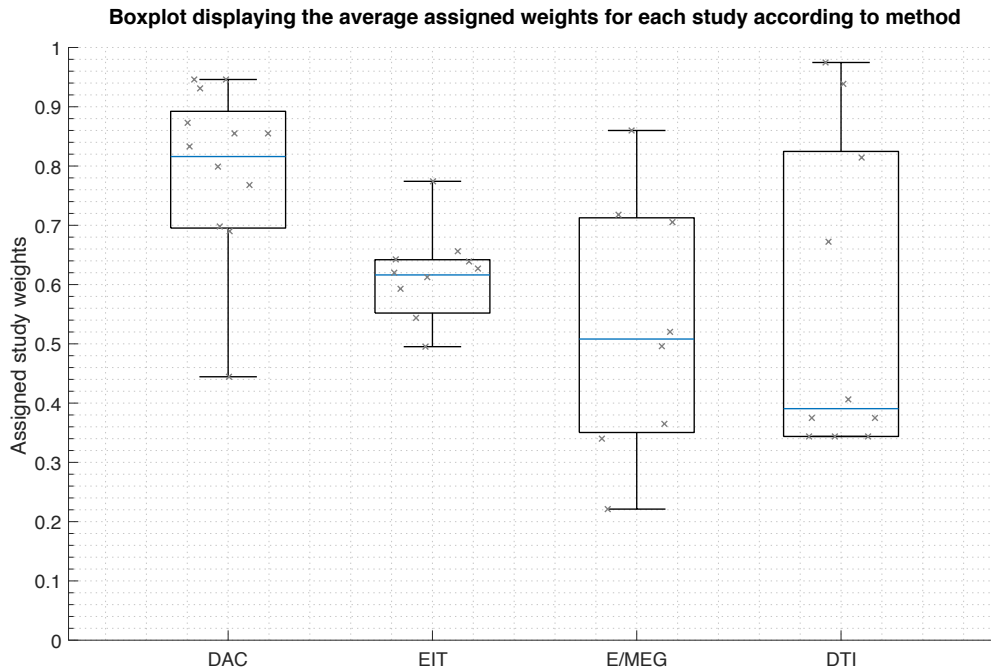


Figure 3.2. Boxplot displaying the mean value of the assigned weights for each study (indicated by a cross) dependent on the employed methodology. The inter-quartile range (box), median (solid blue horizontal line), maximum and minimum (upper and lower whiskers respectively) of all weights displayed for each method.

Following visual inspection, it can be seen conductivity values vary considerably within and between tissue types. Insufficient data was available to calculate regression statistics for muscle, fat, blood, the epileptogenic zone and the dura layer.

3.4.3. Scalp

A weighted multiple regression revealed scalp conductivity variation was insignificantly predicted by the IV's collectively ($p > .05$). Although insignificantly different, a comparison between employed method (as shown in Figure 3.3) was made to graphically display any elevated values and further demonstrate variation despite statistical insignificance. Figure 3.3 further reveals less deviation within values for EIT than for E/MEG. Huang and colleagues (2017) yielded conductivity measurements significantly above the inter-quartile range. Additionally, Baysal and Haueisen (2004) revealed highly elevated conductivity values beyond the axis range displayed in Figure 3.3, with standard deviation $>5000\%$ (see section 3.5.1 for further explanation of outliers).

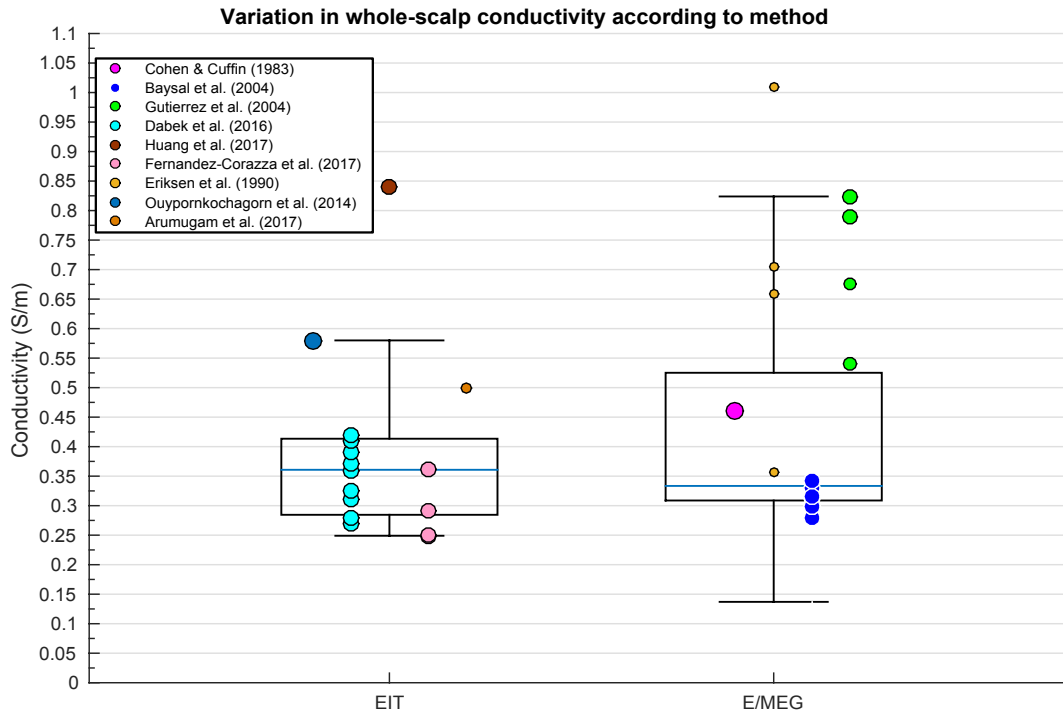


Figure 3.3. Boxplot displaying inter-quartile range (box), medium (solid blue horizontal line), maximum and minimum (upper and lower whiskers respectively) of scalp conductivity (S/m) according to method for each available paper. Each circle corresponds to a conductivity value as measured in the respective paper and the size of the data points indicates relative weight of each value.

3.4.4. Skull

3.4.4.i. Whole-skull

A weighted multiple regression revealed deviation in whole-skull conductivity could be significantly predicted by the methodology, condition, temperature, frequency, pathology, and age collectively [$R^2(6, 36) = .827, p < .001$]. A one-way ANOVA revealed conductivity of the whole skull varied significantly according to employed methodology [Figure 3.4; $F(2, 96) = 4.088, p = .020$]. Differences in conductivity values for the whole-skull were statistically different according to method, where values obtained using EIT were significantly lower than those obtained with DAC and E/MEG.

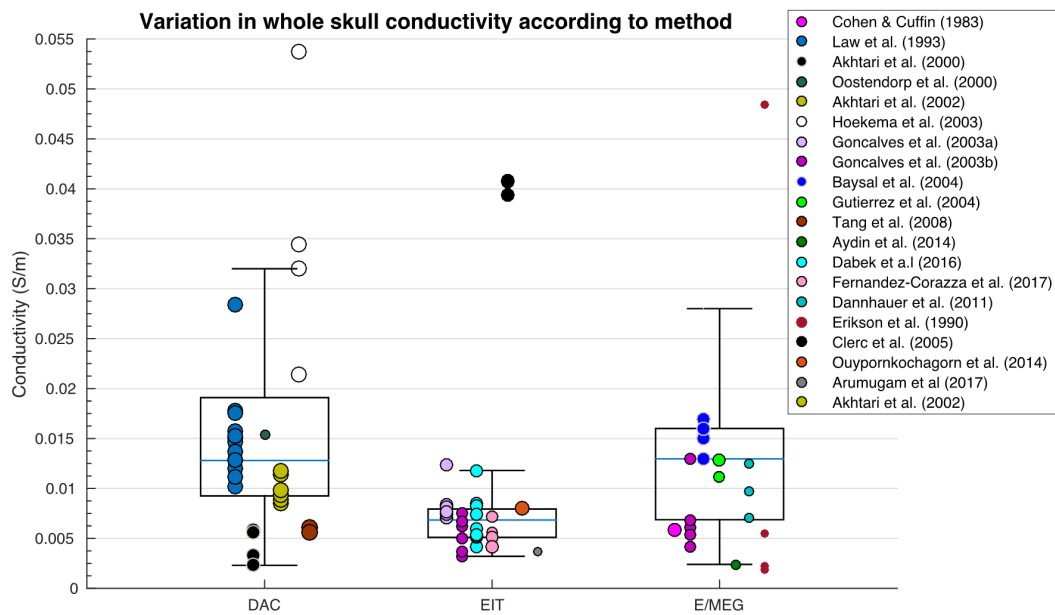


Figure 3.4. Boxplot displaying variation in whole-skull conductivity (S/m) according to method. The inter-quartile range (box), medium (solid blue horizontal line), maximum and minimum (upper and lower whiskers respectively) is graphically depicted. Each circle corresponds to a conductivity value as measured in the respective paper and the size of the data points indicates relative weight of each value.

3.4.4ii. Spongiform Bone Skull Layer

A weighted multiple regression revealed variation in conductivity values of the spongiform bone layer of the skull was significantly predicted by condition, temperature, frequency, pathology and age [$R^2(5, 6) = .832, p = .026$]. Spongiform conductivity measurements were significantly different according to condition [Figure 3.5; $F(2, 15) = 11.357, p = .001$] and temperature [$t(16) = 2.449, p = .001$].

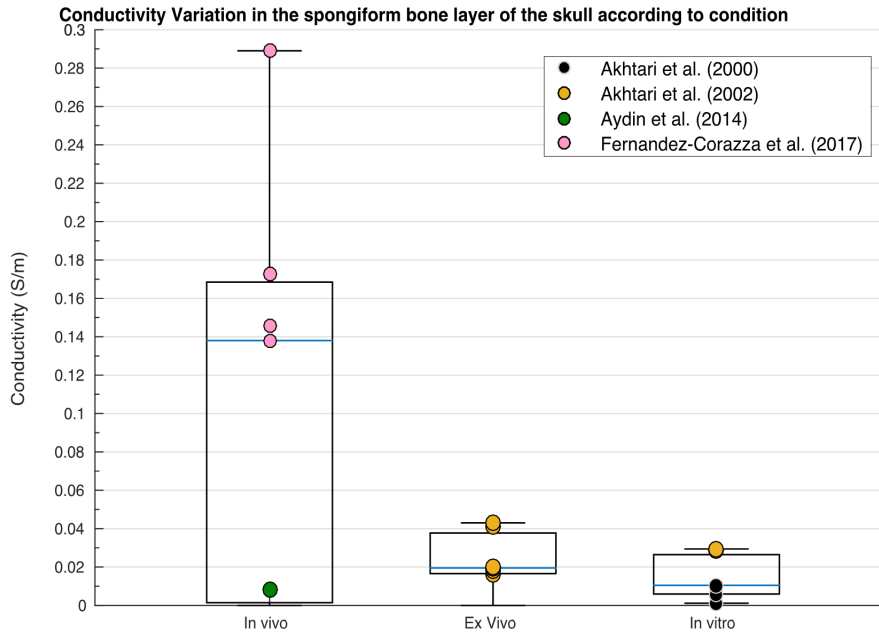


Figure 3.5. Boxplot displaying variation in conductivity (S/m) of the spongiform bone layer of the skull according to condition. The inter-quartile range (box), medium (solid blue horizontal line), maximum and minimum (upper and lower whiskers respectively) is graphically depicted. Each circle corresponds to a conductivity value as measured in the respective paper and the size of the data points indicates the relative weight of each value.

3.4.4iii. Compact bone skull layer

None of the IV's significantly predicted variation in conductivity values of the whole compact layer, the inner compact bone layer or the outer compact bone layer according to the weighted multiple regression analysis. Despite insignificant results, a graphical representation of conductivity for the different compact bone layers revealed clear diversions within and between each of the layers (Figure 3.6).

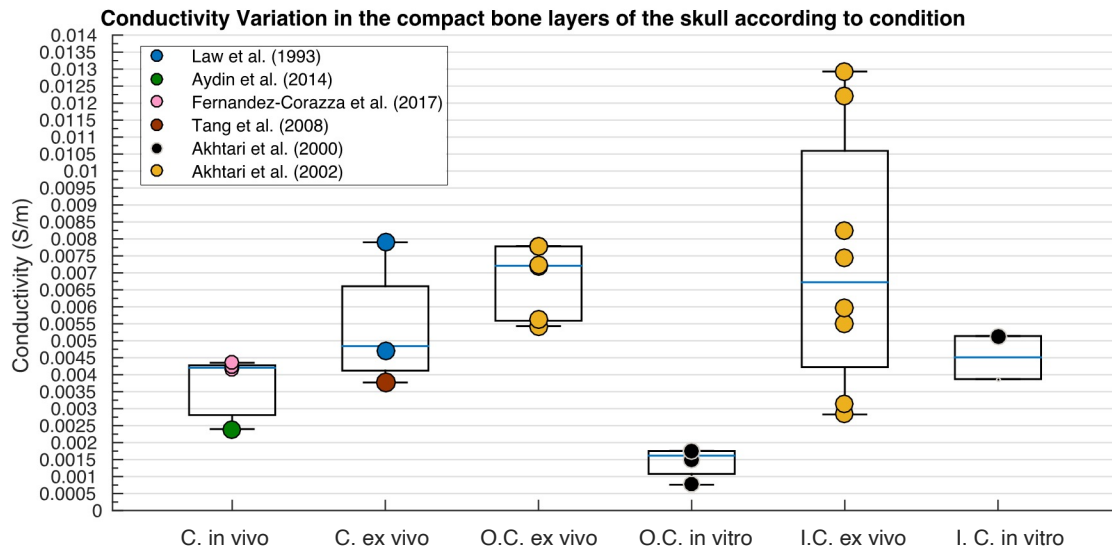


Figure 3.6. Boxplot displaying variation in conductivity (S/m) of the compact layers according to condition. The inter-quartile range (box), medium (solid blue horizontal line), maximum and minimum (upper and lower whiskers respectively) is graphically depicted. Each circle corresponds to a conductivity value as measured in the respective paper and the size of the data points indicates the relative weight of each value.

3.4.5. Cerebrospinal Fluid

Significant differences [$t(36) = 2.695, p=.006$] in measurements obtained at body (~ 1.79 S/m) and room (~ 1.45 S/m) temperature were revealed, as previously found by Baumann and colleagues (1997). Variability in CSF conductivity at room temperature was discovered to be insignificantly explained by the weighted multiple regression model.

3.4.6. Brain

Differences in whole-brain conductivity values were not significantly predicted by the independent variables according to the weighted multiple regression analysis. Figure 3.7 reveals the variation in data obtained for conductivity values of the whole-brain for each methodology, suggesting no one method generates a stable result for conductivity of the brain as a whole compartment.

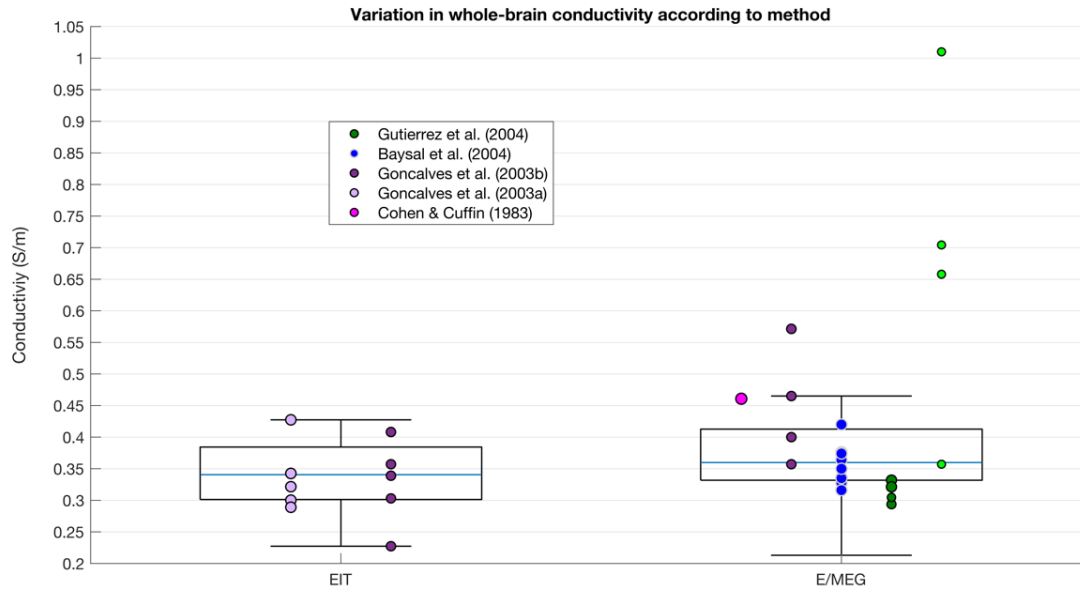


Figure 3.7. Boxplot displaying variation in whole-brain conductivity (S/m) depending on method. The inter-quartile range (box), medium (solid blue horizontal line), maximum and minimum (upper and lower whiskers respectively) is graphically depicted. Each circle corresponds to a conductivity value as measured in the respective paper and the size of the data points indicates the relative weight of each value.

3.4.6i. Grey Matter

Variation in GM conductivity was not significantly explained by the weighted multiple regression model. However, a two-tailed t-test determined significant differences in GM conductivity according to method [Figure 3.8; $t(16) = 2.12$, $p < .05$], where results obtained with DTI were significantly higher than EIT. A variation was also seen in pathology (Figure 3.9).

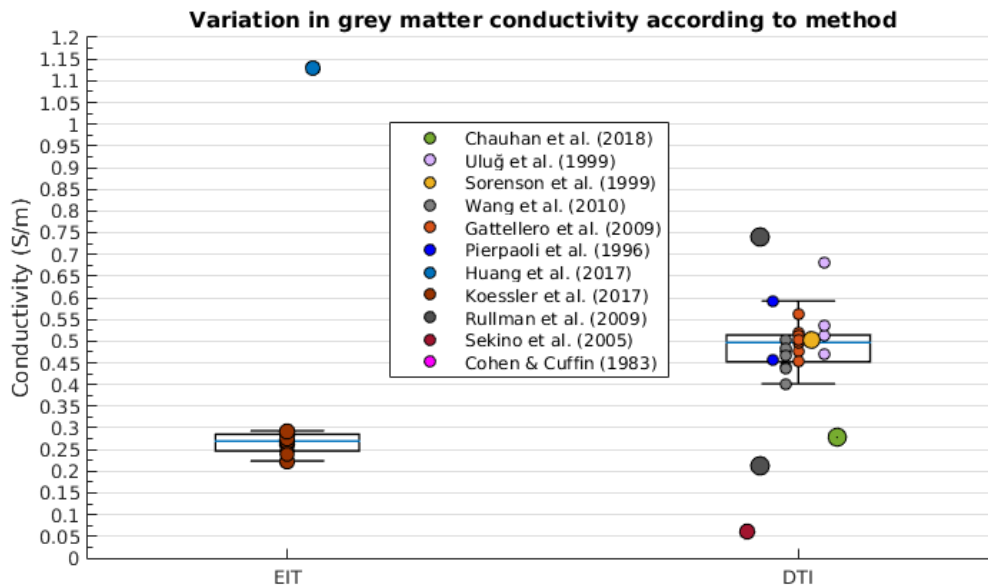


Figure 3.8. Boxplot displaying variation in GM conductivity (S/m) depending on method. The inter-quartile range (box), medium (solid blue horizontal line), maximum and minimum (upper and lower whiskers respectively) is graphically depicted. Each circle corresponds to a conductivity value as measured in the respective paper and the size of the data points indicates the relative weight of each value.

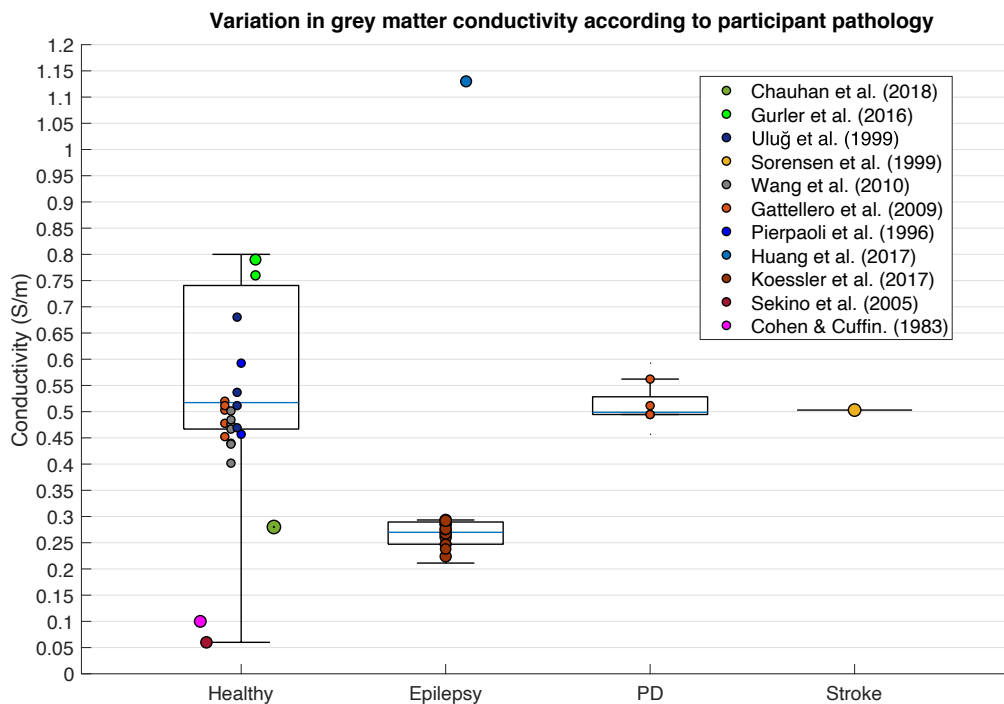


Figure 3.9. Boxplot displaying variation in GM conductivity (S/m) depending on pathology (PD; Parkinson's Disease). The inter-quartile range (box), medium (solid blue horizontal line), maximum and minimum (upper and lower whiskers respectively) is graphically depicted. Each circle corresponds to a conductivity value as measured in the respective paper and the size of the data points indicates the relative weight of each value.

3.4.6ii. White Matter

A weighted multiple regression analysis revealed variation in isotropic WM conductivity was significantly explained by methodology, condition, frequency, pathology and age collectively [$R^2(5, 36) = .696, p < .001$], where values varied significantly according to method [Figure 3.10; $F(3,65) = 12.3, p < .001$], condition [$F(2, 66) = 13.8, p < .001$], pathology [$F(2, 101) = 34.437, p < .001$] and temperature [$t(45) = 1.71, p < .05$]. Furthermore, pathology and age collectively explained a significant proportion of variation in WM conductivity measured perpendicularly [$R^2(2, 14) = .459, p = .014$] and in parallel [$R^2(2, 14) = .677, p < .001$]. Where perpendicular WM values varied according to condition [$F(2, 38) = 36.828, p < .001$], temperature [$t(39) = 1.105, p = .031$] and participant age [$r(41) = .638, p = .006$], whilst parallel WM measurements differed with condition [$F(2, 38) = 9.78, p < .001$] and age [$r(41) = .520, p = .032$].

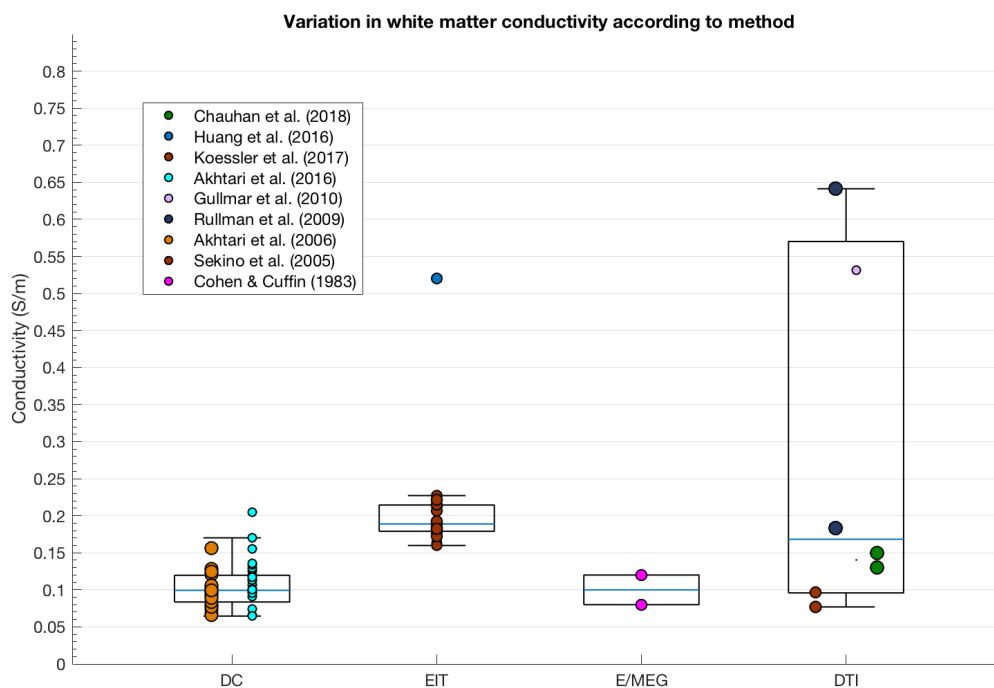


Figure 3.10. Boxplot displaying variation in WM conductivity (S/m) according to method. The inter-quartile range (box), medium (solid blue horizontal line), maximum and minimum (upper and lower whiskers respectively) is graphically depicted. Each circle corresponds to a conductivity value as measured in the respective paper and the size of the data points indicates the relative weight of each value.

3.4.7. Brain to Skull Conductivity Ratio (BSCR)

Variation in BSCR calculations were significantly predicted by methodology, frequency, pathology and age collectively, in the weighted regression analysis [$R^2(4, 26) = .302, p = .046$]. Figure 3.11 displays the variation of BSCR according to method, although a comparison of means revealed no significant differences between employed technique. Additionally, BSCR values correlated positively with participant age [Figure 3.12; $r(51) = .376, p = .014$].

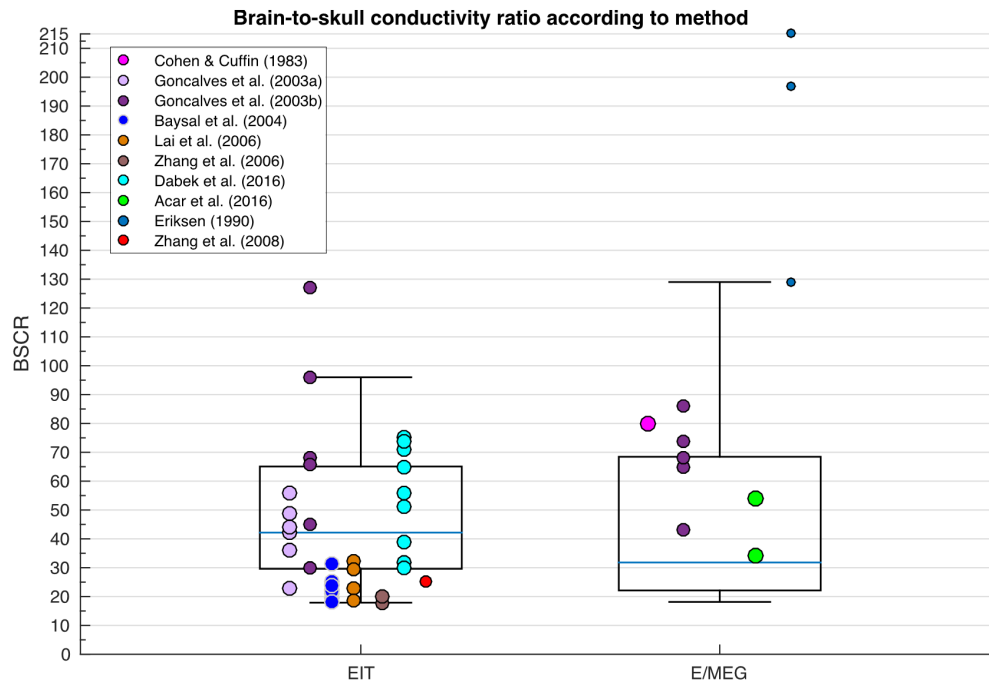


Figure 3.11. Boxplot displaying variation in BSCR depending on method. The inter-quartile range (box), medium (solid blue horizontal line), maximum and minimum (upper and lower whiskers respectively) is graphically depicted. Each circle corresponds to a value as measured in the respective paper and the size of the data points indicates the relative weight.

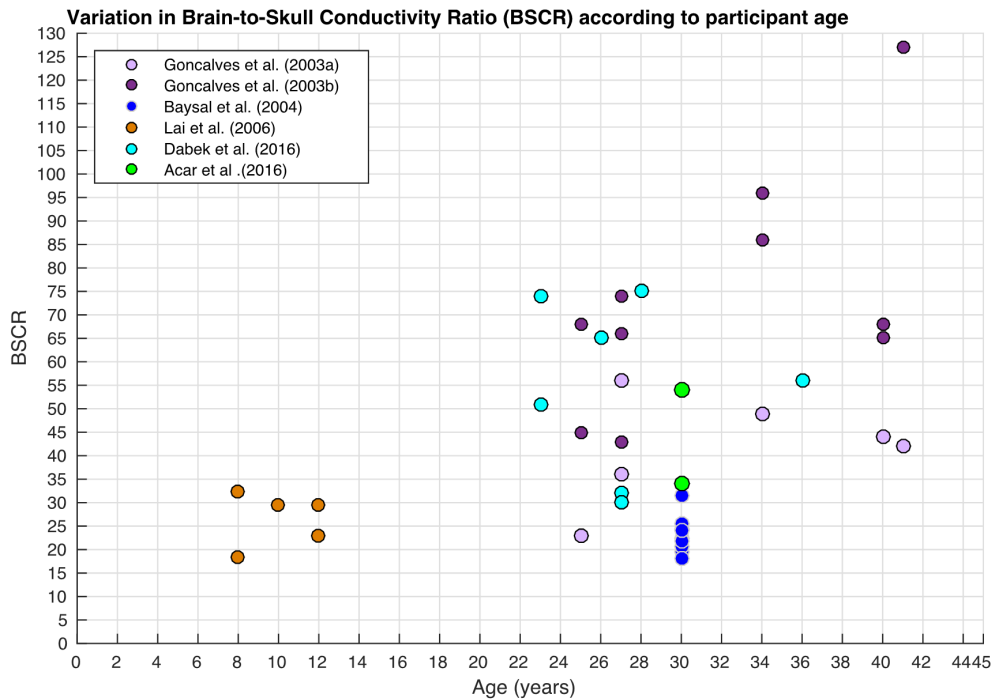


Figure 3.12. Scatter diagram displaying BSCR as a function of participant's age. Each circle corresponds to a value as measured in the respective paper and the size of the data points indicates the relative weight of each value.

3.5. Discussion

This chapter systematically investigated variation in conductivity of 17 different head tissues and the BSCR as reported in 41 research papers, identified through a literature search of three relevant databases. The mean, standard deviation, minimum and maximum were calculated for each tissue type (Table 3.3). In addition, the weighted average mean was computed, which provided an optimum (and therefore suggested) value when conductivity is unable to be obtained on an individual basis. The weighted average means and standard deviation (in S/m) for each tissue type were scalp = 0.4137 ± 0.176 , whole skull = 0.016 ± 0.019 , spongiform skull layer = 0.048 ± 0.0735 , whole compact skull layer = 0.0046 ± 0.0016 , outer compact = 0.0049 ± 0.0029 , inner compact = 0.0068 ± 0.0036 CSF = 1.7358 ± 0.17 , GM = 0.3787 ± 0.16 , WM = 0.1462 ± 0.11 , WM perpendicular = 0.12 ± 0.05 , WM parallel = 0.12 ± 0.09 , blood = 0.57 ± 0.11 and BSCR = 50.4 ± 39 . The differences between values for each tissue were statistically tested against methodological and participant demographical variables to reveal significant predictors. Inadequate data was available for muscle, fat, blood, the epileptogenic zone, or the dura layer to carry out a multiple regression. Collectively, the independent variables (related to both methodology and demographics)

insignificantly explained variation in the scalp, the compact layers of the skull, CSF, the whole-brain, and GM. In contrast, variation in whole-skull conductivity could significantly be explained by all the IV's collectively, where values were revealed to specifically differ significantly depending on method. Variation in the conductivity of the spongiform bone layer of the skull was significantly predicted by condition, frequency, pathology, and age, where values were meaningfully different according to condition and temperature. Despite insignificant results for regression analysis, GM notably differed depending on method and pathology. Variation in isotropic WM electrical conductivity was further predicted by methodology, condition, frequency, pathology, and age collectively in the regression model, where values diverged according to method, condition, pathology, temperature, and frequency. A significant proportion of variation in WM conductivity measured perpendicularly and in parallel was further explained by pathology and age collectively. Specifically, perpendicular WM values differed with condition, temperature, and age, whilst parallel WM measurements fluctuated with condition and age. Lastly, the meta-regression revealed the BSCR could be significantly attributed to variation in methodology, frequency, pathology, and age collectively, revealing a positive correlation between the ratio and participant's age.

3.5.1. Data Exclusions

Explanations for the presence of outliers and reasons for any data exclusion in the meta-analysis are further discussed. Firstly, data acquired at frequencies notably higher than 1000 Hz were removed. These conditions were deemed unnatural, considering the bandwidth of most neuronal signals is 1 Hz – 1 kHz, with resonant frequencies of <100 Hz for the brain (Groppe et al., 2013) and <1000 Hz for the skull (Håkansson et al., 1994). This also included exclusion of papers utilising Magnetic Resonance EIT (MREIT) to reconstruct conductivity from induced magnetic flux as this employed frequencies above 1 kHz. Conductivity results obtained from Baysal and Haueisen (2004) employing a conventional least-squares estimator (LSEE) on E/MEG data were further revealed, and as stated by the authors, as being “unrealistic [negative resistivities] and unstable” (Baysal & Haueisen, 2004). These unstable results were evident from the large standard deviation percentage (>5000% for the scalp, >200% for the skull and >240% for the brain). The authors suggested such inaccuracies occurred from the use of LSEE linearisation in a highly non-linear problem, and hence were omitted from their own analysis. Furthermore, skull conductivity values reported by

Hoekema et al., (2003) were elevated approximately ten-fold, suggested to be “as expected [due to measurements] in non-physiological circumstances” (namely, saline-coated cadaver). These values, however, were not excluded from the current analysis as methodology was in line with previous cadaver studies and therefore should produce similar results. Huang and colleagues (2017) yielded significant outliers for the scalp, skull, whole-brain, GM, and WM, where median optimal conductivity was obtained by fitting model outputs (from literature) to recordings. These deviations may be explained by the use of an optimisation EIT approach where “best-fit” values were free to compensate for all inaccurate/simplified sources, tissue segmentation errors, changes in electrode location, etc. They therefore cannot reflect “true” conductivity values. Outliers were additionally revealed for the spongiform (but not compact) skull layer by Fernández-Corazza and colleagues (2017), which employed boundary EIT (bEIT) for reconstructing the electrical conductivity for a subset of the regional tissue parameters. The authors acknowledged low sensitivity of bEIT to spongiform variations, due to the relatively small proportion of spongiform to head volume and concluded such approximations may be difficult for unbiased bEIT estimators but remain valid for compact bone estimates. The quality analysis utilised in the current chapter attributed a confidence weighting to each value and is thus deemed acceptable to consider the large standard deviations leading to outliers. All outliers were therefore included in order to fully account for and explore reasons for variation in values.

3.5.2. Scalp

Additional eccentric values, although not classified as outliers, were revealed from Gutiérrez et al., (2004) for the scalp, where maximum likelihood estimation (MLE) was used to estimate the electrical conductivity from E/MEG measurements. Such results may be due, in part, to the necessity of accurate source location and head geometry knowledge to avoid estimation bias. The authors suggest the use of a Bayesian approach, which permits incorporating *a priori* information on conductivity distribution to reduce bias. Realistic measurements (excluding outliers and deviations, as discussed) of scalp conductivity, for example, ranged between 0.25 S/m and 0.435 S/m, which could not be attributed to any of the IV's. Such variation can be relevant in source localisation based on E/MEG. In particular, dipole sources close to measurement electrodes are sensitive to scalp conductivity (Gençer & Acar, 2004; Gonçalves et al., 2003). These results coupled with those of the current meta-analysis indicate that assuming scalp conductivity from the literature is not only inaccurate

but can lead to E/MEG source mislocalisation. These errors do not appear to be explainable by anything other than individual variability and hence personalised models of scalp conductivity should be considered to improve electromagnetic source localisation.

3.5.3. Skull

According to the meta-regression, variation in whole-skull conductivity can be accounted for by differences in all of the IVs (methodology, condition, temperature, frequency, pathology, and age), with specific variances between methodology and condition. Such significant results, however, may be due to overfitting of the data and meta-regression parameters employed. Future research could utilise machine learning techniques in order to refine the regression analysis and determine the most influential variables. This analysis was beyond the scope of the current chapter and ideally would require more data which is not presently available.

Values obtained from excised tissue in non-physiological circumstances after undergoing various processing, may change the electrolyte concentration and therefore skull conductivity (Akhtari et al., 2002). Considering the contrast between a saline-soaked processed cadaver and live skulls that remain in natural conditions between the scalp and meninges, differences in conductivity values post-mortem should be expected. Early research determined conductivity of rat femurs to decrease by a factor of 2.5 - 3 from live-to-50 hours post-mortem (Kosterich et al., 1983; 1984). This was further corroborated in the human skull, indicating a scaling factor of 2.5 – 4 from live-to-post-mortem (Wendel et al., 2006). These results are validated by Rush and Driscoll's (1969) mathematical model which states skull conductivity somewhat depends on the fluid (i.e., saline vs blood/CSF naturally positioned between meninges) permeating it. This suggests a live skull has higher conductivity than a saline-soaked cadaver skull (where saline conductivity is 1 S/m). It is consequently unsurprising *in vitro* values of skull conductivity differ from *in vivo* values – predicting increased conductivity *in vivo* (Akhtari et al., 2000; Law, 1993). The results from the previous literature coupled with the current meta-analysis, therefore indicate that skull conductivity should be measured *in vivo* (i.e., at body temperature, within the live head, etc.) to avoid bias and increase reliability.

Within *in vivo* reports, despite all being under similar conditions, skull conductivity values obtained using E/MEG appeared to be elevated compared to those employing EIT. These results may be explained by the use of statistically constrained estimation algorithms for E/MEG measurements. Here, conductivity was optimally estimated from E/MEG arrays acquired during electrical nerve stimulation. Furthermore, whole-skull conductivity was found to vary as a function of frequency, although the nature of the relationship was unclear. Previous literature has examined skull conductivity in wider frequencies, revealing a positive association. This was especially at frequencies higher than 10 kHz (Gabriel et al., 1996b; Tang et al., 2008), and suggest skull conductivity may exponentially increase at high frequencies. Within the relevant range for brain activity, skull conductivity increased by ~6.7% from 11-127 Hz (Dabek et al., 2016) and ~13% from 10-90 Hz (Akhtari et al., 2002), of which the authors developed a non-linear model for frequency dependence of different skull layers (Akhtari et al., 2003). Variation as a function of frequency may be expected due to interactions between mobile electrolytes (i.e., sodium and chloride) and relatively immobile molecules (i.e., proteins and blood components). This effects the relaxation rate of conductivity, dependent on the currents' frequency (Akhtari et al., 2002; Latif et al., 2010). Importantly, such frequency dependence has been implicated in causing the volume conductor to act as a low pass filter, which potentially contributes to E/MEG forward solutions errors and may therefore reduce accuracy in E/MEG source localisation.

Furthermore, results exploring differences according to age in the BSCR (see Figure 3.12) have implications for skull conductivity variation. Research has indicated skull, rather than brain, conductivity plays a larger role in BSCR values (Gonçalves et al., 2003), consequently suggesting skull conductivity varies with age. These results are discussed further in Section 3.5.3i (layered skull conductivity) and 3.5.6 (BSCR).

3.5.3i. Layered Skull

The majority of previous studies simplified the skull as a homogeneous layer, not accounting for differences in conductivity between the compact (upper, lower) and spongiform layers of the skull. Distinct conductivities for the three layers of the skull have previously been indicated (Akhtari et al., 2000; 2002; Fernández-Corazza et al., 2017; Tang et al., 2008), as supported by the current meta-analysis (see Figure 3.1). This is unsurprising considering the higher prevalence of fluid filled pores and cavities in spongiform (and hence higher

conductivity) compared to compact bone. Importantly, neglecting inhomogeneous estimations for a tri-layer skull has yielded significant errors in source localisation irrespective of model parameters (Dannhauer et al., 2011; Haueisen et al., 1999; 2002; Ollikainen et al., 1999; Pohlmeier et al., 1997). These authors have thus concluded realistic modelling of the skull layers to be necessary for accurate EEG source localisation. The current meta-analysis, however, revealed that variations exist between individuals even whilst considering a tri-layer skull. Variation in the electrical conductivity of the spongiform skull layer was revealed to be significant and attributed to deviations in condition, temperature, frequency, pathology, and age. Suggesting true values for conductivity of the spongiform layer will not only depend on methodological parameters but also individual demographics. Likewise, although the compact layers of the skull were insignificantly predicted by any of the parameters, large variation was still evident. This further elucidates the hypothesis that conductivity values fluctuate between individuals and support the suggestion for personalised models of skull conductivity.

Interestingly, a relationship with age was to be expected, regardless of homogeneity. This is due to presence of the fontanelles and open sutures which may remain unfused for several years as well as changes in skull microstructure throughout development, as discussed in greater detail in section 1.6.2. As such, differences between the neonatal and adult skull conductivity was to be expected. Previous studies have revealed higher skull conductivity for infants compared to adults, (Gibson et al., 2000; Pant et al., 2011) and an inverse correlation between skull conductivity and thickness with increasing age (Gibson et al., 2000). Additionally, paediatric skull tissue ordinarily contains greater quantities of ions and water, compared to calcified cranial bones of adults, hence higher conductivity may be expected (Schönborn et al., 1998). Further support from animal studies, although at different frequency ranges, have revealed skull conductivity to decrease with age, for example, in the rat (Peyman et al., 2001), pig (Peyman et al., 2007) and cow (Schmid & Überbacher, 2005). Although this expectation was not confirmed in the current meta-analysis, for accurate electromagnetic source localisation and current propagation, skull conductivity variations with age should be taken into consideration. Specifically, both EEG and MEG require individualised, or in the least an infant-specific volume conductor model to accommodate for relevant developmental changes (Bystron et al., 2008; Flemming et al., 2005; Rakic, 2006; Song et al., 2013).

Following from this, development of the human skull does not cease after infancy, but continues to undergo remodelling, microstructural, density and histological changes until death, further impacting conductivity. Firstly, total cranial thickness has been observed to increase with age (Todd, 1924) notably related to increase in diploë thickness (Hatipoglu et al., 2008; Sabancıoğulları et al., 2012), which in one study was accompanied with inner and outer compact thinning (Skrzat et al., 2004). Antonakakis and colleagues (2018) revealed a trend between participant age and skull conductivity but noted the small sample size (n=15) and large inter-subject variability rendered robust conclusions difficult and inadequate. Their recent study however, revealed a significant decline in conductivity with participant age (Antonakakis et al., 2020). Further results have also been inconsistent in determining the relationship between skull thickness, specifically, and age, finding no such association (Ishida & Dodo, 1990; Lynnerup, 2001; Lynnerup et al., 2005; Pensler & McCarthy, 1985; Sullivan & Smith, 1989). The presence of suture lines, not limited to infants, was furthermore shown to increase conductivity of the skull sample, by providing a path of high conductance (Law, 1993; Tang et al., 2008). Additionally, the percentage of spongiform bone within the skull was positively correlated with skull conductivity (Tang et al., 2008), whilst, skull thickness, which is non-uniform within and between individuals (Lynnerup, 2001; Lynnerup et al., 2005), was inversely correlated with scalp potentials (Chauveau et al., 2004). One paper, for example, revealed that a 20% and 40% decrease in skull thickness resulted in a 5-10% and 20-25% decrease in conductivity, respectively (Lai et al., 2005). Insufficient results were available to analyse the influence of sutures or skull thickness in the presented chapter; however, the discussed structural deviations further illuminate the importance of employing individualised models of head conductivity.

The influence of skull conductivity and segmentation inaccuracies has been explored extensively, revealing overwhelming source localisation errors for EEG (Lanfer et al., 2012; Montes-Restrepo et al., 2014; Wolters et al., 2006) and MEG (Cho et al., 2015; Lau et al., 2016) of up to 2 cm. Aydin and colleagues (2017) recently developed a multimodal technique, of which they emphasised the importance of individualised high-resolution finite element head models with WM anisotropy modelled from DTI and individually calibrated skull conductivity, alongside combined E/MEG and MRI information. Importantly, they note creating such realistic head models may not always be feasible, and therefore recommend, at minimum, skull conductivity to be individually adjusted to improve combined E/MEG source analysis. Variations in skull conductivity have been found to impact transcranial electric

stimulation focality and dose (Santos et al., 2016; Schmidt et al., 2015; Wenger et al., 2015), with one study revealing an error of 8% in dose (Fernández-Corazza et al., 2017). Such inaccuracies are clinically relevant, particularly regarding source estimation for refractory epilepsy (Brodbeck et al., 2011) and determining electrical current dose required for treatment of epilepsy (Berényi et al., 2012; Liebetanz et al., 2006), depression (Kalu et al., 2012) and other psychiatric disorders (Brunoni et al., 2013). Of note, Dannhauer and colleagues (2011) investigated variations in layered skull structures for EEG forward modelling and revealed inhomogenous but not isotropic modelling to be of most importance. For optimum skull modelling, they recommended assigning each skull voxel to a tissue type (compact or spongiform bone) with individually estimated or measured conductivity values. The relevance of skull conductivity on tDCS current propagation and EEG source localisation are discussed in more detail in Chapters 4 and 5, respectively.

3.5.4. Cerebrospinal Fluid

The results of the current meta-analysis are in line with previous report from Baumann and colleagues (1997), displaying significant variation in CSF conductivity dependent on temperature. They revealed 23% higher conductivity at body (37°C), approximately 1.79 S/m, than room (25°C) temperature, which corresponded to the temperature coefficient of 2% per 0.1 ml of potassium chloride (comparable to CSF conductivity and ion concentration (Fishman, 1992; McGale et al., 1977; Wu et al., 1991). The result from Baumann et al.'s (1997) study is frequently considered as a reference value for CSF conductivity. However, the current meta-analysis has revealed some variation in measurements, potentially suggesting instability in CSF conductivity between individuals. Deviating from Baumann's approximation (1.79 S/m), Cohen and Cuffin (1983b) reported a considerably lower conductivity for CSF (1.39 S/m). These results may be explained by their use of optimum estimation, rather than direct measurements, where conductivity was adjusted so the maximum potential in a theoretical EEG map matched the experimental equivalent. Considering the variation due to methodological error, CSF appears to be relatively stable between individuals, with an average conductivity converging around Baumann's results (1.79 S/m). Deviation in CSF conductivity may not significantly affect E/MEG forward and inverse modelling solutions. Future work could therefore employ a sensitivity analysis to explore the influence CSF conductivity has on electromagnetic source localisation and determine the necessity of individualised models.

3.5.5. Whole-Brain

The meta-regression failed to explain variation in conductivity of the brain as a homogeneous compartment, however values were revealed to significantly vary according to the employed method. Despite these significant results, variation between acquisition techniques were minimal, where large dissimilarities within each method remained evident. This further supports the suggestion that individual values of conductivity should be obtained. However, assuming homogeneous conductivity over the whole brain is generally considered a vast oversimplification and highly inaccurate. Such an assumption fails to consider differences between GM and WM conductivity, as well as structural disparity of GM/WM proportion in the brain. Early research determined GM to contain higher proportions of water than WM (Stewart-Wallace, 1939), demonstrating expected higher electrical conductivity for GM, compared to WM. Additionally, extensive literature has shown GM and WM volume to vary with development (Giorgio et al., 2010; Groeschel et al., 2010; Miller et al., 1980) and pathology; i.e. multiple sclerosis (Sastre-Garriga et al., 2005), Alzheimer's Disease (Salat et al., 1999), schizophrenia (Douaud et al., 2007) and ADHD (McAlonan et al., 2007), among others. These observations further support the use of individualised models of head volume and conductivity profiles for the most accurate representation of the human head.

3.5.5i. Grey Matter

The significant variation in GM conductivity may be somewhat explained by increased DTI values relative to EIT. Firstly, the Tuch et al. (1999) model derived the conductivity tensor from the water diffusion tensor through differential effective medium approximation (EMA), which uses an electromagnetic depolarisation factor to consider the impact of cell geometry to overall conductivity. This depolarisation factor was originally developed for WM structure, consisting of myelinated pyramidal cells, and therefore may not be completely translational to GM. Tuch and colleagues' later paper (2001), however, utilised the EMA method to show there exists a strong linear relationship between the conductivity and diffusion tensors, regardless of tissue type. They generated a conductivity tensor image, where conductivity could be assigned to three groups: GM, WM parallel or WM perpendicular to the fibre tract. Their results indicate the EMA method is appropriate for GM conductivity estimation, despite having lower anisotropy than WM. The established linear relationship mapping the diffusion to electrical conductivity tensor (Tuch et al., 1999; 2001)

has been further validated in a silk yarn phantom (Oh et al., 2006). However, Rullmann et al., (2009) detected the use of Tuch's scaling factor would have generated values 3.5 times greater than isotropic values (taken from Ramon et al., 2006). For this reason, they chose to employ a volume constraint approach with scaling factor 0.21 (compared to 0.844) which minimised differences between isotropic and anisotropic EEG forward modelling in their study. Similarly, Sekino et al. (2005) estimated the effective GM conductivity from only the fast diffusion component (attributed to extracellular fluid), rather than both the fast and slow (attributed to intracellular fluid) components. The produced conductivity maps were therefore not simply linearly scaled diffusion maps, and hence may explain their considerable low GM conductivity measurement (0.06 S/m). Importantly, the deviations in GM conductivity, dependent on the chosen diffusion tensor method, are acknowledged, emphasising the non-trivial nature of relating the diffusion and electrical conductivity tensors. Future studies should examine this relationship, in order to accurately determine a realistic scaling factor to improve conductivity tensor estimations.

Additionally, Rullmann and colleagues (2009) results were limited to one paediatric participant with epilepsy, of which their age may have influenced the increased brain conductivity. Higher conductivities in paediatric brains are perhaps expected due to the general abundance of water in GM (Dobbing & Sands, 1973). The current meta-analysis failed to find a significant correlation between GM conductivity and age. However, considering normal GM development and the frequently observed decrease in mean diffusivity of GM with age (Pal et al., 2011), further research may expose such a relationship.

In line with this observation, participant pathology significantly affected GM conductivity, but was not a significant predictor in the regression model. Large variation can be seen within and between different participant pathologies (Figure 3.9), but no clear conclusion could be made. This is perhaps due to the limited number of values available for each classified pathology, reducing the statistical power. Previous literature has indicated abnormalities in GM volume, structure, myelination and topography in Multiple Sclerosis, Parkinson's Disease, Alzheimer's Disease, and other forms of dementia (Compta et al., 2012; Frisoni et al., 2007; Geurts & Barkhof, 2008). As well as abnormalities in psychiatric and developmental disorders (Greimel et al., 2013; Job et al., 2005; Wise et al., 2017). It is therefore unsurprising that GM conductivity varied with participant pathology. Due to the unknown nature of this variation with disease and age, the use of individualised models of

head conductivity that are inhomogeneous and anisotropic are especially essential for electromagnetic source imaging (Biro et al., 2014). Increasing the feasibility and accessibility of this could be explored with further research involving DTI parameters.

3.5.5ii. White Matter

The meta-analysis failed to explain variation in anisotropic WM conductivity. However, this may be due to the limited sample size available for analysis. The crucial consideration of anisotropic conductivities has been more recently determined. Neglecting WM anisotropy produced EEG localisation errors of ~1.6 - 5.1 mm and 4.72 - 8.8 mm for radially and tangentially oriented sources, respectively (Anwander et al., 2002; G llmar et al., 2010). One study additionally reported a maximum error of 26.3 mm (Hallez et al., 2005). Furthermore, disregarding anisotropy had a large influence on the induced electric fields from TMS (De Lucia et al., 2007). Inclusion of WM anisotropy also influenced the electrical potential distribution following application of deep brain stimulation (Butson et al., 2007; McIntyre et al., 2004). Uncertainty in WM conductivity had a further, significantly large, effect on tDCS stimulation amplitudes and current density estimations, which were especially pronounced in the auditory cortex, implying orientation to be a determining factor in tDCS applications (Schmidt et al., 2015).

Isotropic WM conductivities however were found to vary dependent on method, measurement condition, pathology, and age, additionally diverging with temperature and frequency. DTI values produced largely differing results. As previously discussed by Rullmann and colleagues (2009), elevated conductivity values from DTI may be a result of an overestimated scaling factor from the diffusion tensor to the conductivity tensor, proposed by the authors. In line with this, Akhtari and colleagues (2006) failed to verify this relationship and instead revealed an inverse linear relationship with a scaling factor of -0.367, and considerable variability between values. For this reason, G llmar and others (2010) compensated for isotropic variation. They normalised the conductivity tensors (by calculating the anisotropy ratio between eigenvalues) in one model and used fixed artificial anisotropy ratios to preserve diffusion tensor orientation, in another model (volume constraint model). By comparing both models with Tuch's, employing the latter significantly affected MEG and EEG forward computations differently by changing the mean scalar representation of isotropic tensors. This chapter, alongside previous investigations, emphasised the importance

of modelling anisotropy, but has also insinuated further, more detailed research should explore the linear relationship between the diffusion and electrical conductivity tensors.

Moreover, differences were revealed between perpendicularly- and parallelly-oriented WM conductivities that are due to the results being obtained from different papers. Of note, the minimum WM-par conductivity value (0.0543 S/m) is less than the minimum WM-perp value (0.0620 S/m), with only small differences reported between the means. These results are not indicative of WM conductivity themselves, but instead highlight the variation in values between studies. This may reflect the differences between the methods employed for approximating the conductivity tensor from the diffusion tensor, due to the fact that WM is more anisotropic than these results indicate. One paper (Wu et al., 2018) reviewed the current anisotropic conductivity models of WM based on DTI. The linear relation model (i.e., Tuch's model) was discussed as not directly considering the impact of geometrical brain tissue structure. Conversely, the Wang-constraint (Wang et al., 2008) and volume-constraint models, both of which assume diffusion and conductivity tensors share the same eigenvalues (similar to Tuch's model), ignore brain tissue heterogeneity but can relate anisotropy and physiological structure. The equilibrium model (Sekino et al., 2005), which decomposes extracellular and intracellular diffusion, can be less accurate as extracellular diffusion may result difficult to quantify (Jones et al., 2018). Wu et al. (2018) determined that obtaining the conversion coefficient between the anisotropic conductivity tensor and the diffusion tensor eigenvalues to be of most importance. Further, they concluded the optimum model to be the electrochemical model, which calculates the conversion coefficient according to the concentration of charged particles in interstitial fluid. It has the added benefit of being able to calculate a conversion coefficient for GM and avoids having to consider the effect WM structure has on water molecules and electrical charges. They noted however, that the models are not contradictory, but instead complement each other to inform the relationship between conductivity and diffusion tensors. This emphasises the need for more research to elucidate the prime conversion coefficient before robust conclusions can be made. Exploration and evaluation of different diffusion-to-conductivity methods were beyond the scope of the meta-analysis. However, considering the variable results in combination with Wu et al.'s (2018) analysis, caution should be taken when applying conversion algorithms between conductivity and diffusion tensors.

Furthermore, as formerly discussed, measurements obtained *in vitro* or *ex vivo*, as well as at room temperature, are likely to differ from *in vivo* results due to the non-physiological conditions. It is therefore recommended that investigations should be completed at body temperature, *in vivo* and at frequencies in line with resonant frequencies of the brain (<300 Hz). Subsequently, a significant correlation between WM conductivity and applied frequency may have only been revealed due to values obtained at 500 Hz. A large pool of conductivity values were obtained at this frequency, whilst the remainder of values were measured <150 Hz. Hence, elevated conductivity values at a considerably higher frequency than all other results may have skewed the data to reveal a positive relationship. Additional conductivity values measured with frequencies between 150 Hz and 500 Hz are needed to further elucidate the presence or not of a significant relationship.

WM conductivity values were further revealed to vary with pathological condition. However, insufficient results were available to extract clear conclusions. Such a variation with pathology is nevertheless, expected. For example, intracranial pathology from epilepsy patients potentially alters cytoarchitecture of affected and non-affected areas, such as cortical neuronal disorganisation and surplus WM cells (Mathern et al., 1999). Akhtari and colleagues (2006) suggested pathological changes in myelin and diseased-active cells may disrupt cell geometry organisation. When coupled with histological demyelination and cell population alterations, this may increase proton diffusion as it is no longer constrained by myelin walls or tight organisation. Interestingly, a significant relationship between fluctuations in DTI eigenvalues and histological alterations in temporal lobe epilepsy has been found (Kimiwada et al., 2006). Furthermore, extensive research has revealed marked differences in WM structure in numerous diseases and pathologies, such as Multiple Sclerosis, Alzheimer's Disease, Schizophrenia and Parkinson's Disease (Bozzali et al., 2002; Burton et al., 2006; Kubicki et al., 2005; Kutzelnigg et al., 2005). Conductivity and anisotropy surrounding diseased tissues is subsequently likely to affect the generated electrical and magnetic fields from a source, compared to such distributions in healthy individuals (Park et al., 2002; Youn).

Although no significant correlation was revealed, WM conductivity as a function of age was found to contribute to the meta-regression model. This observation is unsurprising considering the well-researched nature of WM development with age, suggesting a decline in WM integrity, WM volume, myelination, and diffusivity, etc. (Gunning-Dixon et al., 2009;

Guttman et al., 1998; Salat et al., 1999; Schmithorst et al., 2002). The degeneration of WM with age allows for higher CSF and liquid concentrations within the WM, therefore increasing conductivity of the tissue. Considering the large variation of WM with methodology, pathology, and participant demographics, assuming conductivity of WM from the literature is clearly insufficient for accurate head conductivity profiles.

Combining the current results for WM and GM conductivity values, a clear discrepancy exists between both tissues, indicating the heterogeneity of the brain. Assuming the brain to have homogeneous and isotropic conductivity is therefore insufficient for accurate conductivity profiles. Such assumptions can consequently result in considerable EEG and MEG source localisation errors (Acar et al., 2016; Awada et al., 1998; Cohen & Cuffin, 1983b).

3.5.6. Brain-to-skull Conductivity Ratio

The ratio between the brain and skull conductivity values was significantly different for epilepsy compared to healthy participants. However, all BSCR values with epileptic pathology were obtained from paediatric samples. In accordance with this observation, BSCR was revealed to increase with age, suggesting paediatric samples, and hence epilepsy in the current review, to have lower conductivity ratios. In support of previous literature examining the influence of age on skull conductivity, such a relationship is expected, considering increased conductivity and decreased thickness of paediatric skulls. In contrast, paediatric brain tissue contains relatively higher water content and lower myelin deposition than adults (Knickmeyer et al., 2008; Peterson et al., 2003), indicating higher conductivity. Together, higher conductivity of both the skull and the brain in paediatric samples would suggest the brain-to-skull ratio to remain relatively stable throughout age. However, this would require an equal rate of decline for both tissues, which is unlikely the case. The role of skull conductivity for BSCR calculations was elucidated by Gonçalves et al. (2003), who concluded their BSCR discrepancies to be a consequence of skull, as opposed to brain, conductivity variation. Their results indicated brain conductivity to be of less importance when calculating BSCR, rendering decline in brain conductivity, whether equal or not to skull conductivity decline, irrelevant.

In contrast, assuming isotropic and homogeneous properties of the skull may contribute to variations in brain-to-skull estimations. For example, current injection at different locations may result in differing impedance distribution within the skull, hence altering BSCR estimations when isotropic compared to anisotropic skull models are used (van den Broek et al., 1998). However, it is noted that more recent papers acknowledge the importance of segmenting the skull layers, hence the use of skull anisotropy to optimise estimates of layered skull conductivity may not be required. Additionally, the heterogeneity in the skull will evidently introduce conductivity variation when homogeneous models are used, hence contributing to variation in BSCR values. These observations similarly apply for brain homogeneity and anisotropy, which would consequently effect BSCR estimations and contribute to variation. Considering BSCR estimations are clearly dependent on accurate conductivity of the skull and brain, which are subject to large variability, it is suggested personalised models of whole-head conductivity are essential to accurately determine the brain-to-skull conductivity ratio.

3.6. Chapter Summary

Chapter 3 outlines a meta-analysis that systematically investigated variation in reported human head electrical conductivity values for 17 different tissue types and the BSCR. Adhering to the hypothesis, conductivity was revealed to significantly vary throughout the literature, specifically for the scalp, different layers of the skull, the whole-brain, grey matter, white matter, and the brain-to-skull conductivity ratio. Important “take-home” messages from the meta-analysis were as follows:

- To decrease variation and increase stability of conductivity estimates, values should be obtained at body temperature, at frequencies less than 100 Hz and in natural, *in vivo* conditions.
- Due to variation between participants personalised models of head electrical conductivity should be obtained for each participant.
- When personalised models are unavailable, weighted average means from the current meta-analysis are suggested: 0.4137 S/m for the scalp, 0.016 S/m for the whole skull, or when better modelled as multiple compartments, 0.048 S/m for the spongiform layer, 0.007 S/m for the inner compact and 0.005 S/m for the outer compact. As well

as 1.7358 S/m for the CSF, 0.3787 S/m for the grey matter, 0.1462 S/m for WM and 50.4 for the BSCR.

- One important finding was that electrical conductivity significantly correlated with participant's age for the skull, WM and BSCR. Potential explanations for this have been provided.

CHAPTER 4. IMPACT OF AGE ON TDCS INDUCED FIELDS

4.1. Chapter Overview

The previous chapter emphasised how electrical conductivities of head tissues vary throughout the literature with employed methodology and participant demographics. In particular, participant age was revealed as an important factor for skull conductivity and BSCR deviations. The specific relationship between age and skull conductivity, however, remains relatively unclear. Accurate representation of head tissue conductivity, of which the skull may deviate due to age, plays a key role in the resulting electrical fields following tDCS stimulations, as discussed in the first two chapters. The current chapter thus explored how variations in skull electrical conductivities, particularly as a suggested function of age, affected tDCS simulated induced electric fields. Simulations were utilised to compare tDCS outcomes for different intensities across head atlases of varying age. To demonstrate differing skull conductivity, values were extracted from three databases revealing a correlation between age and conductivity. The tDCS induced electric fields were compared across all three databases with varying skull, as well as GM, WM, and scalp conductivities.

4.2. Motivation

As discussed in Chapter 1, tDCS involves a constant low direct current delivered via two electrodes: a positive (anodal) electrode placed above the target region, and a negative (cathodal) electrode placed contralaterally, facilitating depolar- and hyperpolarisation of neurons, respectively (Kobayashi & Pascual-Leon, 2003; Nitsche et al., 2008). The effect and application of tDCS on brain function is dependent on the applied region, frequency, duration, and intensity of stimulation. Altering these parameters allows individualised therapeutic and investigative intervention (Peterchev et al., 2015). Understanding the current flow to target brain areas is therefore essential for determining brain stimulation parameters and hence desired clinical outcomes.

Computational models are standardised tools for predicting current flow throughout the brain during neuromodulation (Datta et al., 2011). Current flow estimation depends, between other parameters, on the electrical conductivity of head tissues, as is shown in Chapter 2. Uncertain electrical conductivity, specifically of the skull, has been revealed to influence tDCS

electrical fields and substantially alter optimal tDCS stimulation protocol predictions (Schmidt et al., 2015). Moreover, head model simplifications play an important role in the determination of optimal tDCS doses. For example, Wagner et al. (2013) found that including the (traditionally neglected) spongiform bone compartment within the skull altered tDCS current flow. Geometrical simplifications have been previously employed due to the additional information required for accurate segmentation (e.g., CT scans, as in Fernández-Corazza et al., 2017). However, recent studies, for example from Antonakakis et al. (2020) have developed methods for modelling spongiform bone using T₂ weighted MRI. Nevertheless, some of the most utilised software packages, such as SimNIBS (Thielscher et al., 2015) and ROAST (Huang et al., 2015) do not have the flexibility to exploit such segmentation. These generalisations, as a result of previous literature segmentation limitations, thus alter skull conductivity values and impact the simulated electrical currents. Supplementing this, Fernández-Corazza et al. (2017), using EIT, revealed that skull conductivity was largely overestimated when not distinguishing between compact and marrow bone. Such overestimation resulted in higher transcranial electrical stimulation current intensities than when employing a realistic skull conductivity value. Furthermore, when the presence of spongiform bone was neglected, thinner skull regions resulted in higher field strengths (Opitz et al., 2015). When including the spongiform layer, however, the induced electric field through thicker skull regions was comparable to that of thinner skulls (i.e., high induced field strength) without spongiform bone. This therefore highlights the importance and impact of bone composition. Accompanying the discussed research, using generalised polynomial chaos expansion, Saturnino et al. (2019) revealed tDCS induced electric fields were significantly impacted by scalp and skull conductivity uncertainties. This suggests the importance of skull conductivity and geometry accuracy is not minimal for tDCS field simulations.

As revealed in Chapter 3, one important modulator of conductivity variation is participant's age. Disparity in skull conductivity with age can be partially attributed to differences in skull composition during development, as mentioned in detail in Sections 1.6, and 3.5.3i. In support of this, neonatal skulls were estimated to have higher conductivity in EEG simulation studies (Odabae et al., 2014). Furthermore, a decline with age was indicated when directly measuring skull pieces removed during surgery (Hoekema et al., 2003) and in E/MEG (Gonçalves et al., 2003). Chapter 3 also revealed deviation in whole-skull conductivity values could be partially predicted by participant age and BSCR particularly significantly increased

with age. This was critically interpreted to be primarily due to deviations in skull, rather than brain conductivity. It is additionally noted that skull thickness (Antonakakis et al., 2020) and the percentage of spongiform bone (Tang et al., 2008) may further play a role in skull conductivity variation, particularly as a function of age (Gonçalves et al., 2003).

Comprehending the influence of age on brain stimulation is particularly important to understand treatment and research outcomes for different age groups. For example, tDCS has been employed within older adult populations as a treatment for mild cognitive impairment (MCI) and Dementia (Elder & Taylor, 2014; André et al., 2016). Further treatments for ADHD (Weaver et al., 2012; Bandeira et al., 2016) and autism (Amatachaya et al., 2014; Oberman et al., 2015; 2016) have been applied across children and adolescents. More general applications, for example, treatments for depression and anxiety, are also increasingly applied from both paediatric to geriatric populations (Iriarte & George, 2018) However, the potential influence participant age has on tDCS treatment effects is seldom considered.

Despite evidence that skull conductivity deviates with age and may contribute to electric field dispersions, values are often assumed stable. For example, various papers have noted differences in induced tDCS fields with age (Moliadze et al., 2015; Kessler et al., 2013; Ciechanski et al., 2018; Antonenko et al., 2021; Rezaee & Dutta, 2020). However, none considered the additional impact of skull conductivity variation. This has been noted as a limitation of the respective studies (Moliadze et al., 2015; Kessler et al., 2013; Ciechanski et al., 2018) and differences are often assumed to be due to geometry alone. Furthermore, these existing papers are either limited by participant numbers (Croarkin et al., 2011), only considering one age group (Bandeira et al., 2016; Rezaee & Dutta, 2020), or separate ages in a few pools only rather than continuously (Ciechanski et al., 2018; Antonenko et al., 2021). The following chapter therefore attempts to bridge this gap by characterising the influence that various estimated age-appropriate skull conductivity ranges have on tDCS induced fields using age-specific atlases to represent population heads. Alongside this, different tDCS intensities were considered to highlight the potential importance of individualising tDCS dose as a function of age.

4.3. Materials and Methods

4.3.1. Head Models

Standard structural T₁ and T₂-weighted MRIs were obtained from the publicly available Neurodevelopmental MRI Database. This consisted of age-appropriate average MRI templates ranging from 2 weeks to 89 years old created from different databases of over 400 participants (Richards et al., 2016; Sanchez et al., 2012; Evans, 2006; Richards et al., 2015; Fillmore et al., 2015). The data is publicly available for experimental and clinical research and is shared under a Creative Commons Attribution-NonCommercial-NoDerivs 3.0 Unported License (CC BY-NC-ND 3.0; http://creativecommons.org/licenses/by-nc-nd/3.0/deed.en_US). Six age templates were chosen for the current study at 10, 20, 30, 40, 50 and 60 years old. These templates are based on more than 1000 images, over a large age-group, with an approximately equal number of males and females. They were verified for accuracy and repeatedly visually inspected and manually corrected throughout generation (see the respective papers referenced above for details). Age-specific templates were additionally evaluated to provide more accurate tissue segmentation compared to standard MNI atlas priors (Fillmore et al., 2015). The quality of the templates was further analysed by comparing volumetric measures to literature data, finding similar values, and supporting their correctness and usefulness (Fillmore et al., 2015). Furthermore, the atlases were recently employed in a tDCS computational (Rezaee et al., 2020) and transcranial photobiomodulation simulation (t-PBM; Yuan et al., 2020) study and validated for use in individual modelling to demonstrate aging tDCS effects.

A volume conductor FEM head mesh was created for each model with the SimNIBS v3.1.2. (Thielscher et al., 2015; Nielsen et al., 2018) ‘headreco all’ pipeline which runs all the reconstruction steps, including volume meshing (Nielsen et al., 2018; Saturnino et al., 2019; Penny et al., 2011; Geuzaine et al., 2009). The default parameters of the headreco pipeline were utilised. Mesh density was set as 0.5 (nodes per mm²), with bias regularisation factor for T₂ correction as 0.01 and downsampling factor in the statistical parametric mapping (SPM) segmentation as 3. This pipeline segments the head into seven compartments: eyes, scalp, skull, CSF, GM, WM, and air cavities (paranasal sinuses), without cutting at the base of the skull (Callejón-Leblic et al., 2021). Each generated head model consisted of an average of 3.4M tetrahedra of size 1 mm³ (for visualisation of each head model see Figure 4.3).

Generated head segmentations were overlaid onto the base MRI to inspect the accuracy of the produced head models. They were visually examined for inhomogeneities and irregularities to ensure normality of brain characteristics (Figure 4.2 details the base MRI of each atlas). To aid in the justification of atlases, head compartment volumes for each in-skull tissue were calculated using the Matlab processing toolbox ISO2Mesh (Fang et al., 2009) and compared to literature values. The volumes are provided in Table 4.1 and the comparisons to previous literature discussed briefly in Section 4.4.1 and more extensively the Section 4.5.1. Electric field results were also compared to existing studies utilising individual participant MRIs to confirm they were within expected ranges (specifically ensured comparable to Saturnino et al., 2019, and Antonenko et al., 2021). Corroboration between outcomes employing atlases and those with individual MRIs provided further support for the generated templates.

The average whole skull thickness was also computed for each age atlas. First, a ROI was defined as the skull region, within a 20 mm radius, directly below the tDCS anode (C3, as described in Section 4.3.2). The skull thickness of the ROI, defined for each head model, was estimated following a procedure outlined in (Antonakakis et al., 2020). Briefly, the skull compartments of each model were extracted, and outer and inner surfaces determined. The normal vectors and centre of gravity (CG) were established at each node of the skull segmentation. A positive scalar product of these indicated the corresponding node belonged to an outer surface skull point, whilst a negative product indicated the node belonged to an inner skull point. The thickness of the ROI was thus determined as the average value across the minimum Euclidean distance between each node of the outer surface and all nodes of the inner surface. The ROI whole-skull thicknesses for each head model are presented in Table 4.1.

4.3.2. Conductivity Assignment

The existing literature was extensively searched for all papers reporting both skull conductivity and participant age. From these values, skull conductivity was modelled as a function of age based on three existing datasets: Gonçalves et al. (2003a, 2003b), Antonakakis et al. (2020), and Hoekema et al. (2003). These papers were chosen as they were the only studies to report both participant age and skull conductivity, measured at body temperature, for at least five values, whilst also revealing a relationship between age and

conductivity. These studies were deemed accurate based on a sound method employed in the meta-analysis of Chapter 3 which accounted for methodological and standardised error using an extensive checklist (QAS, Section 3.3.5.). Therefore, the three chosen papers were regarded as providing representative values of skull conductivity within the literature, the differences between them further highlighting conductivity variation. To extract these three studies, five was chosen as the minimum number of measurements presented so a function was able to be determined with the available data. Measurements from each dataset were separately employed to model aging skull conductivity, as the same method was used within each study. This allowed consideration of deviation between values to be due to participant demographics rather than methodology. In addition, these papers represent values measured by the three most employed methodologies (EIT, E/MEG and DAC), again enabling thorough representation of possible conductivity measurements throughout the literature. Gonçalves et al. (2003b) utilised two different techniques, EIT and E/MEG. For comparison purposes and to avoid discrepancies due to methodology (as previously stated), values extracted with EIT only were included. An additional paper found from Dabek et al. (2016) was not included to model the relationship between age and skull conductivity, as they revealed no clear dependencies on age (see Section 4.5.4.). Each value was assigned a weight, reflecting a quality assessment outlined in Chapter 3's meta-analysis (Section 3.3.5.). Two outliers were excluded from the Antonakakis et al. dataset as the authors reported them as outliers in the original paper (Antonakakis et al., 2020) and they were at more than two standard deviations from the mean of the corresponding model.

Following the removal of outliers, for each of the three datasets, an exponential model of the mean as a function of age was determined. An exponential function within the Curve Fitting toolbox of Matlab was employed to fit a mean exponential curve for all values of each dataset. Each value was weighted according to that described in Section 3.3.5. and thus, accounted for limitations in methodology or variation within the extracted paper. Alongside this, a corresponding range that incorporated the majority of all recorded values was estimated (Figure 4.1). This was considered as an average minimum and maximum range for each dataset using all presented conductivity values. An exponential curve was similarly fitted, as described above, but amended to incorporate all values from each dataset and thus representing a range falling between the two exponential fits. One value from the Antonakakis et al. dataset fell outside of the exponential range, however, was incorporated in the generation of the model and exponential fit (see Figure 4.1b). This was the only value that

did not fall within the computed minimum and maximum range of conductivity values, for all the datasets. The exponential model was considered a best fit of the provided data. It ensures non-negative values and follows the described literature where conductivity is theorised to decline more rapidly from birth to adolescence and then slower (Wendel et al., 2010). An exponential relationship was also utilised by Wendel et al. (2010) from Hoekema et al.'s (2003) measurements. This function provided the distribution of skull conductivity with age for each corresponding dataset.

The SimNIBS software's uncertainty quantification (UQ) function was used to determine divergences in the tDCS induced electric fields due to variation in conductivity (uncertainty parameters). This software makes use of the generalised polynomial chaos (gPC) expansion. Briefly, the UQ quantifies the uncertainty of input variables using a probability distribution. A polynomial representation of the output variable (i.e., the electric field), given the input variable (conductivity), was computed using the gPC expansion. An adaptive approach allows for fast convergence, where the iteration stops when a tolerance is reached. The error at each iteration step was evaluated using a K-means cross validation scheme. For a detailed explanation of the UQ, see Saturnino et al. (2019). The UQ input variable was informed by the three conductivity distributions determined from each database. Minimum and maximum (given that the available data do not allow to make further assumptions) values were firstly extracted from the exponential fit range (as discussed in Section 4.3) for each age (see Table 4.1). These ranges were then utilised as the minimum and maximum parameters for a uniform conductivity distribution in the UQ. These are thus referred to as "proposed age-appropriate skull conductivities" (see Figure 4.1). These values represent the variation in skull conductivity as a function of age, according to three chosen datasets.

The UQ was calculated for the automatic standard simulation as provided in SimNIBS for motor cortex tDCS stimulation. This was to provide a frequently employed protocol that would thus represent and be transferable to many stimulation studies. This is using a $5 \times 5 \text{ cm}^2$ anode placed over C3 and a $5 \times 7 \text{ cm}^2$ cathode placed over AF4, the right supraorbital region (the mostly commonly used electrode size in experiments; see, e.g., Thair et al., 2017). The placement of these electrodes was visually checked using the SimNIBS GUI to ensure the location on head models were as expected. Four different intensities were utilised for all UQ simulations and ages: 0.5, 1, 1.5, and 2 mA.

4.3.3. Experiments

Two sets of UQ tDCS simulations were carried out. The first employed the proposed age-appropriate skull conductivity ranges with all other tissues fixed. The second also utilised the proposed age-appropriate skull conductivity ranges but with scalp, GM and WM also varied and CSF conductivity fixed. Three final simulations, not using UQ, were conducted where all tissue conductivities had a fixed value. All simulations were carried out on each age atlas and for all four intensities. Each experiment is outlined in more detail below.

For the first set of simulations, the proposed age-appropriate skull conductivity ranges for each of the three datasets were employed as the UQ input variable. The electrical conductivities of the scalp, CSF, GM, and WM were fixed to 0.4137, 1.7358, 0.3787 and 0.1462 S/m respectively. These were the weighted mean measurements as assigned in Chapter 3 and provided in the GitHub page in Section 4.3.2. and were therefore regarded as the most appropriate values within the available research. This first experiment elucidates the effect that changes in skull conductivity alone, according to participant age, has on tDCS induced electric fields, when all other tissue conductivities are fixed.

The second set of UQ simulations were conducted using the proposed age-appropriate skull conductivity values for each dataset and fixed CSF conductivity (1.7358 S/m, as above), but with differing scalp, GM, and WM values. These were assigned as uniform distributions with minimum and maximum values from Chapter 3 using the same methodology as described in Section 4.3.2. Any deviation between values was therefore more likely to be due to participant variation rather than methodology. The ranges (as provided by EIT methods) were 0.25 – 0.42, 0.22 – 0.29, and 0.16 – 0.23 S/m for scalp, GM, and WM, respectively. CSF conductivity was fixed as it has been revealed to minimally deviate between participants (see Section 3.5.4.). The second experiment aimed to show the effect that the proposed age-appropriate skull conductivity has on tDCS induced fields, whilst soft tissue is also unknown (a more realistic representation). As deviations in soft tissues are identical across all ages, any significant differences between ages would therefore be attributed to changing skull conductivity and head geometries.

The final three, non-UQ simulations utilised non-age-appropriate skull conductivities recommended in the literature: 0.0055 S/m (Fernández-Corazza et al., 2017), 0.01 S/m

(Dannhauer et al., 2011) and 0.016 S/m (Chapter 3, published and thus termed in this thesis as McCann et al., 2019). All other tissues were assigned the weighted mean from Chapter 3, as above. The results from these simulations allowed comparison to the previous two UQ simulations and thus highlighted the importance of adjusted and realistic conductivities for the most accurate representation. Differences between peak fields utilising the three standard skull conductivities (remaining stable for all ages) and the proposed age-appropriate model also allowed disentanglement of geometry and conductivity.

| Age (years) | Skull thickness (mm) | Tissue Compartment Volume ($\times 10^6 \text{ mm}^3$) | | | Skull conductivity ranges (S/m) | | | | | |
|-------------|----------------------|--|--------|--------|---------------------------------|--------|--------------------|--------|----------------|--------|
| | | | | | Gonalves et al. | | Antonakakis et al. | | Hoekema et al. | |
| | | GM | WM | CSF | Min | Max | Min | Max | Min | Max |
| 10 | 5.63 | 0.6291 | 0.5597 | 0.2273 | 0.01 | 0.0167 | 0.0058 | 0.0152 | 0.0803 | 0.095 |
| 20 | 7.21 | 0.6347 | 0.5546 | 0.2165 | 0.0066 | 0.0137 | 0.0041 | 0.0123 | 0.0629 | 0.0784 |
| 30 | 6.84 | 0.5497 | 0.5858 | 0.222 | 0.0043 | 0.0112 | 0.0029 | 0.0106 | 0.0492 | 0.0647 |
| 40 | 6.67 | 0.5618 | 0.5687 | 0.257 | 0.0029 | 0.0092 | 0.0021 | 0.009 | 0.0386 | 0.0534 |
| 50 | 6.26 | 0.556 | 0.5775 | 0.2721 | 0.0019 | 0.0075 | 0.0015 | 0.0078 | 0.0302 | 0.044 |
| 60 | 5.93 | 0.5606 | 0.5807 | 0.3374 | 0.0012 | 0.0062 | 0.001 | 0.0067 | 0.0237 | 0.0364 |

Table 4.1: Summary of tissue compartment volumes (in mm^3) for each head atlas model and proposed age-appropriate skull conductivity values (in S/m) corresponding to each employed dataset.

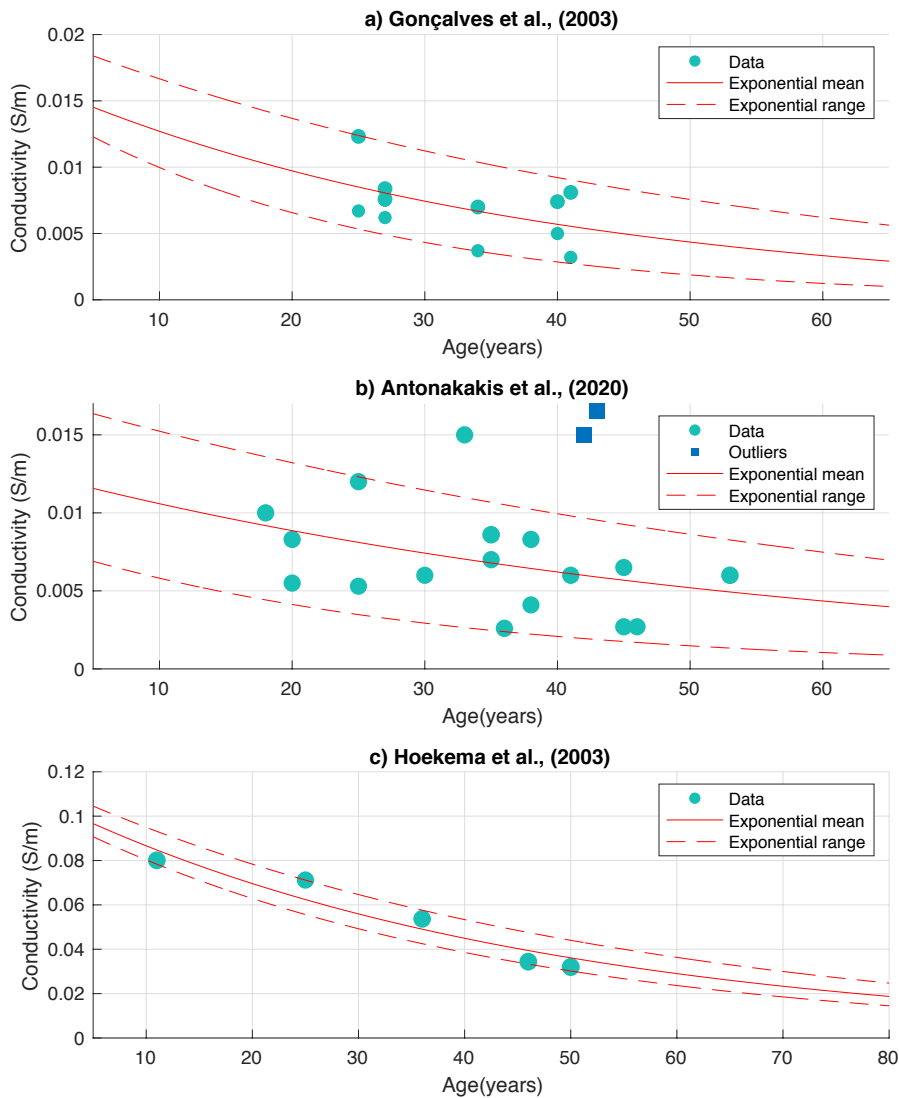


Figure 4.1: Distribution of skull conductivities according to the Gonçalves et al. (4.3a), Antonakakis et al. (4.3b) and Hoekema et al. (4.3c) datasets. Circles represent values from the respective papers, whilst squares are outliers as identified by the corresponding publication. The solid red line signifies the weighted exponential mean, whilst the dashed line denotes the weighted range (minimum and maximum) incorporating all values.

4.3.4. Analysis

For each age atlas, tDCS intensity and conductivity configuration, 1000 UQ calculated values were randomly extracted of the peak electric field at the 99th percentile in GM (measured in V/m). The 99th percentile was chosen as the representative value of the peak field since it is the most employed in the literature (Saturnino et al., 2019; Antonenko et al., 2021) that displays the average of the peak field used (i.e., between the 95% and 99.9% percentile). This

was repeated for GM volume (measured in mm^3) with an electric field greater than 75% of the peak value (referred to as focality [Saturnino et al., 2019]). A skipped Pearson correlation analysis was carried out to explore any significant relationships between age and peak field or focality, as well as with CSF, GM, and WM volumes. This is a non-parametric method, accounting for heteroscedasticity effects, as part of the Robust Correlation Toolbox (Pernet et al., 2013). The significant alpha level was set to 0.05 ($p < 0.05$ rejects the null hypothesis). Differences between these extracted values for each age atlas and conductivity configuration were determined using an ANOVA (Tukey et al., 1949). The p-values for both correlational analysis and ANOVA, were adjusted for multiple comparisons using the Benjamin-Hochberg false discovery rate (FDR) method, with the critical value equally set to 0.05 (Benjamini et al., 1995).

To determine which tissue's conductivity variation contributed most to the electric field uncertainty, the magnitudes of the global derivative-based sensitivity coefficients were calculated. The global derivative-based sensitivity coefficients quantify the average change in electric field with respect to each tissue's conductivity variation. They are calculated by means of the gPC coefficients and the respective basis functions' partial derivatives. The sensitivity coefficients are provided as an outcome variable within the UQ analysis. Further details on their determination can be found in (Saturnino et al., 2019). The respective sensitivity coefficients of peak fields at the GM 99th percentile were calculated according to scalp, skull, GM and WM conductivity variation for each dataset and tDCS intensity. Coefficients were extracted as the respective absolute magnitude for the 99th percentile for each tissue. These sensitivity values were thus an evaluation of the sensitivity of electric field deviation due to varying tissue conductivity. Any differences between the sensitivity coefficients according to tissue type were determined by employing ANOVA and skipped Pearson correlation analysis, corrected for multiple comparisons (as in the method described above). This allowed determination of the most influential tissue for deviation in tDCS electric field with respect to changes in participant age and stimulation intensity.

4.4. Results

4.4.1. Head models

Following the assessment of head mesh quality, the original head model for the 10-year-old atlas was seen to generate thicker scalp regions than the MRI. This was manually corrected by employing a higher threshold for scalp segmentation, before the surface and volume meshing steps of ‘headreco’ (Nielsen et al., 2018). All resultant final overlaid meshes were accurate compared to the MRI (Figure 4.2), and all volumes were as expected, i.e., there was no cortical smoothing, large CSF areas, or otherwise irregular appearances deemed to impact any subsequent analysis. Head meshes for all atlases are provided in Figure 4.3. Electrode placement on the head models was also deemed normal and not impeded by scalp segmentation. Brain volumes were calculated for the original MRI atlases to assess the ability of age-appropriate templates to represent previous findings of the aging brain (see Table 4.1). Before tDCS simulation, the brain volumes in the current study were assessed for normality as presented in previous literature (Giorgio et al., 2010; Good et al., 2001; Gur et al., 2002; Ge et al., 2002; Smith et al., 2007; Groeschel et al., 2010; Sowell et al., 2003; Evans et al., 2012). All volumes were found to be within the normal ranges as reported in the literature, a thorough discussion of this comparison can be found in Section 4.5.1. Of note, for the 30-year-old head mesh, the right side displayed a thicker region (as can be seen in Figure 4.3). Although this was an abnormal presentation, the artifact was not considered to effect consequential tDCS induced field calculations due to no tDCS electrodes being placed above this irregular region.

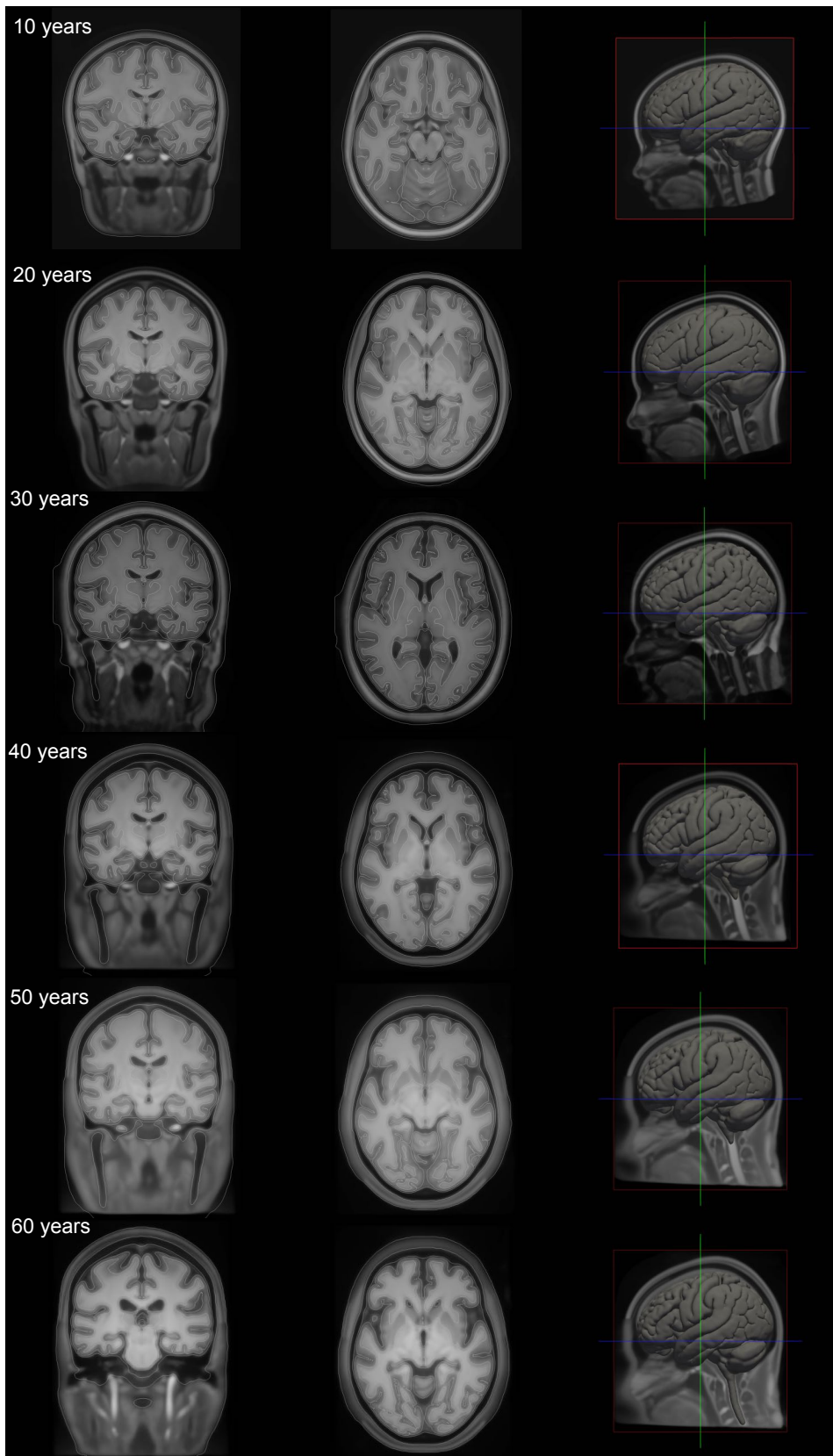


Figure 4.2: Base MRI for each age atlas, 10-60 years respectively, for the coronal, axial, and sagittal volume, visualised using the brain imaging software package Freeview for FreeSurfer. The segmented tissues are outlined by a thin grey line.

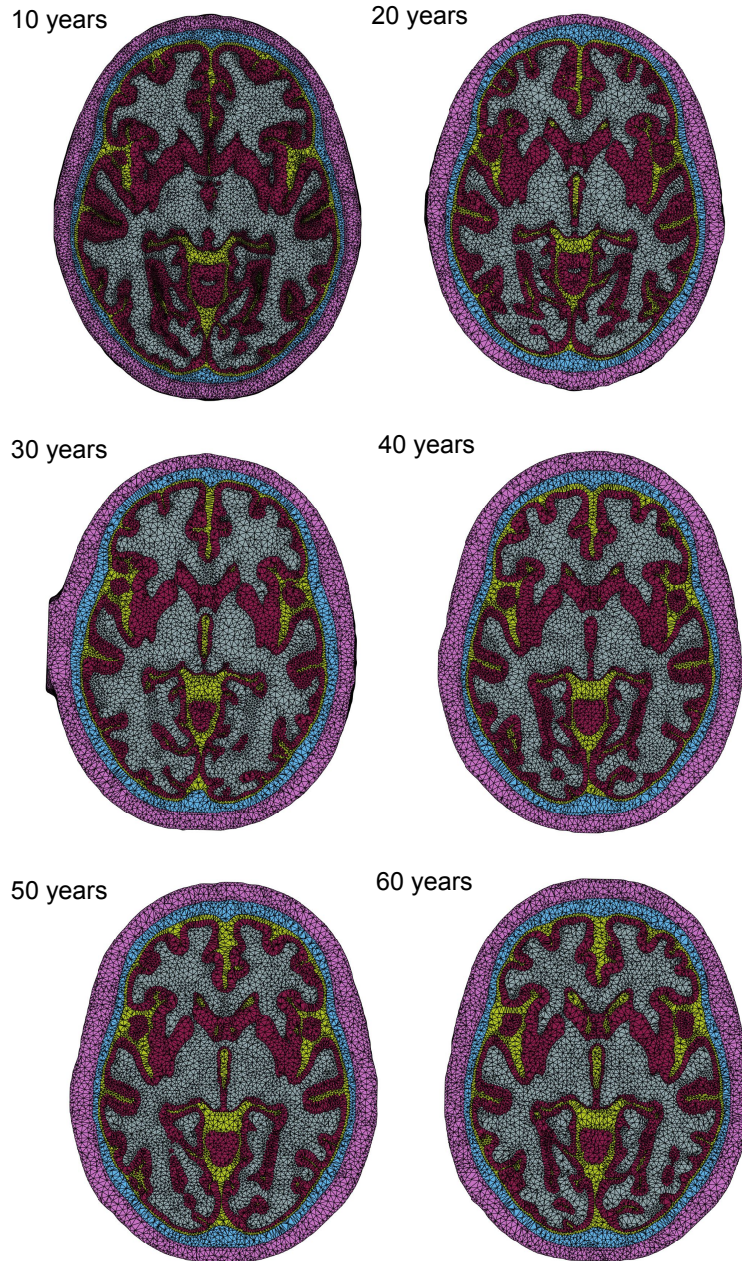


Figure 4.3: Axial views of the generated finite element head meshes for each head atlas, 10-60 years, respectively, visualised using Matlab (Natick, USA). The five head tissues are represented for the scalp (purple), skull (blue), CSF (yellow), GM (pink) and WM (grey). The 10-year-old model consisted of 3.8M tetrahedra of size 1mm^3 and 6.81×10^5 nodes. The 20-year-old model had 3.33M tetrahedra and 6×10^5 nodes. For the 30-year-old mesh, there were 3.35M tetrahedra and 6.14×10^5 nodes. The 40-year-old model contained 3.41M tetrahedra and 6.25×10^5 nodes. For the 50-year-old mesh, there were 3.42M tetrahedra and 6.25×10^5 nodes. Lastly, the 60-year-old model consisted of 3.38M tetrahedra and 6.21×10^5 nodes.

4.4.2. Peak fields

A negative correlation between tDCS induced electric peak fields at the 99th percentile and age using solely proposed age-appropriate skull conductivity was revealed for all tDCS intensities and datasets. The average skipped Pearson correlation (termed r) for all intensities were -0.9060, -0.8578 and -0.9544 for the Gonçalves et al., Antonakakis et al. and Hoekema et al. datasets, respectively (Figure 4.4a, c, and e). The correlational p -value was significant following multiple comparison correction. For all datasets, there was additionally a significant difference (one-way ANOVA $p < 0.001$ for all, after multiple comparison adjustment) and positive correlation between peak field and intensity for all ages. This decreased with age (see Figure 4.4a, c and e; $r > 0.82$, $r > 0.80$, and $r > 0.99$ for Gonçalves et al., Antonakakis et al., and Hoekema et al. datasets, respectively, for all ages). On average, for the Gonçalves et al. dataset (for all intensities), peak fields declined by a factor of 0.7806 per decade. As an example, peak fields for a 60-year-old atlas were analogous to peak fields in a 10-year-old atlas using triple the stimulation dose (1.5 mA in 60 years vs 0.5 mA in 10 years). For the Antonakakis et al. dataset, peak fields typically decayed by a factor of 0.7985 per decade. Here the peak field for a 10-year-old was comparable to that of a 60-year-old when employing one third of the dose (0.5 mA to 1.5 mA for 10 vs 60-year-old atlas). The decline per decade for the Hoekema et al. dataset was reduced with a factor of 0.8892, and similar peak fields for a 10- and 60-year-old employing twice the intensity (0.5 mA vs 1 mA and 1 mA vs 2 mA). Across all three datasets the average decline per decade was thus 0.82.

There were additionally significant differences between the three standard and proposed age-appropriate skull conductivities for all datasets with age (one-way ANOVA $p < 0.001$ for all, after multiple comparison adjustment). Dissimilarities increased with age for the Gonçalves et al. and Antonakakis et al. datasets and decreased for the Hoekema et al. dataset (see Figure 4.4 for comparisons). These disparities are a direct result of conductivity variation, rather than variation in head geometry. For head geometry, there was a significant negative correlation between CSF volume and peak field for all datasets and tDCS intensities as well as a positive significant correlation between GM volume and peak fields. No correlation was revealed for WM volume percentage. Furthermore, no significant correlation was revealed between peak field and skull thickness when including all age ranges. However, as skull thickness linearly declined for ages atlases 20-60 (where, thickness for the 10-year-old atlas was significantly lower, not higher than the 20-year-old atlas), an additional analysis was

conducted excluding the 10-year-old data. These results revealed, for age atlases 20-60, significantly positive correlations between skull thickness and peak field for all intensities and datasets (average for all intensities, $r = 0.83775$, 0.6742 and 0.9146 for the Gonçalves et al., Antonakakis et al. and Hoekema et al. datasets, respectively).

Peak electric field at the 99th percentile for different conductivity variations and tDCS intensities

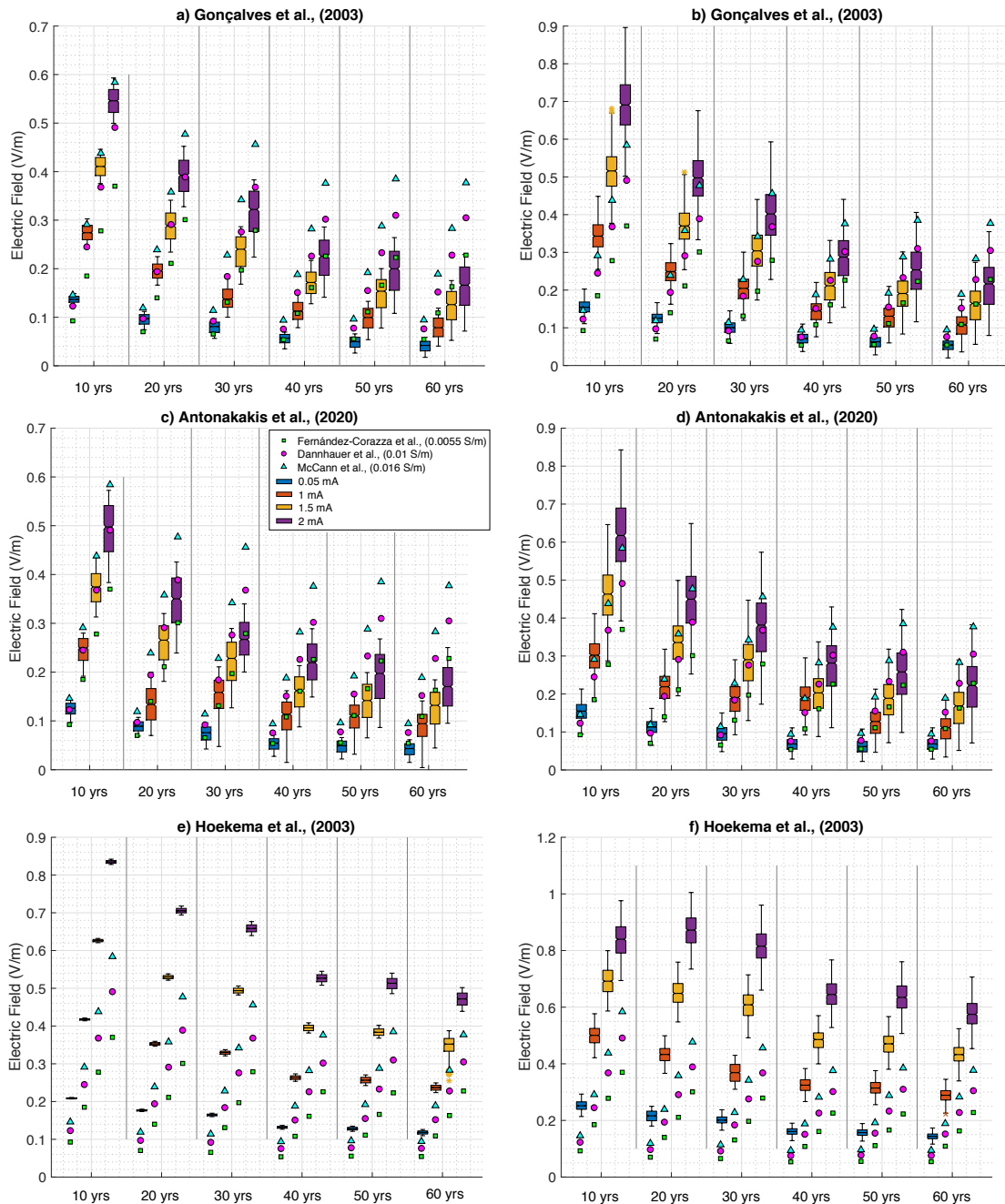


Figure 4.4: Variation in peak electric fields at the 99th percentile depending on tDCS intensity and subject's age. Figures 4.4a, c and e display electric fields where proposed age-appropriate skull conductivity was varied alone and all other head tissues remained at the mean value, for the

Gonçalves et al., Antonakakis et al., and Hoekema et al. datasets, respectively. Figures 4.4b, d and f show electric field where the skull conductivity was varied within proposed age-appropriate values and the remaining head tissues were varied in a stable way across ages, for the Gonçalves et al., Antonakakis et al., and Hoekema et al. datasets, respectively. All boxplots show the minimum and maximum values (extended lines), where the filled box is the inter-quartile range and notch is the medium. Blue, orange, yellow and purple show results for tDCS intensities equal to 0.5 mA, 1 mA, 1.5 mA and 2 mA, respectively. Filled green squares, magenta circles, and blue triangles display the singular peak field value when head tissues are the mean value and skull conductivity is 0.0055 S/m, 0.01 S/m, and 0.016 S/m, respectively (taken from the cited literature).

Comparable results were revealed using proposed age-appropriate skull conductivities and GM, WM, and scalp varied identically across ages. For all datasets, there was a negative significant (following multiple comparison correction) correlation between peak fields and age for all intensities (average $r = -0.8759$, $r = -0.7984$ and $r = -0.8753$ for the Gonçalves et al., Antonakakis et al., and Hoekema et al. datasets, respectively; Figure 4.4b, d and f). Alongside this, a significant difference between intensities and peak fields was found for all ages (one-way ANOVA $p < 0.001$ for all, following multiple comparison correction). This, again, decreased with age (skipped Pearson correlation $r > 0.80$, $r > 0.75$, and $r > 0.97$ for the Gonçalves et al., Antonakakis et al., and Hoekema et al. datasets, respectively, and all ages). Correlations for both age and intensity were of the highest significance for the Hoekema et al. dataset and lowest for the Antonakakis et al. dataset (see Figure 4.5). Correlations employing both varied skull and head tissue conductivities were marginally lower than varied skull conductivity alone for all datasets (see Figure 4.5).

Peak electric field at the 99th percentile for 1mA tDCS for different datasets and conductivity variation

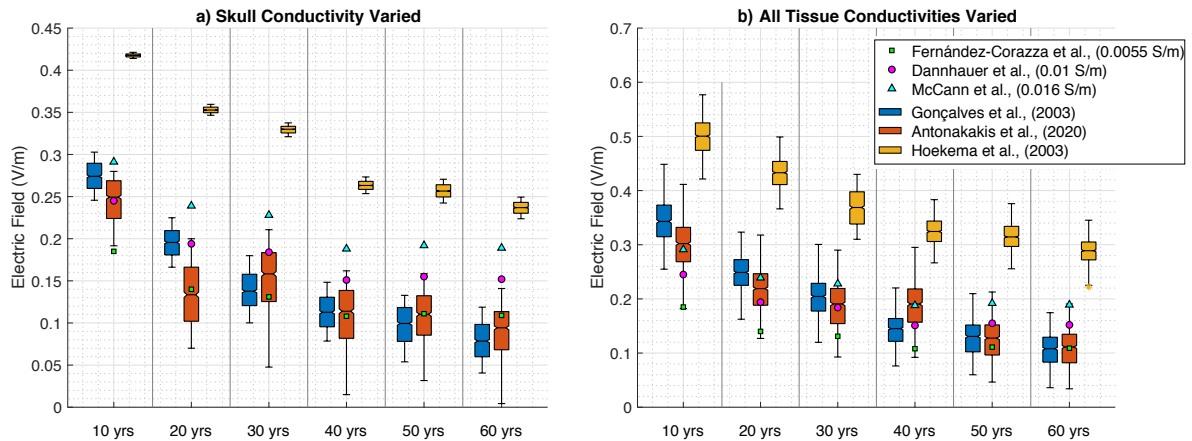


Figure 4.5: Variation in peak electric fields at the 99th percentile for 1 mA tDCS for varying ages, datasets, and electrical conductivities. Figure 4.5a represents peak values where proposed age-appropriate skull conductivity was varied alone and all other head tissues remained at the mean value, for the Gonçaves et al. (blue), Antonakakis et al. (orange), and Hoekema et al. (yellow) datasets. Figures 4.5.b shows peak fields with proposed age-appropriate varying skull conductivity all other head tissues varied as stable across ages for the aforementioned datasets. Filled green squares, magenta circles and blue triangles display the singular peak field value when head tissues are the mean value and skull conductivity is 0.0055 S/m, 0.01 S/m, and 0.016 S/m, respectively (taken from the cited literature).

Significant correlations were revealed between age and the sensitivity coefficients for the scalp, skull, GM, and WM ($p < 0.001$ for all datasets and intensities, corrected for multiple comparisons). Figure 4.6 shows the sensitivity coefficient magnitudes at 1 mA tDCS. Values and subsequent correlations were similar for all four employed intensities. Skull conductivity deviation became the most significantly influential tissue with increasing age for the Gonçaves et al. and Antonakakis et al. datasets. There was a positive correlation between age and the sensitivity of the skull to peak field deviation, weaker for each respective dataset (skipped Pearson correlation average for all intensities, Gonçaves et al.: $r = 0.82145$, Antonakakis et al.: $r = 0.5063$ and Hoekema et al.: $r = 0.9387$). Furthermore, a negative relationship was revealed between age and WM sensitivity (average for all intensities; Gonçaves et al.: $r = -0.8001$, Antonakakis et al.: $r = -0.7320$, Hoekema et al.: $r = -0.5978$). This was repeated for GM sensitivity (for all intensities average; Gonçaves et al.: $r = -0.7834$, Antonakakis et al.: $r = -0.7432$, Hoekema et al.: $r = -0.5867$) and scalp sensitivity (average for all intensities; Gonçaves et al.: $r = -0.8604$, Antonakakis et al.: $r = -0.8051$,

Hoekema et al.: $r = -0.7472$). Uncertainty in skull conductivity was the most influential tissue in the Antonakakis et al. dataset and became the most influential for atlases over 30 years old in the Gonçalves et al. dataset.

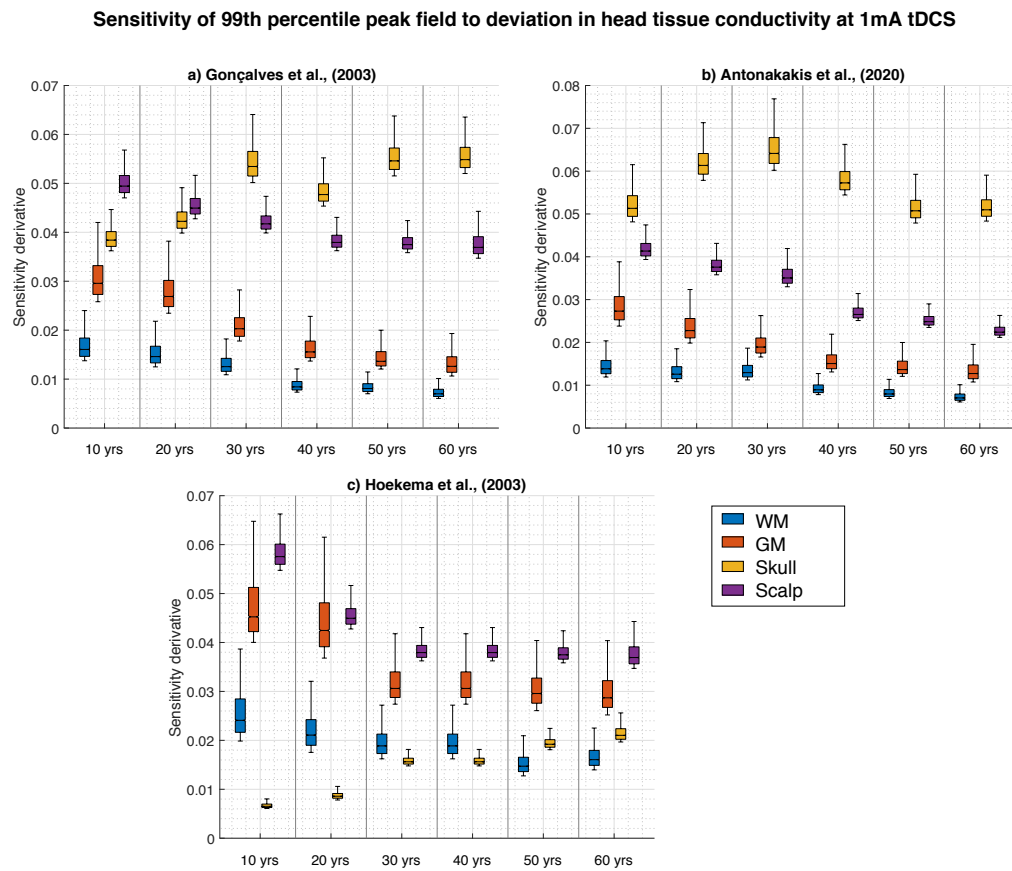


Figure 4.6: Global derivative-based sensitivity coefficient magnitudes of 1 mA tDCS induced electric field change at the 99th percentile with respect to deviations in WM (blue), GM (orange), proposed age-appropriate skull (yellow) and scalp (purple) conductivity for each age atlas. Figures display simulations employing the Gonçalves et al. (4.6a), Antonakakis et al. (4.6b) and the Hoekema et al. (4.6c) datasets.

4.4.3. Focality

Figure 4.7 displays the GM volume (mm^3) with an electric field greater than 75% of the peak value (i.e., focality) for different conductivity configurations, simulated at 1 mA tDCS. As can be seen, a significant difference was revealed between GM volume at different ages. This was across all three datasets and all four intensities when skull conductivity alone was varied (one-way ANOVA, $p < 0.001$ for all). The correlational analysis was insignificant. No differences were found between different intensities for any dataset or age. When skull and other head tissues were varied, focality significantly differed between ages for all datasets

and intensities (one-way ANOVA, $p < 0.001$). There was a significant negative correlation between focality and age (identical for all intensities) for the Gonçalves et al. and Antonakakis et al. datasets (skipped Pearson correlation: $r = -0.7531$ and $r = -0.8023$, respectively). No differences were found between different intensities for any dataset or age. All intensities yielded the same GM volume when proposed age-appropriate skull and all other head tissue values were constant. Furthermore, no significant correlation was revealed between peak field and skull thickness when including all age ranges. However as in Section 4.4.2, an additional analysis was conducted excluding data from the 10-year-old age atlas. Significantly positive correlations were thus revealed between skull thickness and focality solely for the Gonçalves ($r = 0.7010$) and Antonakakis ($r = 0.8081$) dataset (identical for all intensities).

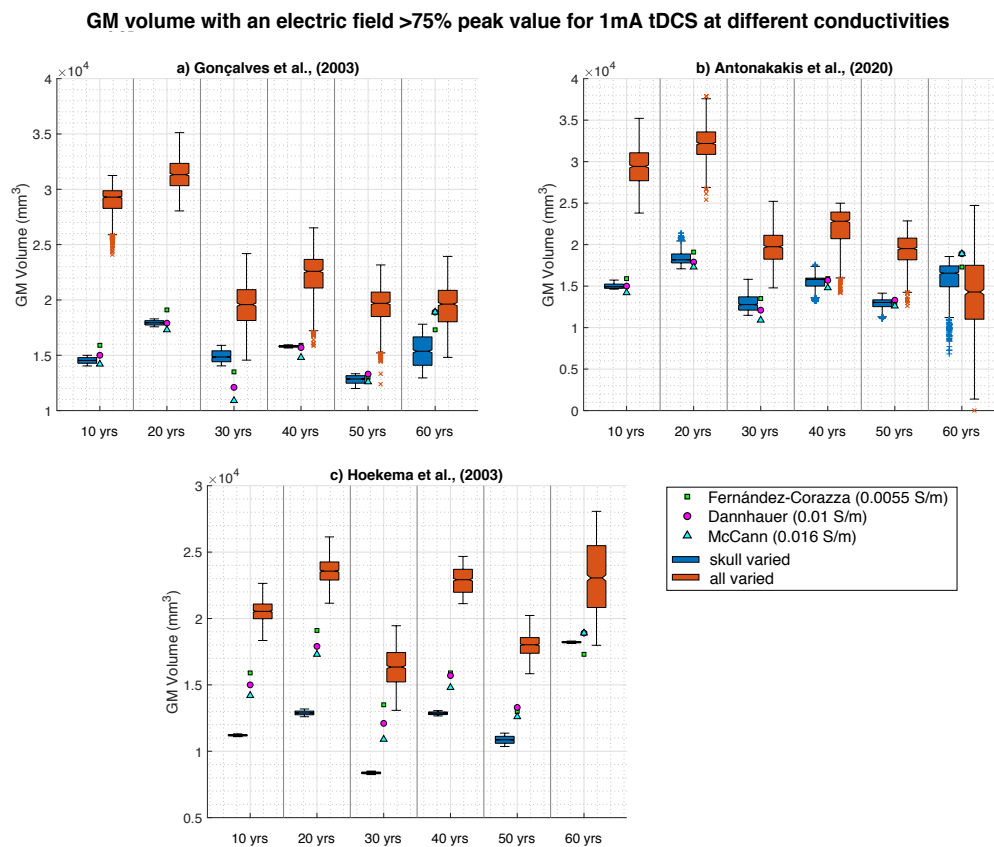


Figure 4.7: Variation of GM volume with an electric field greater than 75% of the peak value for 1 mA for varying ages and conductivity values. Blue boxplots represent values where only proposed age-appropriate skull conductivity was varied for each dataset (4.7a – 4.7c), whilst the orange boxplot shows simulations where both proposed age-appropriate skull ranges were utilised with all the head tissues varied as stable with age. Filled green triangles, magenta circles, and blue squares display the singular peak field value when head tissues are the mean value and skull conductivity is 0.0055 S/m, 0.01 S/m, and 0.016 S/m, respectively (taken from the cited literature).

4.5. Discussion

The current chapter revealed a significant negative correlation between atlas age and peak fields for simulated tDCS stimulation. This was mediated by proposed age-appropriate skull conductivity, irrespective of whether all other head tissue conductivities and tDCS intensity were varied. Deviations in skull conductivity were found to become the most influential tissue for peak field changes with increasing age for two datasets (Gonçalves et al. and Antonakakis et al.). Significant differences were also shown between tDCS focality and atlas age. However, there were only significant correlations when other head tissues were also varied (but stable across age). Focality increased (corresponding to lower GM volumes) with increasing age following scalp, GM, and WM conductivity variation for two datasets (Gonçalves et al. and Antonakakis et al.). These results suggest that skull conductivity, indicated to decline with age, is vital when modelling tDCS induced fields and these deviations should be accounted for. Such changes could account for varying clinical outcomes and suggest tDCS dose should be individualised and adjusted for participant's age.

4.5.1. Atlas Justification

The employed atlas volumes corresponded with individual MRI volumes from the existing literature. The results specifically revealed GM volume linearly decreased, whilst WM remained relatively stable with age, with slight decrease for the youngest and eldest atlases. This is comparable to previous research, where GM generally decreased with age, falling within 0.4 – 0.9 L (Good et al., 2001; Gur et al., 2002; Ge et al., 2002; Smith et al., 2007; Groeschel et al., 2010; Sowell et al., 2003; Evans et al., 2012), whilst WM displays a 'bell-shaped' curve, ranging between 0.3-0.7L (Giorgio et al., 2010; Good et al., 2001; Gur et al., 2002; Smith et al., 2007) and 'peaking' within the fourth decade (Gur et al., 2002; Smith et al., 2007). Moreover, CSF volume for the utilised atlases was revealed to increase with age for which there is a multitude of support from the literature, where volumes have been reported to vary between 0.2-0.6 L (Gur et al., 2002; Smith et al., 2007; Groeschel et al., 2010; Evans et al., 2012). The use of atlases has also previously been established in neuroimaging research, allowing capture of the population mean and variance as a function of age (Evans et al., 2012). Atlases or templates have been utilised, for example, in MEG network analysis, revealing consistent results compared to using individual MRI (Douw et al., 2018). Additionally, the Neurodevelopmental database utilised in the current chapter was

recently employed and validated to build structural templates for use in infant cortical EEG (O'Reilly et al., 2021). This is in addition to recent use in individual modelling with age in a tDCS computation (Rezaee et al., 2020) and t-PBM (Yuan et al., 2020). Head atlases have also been applied to represent average brains and determine tDCS parameters and responses that can generalise to a population. For example, a FE head model was created from a standard brain atlas to establish optimal tDCS positions (Im et al., 2008). Standard templates were further produced from multiple MRIs from participants of varying races, in order to determine the effect of race on tDCS current flow (Datta et al., 2018). Although it is noted the use of head atlases has disadvantages, for example the blurring of sulci and gyri and smoothing of tissue interfaces, particularly at the pial surfaces. Despite this, templates can provide generalised information that is not due solely to individual differences between participants. The smoothing of the utilised atlases was also considered minimal. The inspection and comparison of the current atlases to previous literature demonstrate the integrity of the provided head models and justify their use in the present tDCS simulation study.

4.5.2. Age and peak induced fields

The current results are in support of previous research from multiple participants. For example, using grouped ages, higher peak fields have been revealed in children, declining in adolescence and adulthood (Ciechanski et al., 2018; Antonenko et al., 2021). This is in addition to findings of higher peak fields in younger compared to older adults (Antonenko et al., 2021; Muffel et al., 2019). Furthermore, a slight negative correlation for peak electric fields was displayed between the ages 21 and 55 (Laakso et al., 2015). Importantly, the discussed papers (Ciechanski et al., 2018; Antonenko et al., 2021; Rezaee et al., 2020) have noted a limitation of their results is the exclusion of proposed age-appropriate skull conductivity values, which may exacerbate any relationship, as revealed in the current findings. By including a range of ages across the lifespan, results were able to be concluded as correlational, rather than mere differences between pooled groups of ages. Likewise, induced field variation was assessed as being directly due to proposed age-appropriate skull conductivity deviations. As hypothesised, the decrease in skull conductivity, irrespective of scalp, GM, and WM conductivity diversity, mediated the decline in peak electric fields with age. Not only was this effect not masked by other head tissue variability but remained for all tDCS intensities. Alongside this, changing scalp and skull conductivities, not accounting for

age, has yielded similar electric field deviations across different tDCS montages (Callejón et al., 2021). This suggests the current results can be applied to differing electrode placement parameters.

The significant correlation between the three standard and varying proposed age-appropriate skull conductivity values (varied alone and alongside soft tissues) revealed that most of the electric field uncertainty is a direct result of aging skull conductivity. As changes in skull conductivity were the only varying factor, this variability was concluded not to occur due to head geometry alone (see Figure 4.4). From these results, differences were found to increase with age for the Gonçalves et al. and Antonakakis et al. datasets and decreased for the Hoekema et al. dataset. Head geometry, nevertheless, exacerbated these findings. The opposing correlational effect for the Hoekema et al. dataset is due to considerably higher conductivity values for the skull, compared to the three standard values and other datasets. This means that the decrease with age approached standard conductivities for Hoekema et al. but deviated away for Gonçalves et al. and Antonakakis et al. These results additionally revealed skull conductivity to be of increasing importance with increasing age for peak field variation (see Figure 4.6). This result was as expected as a more highly conductive skull, for younger participants, would allow more tDCS current to reach the brain and in turn increase electric fields. This effect is heightened in combination with geometry, e.g., paediatric skulls being considered significantly thinner than adult skulls (Cvetković et al., 2016; Antonakakis et al., 2020). As such, the current results equally revealed significant correlations with skull thickness and induced field., when the 10-year-old age atlas was excluded for analysis. This atlas, being from a paediatric population, had reduced skull thickness, as expected Cvetković et al., 2016; Antonakakis et al., 2020) due the skull still undergoing development. Therefore, correlational analysis was conducted for atlases 20 years and older. The resultant significant correlation between thickness and induced fields is indicative skull geometry may play a role in tDCS application. However, as induced fields were significantly correlated across all age ranges (10-years included), this parameter is not the sole contributor to deviating results. Skull thickness remains an important inclusion, particularly when considering how conductivity may vary. Previous research (Antonakakis et al., 2020) has revealed, for example, skull thickness to positively correlate with conductivity, which is supported by (Tang et al., 2008). Furthermore, a non-significant negative correlation between thickness and participant age was found (Antonakakis et al., 2020) and it was mentioned skull thickness increases exponentially from birth to adolescence (Delye et al., 2015) then linearly

decreases over time (Lillie et al., 2016). Hence, determining a clear and robust relationship requires essential further research. Skull thickness is therefore expected to play an imperative role in conductivity variation, particularly with age. Future studies should attempt to disentangle this relationship and provide additional conductivity data to allow for assumptions, such as correlation with age.

Brain tissue volumes also differed according to age template. This is reinforced by the significant relationship between induced fields and CSF and GM volume and the negative correlation between age and brain tissue sensitivity to field changes. Paediatric brains contain comparably less CSF than adults, which is supported by the current head models. In these cases, current is less efficiently conducted via CSF, permitting a higher intensity of the remaining field. Moreover, children with lowered CSF have smaller extra-axial CSF space and shorter scalp to skull distances (Rezaee et al., 2020; Sadleir et al., 2010; Fox et al., 2004). This may result in higher peak electric fields and increased current spread as a larger proportion of stimulated current is penetrating the brain and in part due to lessened electrical current shunting. This is thus hypothesised to increase induced fields under the tDCS electrodes (Kessler et al., 2013). The current results are enhanced by Laakso et al. (2015) who revealed reduced peak electric fields with age due to a positive correlation between age and CSF volume. They considered this a measure of brain atrophy. Following from this, an increased number of brain lesions is expected with age, which would further contribute to differing tDCS induced fields. The impact of lesions and their conductivity was beyond the scope of the current chapter. Future studies, however, could incorporate lesions into field modelling, including conductivity estimates. Likewise, Ciechanski et al. (2018) suggested declining GM/WM ratio with age, irrespective of any changes in their conductivity, may relate to tDCS induced field fluctuations. This was in addition to the contribution of alterations in WM microstructure and myelination processes. Future research could explore the influence diffusion characteristics, expected to change with age (Groeschel et al., 2010; Salehinejad et al., 2020) on tDCS induced fields.

The presented research further elucidated the relationship between tDCS dose and age. Peak fields were approximately triple in the eldest (60 years old) compared to the youngest atlas (10-years-old) when dose was kept constant. Generally, peak electric fields following 0.5 mA in the youngest atlas was comparable to 1.5 mA in the oldest atlas. These results are supported by previous similar studies. For example, stimulation intensity for adult ADHD

treatment (2 mA, 0.8 V/m) was double that required in children to produce similar electric fields (1 mA, 0.6 V/m; Gillick et al., 2014). A 0.7 mA in a 10-year-old with perinatal stroke additionally produced a peak brain current intensity equivalent to an adult receiving 1 mA (Im et al., 2008). Deviations in skull conductivity for the presented research, however, were not taken into consideration. The current chapter demonstrates the effect of variable skull conductivity is not minimal and exacerbates relationships between head geometry and induced tDCS fields.

In addition, experimental studies have evidenced the effect of age on clinical and research outcomes. For tDCS motor cortex stimulation, elderly participants' (older than 60 years old) responses were delayed (Heise et al., 2014) or differed (Saldanha et al., 2020) to younger participants (younger than 25 years old). Furthermore, anodal stimulation over the dorsolateral prefrontal cortex (DLPFC) in adolescence increased pain perception, whereas stimulation over the motor cortex using the same intensity increased the pain threshold in adults (Croarkin et al., 2014). The authors suggested age as a central mediator for the tDCS response, providing an explanation for differing treatment outcomes for identical stimulation parameters. Importantly, their results support previous findings that intracortical inhibition increases with age (Gillick et al., 2014). Moliadze et al. (2015) revealed 1 mA cathodal tDCS produced a facilitating brain function in children, originally hypothesised to reduce cortical excitability (where anodal stimulation would increase excitability). They suggested a "ceiling effect" may exist that cannot be overcome by higher tDCS intensity. The proposed "ceiling effect" threshold is dependent on age and therefore identical stimulation intensities may initiate long-term depression changes in adults, but long-term potentiation changes in children. In order to ensure comparable research and clinical outcomes across ages, it may be essential to individually adjust dosages.

The present research revealed an average scaling factor (between all three proposed age-appropriate skull conductivity datasets) of 0.82 per declining decade for induced peak fields. Datta et al. (2011) explored the effect that variation in head geometry has on peak electric fields and thus how doses can be normalised. They suggested the simplest approach would be to scale dosages according to peak electric fields, accounting for variation as a result of head geometry. The current results combine the influence of head geometry with skull conductivity to provide a suggestive scaling factor of 0.82 to tDCS dose per increasing decade. However, this value is arbitrary and still ensues large uncertainties, more evident

across vastly different head models, and is merely a suggestive value. Additional research is essential to determine how to accurately adjust tDCS dosages and montage application for treatment optimisation.

In addition, future research is imperative to fully understanding the relationship between conductivity, electric fields and tDCS parameters (Croarkin et al., 2014). A recent study, for example, revealed the current propagation from the scalp to the brain was unaffected by skull conductivity changes (Forssell et al., 2021). This was found to be due the concept of “skull-transparency”, where using specific current injection patterns without *a priori* skull conductivity values did not result in large induced field errors, as expected. Instead, they depended on the distance from the injection to the source and areas with high spatial frequency. This would be one solution to tDCS injection parameters without accounting for changing head conductivity. However, further research is required in this area and would be useful for tDCS treatment and research. Furthermore, a recent study also utilising gPC analysis, revealed uncertainty in scalp and skull conductivity significantly impact EEG inverse solutions (Vorwerk et al., 2019). This suggests the underlying relationship between electric current and skull conductivity is not minimal and can be extended to work in EEG. Further research could also employ analogous tDCS and EEG monitoring to explore such a relationship.

4.5.3. Age and focality

The presented results revealed no relationship between focality and age except when scalp, GM and WM conductivities were varied alongside proposed age-appropriate skull deviations. This result is as expected as focality has previously been hypothesised to depend on head geometry and GM/WM composition, rather than the contribution of skull conductivity (Callejón et al., 2021; Laakso et al., 2015; Mikkonen et al., 2020; Fernández-Corazza et al., 2017). In support of this, the presented research revealed a significant relationship (when excluding the 10-year-old atlas) between skull thickness and focality for two datasets (Gonçalves et al. and Antonakakis et al.). This suggests skull geometry, particularly thickness, potentially plays a larger role in tDCS focality than skull conductivity, more so than for tDCS field strength. The lack of correlation for all ages however, suggests (as discussed in Section 4.5.2) skull thickness alone cannot account for tDCS variations (both focality and strength). A recent study confirmed the contribution of skull geometry, not

conductivity, to focality, revealing changing scalp and skull conductivities had a greater effect on electric field magnitude than distribution (Callejón et al., 2021). This may also explain why a relationship was revealed when scalp, GM and WM conductivities were varied as these simulations allow for larger overall deviation and an increased likelihood of finding an effect. Mikkonen et al., (2020) for example, found no variation in focality due to tDCS intensity, supporting the current results, but deviations in focality depending on tDCS montage, more specifically the size of the employed electrodes. Variation in electrode size was beyond the scope of the current chapter, however future modelling studies may explore how tDCS montage in combination with age-appropriate geometry and conductivity affect focality.

4.5.4. Limitations

One limitation of the research presented in this chapter is that bone composition in the skull was not taken into consideration. Spongiform bone, more highly conductive than compact bone, is typically increased in thicker skull regions, which could increase tDCS induced field strengths (Fernández-Corazza et al., 2017). The present research, however, did not include spongiform conductivity as a varying factor as the current software (SimNIBS, the most frequently employed software [Thielscher et al., 2015] and ROAST [Huang et al., 2019]) are unable to automatically represent marrow segmentation. The majority of papers exploring tDCS electric fields do not account for marrow tissue, inclusion of which in this research would therefore not be representative of the current standard (Thielscher et al., 2015). The aim was to explore tDCS induced fields in a way frequently employed, thus the most standard software was utilised and deemed appropriate for the current simulations. Furthermore, for accurate spongiform and suture segmentation, additional imaging information, such as that obtained through CT, is required, but often unavailable for brain stimulation treatment and research (Fernández-Corazza et al., 2017). It is acknowledged, however, that segmentation is possible through MRI data (for example in Antonakakis et al., 2020) and could be utilised in further studies. Nevertheless, segmentation stemming from MRI methods are dependent on water content and thus would present variable results according to spongiform bone composition. This chapter allows evaluation of skull conductivity variations when employing the simplifications most frequently used. Nonetheless, the impact of spongiform bone and skull sutures are important and additional information and modelling should be examined in the future.

Further to this, the meninges and blood vessels (most commonly segmented as CSF) may also impact tDCS induced fields, although to a lesser degree, and have been neglected in this research (Jiang et al., 2020). For example, accounting for differing conductivity of the dura in tDCS simulation improved correlational accuracy with intracranial recordings (Jiang et al., 2020). Similarly, errors caused by neglecting blood vessels in EEG source analysis (employing similar underlying electrical biology as tDCS) were analogous to omitting CSF conductivity (Fiederer et al., 2016). Following from this, CSF is frequently overestimated within the brain compartment (i.e., segmenting the meninges as CSF) and near the skull boundaries, notably of the occipital lobe, where the brain should contact the skull (Jiang et al., 2020). This is particularly evident for FEM modelling employing tetrahedral meshes, as in the presented research, which typically overestimate CSF perimeters. Moreover, tetrahedral meshes may be prone to errors due to bad quality elements if not appropriately treated (Beltrachini et al., 2018). It is acknowledged that omitting segmentation of the meninges, blood vessels and not accounting for CSF overestimation may, have impacted on tDCS induced fields. Future studies could thoroughly check and enhance the quality of tetrahedral meshes or employ hexahedral domain discretisations and further analyse the effect such CSF overestimation, alongside accurate segmentation of the meninges and blood vessels has on tDCS. This may have a greater impact as a function of age, particularly considering vast variation in CSF volume with age.

An additional limitation is that the utilised proposed age-appropriate conductivity ranges are based on limited data from the literature and do not accurately depict how skull conductivity changes with age. The existing literature was extensively searched for papers explicitly reporting skull conductivity and participant age. However, only papers reporting more than five measurements and where a relationship with age could be extracted were included. Consequently, not all skull electrical conductivities were represented, which may influence the resultant correlation with age. Despite reporting more than five values, Dabek et al. (2016) were excluded due to no relationship with age being stated and their utilised method (EIT) being represented from the Gonçalves et al. dataset. More research, however, is essential to accurately determine the relationship of skull conductivity with age. Furthermore, values extracted from the Hoekema et al. database were considerably higher (up to 10-fold) than those found in all other literature (Chapter 3) and may skew results from this database. For example, the resulting peak fields stemming from Hoekema et al.'s proposed age-appropriate skull conductivities have a smaller range compared to the Gonçalves et al. and

Antonakakis et al. datasets. The contribution of skull conductivity uncertainty to peak field changes is also lower for Hoekema et al. versus the remaining two datasets. Both of these discrepancies are suggested to be due to a lower relative difference between skull conductivity values within the UQ simulations. Therefore, all effects are dimmed. Furthermore, the considerably higher conductivity measurements for the Hoekema dataset may be due to the fact measurements were acquired *in vitro*, compared to under *in vivo* conditions. Consequently, skull conductivity values may decay with time away from the biological host, as well as the influence of temperature. However, similar *in vitro* methods have been employed (for example in Tang et al., 2008) and conductivity values found within a similar range to the Antonakakis and Gonçalves datasets. Equally, the methodology in Hoekema et al. was previously assessed and considered reliable (in the QAS, Section 3.5.5). Irrespective of the deviations, due to an identical method being employed for Hoekema et al.'s extracted measurements, any deviations were appointed to be due to participant demographics and therefore reliably depict how induced fields may change with age. This is thus irrespective of the particular skull conductivity values. Furthermore, it is noted that the calibrated bulk conductivity values extracted from Antonakakis et al. are redefined based on a fixed compact and spongiform bone conductivity ratio (according to Akhtari et al., 2002). Compact bone was estimated from the procedure and spongiform conductivity assigned following a fixed ratio to calibrate whole skull conductivity. Therefore, Antonakakis et al. accounted for differing bone composition conductivity and geometry within their whole skull estimations, which the other papers did not, making comparisons between the three methodologies incomplete. However, three methods under differing conditions were chosen to elucidate the variability within the literature and to represent the resultant changing tDCS induced fields. This was, firstly, as a hypothesised function of age (as shown by variability within the results for each dataset) and secondly, due to chosen methodology and skull conductivity values from the literature (shown by the variability between datasets). Nonetheless, supplementary research to determine the influence age has on skull conductivity, particularly of the layered skull, is essential.

Additional values would be imperative to understanding induced tDCS fields for participants beyond the ages discussed here. It is hypothesised that peak field would decay further for older ages, particularly in combination with brain atrophy and degradation and the higher likelihood of lesions.

4.6. Chapter Summary

The current chapter illuminated the importance of accurate and individualised head anatomy and proposed age-appropriate skull conductivity values in tDCS experiments. A computer simulation study was carried out in order to determine the impact deviation in skull conductivity as a function of age affected tDCS induced fields. Significant points are outlined below:

- Induced peak tDCS field strengths were revealed to correlate with age significantly negatively for four different intensities employing three databases proposed age-appropriate skull conductivity models. Irrespective of whether GM, WM and scalp conductivities were additionally varied.
- Skull conductivity deviation was found to be the most important tissue with increasing age to peak field changes.
- Peak field significantly negatively correlated with CSF volume and positively correlated with GM volume for all simulated parameters.
- An average scaling factor of 0.82 per declining decade for peak tDCS fields across all intensities and skull conductivities datasets was found.
- Precise conductivity values and individual head models considering participant age are therefore considered to be vital for full understanding of tDCS current propagation. Inaccuracies in both could contribute to deviations in tDCS clinical and research outcomes.
- Future studies are suggested to consider age when calculating tDCS dosage for paediatric and elderly participants and understanding the underlying physiological mechanisms responsible for such induced fields.

CHAPTER 5: SKULL CONDUCTIVITY AND EEG

5.1 Chapter Overview

Chapters 1 and 2 outlined the neurophysiological basis of electrical brain activity and the methodology of characterising this activity through EEG, where imaging the source and distribution of the electrical potential is essential. Solving the respective inverse and forward problems in EEG requires realistic, anatomically correct volume conductors and accurate tissue conductivities. Chapter 3 and 4 highlighted the particular importance of skull conductivity for electrical current propagation, which deviates across participants, particularly considering age, and according to bone composition and the presence of adult sutures. The current chapter therefore analysed the effect considering adult sutures and differing bone composition had on the EEG-FP and IP solutions utilising a well-established and detailed head atlas. The true skull conductivity was considered as inhomogeneous according to spongiform bone proportion and sutures. The EEG-FP and IP were solved and compared to results employing homogeneous skull models, with varying conductivities and omitting sutures, as well as using a hypothesised aging skull conductivity model. This chapter aimed to elucidate the significance that neglecting adult sutures and bone composition distribution, as well as assuming a homogeneous skull volume and when age was considered, had on EEG analysis.

5.2. Motivation

EEG is a non-invasive imaging modality used for characterising the electrical activity of the brain (Henry, 2006; Chapter 1). Localising the source of such activity provides valuable information for understanding brain function in health and disease, as well as aiding in the diagnosis of neurological disorders and syndromes such as epilepsy (Michel et al., 2004) and ADHD (Ibáñez et al., 2011). As outlined in Chapters 1 and 2, source analysis involves, in a first instance, the characterisation of the current propagation from a known endogenous source to the scalp, the EEG-FP. The signal origin can then be estimated from the recorded data and personalised FP computations – the EEG-IP (Haueisen et al., 1999). Accurate solutions to these problems require the adoption of realistic and individualised volume conductor models incorporating precise anatomical tissues' geometries and their electrical conductivities. Within all tissue compartments, the skull has been pointed as the most

relevant for EEG signal analysis, mostly due to its high resistivity (Chapter 3; Dannhaeur et al., 2011; Gençer et al., 2004; Vorwerk et al., 2019). Although the majority of current studies incorporate realistic geometries from complementary medical images, the conductivities of all tissues, including the skull, are typically assumed from existing literature. This poses a limitation to model personalisation as it is now accepted that most tissues, and in particular the skull, are subject to large variability between participants and measurement methods and protocols (Chapter 3). Misspecification of this conductivity, when considered as one compartment, has resulted in significant EEG forward and inverse solution errors (Vallaghé et al., 2008; Acar et al., 2013; Chen et al., 2010; Vorwerk et al., 2019). Incorporating accurate skull conductivity volumes is therefore imperative for the most precise resolution to the EEG-FP and IP.

The skull, however, is geometrically complex and its simplification into one homogeneous layer is insufficient for accurate EEG source localisation (Dannhaeur et al., 2011). Within the field, the skull is accepted to be composed of three layers: a diploë (spongiform/marrow bone) layer, sandwiched between two compact bone compartments that are less conductive than the former (Tang et al., 2008; see also Section 1.6.2. and 3.5.3.). The percentage of bone marrow varies throughout the skull depending on overall skull thickness and location, leading to an inhomogeneous conductivity profile (Law, 1993; Tang et al., 2008). Accounting for the varying presence of spongiform and compact bone is essential, which can be only done in detail by means of CT (Fernández-Corazza et al., 2017) or unconventional MRI (Antonakakis et al., 2020), as discussed in Chapter 4. Previous research has indicated that neglecting such detailed segmentation and assuming the skull as one homogeneous conductivity layer can result in EEG inverse solution errors of up to 2 cm (Dannhaeur et al., 2011; Lanfer et al., 2012; Montes-Restrepo et al., 2014; Montes et al., 2011; Wolters et al., 2006).

Although inhomogeneous skull models accounting for both spongiform and compact bone are increasingly employed, adult sutures are omitted, mainly due to the necessity of CT data and unclarity regarding their impact. As discussed in Section 1.6 the sutures are dense, fibrous, immovable joints mostly made up of collagen (a protein found in connective tissue) that connect the various skull bones (Tang et al., 2008; Gray, 1878). They are wide to allow movement at birth, and remain open at various stages of development, differing between cases. For example, the frontal suture fuses between 3-9 months old (Vu et al., 2001), whilst the sphenosquamosal suture usually closes by 6 years, but can take as long as 10 (Idriz et al.,

2015). In comparison, during adulthood, the coronal, sagittal, lambdoid, and squamosal sutures do not close until approximately 45, 50, 55, and 70 years of age, respectively (Russell & Russell, 2018; Idriz et al., 2015; Kumar et al., 2018; Singh et al., 2004; Nakahara et al., 2006; see also Section 1.6.2.). An exemplar diagram of the adult skull sutures and their positions are displayed in Figure 5.1. Neglecting the presence of sutures, which have differing conductivity to spongiform and compact bone (Tang et al., 2008), can thus result in large and localised EEG source reconstruction errors. Previous research has evaluated the impact that infant fontanelles have on EEG source analysis, which, although geometrically larger in comparison, is hypothesised to yield similar results when accounting for adult sutures. For example, Lew and colleagues (2013) revealed that omitting the fontanelles but assuming correct skull conductivity (compared to a model with equivalent skull conductivity and fontanelle inclusion) produced maximum EEG source errors of 3.6 mm. A recent study further confirmed that the exclusion of fontanelles in neonates resulted in the largest source localisation errors directly below the fontanelles (Azizollahi et al., 2020). Previously, Darbas and colleagues (2019) similarly concluded that including the fontanelles significantly improved EEG source reconstruction. They also revealed conductivity variation near to the fontanelles and that eccentricity and orientation of dipolar sources significantly influenced EEG source localisation. The effect of adult sutures in EEG source analysis, however, has yet to be assessed.

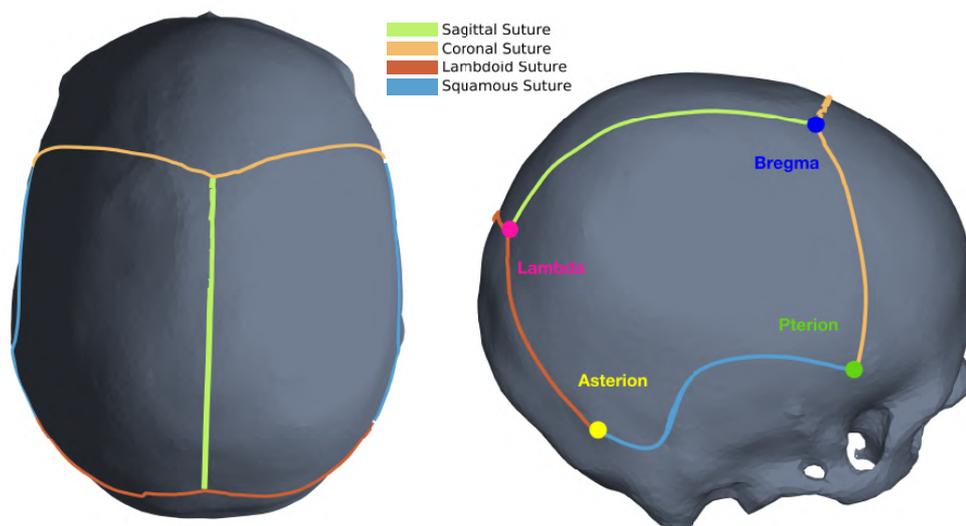


Figure 5.1: Schematic representation of the generated sagittal (green), coronal (orange), lambdoid (red) and squamous (blue) sutures on the skull with the anatomical landmarks bregma (blue circle), lambda (pink circle), pterion (green circle) and asterion (yellow circle).

Realistic head modelling, particularly of the skull, is therefore evidently an essential aspect of EEG forward and inverse computation. Numerical methods, as opposed to analytical approaches, are required to account for a realistic head shape, allowing for multiple non-spherical compartments. As discussed in Chapter 2, Section 2.3.3ii, the FEM is one such numerical approach that can consider realistic models of arbitrary geometry, being able to incorporate anisotropy and heterogeneity between tissues, an advantage over other existing numerical approaches (Vorwerk et al., 2012). The BEM, on the other hand, approximates the head as compartments with isotropic conductivities and computes EEG surface potentials produced by current sources at the interface and boundary of a homogeneous volume conductor. Importantly, FEM, differing from BEM, can additionally distinguish between spongiform and compact bone and accurately incorporate CSF without substantially increasing computation complexity. It can also represent a homogeneous skull, such as including the sutures (Vorwerk et al., 2012; Beltrachini, 2019). FEM is therefore frequently employed for EEG forward analysis utilising realistic and inhomogeneous conductivities and is integrated into known EEG analysis toolboxes such as FieldTrip (Oostenveld et al., 2011) and BrainStorm (Tadel et al., 2011).

This chapter thus aimed at evaluating the contribution that adult sutures had on the EEG forward and inverse solutions and their effect compared to neglecting deviations in bone composition. A detailed head model with inhomogeneous conductivity profiles that accounted for spongiform bone distribution throughout the skull and the presence of four adult sutures was developed. The FEM was then utilised to simulate the forward problem solution. Source analysis employing the “true” inhomogeneous skull conductivity model was compared to simplified representations omitting the sutures and bone composition distribution. Homogeneous model conductivity values frequently employed in the literature were also used for comparisons. Moreover, aging skull conductivity profiles that accounted for variation in conductivity and suture closure with age were simulated to determine source analysis differences considering participant age. The results therefore highlight the importance that geometrically accurate head models with appropriate electrical conductivity are for EEG source localisation, with particular focus on the critical inclusion of adult sutures.

The chapter is organised as follows. The generation of the utilised head model, including tissue segmentation, calculation of bone composition proportion and suture position

assignment, is described in Section 5.3.1. An outline of each of the experiments, including the model comparisons and their justifications is provided in Section 5.3.2. The computation methodology for the models employed in each of the experiments (as described in Section 5.3.2) is discussed in Section 5.3.3. Specifically, 5.3.3i details the generation of the ground truth model, 2.3ii outlines an EIT protocol for estimating homogeneous conductor models and 5.3.3iii describes development of the age-appropriate skull conductivity models. Section 5.3.4 described the forward and inverse solution methodology and error measurements. The results are provided in Section 5.4, discussing the contribution of the sutures and bone composition in 5.4.1, the impact of different homogeneous models in 5.4.2 and the results of the age-appropriate models in 4.3. Finally, a discussion of these three main results is provided in Section 5.5.1, 5.5.2 and 5.5.3, respectively, with considerations for future research in 5.5.4.

5.3. Methods

5.3.1. Head model construction

A realistic detailed head model was developed from the high-resolution Colin27 MRI segmentation (Aubert-Broche et al., 2006). Colin27 provided the segmented head model, which utilised combined T_1 and T_2 MRI data from repeated scans of a single participant with CT and MR angiography to provide better bone and vascular structure segmentation as well as high resolution (Aubert-Broche et al., 2006). FreeSurfer (Fischl, 2012) was then employed to compute the surface where the sources were placed, residing in the GM, by calculating the midpoint between the GM/WM and GM/CSF interface (as described in Section 5.3.4). This, together with the segmentations provided by the Colin27 atlas, resulted in five compartments: scalp, skull, CSF, GM, and WM. Further refinement provided bone marrow classification, enabling the creation of a detailed inhomogeneous skull map. The ISO2Mesh toolbox (Fang & Boas, 2009) was then utilised to first compute surface meshes from the available segmentations. These meshes were subsequently employed to build a 3D tetrahedral discretisation resulting in 6.8M elements and 1.1M nodes into the five compartments (Figure 5.2a). Each compartment and the resultant head model were manually checked for abnormalities and to ensure high quality of the mesh. Special refinements of the skull layer (0.4M nodes) allowed for inclusion of differing bone composition and adult sutures by changing the individual element's conductivity. To calculate the percentage of spongiform

and compact bone, the points at all interfaces between skull/CSF and skull/scalp were firstly computed. For each point on the skull/CSF interface, a straight line perpendicular to the interface was drawn until reaching the skull/scalp interface. The percentage of spongiform bone at that point was then determined as the percentage of the line belonging to the soft bone compartment (based on the segmentation). Figure 5.2b displays the skull conductivity distribution as a function of spongiform bone proportion, computed according to Tang et al. (2008) and further described in Section 5.3.2i. The presence of sutures was evidenced by the lack of spongiform bone in the corresponding regions and were clearly visible in the model, which merged CT and MRI data. The suture segmentation also followed the standard locations as displayed in Figure 5.1. On the surface of the scalp layer, a total of 164 (point) electrodes were positioned according to the ABC-160 positioning system (BioSemi B.V., Amsterdam, Netherlands), plus an additional four fiducials (nasion, inion, left and right pre-auricular).

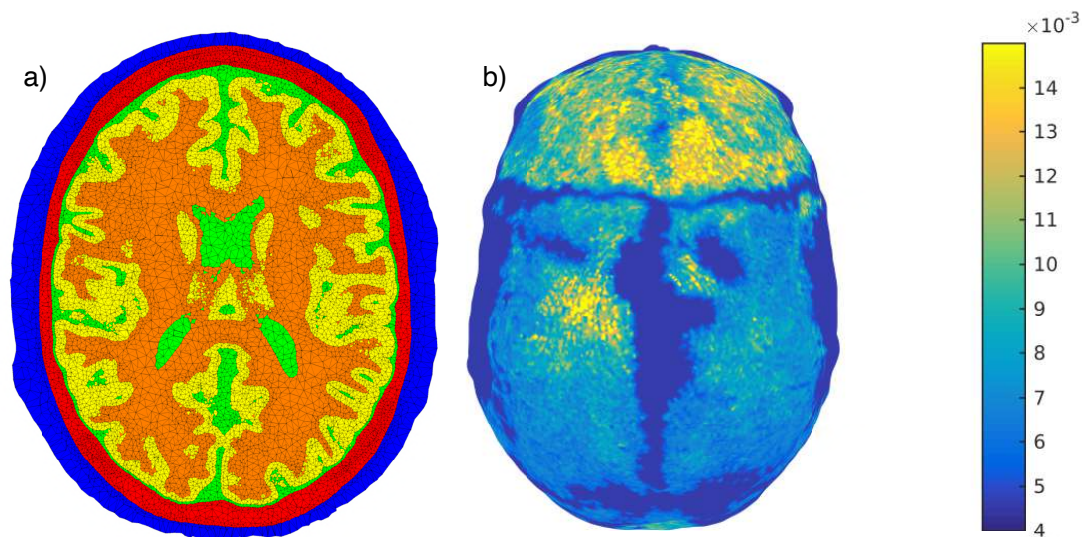


Figure 5.2: a) Head model discretisation (mesh) showing the five layers; scalp (blue), skull (red), CSF (green), GM (yellow) and WM (orange). b) Skull conductivity distribution (in S/m) throughout the skull based on spongiform proportion according to Tang et al. (2008) (see Section 5.3.2i for details of the computation of the conductivity from the available percentage of marrow). The sutures are located within areas lacking spongiform bone (dark blue sections), and following the lines as presented in Figure 5.1.

The adult sutures were manually segmented and incorporated into the head model. Skull elements along the suture lines and without spongiform bone (and thus assumed most likely

to be sutures) were extracted and visualised using Matlab (Natick, USA). This visualisation confirmed the suture location was according to previously defined anatomical landmarks (Miura et al., 2009; see also Figure 5.1). The intersecting points where the generated sutures meet (i.e., bregma, lambda, asterions, and pterions) were then found. Elements along the path connecting the intersections with the least proportion of spongiform bone, and following previously defined anatomical landmarks, were manually selected, and interpolated. All the elements fully composed of hard bone and with centroids at 10 mm from the sutures were considered part of them. This was done to comply with the conductivities provided by Tang et al. (2008), which were measured in samples of approximately that size. This produced five subject-specific anatomically correct non-smooth sutures: the sagittal, coronal, lambdoid, and the left and right squamous (see Figure 5.1). These were defined as either dentate (sagittal, corona, and lambdoid) or squamosal (squamous), which have differing properties and thus conductivities (Tang et al., 2008; Gray, 1878).

The electrical conductivities of the scalp, CSF, GM, and WM were assigned as 0.4137, 1.7358, 0.3787 and 0.1462 S/m, based on Chapter 3. The conductivity assignment of the skull for each model, including that of the sutures, is described in Section 5.3.2.

5.3.2. Experiments

The electrical conductivity of the skull was varied to develop differing volume conductor models and demonstrate the impact such simulated deviations have on the EEG forward and inverse solutions. A ground truth model was first generated, which incorporated variation in spongiform and compact bone distribution throughout the skull, as well as the presence of sutures. The corresponding models were variations of the ground truth model, deviating according to skull conductivity alone. The experiments comparing the various models and their purpose are outlined below. The methodology involved for generating each of these models is outlined in Section 5.3.3 and the forward and inverse solution computation and comparison calculations between models is described in Section 5.3.4.

1. Omitting Sutures: the ground truth model (generation outlined in Section 5.3.3i) was compared against a model in which the distribution of spongiform and compact bone was that of the ground truth, but the presence of sutures was neglected, and their conductivity considered that of hard bone. This experiment set out to determine the impact solely omitting

the sutures, whilst accounting for variation in overall bone composition has on EEG source analysis.

2. Neglecting Spongiform: the model omitting the sutures (but with spongiform distribution intact) was compared against a homogeneous skull conductivity model that did not account for bone composition variation nor the presence of sutures. The homogeneous skull conductivity was calculated as a global representation of the model that omitted the sutures utilising EIT (method described in Section 5.3.3ii). This produced a one-layered skull conductivity value not influenced by sutures, and assuming no bone composition variation throughout the skull. The appraisal between this homogeneous model and that omitting the sutures aimed to assess the impact neglecting spongiform distribution variation throughout the skull had on EEG-FP and IP solutions. Comparing against the model omitting the sutures ensured any discrepancies were solely due to disregarding the variation in spongiform proportion, rather than also accounting for adult sutures.

3. Homogeneous 0.01 and 0.0055 S/m: the ground truth model was assessed against two models where the skull was assumed as one homogeneous layer with a single conductivity, taken from existing literature: either 0.01 S/m or 0.0055 S/m. These comparisons aimed to indicate potential global inaccuracies when not accounting for inhomogeneity and taking a literature value as the truth, a very common practice in the field. The first homogeneous value (0.01 S/m) was extracted as the most frequently employed value in existing literature (Dannhauer et al., 2011) and highlighted EEG source analysis discrepancies for a relatively high assumption of skull conductivity. The second homogeneous literature value (0.0055 S/m; Fernández-Corazza et al., 2017) aimed to reveal such errors when assuming low skull conductivity, potentially in contrast to the previous high homogeneous value.

4. Homogeneous EIT Estimated: the ground truth model was evaluated against a homogeneous skull model, where the global conductivity was estimated using an EIT protocol that accounted for variation in spongiform proportion and the presence of sutures (protocol described in Section 5.3.3ii). The EIT homogeneous model aimed to provide a ‘best guess’ of a homogeneous volume given the ground truth model input, rather than assuming specific values according to previous literature. This experiment set out to determine EEG-FP and IP solution inaccuracies when analysing discrepancies between homogeneous and inhomogeneous (i.e., the true) skull models.

5. Age estimated models: a separate set of experiments was carried out to determine the impact that not accounting for suture closure according to age has on EEG source analysis. The same realistic head model geometry (as described in Section 5.3.1) was utilised, and five age-appropriate volume conductor models created from this identical geometry at 20, 30, 40, 50, and 60 years of age. For these models, only the conductivity of the skull differed from the ground truth model as a general decline in global skull conductivity and suture closure with age was hypothesised (computation outlined in Section 5.3.3iii). An identical head geometry was thus employed for all age-appropriate models (see Section 5.5.3 for a discussion on the necessity of additional data and research for more accurate age-appropriate representations). Source analysis for each of the hypothesised age models were compared to those of an EIT estimated homogeneous skull conductivity value for each corresponding age (where the input for EIT estimation was the hypothesised age-appropriate model, as described in the EIT protocol in Section 5.3.3ii). These evaluations aimed to elucidate the effect sutures has on EEG source localisation when an aging skull is taken into account.

| Model | Distribution | Whole skull | Sutures | F/IP Comparison | Aims to highlight |
|---------------------------|---------------|--|--|---|--|
| Ground Truth | Heterogeneous | Computed according to spongiform proportion | Dentate - 0.0173 Squamous - 0.0079 | NA | Reference model |
| Omitting Sutures | Heterogeneous | | Equal to hard bone | Ground Truth | Importance of including sutures |
| Neglecting Spongiform | Homogeneous | Whole skull 0.0061 S/m | | Omitting Sutures | Discrepancies when spongiform omitted |
| Homogeneous 0.01 S/m | Homogeneous | Whole skull 0.01 S/m | | Ground Truth | Errors when assuming high homogeneous value |
| Homogeneous 0.0055 S/m | Homogeneous | Whole skull 0.0055 S/m | | Ground Truth | Errors when assuming a low conductivity value |
| Homogeneous EIT Estimated | Homogeneous | Whole skull 0.0072 S/m | | Ground Truth | Errors when providing 'optimum' homogeneous value |
| Age 20 | Heterogeneous | Scaled function of ground truth to account for age variation | Scaled according to Figure 3 to account for state of closure at different ages | Scaled homogeneous value estimated from EIT as described in 5.3.3ii | Effect of omitting the sutures for each age when considering approximate conductivity of aging skull |
| Age 30 | Heterogeneous | | | | |
| Age 40 | Heterogeneous | | | | |
| Age 50 | Heterogeneous | | | | |
| Age 60 | Heterogeneous | | | | |

Table 5.1: *A summary of each employed model, outlining the distribution (homogeneous or heterogeneous), the computation of the whole skull conductivity, not including the sutures (either homogeneous with one conductivity or accounted for spongiform proportion variation), the conductivity of the sutures and how they were computed, and the model utilised for comparison in the FP and IP computation and the purpose and research aims of each model. All conductivity values are in S/m if not explicitly mentioned.*

5.3.3. Model computation methodology

This section describes the methodology employed to generate each of the volume conductor models. The computation of the ground truth model is outlined in Section 5.3.3i. The EIT protocol utilised to estimate the model neglecting spongiform, the homogeneous EIT estimated model and the age-appropriate homogeneous models that were used as comparison models for the hypothesised inhomogeneous age estimated models is described in Section 5.3.3ii. The development of the heterogeneous age estimated models is outlined in Section 5.3.3iii.

5.3.3i Ground truth model

The ground truth model was regarded as the reference and absolute truth, where the proportion of spongiform and compact bone throughout the skull and the sutures were accounted for. The skull conductivities were taken from Tang et al. (2008), where resistivity measurements were extracted from 388 excised skull samples of differing structure. These values were utilised as they represented the most comprehensive average conductivity values from a large sample size, across varying participants and skull regions using a robust method. The employed methodology was assessed in Chapter 3 and regarded as high quality in the Quality Assessment due to measurements being obtained from freshly excised tissue, in a carefully controlled situation, at stable (body) temperature and across many participants.

The sagittal, coronal, and lambdoid sutures were assigned the average conductivity for dentate sutures, i.e., 0.0173 S/m. The squamous sutures' conductivities were assigned the average reported values, i.e., 0.0079 S/m. The conductivity of the remaining skull was modelled as a function of the cross-sectional proportion of spongiform bone. This was taken from Figure 6b of Tang et al. (2008), where $\sigma^{-1} = 215 - 231.25 \times p$, with p being the

spongiform thickness percentage. This corresponds with the EMA for the effective conductivity of a material given a number of compartments with different conductivities (Torquato & Hyan, 2001). The maximum value of p was set to 80% to account for the fact a skull region cannot be completely spongiform. Compact bone was modelled with a conductivity value of 0.003787 S/m. This resulted in an inhomogeneous skull conductivity model incorporating sutures and deviations in skull composition, termed the ground truth model.

5.3.3ii. EIT protocol

Models employing a personalised homogeneous skull layer were estimated using an EIT simulation protocol (Fernández-Corazza et al., 2017). EIT is a non-invasive imaging modality where electrical conductivity is estimated following current injection between electrodes and measurement of the resultant electric potentials from the remaining electrodes. The EIT current injected can be simulated given an input volume conductor model and the global conductivity of each compartment (e.g., the skull) estimated. EIT was thus utilised to approximate homogeneous skull conductivity values, given an inhomogeneous input model. The employed Colin27 input model was either the ground truth, the model omitting sutures, or one of the five hypothesised age-appropriate models. For all the input models, the conductivities of the scalp, GM, WM, and CSF were fixed according to the literature (see Section 5.3.1) and only the skull conductivity was estimated. This was as the current chapter aimed to focus on the contribution of variation in skull conductivity alone.

For each of the EIT estimation protocols, first the ideal EIT measurements were computed based on the reference input model. This was thus the most detailed model and was either the ground truth, the model omitting sutures or one of the five age-appropriate models (as above). The conductivity value for the skull as one homogeneous (and thus simplified) compartment was then determined using EIT simulation. The current injection was simulated between electrodes located on the scalp of the appropriate model and the conductivity estimated from simultaneous potential recordings. A current amplitude of 0.25 mA was passed from one ‘source’ to one ‘sink’ for 32 pairs of electrodes, located on the scalp of the model, optimised so that the injection points were at the most maximum distance from one another (Mamatjan et al., 2012). These pairs were evenly distributed across the skull and utilised a pair number (32) in typical EIT systems (Avery et al., 2017; McCann et al., 2011;

Oh et al., 2011; Khan et al., 2014). The resulting voltage was calculated on the remaining electrodes not involved in current injection (called EIT-FP) and used to estimate the equivalent conductivity (referred to as EIT-IP). The EIT-FP was solved numerically using the FEM and a PCG algorithm, with LU factorisation matrices (factoring a matrix as the product of an upper and lower triangular matrix) as preconditioners, as described in Fernández-Corazza et al. (2013) and briefly in Section 2.3.3ii. The EIT-IP then estimated the compartmental electrical conductivity from the simulated potential measurements using the least squares approach to minimise the ℓ_2 -norm of the difference between measurements and model estimations. The quasi-Newton numerical optimisation method was utilised to solve this due to less iterations required and higher stability. It has been previously shown that employing initial values lower than the true conductivity further increases stability and convergence speed to the global minimum (Fernández-Corazza et al., 2017). Thus, the initial guess for skull values was set to 0.005 S/m. The final homogeneous value was taken as an average of estimations from all injection pairs, providing a global and homogeneous estimate (as carried out in Fernández-Corazza et al., 2017). A more detailed description of an EIT protocol is described in Fernández-Corazza et al. (2013) and (2017).

5.3.3iii. Age-appropriate models

Five age-appropriate models at 20, 30, 40, 50 and 60 years, were created to account for general decline in global skull conductivity (Antonakakis et al., 2020, see also Chapter 4) and suture closure with age. The estimated decrease with age was taken from the mean function in Figure 4.1a. The relationship was computed according to the data acquired in Gonçalves et al. (2003a, b) and chosen in the current study as they utilised an EIT method, similar to the homogeneous EIT estimations. Bone composition and the resulting conductivity distribution were firstly modelled as in the ground truth model. The whole conductivity distribution, accounting for variation in spongiform and compact bone proportion, was then scaled for each age according to the sigmoid function described in Chapter 4, Figure 4.1a. This sigmoid function was first assumed as the general function describing decline in whole skull conductivity. The distribution was then adjusted and scaled accordingly, so the global conductivity value estimated from the function, at age 28 (the age of Colin27 at scanning; Aubert-Broche et al., 2006), aligned with the EIT estimated homogeneous value of the Colin27 model. This standardised the hypothesised aging skull conductivity with the estimated homogeneous conductivity of the utilised volume conductor model (Colin27). As a

result, a final function describing the decline in conductivity with participant age was thus determined, where $T_{sc} = T \times 0.0187e^{age \times -0.0268}$. Here, T is the vector describing the conductivity distribution in the skulls' tetrahedra according to bone composition (as computed from Colin27 and described in Section 5.3.1) and T_{sc} is the new distribution according to modelled age. The scale is thus determined by participant age at $0.0187e^{age \times -0.0268}$.

The closure of the adult sutures was then modelled considering fusion at 45, 50, 55, and 70 years for the coronal, sagittal, lambdoid and squamosal sutures, respectively, as mentioned in the literature (Russell & Russell, 2018; Idriz et al., 2015; Kumar et al., 2018; Singh et al., 2004; Nakahara et al., 2006). The sutures were assumed to close at a sigmoid rate from age 20, in accordance with previous publications (Figures 3-5 in Todd and Lyon, 1925; Figure 3 from Jangietriew et al., 2007; and Figure 3a from Chiba et al., 2013). This choice was additionally supported by Ruengdit et al. (2020), who reviewed cranial sutures' closure. They found that the sutures typically progress slowly in early adulthood from age 20, then rapidly until approximately $\frac{3}{4}$ of the age at complete closure, and finally slowly again towards absolute fusion age. The conductivities at age 20 for all suture types were assigned according to Tang et al. (2008), whereas the values at closure were assumed as that of hard bone.

The resultant conductivities of the sutures as a function of age are depicted in Figure 5.3. From age 20 to closure age, a sigmoid function was generated where conductivity equalled the median between that of hard bone and the respective suture at the midway point between age 20 and suture fusion.

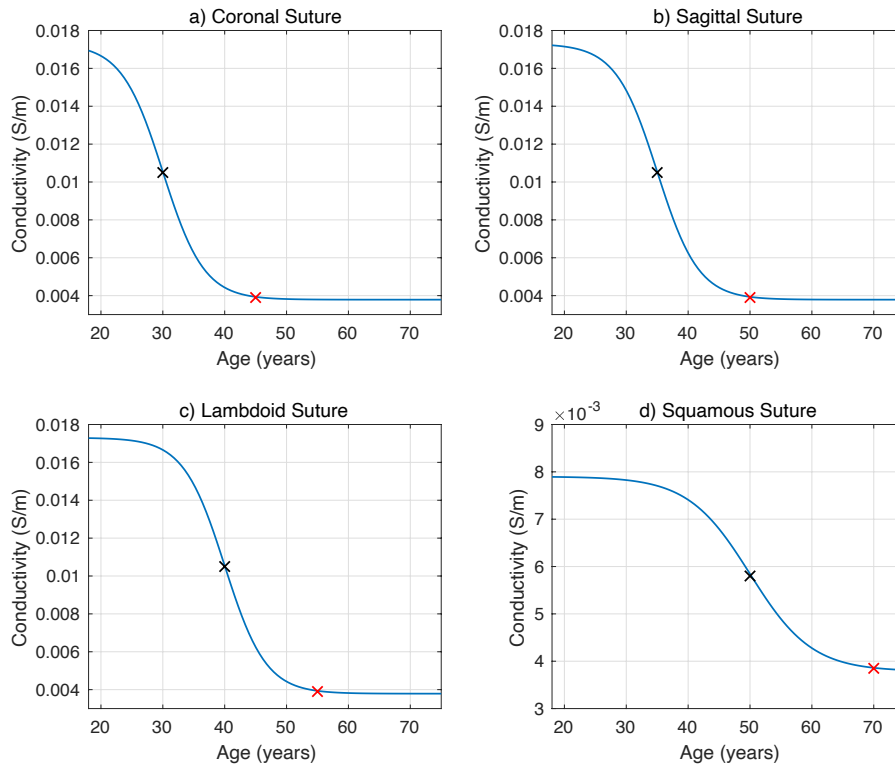


Figure 5.3: Hypothesised conductivity (S/m) as a function of age (years) for the a) coronal, b) sagittal, c) lambdoid, and d) squamous sutures. A sigmoid model was assumed where the conductivity was that of the respective suture at age 20, the median conductivity between hard bone and respective suture at the midway point between 20 and suture fusion age (black cross), and then that of hard bone at closure (red cross). The blue line indicates this function for each of the sutures.

5.3.4. EEG forward and inverse problems

The EEG-FP was solved using the FEM and the analytical subtraction approach (Beltrachini, 2019) with a PCG algorithm and LU factorisation matrices as preconditioners. This method has been previously shown to perform well compared to other subtraction-based approaches and was the most robust against deformation of individual elements and eccentric sources (Beltrachini, 2019). A detailed explanation of this solver can also be found in Beltrachini (2019). A total of 20,119 sources were placed centrally in the GM compartment. This was done by computing the mid surface between those corresponding to the GM/CSF and GM/WM interfaces provided by FreeSurfer (Fischl, 2012). All source positions were checked to belong to the resulting GM compartment. Normal constraint is a reasonable physiological assumption due to the fact apical dendrites produce a measured field oriented normal to the surface (Baillet et al., 2001). Furthermore, when the head model is known from MRI/CT data

and is considered as a true, not approximate, model with pre-defined source positions, normal constraint is realistic and frequently employed (Grech et al., 2008; Valdés-Hernández et al., 2009). Average reference was considered in all simulations.

The sLORETA method was used to solve the EEG-IP (Pascual-Marqui, 2002) given the electrical potential input as estimated from the EEG-FP (see above). This employs the current density estimate provided by a standardisation of the minimum norm solution to infer localisation based on these estimates (see Chapter 2, Section 2.5.3). sLORETA calculates the smoothly distributed electric activity whilst assuming synchronous and simultaneous neuronal firing of adjacent neurons and no noise and is thus capable of exact (zero-error) localisation under specific scenarios (Pascual-Marqui, 2002). The method computes the equivalent dipole location as the maximum measurements of the standardised power. sLORETA was chosen due to its discussed capability of yielding zero localisation error when utilising the actual head model and assuming no noise, as well as a reduced likelihood of locating deep sources as residing on the surface (as with minimum norm estimation). Furthermore, non-standardised LORETA can result in zero electrical activity estimation at superficial sources, which sLORETA avoids (Pascual-Marqui, 2002).

The EEG-FP was solved for all proposed models. Comparisons were made between the FP electric potentials of two models, as necessary for the experiments outlined in Section 5.3.2. The relative error (RE) metric was employed to characterise errors in the FP, defined as $RE = \|u_t - u_n\|/\|u_t\|$, where u_t and u_n are the potentials generated by a given source employing the input and approximated models, respectively. The RE describes the overall difference between the two employed models. The MAGnification factor (MAG) was also computed to indicate the errors in magnitude between the two comparison models, where $MAG = \|u_t\|/\|u_n\|$. The relative difference measure (RDM) was additionally calculated as a measure of topographical error with minimal error as $RDM = 0$. Here, $RDM = \|(u_t/\|u_t\|) - (u_n/\|u_n\|)\|$. These error measurements are frequently used in addition to RE within EEG analysis fields (Wolters et al., 2003).

The EEG-IP was solved for each generated leadfield given the potentials calculated for the input model. For each source, the distance between estimated locations using the input and approximated models was calculated, to result in an absolute error (AE, measured in cm)

between the input and comparison models (according to the required models for each experiment, described in Section 5.3.2).

5.4. RESULTS

The EIT estimated homogeneous skull conductivity for the model neglecting spongiform proportion was found to be 0.0061 S/m. When accounting for a “ground truth” of both variation in bone composition and the presence of sutures the EIT estimated homogeneous model conductivity was estimated as 0.0072 S/m. Hypothesised age-appropriate homogeneous skull conductivity values considering both spongiform proportion and sutures were estimated as 0.0086, 0.0068, 0.005, 0.0037, 0.0029 S/m for 20, 30, 40, 50 and 60 years old, respectively.

5.4.1. Impact of sutures and bone composition

As can be seen in Figure 5.4, omitting the presence of sutures, compared to the ground truth model, resulted in the largest FP-RE (Figure 5.4a, maximum 67.72 %) and IP-AE (Figure 5.4c, maximum 4.14 cm) across the suture lines, particularly the dentate. Figure 5.5 equally displays high MAG and RDM values across suture lines, particularly noticeable across the dentate sutures. When neglecting variation in spongiform and compact bone distribution throughout the skull, the greatest FP-RE (maximum 47.47 %) and IP-AE (maximum 2.19 cm) was evident across areas of high spongiform proportion, particularly in frontal regions (Figure 5.4b and d, respectively). Deep sources also produced relatively large IP-AEs (Figure 4c, inferior view). Highest MAG values were revealed in high spongiform proportion areas (Figure 5.5b), with low values in high compact bone (Figure 5.5, lateral view). Topological errors were decreased compared to magnification factor values when neglecting the spongiform proportion (Figure 5.5d). Omitting the sutures produced the largest maximum and localised forward solution errors for both the FP (Figure 5.4e, inset) and IP (Figure 5.4f). However, neglecting spongiform proportion resulted in higher global FP errors than omitting the sutures (Figure 5.4e).

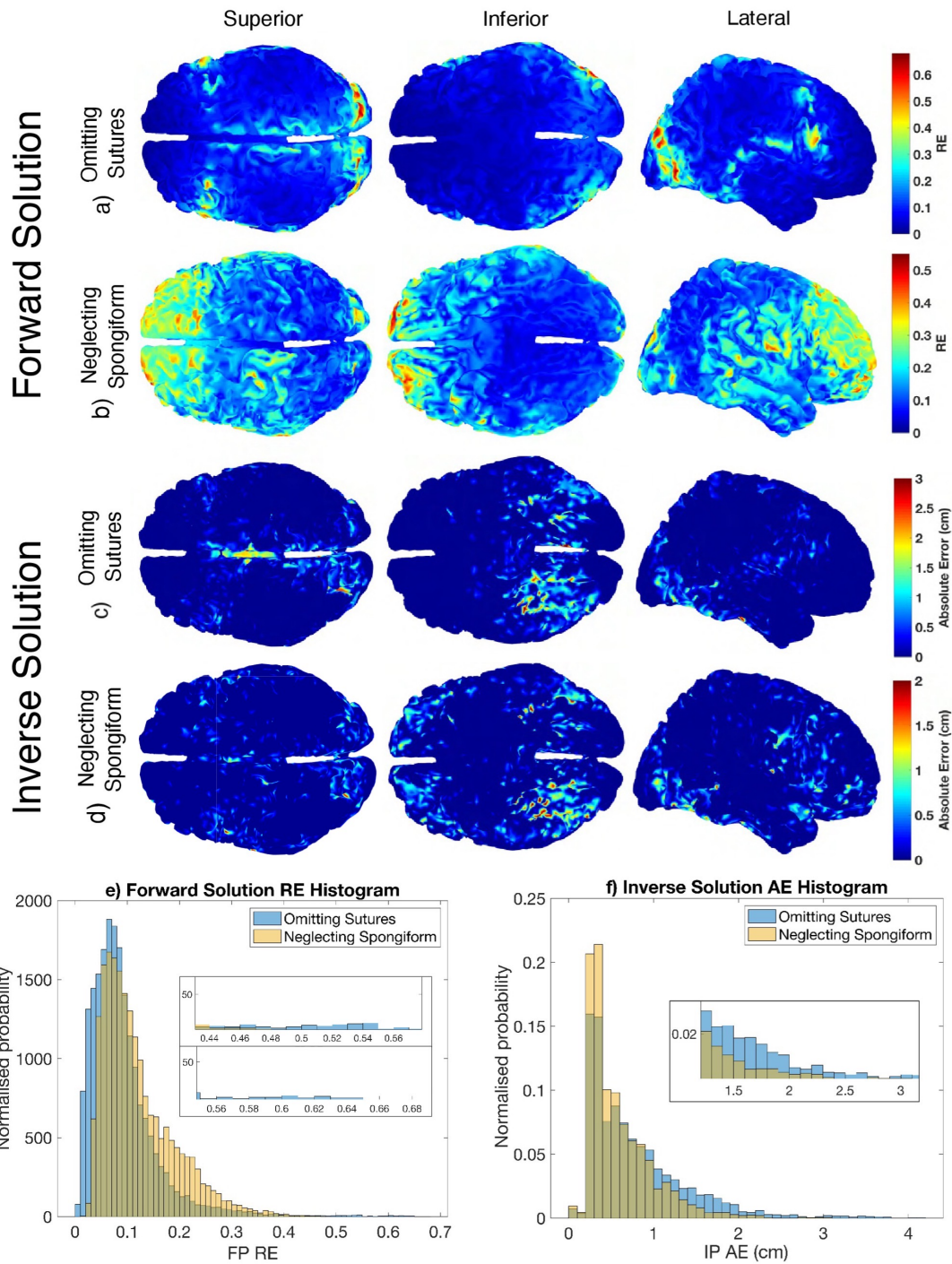


Figure 5.4: Error distribution when omitting the sutures (compared to the ground truth) for the EEG forward (a) and inverse (b) solution and when neglecting the spongiform distribution (compared to an EIT estimated homogeneous value when omitting the sutures) for the forward (a) and inverse (b) solution. The colour scale for the FP-RE is presented in percentage, where 1 would indicate 100% error, whilst the IP-AE is measured in cm, the maximum (red) differs for each comparison. The normalised probability histogram of the e) EEG-FP RE and f) EEG-IP AE (cm) when omitting the sutures (blue histogram) and neglecting the spongiform distribution (yellow) is presented, where the inset for each figure is a zoomed portion of the x axis to add clarity.

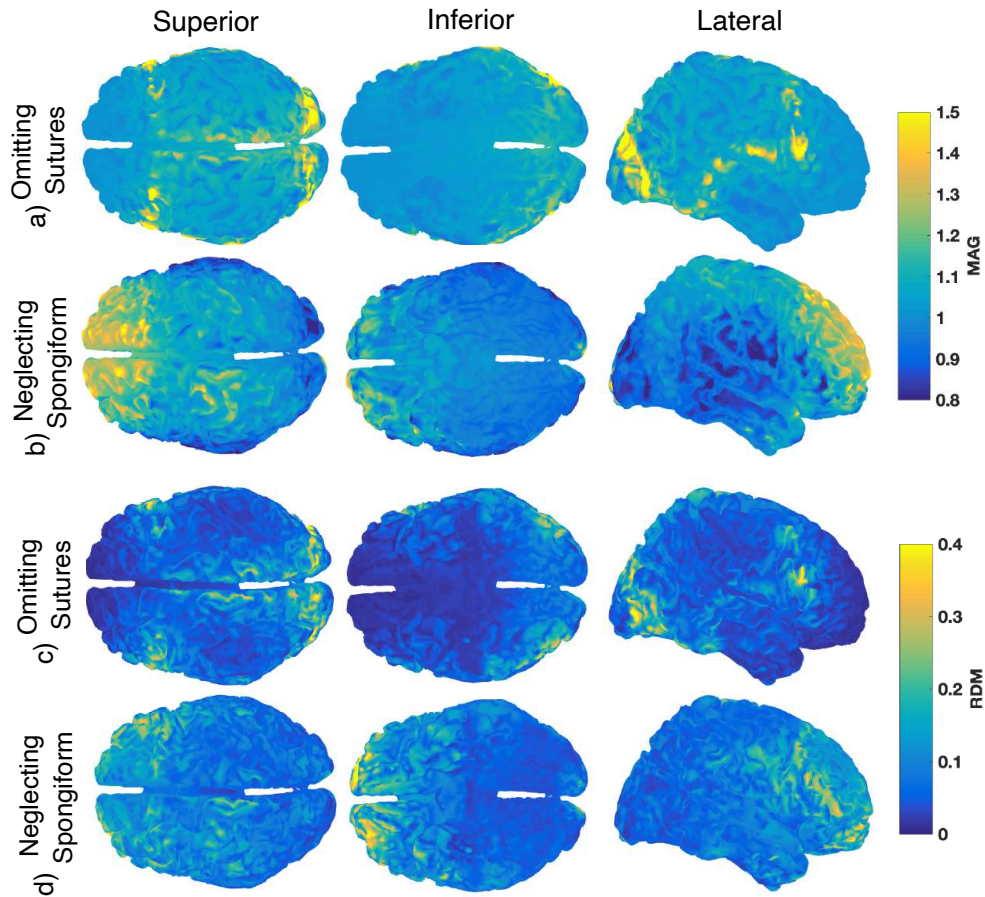


Figure 5.5: Forward problem MAGnification factor when omitting the sutures compared to the ground truth (a) and when neglecting the spongiform distribution compared to an EIT estimated homogeneous value when omitting the sutures (b). The colour scale represents a factor from 0.8 to 1.5, for all models. The forward problem relative difference measure (RDM) is also depicted when omitting the sutures (c) and neglecting spongiform (d), with minimum RDM at 0. The superior, inferior, and lateral views are displayed.

5.4.2. Homogeneous skull models

Figure 5.6 indicates that assigning the most frequently employed homogeneous skull conductivity value (0.01 S/m) produced the greatest FP (maximum 85.49 %) and IP (maximum 2.7cm) error across complete compact bone regions (Figure 5.6a and d for the FP and IP, respectively). This also produced the largest maximum FP-RE of all the computations, most notably in the temporal and lower parietal regions. Comparably, assigning a lower value (0.0055 S/m) resulted in the largest FP (maximum 56.81 %) and IP (maximum 3.03 cm) errors across areas of high spongiform proportion, particularly pronounced in the frontal cortex, and through suture lines (Figure 5.6b and e for the FP and

IP, respectively). Similar results were revealed for magnitude errors, with high MAG values across high areas of spongiform bone for the 0.0055 S/m model (Figure 5.7b) and low values across high compact bone proportion for the 0.01 S/m model (Figure 5.7a). The EIT estimated model produced relatively lower overall MAG in both high spongiform and compact bone, similar to RE (Figure 5.7c). The greatest topographical errors were across areas of particularly high spongiform or compact bone proportion (Figure 5.7d-f). Of the three homogeneous skull models, the EIT estimated value produced the lowest RE and AE, with the greatest FP (maximum 53.28 %) and IP (maximum 3.03 cm) solution error across regions of very high (i.e., frontal areas) or no (particularly temporal regions) spongiform proportion (Figure 5.6c and f for the FP and IP, respectively). The EIT estimated homogeneous model generated the lowest overall distribution of FP and IP error of the homogeneous models (Figure 5.8).

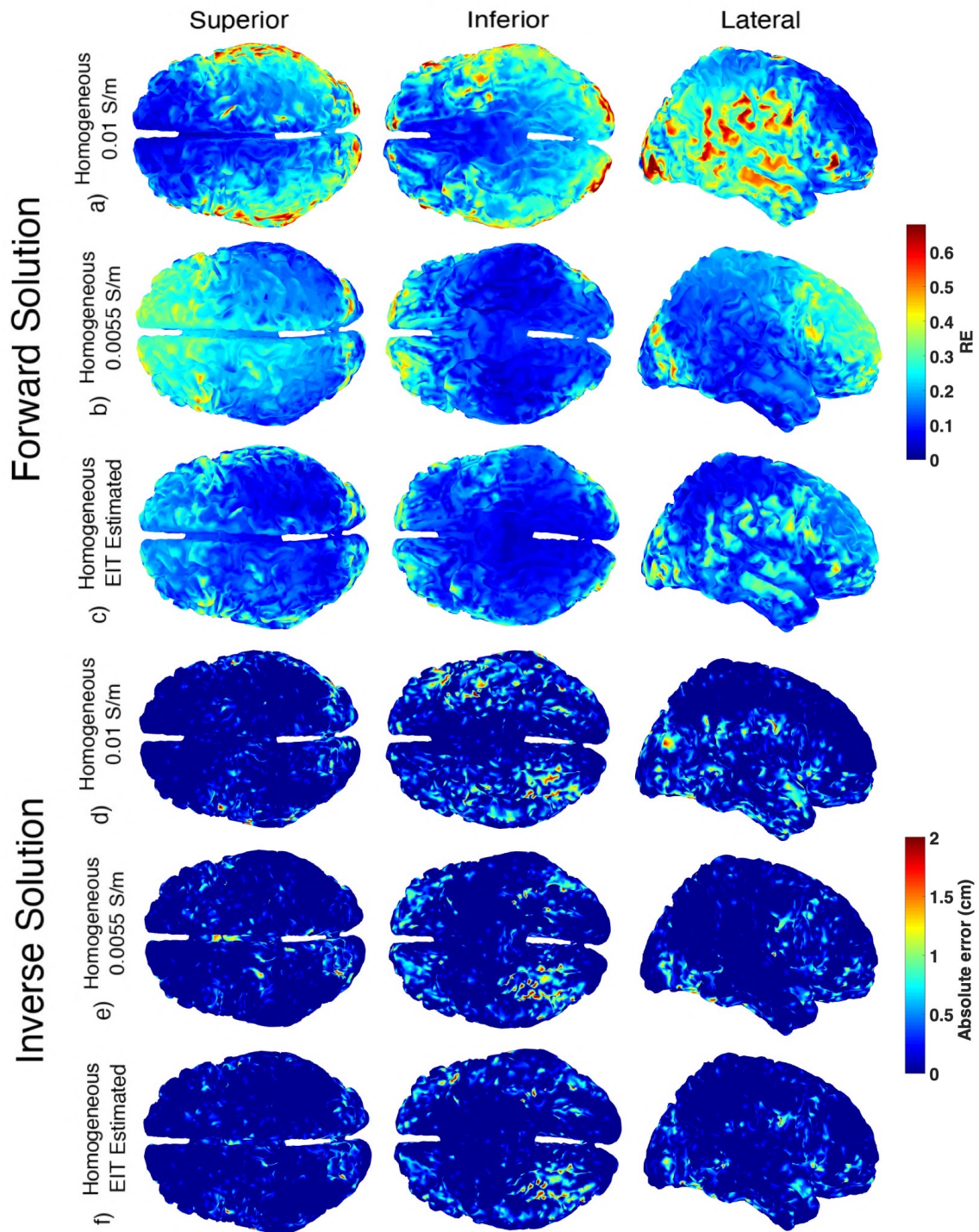


Figure 5.6: Error distribution for the EEG forward and inverse solution when skull conductivity was assigned a homogeneous value of 0.01 S/m (a and d, respectively), a homogeneous value of 0.0055 S/m (b and e, respectively), and the EIT estimated homogeneous value of 0.072 S/m (c and f, respectively), all compared to the ground truth model. Three views, superior, inferior, and lateral are displayed for each comparison. The colour scale for the FP-RE is presented in percentage, where 1 would indicate 100% error, whilst the IP-AE is measured in cm, the maximum (red) differs for each comparison.

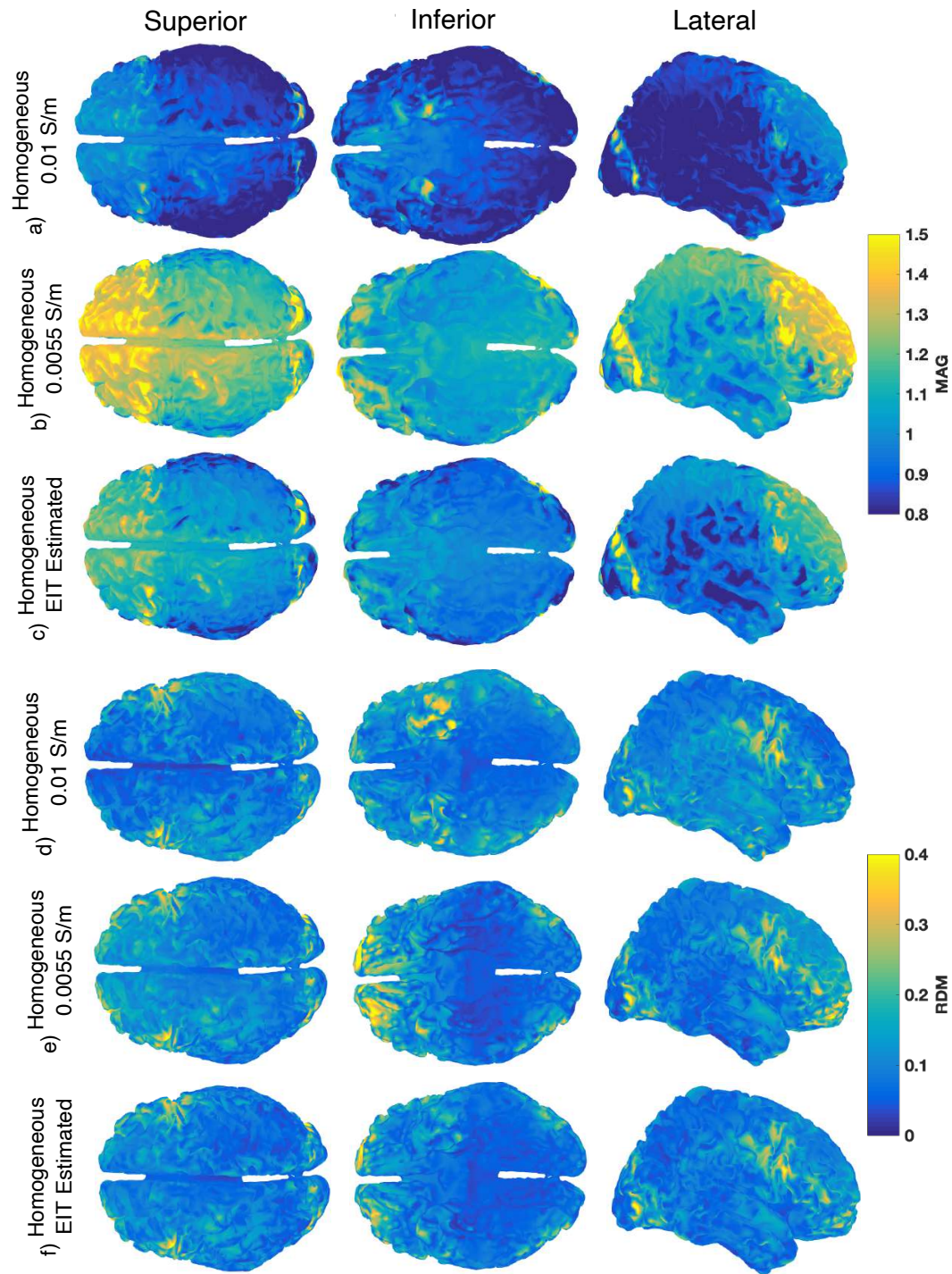


Figure 5.7: Forward problem MAGnification factor and relative difference measure (RDM) when skull conductivity was assigned a homogeneous value of 0.01 S/m (a and d, respectively), a homogeneous value of 0.0055 S/m (b and e, respectively), and the EIT estimated homogeneous value of 0.072 S/m (c and f, respectively), all compared to the ground truth model. Three views, superior, inferior, and lateral are displayed for each comparison. The MAG colour scale represents a factor from 0.8 to 1.5, for all models, whilst the minimum RDM is at 0.

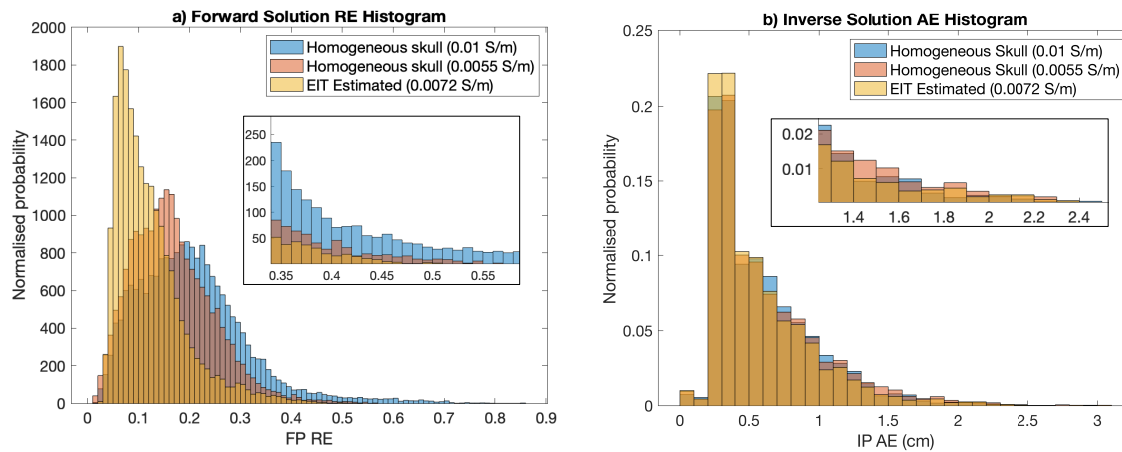


Figure 5.8: Normalised probability histogram of the a) EEG-FP RE and b) EEG-IP AE (cm) for a homogeneous skull of 0.01 S/m (blue), 0.0055 S/m (red) and EIT estimate of 0.0072 S/m (yellow) conductivity, compared to the ground truth model. The inset for each figure is a zoomed portion of the x axis to add clarity.

5.4.3. Age-appropriate models

The forward and inverse solution error between the hypothesised age-appropriate models (ages 20-60) and their respective EIT estimated age-appropriate homogeneous value are depicted in Figure 5.9. The largest FP-RE for all (with the exception of the 30-year-old models experiment, due to similarity with the corresponding EIT estimated model) was revealed across regions of high spongiform proportion, in the frontal brain area. The greatest FP-RE for the 30-year-old model was across suture lines, as in the model omitting sutures (see Figure 5.6b). Errors across suture lines were also evident for the 20- and 40-year-old model experiments (Figures 5.9a and c), particularly across the lambdoid and coronal sutures, whilst FP-RE can be seen along the squamous suture for the 50-year-old (Figure 5.9d). The MAG value was revealed to be low across high areas of spongiform bone (the frontal region) and greater across areas of high compact bone (temporal areas), as can be seen in Figure 5.10 (MAG values) for all of the age-appropriate models. The topographical (RDM) error revealed increased values in deep frontal sources and across higher compact bone areas, this was evident for all models (Figure 5.10, RDM values). The greatest IP-AE for all ages, however, were in regions with the highest proportion of spongiform bone (frontal and right central areas) and at the base of the brain (see inferior view). The maximum FP-REs for the 20, 30-, 40-, 50- and 60-year-old evaluations were 66.2, 42.14, 72.06, 78.63 and 78.77 %, respectively.

respectively, whilst the maximum IP-REs were 1.95, 2.29, 2.04, 2.76 and 2.21 cm, respectively.

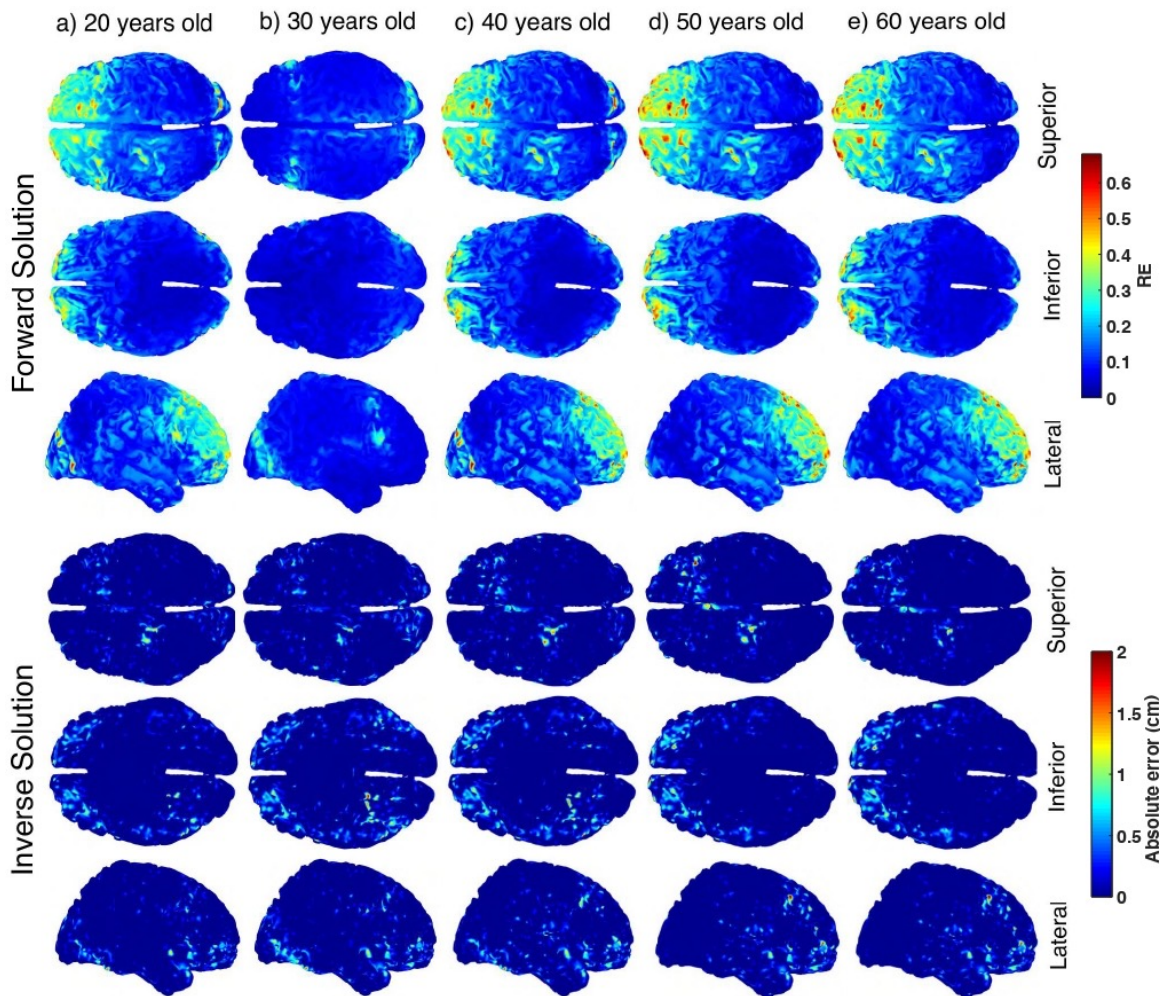


Figure 5.9: Error distribution for the EEG forward and inverse solution when omitting the sutures compared to EIT estimated age-appropriate homogeneous skull models accounting for suture closure and global conductivity variation, for ages 20, 30, 40, 50 and 60 (a-e respectively). Three views, superior, inferior, and lateral are displayed for each comparison, respectively. The colour scale for the FP-RE is presented in percentage, where 1 would indicate 100% error, the maximum RE for all simulations is 68%. The IP-AE is measured in cm, with the maximum (red) at 2 cm.

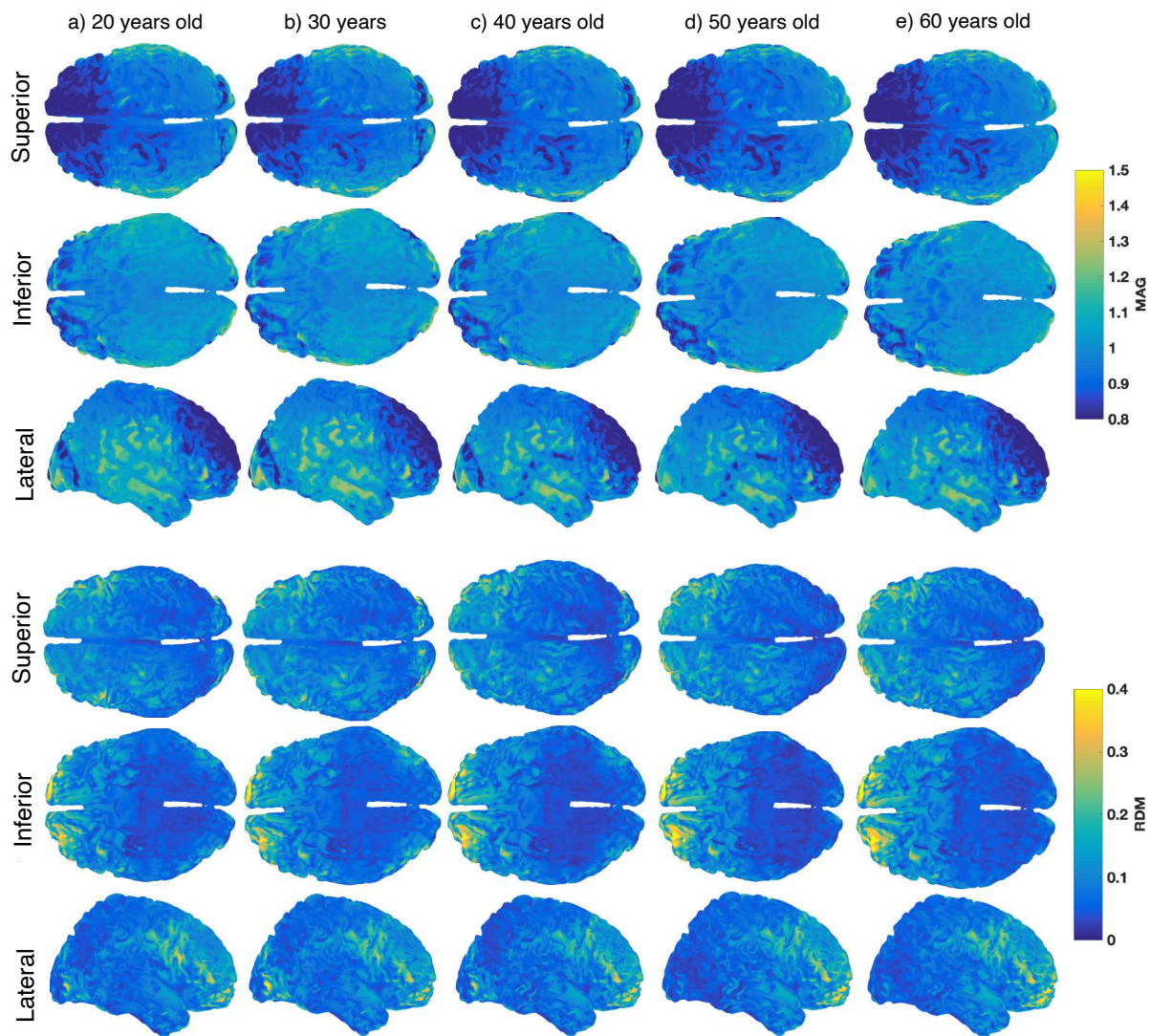


Figure 5.10: Forward problem MAGnification factor and relative difference measure (RDM) when omitting the sutures compared to EIT estimated age-appropriate homogeneous skull models accounting for suture closure and global conductivity variation, for ages 20, 30, 40, 50 and 60 (a-e respectively). Three views, superior, inferior, and lateral are displayed for each comparison, respectively. The MAG colour scale represents a factor from 0.8 to 1.5, for all models, whilst the minimum RDM is at 0.

5.5. DISCUSSION

The current chapter assessed the impact that neglecting adult sutures and differing bone composition has on EEG forward and inverse solutions. An inhomogeneous skull conductivity head model was created that accounted for variations according to proportion of

spongiform and compact bone as well as the presence of adult sutures. This model was compared to others omitting sutures and/or spongiform bone with differing homogeneous conductivity values. A hypothesised aging skull was further computed to assess the contribution of suture closure with age on EEG source computations. The results revealed large forward solution relative errors, up to 85%, between models, particularly evident across suture lines when omitted and directly related to proportion of spongiform. Inaccuracies of up to 4.14 cm were revealed for the EEG inverse solutions when the sutures were not taken into account. Source localisation errors were also particularly related to proportion of spongiform and across suture lines. This result was not eradicated when an aging skull was estimated as significant FP errors across suture lines remained evident at ages 20-50 years old.

5.5.1. Impact of sutures and bone composition

The presented results importantly elucidated the novel significance of adult sutures. When omitting the presence of sutures and considering them as compact bone, the highest forward and inverse inaccuracies were revealed directly beneath suture lines (see Figure 5.4a and c and Figure 5.5a and c). Specifically, when sutures were neglected, forward solutions may have a relative error of up to 67%, with erroneous source localisation of up to 4.14 cm. This is more evident for the dentate (coronal, sagittal and lambdoid) than squamosal sutures, where the conductivity of hard bone deviated further from the respective suture. Of note, omitting the presence of sutures resulted in the greatest general IP solution errors of the first five core experiments. Moreover, when accounting for variation in suture closure, as well as the deviation in whole skull conductivity according to age, the impact of sutures remained. Specifically, the dentate sutures resulted in noticeable FP-RE for ages 20-40 years old (Figures 5.9a-c), whilst the squamosal sutures retained a visible error for the hypothesised 50-year-old (Figure 5.9d). As when omitting the sutures (Figure 5.4 and 5.5, a and c), this is due to the whole skull conductivity (as estimated with EIT) being closer to that of the dentate sutures for the 20-40 age ranges, whilst the opposite is true for the 50-60 range. Furthermore, results obtained with the hypothesised 30-year-old head model are comparable to that of the model omitting the sutures, as the age of the utilised head model in all simulations is similar. Thus, significant differences between these models were not expected. These results suggest the influence of the adult sutures is not minimal and remains regardless of suture closure. In support, Azizollahi et al. (2016) varied fontanelle conductivity, which they suggested would decrease during infant development due to the ossification process. Skull conductivity

decreases during this process and causes the fontanelles to close and be replaced by less conductive bony structures (Lipsett et al., 2019). Such variation in fontanelle conductivity as in Azizollahi et al. (2016), mimics the presented hypothesised deviation due to age in adult sutures and local REs beneath fontanelle lines were revealed. The forward solution errors were notably large particularly along suture lines which also corresponded to high magnitude errors, suggesting incorporating accurate suture conductivities is essential for determining electrical current propagation.

The exploration of sutures on EEG forward and inverse solutions has not yet been previously investigated, due to the necessity of CT data for accurate skull segmentation. Although the utilised head model represents one head alone and results may not be generalisable to the entire population, high resolution MRI and CT information has been employed providing essential contributions. This allowed representation of 10 tissue types including four sutures, thus is considerably detailed compared to typical realistic models and permitted novel conclusions, such as the contribution of the sutures, to be made.

The presented results can be related to previous research discussing the influence of neonatal sutures and fontanelles, which provided analogous findings. For example, Lew et al., (2013) demonstrated the conductivity difference between the skull and fontanelles significantly impacted EEG forward and inverse solutions. They demonstrated source reconstruction errors were considerably lower than the presented chapter (maximum 2.4 mm when the sources were normally constrained, as in this method). One explanation for this, as the authors mentioned, is the relative size of infant heads. The method employed in this chapter utilised adult head sizes, inaccuracies from Lew et al., (2013) may therefore be equivalent in adult heads and result in higher significance of the misspecification. There also exists additional differences between infant and adult head models such as the presence of large fontanelles, skull and scalp thickness, percentage of spongiform bone, CSF volume and GM/WM distribution which may account for such discrepancies. The current chapter used a particular head model that did not account for complete differences between infant and adult head geometries, which is acknowledged as a limitation. Future research should implore to utilise accurate neonatal and infant head models for the most precise comparisons. Moreover, the conductivity values of all the compartment tissues differed considerably in Lew et al.'s paper (2013), compared to this experiment. Of particular note is that of skull conductivity which was assigned a value of 0.04 S/m (or between a range of 0.03 – 0.05 S/m for comparison

models). This was more than double and, in some cases, quadruple any skull conductivity value utilised in the presented chapter. Additionally, Lew et al. (2013) employed 277 EEG and MEG electrodes, compared to 164 in this study, which may further contribute to localisation error differences. Such source localisation differences may also be explained by their use of unconstrained sources compared to normally constrained sources. In the presented chapter, normal constraint may have, in comparison, resulted in the higher source localisation areas. Additionally, a different IP methodology was employed, using a single dipole fit compared to sLORETA in this research, which may contribute to the inverse solution differences. Furthermore, in Lew et al.'s (2013) study, the initial guess of the dipole fit was set to the original position and orientation, which may have also minimised the inverse solution errors.

Comparable local effects to the presented results, however, have additionally been revealed in previous research, where Azizollahi et al. (2016) discovered forward errors directly below the fontanelles. Likewise, Lanfer et al. (2012) found local defects in skull geometry, such as simulating sinuses as compact bone and skull holes resulted in forward and inverse miscalculations within the vicinity of the deficiency. This was additionally supported by Bénar and Gotman (2002), Vanrumste et al. (2000) and more thoroughly in von Ellenrieder et al. (2014). High source localisation errors in the current chapter may, however, be also somewhat explained by the use of normally constrained sources. As revealed in Valdés-Hernández et al. (2009), normal constrained sources caused increased localisation errors when the head model was approximated due to potential large differences in the actual and approximate normal direction, as the normal may not point in the same direction. This is supported by a more recent study by Vorwerk et al. (2019) where source reconstruction errors were reduced for sources with 'free' orientation and these errors, as a result of conductivity deviations, could be moderately compensated by source orientation modifications. The sources and head model in the current chapter, however, were geometrically accurate and only the conductivity distribution of the head model was simplified. Thus, a lesser effect of normal constraint was assumed and was deemed suitable for the purposes of this research. Nevertheless, further research, particularly when the head model and participant MRI or CT is unavailable, or sources are unknown, as can be the case in infants, should consider utilising unconstrained moments to reduce such an impact of orientational differences.

It is noted that when neglecting the presence of sutures, the conductivity was assumed to equal that of hard bone, however, this may not be the case for all individuals. Furthermore, suture closure was assumed from literature data to decline in a sigmoid fashion. However, such closure may not relate directly to conductivity values. Knowledge of suture conductivity and their closure is limited from the existing literature, and therefore future research that explores this in more detail is imperative for detailed understanding and EEG source analysis. Alongside this, it is noted that skull conductivity values are taken from Tang et al. (2008) alone or estimated from an EIT methodology (Fernández-Corazza et al., 2017), which does not account for measurement variation across participants and studies and the relative quality of the utilised method. The true conductivity of the utilised head model (Colin27) will differ from these proposed values; however, this highlights the necessity of individualised conductivity measurements for the most accurate EEG forward and inverse computation. Furthermore, conductivities of soft tissues were assigned as the weighted average from Chapter 3, weighted according to the quality of each respective study. This provided the optimum conductivity value given the available data. Skull conductivity estimations were, however, not weighted as they were employed to highlight specific inhomogeneous differences. It is acknowledged that the quality and methodology (for example E/MEG compared to EIT protocols) will impact the obtained inhomogeneous skull conductivity values. Future studies may therefore utilise different techniques for obtaining conductivities and compare their effects on EEG forward and inverse computations

The present simulations further revealed that neglecting an assumed variation in spongiform proportion resulted in maximum forward relative errors of 47% and maximum source localisation errors of 2.19 cm. As expected, this was considerably more evident across regions with high marrow bone concentration, particularly in the frontal skull regions as well as within the temporal lobe (Figure 5.4b). Peak forward and inverse errors were greater when omitting the sutures than when neglecting spongiform variation. However, the relative forward error across the whole skull was more widespread (see Figure 5.4a and b and Figure 5.5b). Overlooking differing bone composition indicates greater global error than omitting the sutures alone. This is supported by Lew et al. (2013) results, where skull conductivity mismatch produced broader errors than excluding infant sutures and fontanelles. Comparable to the presented findings, previous research has revealed inaccurate skull segmentation of the compact and spongiform bone results in considerable forward and inverse solution errors up to 2 cm (Lanfer et al., 2012; Montes-Restrepo et al., 2014; Wolters et al., 2006; Dannhauer et

al., 2011). Vorwerk et al. (2014) notably revealed significant EEG source localisation errors within temporal regions, similar to the presented EEG-FP results (Figure 5.4b), but not frontal areas. This may be explained by the specific distribution of spongiform bone, the proportion of which was high for the utilised model in both frontal and temporal regions. Neglecting the distinction between bone composition is thus hypothesised to result in increased FP and IP EEG errors in both high compact and spongiform regions, differing between participants and head models. Furthermore, the skull tissue conductivities utilised in Vorwerk et al. (2014) were considerably higher and with a greater difference between compact and spongiform conductivities than in the presented study. For example, compact bone was assigned a value of 0.008 S/m (compared to a value of 0.0038 in the current experiment), whilst areas of the highest spongiform bone proportion in the current methodology reached a maximum conductivity of 0.014 S/m compared to 0.025 in Vorwerk et al. An approximately 2-fold difference between these values may explain differing results. This is alongside greater disparity between the spongiform, compact bone and whole skull conductivities in Vorwerk et al. (2014) than the current study and thus larger errors would be present in high spongiform areas (such as the temporal lobe). Aside from this, the present results are further supported by comparisons between homogeneous and inhomogeneous skull models, where using CT, heterogeneous skull conductivity yielded the lowest errors compared to homogeneous models (Montes-Restrepo et al., 2014; Sadleir & Argibay, 2007; Dannhauer et al. 2011). Dannhauer and colleagues (2011) additionally showed that employing local heterogeneous models produced source localisation errors up to 4 mm, compared to 2 cm with global homogeneous models.

5.5.2. Impact of a homogeneous skull

As revealed in the study by Dannhauer et al. (2011), as well as previous literature, assuming homogeneous skull conductivity values can result in significant propagated electric potential errors and source localisation (Vorwerk et al., 2019; Vallaghé et al., 2008; Chen et al., 2010; Acar et al., 2013). The current chapter supports these findings, where homogeneous skull models compared to the ground truth value led to forward solution relative errors of up to 85% (for a homogeneous value of 0.01 S/m) and 57% (for a value of 0.0055 S/m). The region of greatest error also depended on spongiform and compact proportion distribution. For the 0.01 S/m homogeneous skull model, the highest errors occurred in areas of complete compact bone (with a conductivity of 0.0047 S/m). This is as expected as the homogeneous

conductivity deviated further from compact than spongiform bone (with approximate conductivity between 0.013 – 0.016 S/m). Conversely, employing a lower homogeneous skull conductivity (0.0055 S/m) resulted in lower REs, with the highest miscalculation across regions of high spongiform proportion. This homogeneous conductivity deviated further from that of marrow than compact bone, hence the greatest errors were revealed across these areas. The presented results suggest forward solution errors may be a direct result of skull bone composition errors and the approximated homogeneous value. The highest proportion of marrow bone is across the frontal skull region (see Figure 5.2), whereas the areas of complete compact bone are typically across temporal regions. Homogeneous conductivities considerably different from complete compact and high marrow bone values would yield the greatest forward solution errors within the respective regions. Notably, a higher homogeneous conductivity value in this chapter produced the greatest FP-REs of the first five core experiments. These results suggest that, when assuming a homogeneous skull value, the differences between compact and marrow bone should be minimised.

EIT provided a method to estimate homogeneous skull conductivity and thus minimise eccentricities due to sutures and bone composition across a heterogeneous model. It computed the most likely homogeneous global conductivity value given an inhomogeneous model. The forward solution RE was smaller when utilising EIT estimated conductivity (0.0072 S/m), with a maximum error of 53% (Figure 5.6c; Figure 5.8a). Similarly, localisation errors were largely reduced for this model (Figure 5.6f), producing the lowest IP-AE of the first five core experiments (Figure 6b), with additionally lower MAG and RDM errors (see Figure 5.7). However, this model did result in a maximum absolute error of 3.03 cm, marginally higher than a high homogeneous value and identical to the low value, assumed from the literature. As expected, regions with the greatest error were both in areas of complete compact bone and the highest spongiform proportion. EIT estimated homogeneous conductivity, however, minimised deviations between the bone composition and thus produce less concentrated inaccuracies. This was particularly evident when compared with the high and low skull conductivity values, assigned from literature. EIT is typically considered non-invasive, safe, cost and time-effective, easily portable and acquired (Holder, 2004), with relatively good skull conductivity characterisation, therefore it is suggested as one such method for easily obtaining individualised conductivity measurements. The presented EIT method may therefore be one technique to reduce errors incurred when assuming a homogeneous skull. The global homogeneous conductivity can be estimated during EEG acquisition, based on

real EEG electrical potentials and solved accordingly (Gonçalves et al., 2000), using a standard EIT application. Applying EIT during EEG acquisition to determine equivalent head tissue conductivities reduced systematic EEG-IP inaccuracies by up to 1 cm and obtained conductivities within 5% of the true value (Gonçalves et al., 2000). This may be especially useful when MRI alone, and not CT or x-ray information, is available, essential to most accurately segment bone compartments and sutures (Fernández-Corazza et al., 2017; Bayford et al., 2001). Furthermore, a recently developed protocol employed EIT using injection patterns with one source and multiple sinks to generate an inhomogeneous conductivity map of the skull (Fernández-Corazza et al., 2020). This novel method may enhance the current proposed EIT homogeneous model, to produce the most accurate heterogeneous representation of skull conductivity and thus reduce FP and IP errors further. Additional methodologies exist to determine individualised skull conductivities, such as those obtained with EEG and MEG (i.e., as in Gonçalves et al., 2003a). Despite good characterisation of personalised skull conductivity using EIT, further research could employ these additional methods and determine differences between them and the impact of sutures and bone composition using these measurements.

5.5.3. Influence of age

The current findings employing age-appropriate conductivity values also indicate the importance of accounting for suture closure as a function of age for EEG source analysis. Specifically, the greatest FP-RE was shown across regions of high spongiform proportion, typically frontal regions, for all age-appropriate models. This error increased with increasing age, due to a higher relative difference between the EIT estimated global conductivity value and that of spongiform bone. Conversely, a greater error was revealed across areas of high compact bone for the 20-year-old model, which is also supported by Azizollahi et al. (2016) findings that skull conductivity affected EEG forward modelling in regions covered by cranial bones. In line with Azizollahi et al.'s (2016) and the current results, younger ages, particularly children with higher skull conductivities, may yield greater inaccuracies in regions of complete compact bone (typically temporal areas). Importantly, as discussed more thoroughly in Section 5.4.1, accounting for suture closure, and thus differing conductivity, as a function of age further impacted EEG source analysis. These results outline not only the importance of including the sutures in EEG analysis, but also that accounting for their variation and fusion across the lifespan is imperative.

The relationship between skull conductivity and age, however, remains relatively unknown, with such a relationship being hypothesised from previous data in the current analysis. Future research should determine accurate and precise *in vivo* conductivity values as a function of age to assess the impact on EEG source analysis. Alongside this, the current volume conductor models assumed known and fixed non-skull tissue conductivity values. This also avoided unstable estimation and negative conductivities for EIT conductivity estimation. However, these tissues are equally subject to variation in the literature (see Chapter 3), of which participant age, gender and measurement methodology may influence. Furthermore, skull and brain geometry, such as skull thickness and size, is also affected by participant age but was beyond the scope of the presented study, which utilised identical head geometries for all age-appropriate models. An important future avenue thus involves evaluating the influence that varying soft tissue conductivities has on EEG source estimation as well as including these unknown parameters for EIT skull and non-skull conductivity computation. Particularly imperative is including the changing head geometry as a function of participant age, alongside deviating conductivity values, and ascertaining a more accurate representation of EEG forward and inverse computations when considering age-appropriate models.

5.5.4. Research and clinical applications

The source localisation errors from the current chapter are important for both research and clinical applications. Particularly in a clinical setting, head models are typically segmented using typical MRI procedures which are unable to accurately account for compact and spongiform layers or include the sutures (Fernández-Corazza et al., 2017). Furthermore, suture closure cannot be obtained directly from CT and thus such deviation as a function of age has been omitted. As presented, this could yield source localisation errors between 2 – 4 cm, potentially crucial for resection and treatment purposes. For example, Aydin et al. (2014) revealed source localisation inaccuracies of an approximately 1.5 cm radius for epileptic spikes when the skull was considered to have a global conductivity that approximated both compact and spongiform layers into one compartment (compared to a model with distinction between the layers). This would greatly impact epilepsy resection surgeries. Further research, however, is imperative to explore real-world applications of neglecting the sutures, bone composition distribution, and aging skull conductivity. This can be done, for example, by utilising individualised, realistic, inhomogeneous skull conductivity models (as determined

through high-quality CT and EIT acquisition) on evoked and event-related EEG data to further determine their clinical and research importance. Moreover, concurrent EEG and EIT methodologies can be employed in the future to non-invasively and cost-effectively obtain individualised and inhomogeneous conductivities (i.e., using the method proposed by Fernández-Corazza et al., 2020) for such applications

The presented inverse solution calculations were also in a noiseless situation and therefore represent errors in the most optimum circumstances. In a more realistic setting, where noise (such as participant motion, physiological artifacts, and environmental interference), is expected, these errors are hypothesised to increase. Similarly, real EIT data would incur artifacts due to participant movement, physiology, and environmental factors, triggering potential inaccuracies in conductivity estimation (Lionheart, 2004). For EEG source analysis, the effect of noise is supported by Montes-Restrapo et al., (2014) where dipole estimation errors were considerably large for high levels of noise. Interestingly, the employed model accuracy was more important at lower levels of noise, where very noisy environments yielded similarly elevated errors across models. Understanding the influence of spatiotemporally correlated noise, for example incorporating spatiotemporally correlated Gaussian noise for both the EIT and EEG forward and inverse solutions is imperative for future research (Lionheart, 2004; Beltrachini et al., 2013).

5.6. Chapter Summary

The current chapter highlighted the importance skull conductivity deviation has on EEG forward solutions and source localisation. The EEG-FP and EEG-IP were solved for a true inhomogeneous skull conductivity model and compared to solutions with varying conductivities and omitting sutures, assuming homogeneous conductivity and using a hypothesised aging skull conductivity model. Significant findings are outlined below:

- Omitting the presence of adult sutures incurred large EEG source analysis inaccuracies, up to 4.14 cm, directly beneath suture lines, particularly evident for dentate sutures.
- These inaccuracies remained even when suture closure and global conductivity variation as a function of age was accounted for, particularly from 20 - 50 years old.

- When neglecting changes in spongiform and marrow proportion across the skull, and thus assuming a homogeneous model, errors were reported up to 85% in the EEG-FP and 3.03 cm in the EEG-IP.
- Assuming higher homogeneous skull conductivity increased global errors across areas of complete compact bone, such as temporal regions, whereas lower conductivity yielded greatest miscalculations across high spongiform proportion, such as the frontal region.
- Estimating equivalent homogeneous conductivity from EIT reduced such errors.
- Future research is suggested to account for the presence of sutures and incorporate a heterogeneous model, as well as employ individualised in vivo conductivity values for the skull.

CHAPTER 6. GENERAL DISCUSSION

6.1. Thesis Overview

A fundamental aspect of brain activity involves electric and induced magnetic fields generated during neurotransmission, responsible for information and stimulus processing and communication. The produced neuronal activity can provide essential knowledge regarding brain behaviour and diseases such as sleep, memory, language, and neurological disorders. EEG is a non-invasive neuroimaging technique capable of detecting electrical fields at high temporal resolution, whilst tDCS is a neuromodulatory method able to non-invasively stimulate electrical activity within the brain. Both measurement and modulation approaches are complementary and aid in informing neurophysiological processes, disorder diagnoses and treatments. Reconstructing the source of such electromagnetic activity and distribution of current involves solving the forward and ill-posed inverse problems. Accurate solutions to these problems require realistic volume conductor models incorporating precise anatomical head geometry and tissue conductivities. However, large variations in employed head models and assigned tissue conductivities exist, misspecifications of which can result in considerable forward and inverse solution errors.

The current thesis therefore delved further into aspects of head anatomy and electrical conductivity of head tissues to assess variation across literature and participants and the impact that such deviation has on neurophysiological modalities. Firstly, a systematic meta-analysis was completed to determine the variation and contributing factors in head tissue conductivities. A notable finding from this initial study was the deviation in conductivity of the skull and its inner compartments, throughout methodologies and between participant demographics. Particularly, such discrepancies as a function of age resulted noticeable. Following from this enlightenment, a simulation study was conducted to determine the impact that the proposed variation in whole skull conductivity, as a function of age, had on tDCS induced fields. As expected, tDCS induced electric field intensity significantly decreased with age due to the hypothesised decline in skull conductivity. Participant age was therefore suggested to be crucial for tDCS modelling as such changes could account for varying clinical outcomes. This indicated tDCS dose should therefore be individualised and adjusted for participant age to achieve the desired result. Alongside deviations in skull conductivity are the differences in skull anatomy that contribute to changing conductivities.

For example, the proportion of spongiform bone alters throughout the skull and the presence of adult sutures, which close at various ages, provide a path of least electrical current resistance. The impact of head geometry and homogeneous conductivity values were therefore assessed for EEG forward and inverse solutions. Omitting the adult sutures resulted in considerable localised EEG source reconstruction errors, of up to 4.14 cm, whilst neglecting deviations in spongiform and marrow bone proportion additionally instigated inaccuracies of up to 3.03 cm, although to a wider extent. Furthermore, assuming a homogeneous skull layer resulted in forward solution errors, up to 85%. These results remained when skull conductivity was considered as a function of age. Similar to conclusions stemming from tDCS simulation, individualised inhomogeneous conductivity values, accounting for skull geometry discrepancies were suggested to be essential for a most accurate EEG source reconstruction.

6.2. Summary of Findings

The current thesis aimed to illuminate the contribution that head conductivity and geometry have on electromagnetic imaging and stimulation techniques, particularly tDCS and EEG. Important and significant findings are outlined below.

Firstly, Chapter 3 systematically analysed how head tissue conductivity varies throughout the literature according to methodology and participant demographics. Research papers reporting electric conductivity of human head tissues utilising any method, below 1 kHz frequency, were evaluated and deviations according to employed methodology, temperature, condition, frequency, participant age and pathology were analysed. Each included paper was assessed for quality (see Appendix C) and reported values correspondingly adjusted to calculate weighted means and standard deviations for each tissue type. These averages were thus considered the most appropriate value according to the existing literature, when not individualising across participants. Statistics for each tissue type were found, e.g., the scalp = 0.414 ± 0.18 , whole skull = 0.016 ± 0.02 , spongiform skull layer = 0.048 ± 0.07 , whole compact skull layer = 0.005 ± 0.002 , CSF = 1.736 ± 0.3 , GM = 0.3787 ± 0.16 , WM = 0.1462 ± 0.11 S/m and BSCR = 50.4 ± 39 . Supporting previous literature, CSF conductivity was considered stable across participants and methodology, deviating only according to temperature (Baumann et al., 1997). On the other hand, scalp conductivity varied considerably. This variation, however, was found not to be explainable by anything other

than individual differences, providing the first support for the necessity of personalised head conductivity models. More realistic and detailed models consider the brain as GM and WM separately, both of which significantly deviated throughout the literature. Notably, participant pathology contributed to GM and WM variation. Alongside this, deviations according to employed methodology were not minimal. Considerable differences were revealed when utilising DTI methods, particularly according to the chosen DTI scaling factor.

An overwhelming finding from the meta-analysis was the variation across the literature and between participants for whole-skull and layered-skull conductivity values. Significant differences in skull conductivity were revealed between methodologies, for example *in vivo* measurements were generally increased, alongside those obtained with E/MEG, compared to EIT, techniques. Furthermore, deviation was found according to employed frequency. However, this relationship was unknown. Importantly, skull conductivity was further implicated to vary as a function of participant's age, supported by results in the BSCR (Figure 3.12 and Gonçalves et al., 2003a) and of layered-skull conductivity. Distinct conductivities for the spongiform and compact layers of the skull were indicated, supported by a breadth of previous research (Akhtari et al., 2000; Akhtari et al., 2002; Fernández-Corazza et al., 2017; Tang et al., 2008). This suggests a homogeneous skull is a simplification of a true skull model and thus can result in significant electromagnetic forward and inverse errors (Dannhauer et al., 2011; Haueisen et al., 1999; Haueisen et al., 2002; Ollikainen et al., 1999; Pohlmeier et al., 1997). However, even when considering a tri-layer skull, deviations remained between conductivity values. The spongiform layer in particular could be attributed to divergences in condition, temperature, frequency, pathology, and age. Contributions to these significant differences involve the presence of infant fontanelles, adult sutures (both of which close at various stages in life), head geometry, proportion of spongiform bone and bone composition variation throughout the lifespan. Thus, skull conductivity was hypothesised to decline as a function of age, as supported by previous studies (Gibson et al., 2000; Pant et al., 2011, Antonakakis et al., 2020; Hoekema et al., 2003; Wendel et al., 2010). Such discrepancies in skull conductivity can result in considerable source localisation errors for EEG (Lanfer et al., 2012; Montes-Restrepo et al., 2014; Wolters et al., 2006), MEG (Cho et al., 2015; Lau et al., 2016) and tDCS electric fields (Schmidt et al., 2015; Antonenko et al., 2021; Fernández-Corazza et al., 2017).

Following from the hypothesised contribution age has on skull conductivity and thus electromagnetic fields, Chapter 4 aimed to determine the impact this has on tDCS application. Despite previous research indicating the significant influence participant age has on electrical induced fields (Moliadze et al., 2015; Kessler et al., 2013; Ciechanski et al., 2018; Antonenko et al., 2021; Rezzaee & Dutta, 2020), none considered the contribution of skull conductivity variation as a function of age. The presented research chapter thus aimed to elucidate this by using age-specific head atlases to characterise the influence various estimated age-appropriate skull conductivity ranges has on tDCS induced fields. Six volume conductor FEM head meshes were created at ages 10, 20, 30, 40, 50 and 60 years old, from age templates based on more than 1000 images (Richards et al., 2015; 2016), using a specific head model pipeline (SimNIBS v3.1.2; Thielscher et al., 2015; Nielsen et al., 2018). Skull conductivity ranges, as a function of age, were hypothesised according to three separate research studies (see Figure 4.1): Gonçalves et al., (2003a), Antonakakis et al., (2020) and Hoekema et al., (2003). A UQ analysis determined divergences in motor cortex tDCS induced electric fields at four different intensities due to variation in skull conductivity according to the age-appropriate ranges. Soft tissue (scalp, GM, and WM) conductivities were either fixed or varied (according to Chapter 3) and these results were also compared to three fixed skull conductivity values (see Section 4.2.2. and Table 4.1. for details).

A significant negative correlation between tDCS induced electric peak fields and age was revealed for all utilised age-appropriate datasets and intensities, both when soft tissue conductivities were fixed and varied. Additionally, peak field and intensity, as well as GM volume were significantly positively correlated, whilst CSF volume and peak fields resulted in a significant negative association. This emphasises the importance of accurate head volume modelling, particularly accounting for participant age, for electrical stimulation application. Furthermore, skull thickness, at ages greater than 20, was significantly positively correlated with induced fields. Previous research has also indicated skull conductivity to deviate with skull thickness (Tang et al., 2008), thus supporting the imperative nature of accurate skull modelling and conductivity estimation for tDCS stimulation. No relationship between the focality of tDCS induced fields and age were revealed, except when soft tissue, alongside age-appropriate skull conductivity values were varied. This was expected as focality has previously been hypothesised to depend on head geometry and brain composition, rather than skull conductivity variation (Callejón et al., 2021; Laakso et al., 2015; Mikkonen et al., 2020; Fernández-Corazza et al., 2017). This finding is further

reinforced by a significant relationship between skull thickness and focality. Importantly, the presented research discovered deviation in skull, compared to soft tissue, conductivity generally became the most significant factor with increasing age, for tDCS peak fields. This insinuates aging skull conductivity to be the most influential element for the respective tDCS electric fields.

On average, across the three datasets, peak fields declined by a factor of 0.82 per decade. This, for example, was analogous to peak fields being triple in the eldest, compared to the youngest atlas when the dose was constant. Generally, the peak field for the 10-year-old model was comparable to that of the 60-year-old when employing one third of the stimulation dose. The presented results provide support for age, potentially as a result of changing skull conductivity, being a central mediator for tDCS clinical and research response. Supporting this, Moliadze and colleagues (2015) suggested the induced tDCS effect may be dependent on age, where identical dosages could initiate long-term depression changes in adults, but long-term potentiation changes in children. Individualised patient-specific dosage may therefore be essential. Such dosages could be adjusted by the suggested declining factor (of 0.82 per decade). However, it is appreciated this value is arbitrary and likely to differ across varying head models. The overwhelming findings suggest accurate and individualised head anatomy and age-appropriate skull conductivity values are fundamental for tDCS research and clinical application.

Considering the significant impact that the skull conductivity variation, particularly as a function of age, has on tDCS induced electric fields, it was hypothesised such variation would also effect EEG electrical potential propagation due to the reciprocity theorem. The previous chapter included the skull as one homogeneous layer, however, assuming it as a single conductivity compartment has resulted in significant EEG-FP and IP solution errors (Vallaghé et al., 2008; Acar et al., 2013; Chen et al., 2010; Vorwerk et al., 2019). The skull consists of three layers: a spongiform layer, sandwiched between two compact bone compartments that are less conductive than the former, the proportion of which varies throughout the skull. As well as this, sutures connect the individual skull bones and remain open at various stages of development, with differing conductivity values. The influence of these sutures was yet to be evaluated, thus Chapter 5 aimed to analyse the contribution that adult sutures had on the EEG forward and inverse solutions and their effect compared to neglecting deviations in bone composition, as well as accounting for participant's age. A

detailed realistic head model with inhomogeneous skull conductivity volumes was developed that accounted for the presence of four adult sutures and spongiform bone distribution throughout the skull. The FP (using a FEM) and IP (using sLORETA) solutions for a “true” heterogeneous skull conductivity model were compared to those omitting the sutures, neglecting bone composition distribution and homogeneous models. Aging skull conductivity volumes, accounting for suture closure with age and overall decline in skull conductivity (taken from Chapter 4) were also compared.

Omitting the presence of adult sutures resulted in the largest IP errors (a maximum of 4.14 cm) across all the comparison models, as well as considerable FP errors (maximum 68%), notably across the suture lines. These results highlight that modelling the skull sutures for adults is essential for accurate EEG-FP and IP solutions, similar to accounting for the fontanelles in infants (Lew et al., 2013; Azizollahi et al., 2016). When accounting for suture closure and overall skull conductivity variation with age, the impact of sutures remained, signifying that accounting for the skull sutures is imperative. This is firstly due to potential variation in conductivity of the sutures with participant’s age, which has not been explicitly measured. Secondly, as sutures close during different developmental stages, the impact of the sutures consequently deviate across skull regions, dependent on state of suture closure. Furthermore, the greatest FP errors were revealed across regions of high spongiform proportion. This was typically found in frontal regions, for all age-appropriate models and generally increased with age. Including variation in skull conductivity, alongside the presence of sutures and suture closure as a function of age, is therefore fundamental for the most accurate EEG-FP and IP solutions.

Considerable FP and IP solution errors also occurred when spongiform distribution across the skull was neglected, particularly evident across regions of high spongiform bone content. This emphasises the necessity of a heterogeneous skull volume, supported by previous research (Lanfer et al., 2012; Montes-Restrepo et al., 2014; Wolters et al., 2006; Dannhauer et al., 2011). Further to this, assuming homogeneous skull conductivity produced substantial errors. Of note, a high skull conductivity value (0.01 S/m) resulted in up to an 85% FP solution error, with up to 57% for a lower value (0.0055 S/m). The area of greatest error specifically depended upon bone composition, occurring within complete compact bone regions for the high homogeneous skull value and in low compact bone areas for the 0.0055 S/m skull conductivity. Importantly, EIT provided a method to estimate homogeneous

conductivity whilst minimising eccentricities due to sutures and bone composition. The global FP and IP errors were largely reduced compared to the literature assumed values, producing less concentrated inaccuracies. Utilising EIT to estimate a homogeneous skull conductivity volume may therefore be advantageous when accurate individualised heterogeneous models are unavailable (i.e., from CT data). However, the findings from Chapter 5 highlight that incorporating adult sutures and bone composition in an inhomogeneous model, particularly considering deviation according to participant age is imperative for EEG analysis, misspecification of which can have severe research and clinical consequences.

6.3. Future Directions

A prominent conclusion from the presented research is the need for individualised, *in vivo*, inhomogeneous skull conductivity values. Chapter 3 provided an overview of the existing literature examining skull conductivity, finding significant variation due to methodology and participant demographics. Chapters 4 and 5 elucidated the importance that accounting for such variation has for tDCS application and EEG analysis, respectively. Of particular note was the lack of data available for determining the relationship between skull conductivity and age, especially for a heterogeneous layer that included the skull sutures. However, the available data is insufficient, thus assumptions were made within the current thesis to account for inconsistencies and lacking measurements. Firstly, despite a breadth of research indicating that the electrical conductivity of a homogeneous skull would decline with age, for example due to changes in geometry and composition (Silau et al., 1995; Christie, 1949; Nakahara et al., 2006; Tang et al., 2008; Spence, 1990; Peyman et al., 2001; Ross et al., 1998), limited research existed specifically analysing skull conductivity with age. As discussed in Chapter 4, an association was extracted from three such studies (Gonçalves et al., 2003a; Hoekema et al., 2003; Antonakakis et al., 2020), however it is noted these papers are limited in participant numbers and complete age range. Additional, *in vivo* measurements are therefore required, for an accurate depiction of this relationship, utilising a greater number of participants stemming from infancy to older age.

Alongside this, Chapter 4 assumed such variation across a homogeneous skull, whereas it is acknowledged a one-layered skull is misrepresentative. As discussed in more detail in Chapters 3 and 5 the skull consists of multiple compartments, spongiform and compact bone,

as well as sutures, all with differing conductivities. Accounting for a heterogeneous skull model is thus essential when determining the influence of age on conductivity. EIT provided a method to estimate homogeneous skull conductivity and is suggested as one technique to minimise eccentricities due to bone composition and sutures for research and clinical application. It is a safe, cost and time effective, portable, and easy to use methodology that can be estimated during EEG acquisition (Gonçalves et al., 2000). Thus, it can be easily exploited for determining associations between age and electrical skull conductivity in large scale studies. A recent EIT protocol has further been developed which can generate inhomogeneous conductivity maps of the skull by employing injection patterns with one source and many sinks (compared to the standard of one source to one sink; Fernández-Corazza et al., 2020). In a preliminary study this novel method was able to produce reliable and accurate smooth inhomogeneous skull conductivity reconstructions that were correlated with deviations in spongiform bone distribution (Fernández-Corazza et al., 2020). This technique may therefore provide a revolutionary procedure for generating geometrically accurate, inhomogeneous skull conductivity measurements. Such an application could be utilised in the future to firstly, determine a relationship with age and secondly, enhance head modelling for tDCS and EEG research and clinical application.

Further to this, assumptions were made regarding the conductivity of adult sutures and their decrease with age. Existing research has suggested age of closure for each suture (Russell & Russell, 2018; Idriz et al., 2015; Kumar et al., 2018; Singh et al., 2004; Nakahara et al., 2006). However, conductivity at closure may not equal that of hard bone, nor decline in a sigmoid fashion. Moreover, suture conductivity is likely to differ between participants and methodologies, specifically when obtained *in vivo*, as opposed to the *in vitro* measurements utilised in Chapter 5 (Tang et al., 2008). Supplementary knowledge of suture conductivity and the progression of their closure from infancy to old age is thus vital for the most accurate representation. Complementary CT or unconventional MRI techniques using T₂ weighting (Antonakakis et al., 2020) could be employed to ascertain such information from a greater number of participants within a large age range. Moreover, four specific skull sutures were considered for the EEG analysis chapter, however additional sutures exist, typically closing during childhood and adolescence. For example, the frontal suture, running mid-line of the frontal bone, normally fuses between 3-9 months old (Vu et al., 2001), whilst the sphenosquamosal suture usually closes by 6 years, but can take as long as 10 (Idriz et al., 2015). On the other hand, the sphenofrontal suture, lying between the sphenoid bone and

posterior horizontal orbital plates, and the occipitomastoid suture, extending between the occipital bone and mastoid of temporal bone, typically close at 15 and 16 years respectively (Captier et al., 2003; Madeline & Elster, 1995). Characterising complete skull composition throughout all ages is therefore essential, particularly for tDCS application and EEG analysis in children and the elderly.

Skull thickness is an additional notable aspect of skull geometry influential to tDCS application and EEG analysis (as discussed in Chapters 4 and 5 respectively). However, the association with participant age and electrical conductivity is inconclusive. For example, skull thickness has been revealed to increase with age during early adulthood (Despotovic et al., 2013; Hansman, 1966), but this is non-linear (Li et al., 2015) and several studies have found no such a relationship (Ishida & Dodo, 1990; Lynnerup, 2001; Lynnerup, Astrup, & Sejrsen, 2005; Pensler & McCarthy, 1985; Sullivan & Smith, 1989). An inverse correlation between skull thickness and conductivity with increasing age has additionally been reported (Lai et al., 2005; Gibson et al., 2000; Antonakakis et al., 2020). This may relate to a proportion of spongiform bone increase with age (Hatipoglu et al., 2008; Sabancıoğulları et al., 2012), accompanied with inner and outer compact thinning (Skrzat et al., 2004). Such a relationship between skull thickness, age, and conductivity, however, has been insufficiently and inconsistently explored within the literature and thus no concrete conclusions can be made. Future research is therefore essential to disentangle their association, as well as the impact on tDCS induced fields and EEG analysis. One avenue of future research could employ CT with a large number of participants of varying ages and both genders, to analyse skull thickness, specifically, the differentiation between spongiform and compact bone. Alongside this, applying an EIT method would enable associations with electrical conductivity.

EIT has been suggested as providing a cost and time effective, non-invasive, and easily applicable estimation of skull conductivity (Fernández-Corazza et al., 2020; Fernández-Corazza et al., 2017, Dabek et al., 2016). Further developments of this technique as well as additional methodologies may provide complementary information. The quality and accuracy of EIT measurements are dependent on various factors such as electrode configuration, number of electrodes and injected current distribution. Such factors require consideration to provide adequate sensitivity and spatial resolution across a complete head model. Additional research could therefore explore electrode placement, number of sinks and sources, *a priori*

information regarding soft tissue conductivity and initial guesses, and computational iteration parameters, in order to fully optimise EIT conductivity estimation.

The current thesis specifically focused on the importance of skull conductivity, however accurate GM, WM, and scalp conductivity values are also essential for the most precise head models. The scalp conductivity, for example, is subject to variation between participants (Chapter 3), inaccuracies of which may impact EEG source analysis and tDCS induced fields, particularly for shallow brain regions (Gençer & Acar, 2004; Gonçalves et al., 2003a). A range of scalp conductivities were considered within the tDCS simulations (Chapter 4), but future research should aim to determine the impact that scalp conductivity also has on EEG-FP and IP analysis. Furthermore, fluctuations in GM and WM were regarded for tDCS application, but the influence on EEG analysis is not minimal. Alongside deviations throughout participants, GM and WM volume has been shown to vary with development (Giorgio et al., 2010; Groeschel et al., 2010) and pathology (Sastre-Garriga et al., 2005; Douaud et al., 2007; McAlonan et al., 2007) and can be related to conductivity (see Chapter 3). In particular, WM conductivity has been associated with deviations according to participant age (Cheng, & Alexopoulos, 2009; Schmithorst et al., 2002). Additional research is thus essential to determine GM and WM conductivity variation between participants and the respective influence on tDCS application and EEG analysis.

One such method not explored in depth in the presented thesis is DTI, which, as shown in Chapter 3, provided multiple conductivity measurements for GM and WM. DTI is an *in vivo*, non-invasive method capable of estimating the electrical conductivity tensor from diffusion tensor eigenvalues measured with diffusion-weighted MRI (Tuch et al., 1999). Notably, this technique can account for anisotropy within tissues, which was neglected in the current thesis. Previous research has indicated that overlooking WM anisotropy resulted in significant EEG localisation (Anwander et al., 2002; Gullmar et al., 2010), tDCS (Schmidt et al., 2015; Ciechanski et al., 2018), especially for deep sources, and TMS induced fields (De Lucia et al., 2007) errors. Future research could therefore incorporate discrepancies in GM and WM conductivity according to DTI measured anisotropy for electromagnetic imaging methods. As discussed in Chapter 3 (Section 3.5.5ii), however, there are different anisotropic conductivity models of WM based on DTI (as reviewed in Wu et al., 2018). Thus, care should be taken when estimating conductivity from diffusion measurements and additional research is required to determine the optimal transformation.

Further to this, the skull can also be considered as anisotropic, with increased conductivity in tangential compared to radial directions (Law, 1993). Not accounting for this anisotropy has resulted in significant EEG forward and inverse solution errors (Marin et al., 1998; Chauveau et al., 2004; Hallez et al., 2005). Skull anisotropy may be determined using layered isotropic elements with an anisotropy ratio, as described in detail in Sadleir and Argibay (2008). Future research could thus include skull anisotropy, particularly alongside accurate inhomogeneity to ascertain the impact on EEG analysis and tDCS induced fields. The importance of incorporating a heterogeneous layered skull, however, is acknowledged in more recent research, therefore inclusion of skull anisotropy may not be necessary. Additional research is hence required to establish its usefulness, particularly when individualised, *in vivo*, heterogeneous skull conductivities are considered.

The inclusion of additional tissues, such as the meninges, blood vessels, fat, and muscle, as well as lesions and brain atrophy were also neglected for tDCS induced field and EEG analysis but, have previously been found to impact such investigations, although to a lesser degree (Jiang et al., 2020; Fiederer et al., 2016; Laakso et al., 2015). Alongside this, CSF is also frequently overestimated within head modelling, due to including the blood vessels and meninges as CSF and can equally result in notable errors (Jiang et al., 2020). As discussed in Section 4.5.2., additional research is therefore necessary to elucidate the importance of accounting for these additional tissues, as well as accurately segmenting CSF, for example using tetrahedral FEM discretisations (Beltrachini et al., 2018). The presence of lesions and brain atrophy is increasingly likely with participant age and hence may therefore be progressively critical to include for both EEG and tDCS evaluations.

Following from Chapter 4, a supplementary essential avenue for research is determining the optimum solution for the effect of age on tDCS. The current thesis suggested a scaling factor of 0.82 per decade which could be related to applied dosage. However, as discussed in Section 4.5.2. this value is arbitrary and subject to large uncertainties throughout participants. The use of a scaling factor was supported by Datta and colleagues (2011), thus larger scale studies incorporating true head models and individualised, *in vivo* conductivities could be employed to inform such a value more accurately. Alternatively, when equipment and time permitting, tDCS simulation utilising these individualised head conductivity models could be employed prior to tDCS application. Adjusting the tDCS dose appropriately has been relatively unexplored but remains fundamental for future tDCS clinical and research

application. Alongside this, examining the influence of tDCS electrode size and placement was beyond the scope of the current thesis, however forthcoming modelling analyses could explore their effect on tDCS induced fields, in combination with age-appropriate geometry and conductivity.

Due to the reciprocity theorem and dual relationship between tDCS and EEG, a further and informative aspect of research would be analogous tDCS and EEG monitoring. Combining such complementary modalities can enlighten additional aspects of brain function. For example, concurrent analysis can aid in revealing the underlying biological mechanisms behind both tDCS and EEG, as well as the in-depth effect of skull conductivity and its relationship with electric current. Concurrent tDCS and MEG has also previously been employed to derive conclusions on the cortical mechanisms of tDCS (Hanley et al., 2016) and evidence the ability of MEG for characterising tDCS induced brain changes (McGonigle et al., 2015). Further to this, the presented thesis focused on application to electrical imaging methods. However, the effect of conductivity on magnetic fields is not minimal. For example, existing research has revealed significant effects on TMS induced fields when neglecting WM anisotropy (De Lucia et al., 2007) and inaccurate GM/WM conductivity (Saturnino et al., 2019) and MEG analysis when employing inaccurate GM and WM (Wolters et al., 2006; Gençer et al., 2004; Güllmar et al., 2010), skull (Cho et al., 2015; Lau et al., 2016) and scalp (Gençer et al., 2004) conductivities. Further research should therefore attempt to disentangle the relationship between soft and hard tissue conductivities and TMS/MEG analysis, particularly when age is taken into consideration.

6.4. Overall Conclusion

The presented thesis aimed to determine the influence that variability in head tissue electrical conductivity had on corresponding electrical brain imaging research. A systematic meta-analysis revealed electrical conductivity, predominantly of the scalp, skull, GM, and WM deviated according to both participant demographics and employed methodology. The variation of skull conductivity was of particular note, consisting of multiple layers and associated with participant age. Correspondingly, the proposed decline in homogeneous skull conductivity as a function of age resulted in reduced tDCS induced fields, leading to the suggestion tDCS dosages should be individualised, particularly to account for participant age. Following from this, accounting for the presence of adult sutures and proportion in

spongiform and compact bone distribution throughout the skull, was found to be vitally important in EEG analysis. Omitting the sutures, deviations in bone composition, and assuming various homogeneous skull conductivity values resulted in considerable EEG forward and inverse solution errors, discrepancies of which remained even when accounting for age.

The overwhelming conclusion from the presented research is the imperative nature of incorporating geometrically accurate and precise volume conductors for the skull. Not accounting for its heterogeneity, including sutures, bone composition and deviations according to participant demographics can result in significant tDCS and EEG analysis errors. The sutures, all of which vary in closure rate and deviate between participants, which in turn effects their conductivity, are vital within head modelling methodologies but are frequently omitted. Furthermore, the influence of participant age is imperative for accurate skull conductivity values, however existing data is limited. Additional measurements are required to ascertain such a relationship between homogeneous skull conductivity values, the conductivity of the sutures, deviations in spongiform and compact bone thickness and conductivity and participant age. It is suggested that research involving both tDCS and EEG should include *in vivo*, individualised skull conductivity values and head geometries, through for example, EIT and MRI acquisition, respectively, for the most accurate representation and analysis.

REFERENCES

- Acar, Z. A., & Makeig, S. (2013). Effects of forward model errors on EEG source localization. *Brain topography*, 26(3), 378-396.
- Acar, Z. A., Ortiz-Mantilla, S., Benasich, A., & Makeig, S. (2016). High-resolution EEG source imaging of one-year-old children. In *2016 38th Annual International Conference of the IEEE Engineering in Medicine and Biology Society (EMBC)* (pp. 117-120). IEEE.
- Agarwal, S. M., Shivakumar, V., Bose, A., Subramaniam, A., Nawani, H., Chhabra, H., ... & Venkatasubramanian, G. (2013). Transcranial direct current stimulation in schizophrenia. *Clinical Psychopharmacology and Neuroscience*, 11(3), 118.
- Ahlfors, S. P., Han, J., Belliveau, J. W., & Hämäläinen, M. S. (2010). Sensitivity of MEG and EEG to source orientation. *Brain topography*, 23(3), 227-232.
- Akhtari, M., Bryant, H. C., Mamelak, A. N., Heller, L., Shih, J. J., Mandelkern, M., . . . Sutherling, W. W. (2000). Conductivities of three-layer human skull. *Brain Topography*, 13(1), 29-42.
- Akhtari, M., Bryant, H. C., Marnelak, A. N., Flynn, E. R., Heller, L., Shih, J. J., . . . Sutherling, W. W. (2002). Conductivities of three-layer live human skull. *Brain Topography*, 14(3), 151-167.
- Akhtari, M., Bryant, H., Emin, D., Merrifield, W., Mamelak, A., Flynn, E., . . . Ranken, D. (2003). A model for frequency dependence of conductivities of the live human skull. *Brain Topography*, 16(1), 39-55.
- Akhtari, M., Emin, D., Ellingson, B. M., Woodworth, D., Frew, A., & Mathern, G. W. (2016). Measuring the local electrical conductivity of human brain tissue. *Journal of Applied Physics*, 119(6).
- Akhtari, M., Mandelkern, M., Bui, D., Salamon, N., Vinters, H. V., & Mathern, G. W. (2010). Variable Anisotropic Brain Electrical Conductivities in Epileptogenic Foci. *Brain Topography*, 23(3), 292-300.
- Akhtari, M., Salamon, N., Duncan, R., Fried, I., & Mathern, G. W. (2006). Electrical conductivities of the freshly excised cerebral cortex in epilepsy surgery patients; Correlation with pathology, seizure duration, and diffusion tensor imaging. *Brain Topography*, 18(4), 281-290.
- Amatachaya, A., Auvichayapat, N., Patjanasontorn, N., Suphakunpinyo, C., Ngernyam, N., Aree-Uea, B., ... & Auvichayapat, P. (2014). Effect of anodal transcranial direct

- current stimulation on autism: a randomized double-blind crossover trial. *Behavioural neurology*, 2014.
- André, S., Heinrich, S., Kayser, F., Menzler, K., Kesselring, J., Khader, P. H., ... & Mylius, V. (2016). At-home tDCS of the left dorsolateral prefrontal cortex improves visual short-term memory in mild vascular dementia. *Journal of the neurological sciences*, 369, 185-190.
- Antonakakis, M., Oostenveld, R., Wellmer, J., Möddel, G., Haueisen, J., Rampp, S., & Wolters, C. (2018). Age-related skull conductivity estimated by a calibration procedure using combined somatosensory evoked potentials and fields on realistic head models. Paper presented at *50 years of MEG, ISACM/EMEGS conference*, April 2018, Poros, Greece.
- Antonakakis, M., Schrader, S., Aydin, Ü., Khan, A., Gross, J., Zervakis, M., ... & Wolters, C. H. (2020). Inter-subject variability of skull conductivity and thickness in calibrated realistic head models. *Neuroimage*, 223, 117353.
- Antonenko, D., Grittner, U., Saturnino, G., Nierhaus, T., Thielscher, A., & Flöel, A. (2021). Inter-individual and age-dependent variability in simulated electric fields induced by conventional transcranial electrical stimulation. *NeuroImage*, 224, 117413.
- Anwander, A., Wolters, C. H., Dümpelmann, M., & Knösche, T. (2002). *Influence of realistic skull and white matter anisotropy on the inverse problem in EEG/MEG-source localization*. Paper presented at the *Proceedings of The 13th International Conference on Biomagnetism*
- Arnould-Taylor, W. (1998). *A textbook of anatomy and physiology*. Nelson Thornes.
- Aubert-Broche, B., Evans, A. C., & Collins, L. (2006). A new improved version of the realistic digital brain phantom. *NeuroImage*, 32(1), 138-145.
- Avery, J., Dowrick, T., Faulkner, M., Goren, N., & Holder, D. (2017). A versatile and reproducible multi-frequency electrical impedance tomography system. *Sensors*, 17(2), 280.
- Awada, K. A., Jackson, D. R., Baumann, S. B., Williams, J. T., Wilton, D. R., Fink, P. W., & Prasky, B. R. (1998). Effect of conductivity uncertainties and modeling errors on EEG source localization using a 2-D model. *IEEE Transactions on Biomedical Engineering*, 45(9), 1135-1145.
- Aydin, Ü., Rampp, S., Wollbrink, A., Kugel, H., Cho, J.-H., Knösche, T. R., . . . Wolters, C. (2017). Zoomed MRI guided by combined EEG/MEG source analysis: a multimodal

- approach for optimizing presurgical epilepsy work-up and its application in a multi-focal epilepsy patient case study. *Brain topography*, 30(4), 417-433.
- Aydin, Ü., Vorwerk, J., Kupper, P., Heers, M., Kugel, H., Galka, A., . . . Wolters, C. H. (2014). Combining EEG and MEG for the Reconstruction of Epileptic Activity Using a Calibrated Realistic Volume Conductor Model. *Plos One*, 9(3).
- Azevedo, F. A., Carvalho, L. R., Grinberg, L. T., Farfel, J. M., Ferretti, R. E., Leite, R. E., ... & Herculano-Houzel, S. (2009). Equal numbers of neuronal and nonneuronal cells make the human brain an isometrically scaled-up primate brain. *Journal of Comparative Neurology*, 513(5), 532-541.
- Azizollahi, H., Aarabi, A., & Wallois, F. (2016). Effects of uncertainty in head tissue conductivity and complexity on EEG forward modeling in neonates. *Human brain mapping*, 37(10), 3604-3622.
- Azizollahi, H., Aarabi, A., & Wallois, F. (2020). Effect of structural complexities in head modeling on the accuracy of EEG source localization in neonates. *Journal of Neural Engineering*, 17(5), 056004.
- Baillet, S., Mosher, J. C., & Leahy, R. M. (2001). Electromagnetic brain mapping. *IEEE Signal processing magazine*, 18(6), 14-30.
- Baillet, S., Riera, J. J., Marin, G., Mangin, J. F., Aubert, J., & Garnero, L. (2001). Evaluation of inverse methods and head models for EEG source localization using a human skull phantom. *Physics in medicine and biology*, 46(1), 77-96.
- Bandeira, I. D., Guimarães, R. S. Q., Jagersbacher, J. G., Barretto, T. L., de Jesus-Silva, J. R., Santos, S. N., ... & Lucena, R. (2016). Transcranial direct current stimulation in children and adolescents with attention-deficit/hyperactivity disorder (ADHD) a pilot study. *Journal of child neurology*, 31(7), 918-924.
- Barber, D. C., & Brown, B. H. (1984). Applied potential tomography. *Journal of Physics E: Scientific Instruments*, 19(9), 220-223.
- Bashar, M. (2011). *Tissue conductivity based human head model study for EEG* (Doctoral dissertation, University of Southern Queensland).
- Batsikadze, G., Moliadze, V., Paulus, W., Kuo, M. F., & Nitsche, M. A. (2013). Partially non-linear stimulation intensity-dependent effects of direct current stimulation on motor cortex excitability in humans. *The Journal of physiology*, 591(7), 1987-2000.
- Baumann, S. B., Wozny, D. R., Kelly, S. K., & Meno, F. M. (1997). The electrical conductivity of human cerebrospinal fluid at body temperature. *Ieee Transactions on Biomedical Engineering*, 44(3), 220-223.

- Bayford, R. H., Gibson, A., Tizzard, A., Tidswell, A. T., & Holder, D. S. (2001). Solving the forward problem for the human head using IDEAS (Integrated Design Engineering Analysis Software) a finite element modelling tool. *Physiol. Meas*, 22(1), 55-63.
- Baysal, U., & Haueisen, J. (2004). Use of a priori information in estimating tissue resistivities - application to human data in vivo. *Physiological Measurement*, 25(3), 737-748.
- Bean, A. J. (Ed.). (2006). *Protein trafficking in neurons*. Elsevier.
- Bear, M. F., Connors, B. W., & Paradiso, M. A. (2001). *Neuroscience: Exploring the Brain*. Jones & Bartlett Learning, LLC.
- Beltrachini, L. (2018). A finite element solution of the forward problem in EEG for multipolar sources. *IEEE Transactions on Neural Systems and Rehabilitation Engineering*, 27(3), 368-377.
- Beltrachini, L. (2018). Sensitivity of the projected subtraction approach to mesh degeneracies and its impact on the forward problem in EEG. *IEEE Transactions on Biomedical Engineering*, 66(1), 273-282.
- Beltrachini, L. (2019). The analytical subtraction approach for solving the forward problem in EEG. *Journal of neural engineering*, 16(5), 056029.
- Beltrachini, L., Von Ellenrieder, N., & Muravchik, C. H. (2013). Shrinkage approach for spatiotemporal EEG covariance matrix estimation. *IEEE Transactions on Signal Processing*, 61(7), 1797-1808.
- Bénar, C. G., & Gotman, J. (2002). Modeling of post-surgical brain and skull defects in the EEG inverse problem with the boundary element method. *Clinical Neurophysiology*, 113(1), 48-56.
- Benjamini, Y., & Hochberg, Y. (1995). Controlling the false discovery rate: a practical and powerful approach to multiple testing. *Journal of the Royal statistical society: series B (Methodological)*, 57(1), 289-300.
- Benning, M., & Burger, M. (2018). Modern regularization methods for inverse problems. *arXiv preprint arXiv:1801.09922*.
- Berényi, A., Belluscio, M., Mao, D., & Buzsáki, G. (2012). Closed-loop control of epilepsy by transcranial electrical stimulation. *Science*, 337(6095), 735-737.
- Biot, G., Albera, L., Wendling, F., & Merlet, I. (2011). Localization of extended brain sources from EEG/MEG: the ExSo-MUSIC approach. *NeuroImage*, 56(1), 102-113.
- Biot, G., Spinelli, L., Vulliémoz, S., Mégevand, P., Brunet, D., Seeck, M., & Michel, C. M. (2014). Head model and electrical source imaging: a study of 38 epileptic patients. *NeuroImage: Clinical*, 5, 77-83.

- Bodenstein, M., David, M., & Markstaller, K. (2009). Principles of electrical impedance tomography and its clinical application. *Critical Care Medicine*, 37(2), 713-724.
- Borenstein, M., Hedges, L. V., Higgins, J. P., & Rothstein, H. R. (2011). *Introduction to meta-analysis*: John Wiley & Sons.
- Bozzali, M., Falini, A., Franceschi, M., Cercignani, M., Zuffi, M., Scotti, G., . . . Filippi, M. (2002). White matter damage in Alzheimer's disease assessed in vivo using diffusion tensor magnetic resonance imaging. *Journal of Neurology, Neurosurgery & Psychiatry*, 72(6), 742-746.
- Brette, R., & Destexhe, A. (2012). Handbook of neural activity measurement. *Cambridge University Press*.
- Brodbeck, V., Spinelli, L., Lascano, A. M., Wissmeier, M., Vargas, M.-I., Vulliemoz, S., . . . Seeck, M. (2011). Electroencephalographic source imaging: a prospective study of 152 operated epileptic patients. *Brain*, 134(10), 2887-2897.
- Brunoni, A. R., Fregni, F., Priori, A., Ferrucci, R., & Boggio, P. S. (2013). Transcranial direct current stimulation: challenges, opportunities, and impact on psychiatry and neurorehabilitation. *Frontiers in psychiatry*, 4, 19.
- Burger, H. C., & van Milaan, J. B. (1943). Measurements of the specific resistance of the human body to direct current. *Acta Medica Scandinavica*, 114(6), 584-607.
- Burger, H., & Van Dongen, R. (1961). Specific electric resistance of body tissues. *Physics in Medicine & Biology*, 5(4), 431.
- Burgess, R. C. (2020). Recognizing and correcting MEG artifacts. *Journal of Clinical Neurophysiology*, 37(6), 508-517.
- Burton, E. J., McKeith, I. G., Burn, D. J., Firbank, M. J., & O'Brien, J. T. (2006). Progression of white matter hyperintensities in Alzheimer disease, dementia with lewy bodies, and Parkinson disease dementia: a comparison with normal aging. *The American journal of geriatric psychiatry*, 14(10), 842-849.
- Butson, C. R., Cooper, S. E., Henderson, J. M., & McIntyre, C. C. (2007). Patient-specific analysis of the volume of tissue activated during deep brain stimulation. *Neuroimage*, 34(2), 661-670.
- Bystron, I., Blakemore, C., & Rakic, P. (2008). Development of the human cerebral cortex: Boulder Committee revisited. *Nature Reviews Neuroscience*, 9(2), 110.
- Callejón-Leblic, M. A., & Miranda, P. C. (2021). A comprehensive analysis of the impact of head model extent on electric field predictions in transcranial current stimulation. *Journal of Neural Engineering*, 18(4), 046024.

- Campbell, I. G., Grimm, K. J., De Bie, E., & Feinberg, I. (2012). Sex, puberty, and the timing of sleep EEG measured adolescent brain maturation. *Proceedings of the National Academy of Sciences*, *109*(15), 5740-5743.
- Captier, G., Cristol, R., Montoya, P., Prudhomme, M., & Godlewski, G. (2003). Prenatal organization and morphogenesis of the sphenofrontal suture in humans. *Cells Tissues Organs*, *175*(2), 98-104.
- Cervantes, G. A. (2016). *Technical fundamentals of radiology and CT*. IOP Publishing.
- Chatterjee, S., Thakur, R. S., Yadav, R. N., Gupta, L., & Raghuvanshi, D. K. (2020). Review of noise removal techniques in ECG signals. *IET Signal Processing*, *14*(9), 569-590.
- Chauhan, M., Indahlastari, A., Kasinadhuni, A. K., Schär, M., Mareci, T. H., & Sadleir, R. J. (2018). Low-frequency conductivity tensor imaging of the human head in vivo using DT-voi: first study. *IEEE transactions on medical imaging*, *37*(4), 966-976.
- Chauveau, N., Franceries, X., Doyon, B., Rigaud, B., Morucci, J. P., & Celsis, P. (2004). Effects of skull thickness, anisotropy, and inhomogeneity on forward EEG/ERP computations using a spherical three-dimensional resistor mesh model. *Human brain mapping*, *21*(2), 86-97.
- Chen, F., Hallez, H., & Staelens, S. (2010). Influence of skull conductivity perturbations on EEG dipole source analysis. *Medical physics*, *37*(8), 4475-4484.
- Chiba, F., Makino, Y., Motomura, A., Inokuchi, G., Torimitsu, S., Ishii, N., ... & Iwase, H. (2013). Age estimation by multidetector CT images of the sagittal suture. *International journal of legal medicine*, *127*(5), 1005-1011.
- Cho, J.-H., Vorwerk, J., Wolters, C. H., & Knösche, T. R. (2015). Influence of the head model on EEG and MEG source connectivity analyses. *Neuroimage*, *110*, 60-77.
- Christie, A. (1949). Prevalence and distribution of ossification centers in the newborn infant. *American Journal of Diseases of Children*, *77*(3), 355-361.
- Ciechanski, P., Carlson, H. L., Yu, S. S., & Kirton, A. (2018). Modeling transcranial direct-current stimulation-induced electric fields in children and adults. *Frontiers in human neuroscience*, *12*, 268.
- Clerc, M., Adde, G., Kybic, J., Papadopoulo, T., & Badier, J.-M. (2005). In vivo conductivity estimation with symmetric boundary elements. *International Journal of Bioelectromagnetism*, *7*, 307-310.
- Clerc, M., Leblond, J., Marmorat, J. P., & Papadopoulo, T. (2012). Source localization using rational approximation on plane sections. *Inverse Problems*, *28*(5), 055018.

- Cohen, D., & Cuffin, B. N. (1983a). Demonstration of useful differences between magnetoencephalogram and electroencephalogram. *Electroencephalography and Clinical Neurophysiology*, 56(1), 38-51.
- Cohen, D., & Cuffin, B. N. (1983b). Demonstration of useful differences between magnetoencephalogram and electroencephalogram. *Electroencephalography and Clinical Neurophysiology*, 56(1), 38-51.
- Compta, Y., Ibarretxe-Bilbao, N., Pereira, J. B., Junqué, C., Bargalló, N., Tolosa, E., . . . Buongiorno, M. (2012). Grey matter volume correlates of cerebrospinal markers of Alzheimer-pathology in Parkinson's disease and related dementia. *Parkinsonism & related disorders*, 18(8), 941-947.
- Corp, I. (2013). IBM SPSS statistics for Macintosh. *Version 22.0*.
- Costa, F., Batatia, H., Oberlin, T., d'Giano, C., & Tourneret, J. Y. (2017). Bayesian EEG source localization using a structured sparsity prior. *NeuroImage*, 144, 142-152.
- Croarkin, P. E., Nakonezny, P. A., Lewis, C. P., Zaccariello, M. J., Huxsahl, J. E., Husain, M. M., ... & Daskalakis, Z. J. (2014). Developmental aspects of cortical excitability and inhibition in depressed and healthy youth: an exploratory study. *Frontiers in human neuroscience*, 8, 669.
- Croarkin, P. E., Wall, C. A., & Lee, J. (2011). Applications of transcranial magnetic stimulation (TMS) in child and adolescent psychiatry. *International Review of Psychiatry*, 23(5), 445-453.
- Cuffin, B. N. (1990). Effects of head shape on EEGs and MEGs. *IEEE Transactions on Biomedical Engineering*, 37(1), 44-52.
- Cuffin, B. N., & Cohen, D. (1977). Magnetic fields of a dipole in special volume conductor shapes. *IEEE Transactions on Biomedical Engineering*, (4), 372-381.
- Cvetković, M., Poljak, D., Rogić Vidaković, M., & Đogaš, Z. (2016). Transcranial magnetic stimulation induced fields in different brain models. *Journal of Electromagnetic Waves and Applications*, 30(14), 1820-1835.
- Da Silva, F. L. (2009). EEG: origin and measurement. In *EEG-fMRI* (pp. 19-38). Springer, Berlin, Heidelberg.
- Dabek, J., Kalogianni, K., Rotgans, E., van der Helm, F. C. T., Kwakkel, G., van Wegen, E. E. H., . . . de Munck, J. C. (2016). Determination of head conductivity frequency response in vivo with optimized EIT-EEG. *Neuroimage*, 127, 484-495.
- Dale, B. M., Brown, M. A., & Semelka, R. C. (2015). *MRI: basic principles and applications*. John Wiley & Sons.

- Dannhauer, M., Lanfer, B., Wolters, C. H., & Knosche, T. R. (2011). Modeling of the Human Skull in EEG Source Analysis. *Human Brain Mapping*, 32(9), 1383-1399.
- Darbas, M., Diallo, M. M., El Badia, A., & Lohrengel, S. (2019). An inverse dipole source problem in inhomogeneous media: application to the EEG source localization in neonates. *Journal of Inverse and Ill-posed Problems*, 27(2), 255-281.
- Darvas, F., Pantazis, D., Kucukaltun-Yildirim, E., & Leahy, R. M. (2004). Mapping human brain function with MEG and EEG: methods and validation. *NeuroImage*, 23, S289-S299.
- Datta, A., Baker, J. M., Bikson, M., & Fridriksson, J. (2011). Individualized model predicts brain current flow during transcranial direct-current stimulation treatment in responsive stroke patient. *Brain stimulation*, 4(3), 169-174.
- Datta, A., Thomas, C., Huang, Y., & Venkatasubramanian, G. (2018). Exploration of the effect of race on cortical current flow due to transcranial direct current stimulation: comparison across Caucasian, Chinese, and Indian Standard Brains. In *2018 40th Annual International Conference of the IEEE Engineering in Medicine and Biology Society (EMBC)*(pp. 2341-2344). IEEE.
- Datta, A., Zhou, X., Su, Y., Parra, L. C., & Bikson, M. (2013). Validation of finite element model of transcranial electrical stimulation using scalp potentials: implications for clinical dose. *Journal of neural engineering*, 10(3), 036018.
- De Lucia, M., Parker, G. J. M., Embleton, K., Newton, J. M., & Walsh, V. (2007). Diffusion tensor MRI-based estimation of the influence of brain tissue anisotropy on the effects of transcranial magnetic stimulation. *Neuroimage*, 36(4), 1159-1170.
- De Munck, J. C. (1988). The potential distribution in a layered anisotropic spheroidal volume conductor. *Journal of applied Physics*, 64(2), 464-470
- De Munck, J. C., & Peters, M. J. (1993). A fast method to compute the potential in the multisphere model. *IEEE Trans. Biomed. Eng.*, 40(11), 1166-1174
- De Munck, J. C., Van Dijk, B. W., & Spekreijse, H. E. N. K. (1988). Mathematical dipoles are adequate to describe realistic generators of human brain activity. *IEEE transactions on biomedical engineering*, 35(11), 960-966.
- Debanne, D., Campanac, E., Bialowas, A., Carlier, E., & Alcaraz, G. (2011). Axon physiology. *Physiological reviews*, 91(2), 555-602.
- Delye, H., Clijmans, T., Mommaerts, M. Y., Sloten, J. V., & Goffin, J. (2015). Creating a normative database of age-specific 3D geometrical data, bone density, and bone

- thickness of the developing skull: a pilot study. *Journal of Neurosurgery: Pediatrics*, 16(6), 687-702.
- Deng, Z. D., Lisanby, S. H., & Peterchev, A. V. (2013). Electric field depth–focality tradeoff in transcranial magnetic stimulation: simulation comparison of 50 coil designs. *Brain stimulation*, 6(1), 1-13.
- Despotovic, I., Cherian, P. J., De Vos, M., Hallez, H., Deburchgraeve, W., Govaert, P., . . . Vansteenkiste, E. (2013). Relationship of EEG sources of neonatal seizures to acute perinatal brain lesions seen on MRI: a pilot study. *Human brain mapping*, 34(10), 2402-2417.
- Ding, L., & Yuan, H. (2012). Inverse source imaging methods in recovering distributed brain sources. *Biomedical Engineering Letters*, 2(1), 2-7.
- Dmochowski, J. P., Datta, A., Bikson, M., Su, Y., & Parra, L. C. (2011). Optimized multi-electrode stimulation increases focality and intensity at target. *Journal of neural engineering*, 8(4), 046011.
- Dmochowski, J. P., Koessler, L., Norcia, A. M., Bikson, M., & Parra, L. C. (2017). Optimal use of EEG recordings to target active brain areas with transcranial electrical stimulation. *Neuroimage*, 157, 69-80.
- Dobbing, J., & Sands, J. (1973). Quantitative growth and development of human brain. *Archives of disease in childhood*, 48(10), 757-767.
- Douaud, G., Smith, S., Jenkinson, M., Behrens, T., Johansen-Berg, H., Vickers, J., . . . Matthews, P. M. (2007). Anatomically related grey and white matter abnormalities in adolescent-onset schizophrenia. *Brain*, 130(9), 2375-2386.
- Douw, L., Nieboer, D., Stam, C. J., Tewarie, P., & Hillebrand, A. (2018). Consistency of magnetoencephalographic functional connectivity and network reconstruction using a template versus native MRI for co-registration. *Human brain mapping*, 39(1), 104-119.
- Elder, G. J., & Taylor, J. P. (2014). Transcranial magnetic stimulation and transcranial direct current stimulation: treatments for cognitive and neuropsychiatric symptoms in the neurodegenerative dementias?. *Alzheimer's research & therapy*, 6(5), 1-11.
- Engel, J. (2013). *Seizures and epilepsy* (Vol. 83). Oxford University Press.
- Eriksen, K. J. (1990). *In vivo human head regional conductivity estimation using a three-sphere model*. Paper presented at the Engineering in Medicine and Biology Society, 1990., Proceedings of the Twelfth Annual International Conference of the IEEE.

- Essaki Arumugam EM, Turovets S, Price N, Rech D, Luu P, Tucker D (2017) In-vivo estimation of the scalp and skull conductivity using bEIT for non-invasive neuroimaging and stimulation. In: June 2017 conference: brain stimulation and imaging meeting, Vancouver, BC.
- Evans, A. C. (2006). Brain Development Cooperative Group The NIH MRI study of normal brain development. *Neuroimage*, 30(1), 184-202.
- Evans, A. C., Janke, A. L., Collins, D. L., & Baillet, S. (2012). Brain templates and atlases. *Neuroimage*, 62(2), 911-922.
- Fabrizi, L., Sparkes, M., Horesh, L., Abascal, J., McEwan, A., Bayford, R. H., . . . Holder, D. S. (2006). Factors limiting the application of electrical impedance tomography for identification of regional conductivity changes using scalp electrodes during epileptic seizures in humans. *Physiological Measurement*, 27(5), S163-S174.
- Faes, T. J. C., van der Meij, H. A., de Munck, J. C., & Heethaar, R. M. (1999). The electric resistivity of human tissues (100 Hz-10 MHz): a meta-analysis of review studies. *Physiological Measurement*, 20(4), R1-R10.
- Fang, Q., & Boas, D. A. (2009). Tetrahedral mesh generation from volumetric binary and grayscale images. In *2009 IEEE International Symposium on Biomedical Imaging: From Nano to Macro* (pp. 1142-1145). Ieee.
- Farahibozorg, S. R., Henson, R. N., & Hauk, O. (2018). Adaptive cortical parcellations for source reconstructed EEG/MEG connectomes. *NeuroImage*, 169, 23-45.
- Fernández-Corazza, M., Beltrachini, L., Von Ellenrieder, N., & Muravchik, C. H. (2013). Analysis of parametric estimation of head tissue conductivities using electrical impedance tomography. *Biomedical Signal Processing and Control*, 8(6), 830-837.
- Fernández-Corazza, M., Turovets, S., & Muravchik, C. H. (2020). A novel bounded EIT protocol to generate inhomogeneous skull conductivity maps non-invasively. In *2020 42nd Annual International Conference of the IEEE Engineering in Medicine & Biology Society (EMBC)* (pp. 1440-1443). IEEE.
- Fernández-Corazza, M., Turovets, S., Luu, P., & Tucker, D. (2015). Optimization in transcranial electrical neuromodulation based on the reciprocity principle. *Brain Stimulation: Basic, Translational, and Clinical Research in Neuromodulation*, 8(2), 403.
- Fernández-Corazza, M., Turovets, S., Luu, P., Anderson, E., & Tucker, D. (2016). Transcranial electrical neuromodulation based on the reciprocity principle. *Frontiers in psychiatry*, 7, 87.

- Fernández-Corazza, M., Turovets, S., Luu, P., Anderson, E., & Tucker, D. (2016). Transcranial electrical neuromodulation based on the reciprocity principle. *Frontiers in psychiatry*, 7, 87.
- Fernández-Corazza, M., Turovets, S., Luu, P., Price, N., Muravchik, C. H., & Tucker, D. (2017). Skull modeling effects in conductivity estimates using parametric electrical impedance tomography. *IEEE Transactions on Biomedical Engineering*, 65(8), 1785-1797.
- Fiederer, L. D. J., Vorwerk, J., Lucka, F., Dannhauer, M., Yang, S., Dümpelmann, M., . . . Wolters, C. H. (2016). The role of blood vessels in high-resolution volume conductor head modeling of EEG. *NeuroImage*, 128, 193-208.
- Fiedler, P., Haueisen, J., Jannek, D., Griebel, S., Zentner, L., Vaz, F., & Fonseca, C. (2014). Comparison of three types of dry electrodes for electroencephalography. *Acta Imeko*, 3(3), 33-37.
- Fieseler, T. (1999). *Analytic Source and Volume Conductor Models for Biomagnetic Fields* (Doctoral dissertation, Verlag nicht ermittelbar).
- Fillmore, P. T., Phillips-Meek, M. C., & Richards, J. E. (2015). Age-specific MRI brain and head templates for healthy adults from 20 through 89 years of age. *Frontiers in aging neuroscience*, 7, 44.
- Fischl, B. (2012). FreeSurfer. *Neuroimage*, 62(2), 774-781.
- Fishman, R. A. (1992). *Cerebrospinal fluid in diseases of the nervous system*: Saunders Philadelphia.
- Fitzgerald PB, Fountain S, Daskalakis ZJ (2006). A comprehensive review of the effects of rTMS on motor cortical excitability and inhibition. *Clinical Neurophysiology*. 117 (12): 2584–96.
- Flemming, L., Wang, Y., Caprihan, A., Eiselt, M., Haueisen, J., & Okada, Y. (2005). Evaluation of the distortion of EEG signals caused by a hole in the skull mimicking the fontanel in the skull of human neonates. *Clinical neurophysiology*, 116(5), 1141-1152.
- Flöel, A. (2014). tDCS-enhanced motor and cognitive function in neurological diseases. *Neuroimage*, 85, 934-947.
- Forssell, M., Goswami, C., Krishnan, A., Chamanzar, M., & Grover, P. (2021). Effect of skull thickness and conductivity on current propagation for noninvasively injected currents. *Journal of Neural Engineering*.

- Fox, P. T., Narayana, S., Tandon, N., Sandoval, H., Fox, S. P., Kochunov, P., & Lancaster, J. L. (2004). Column-based model of electric field excitation of cerebral cortex. *Human brain mapping*, 22(1), 1-14.
- Frank, E., Wilfurth, S., Landgrebe, M., Eichhammer, P., Hajak, G., & Langguth, B. (2009). Anodal skin lesions after treatment with transcranial direct current stimulation. *Brain stimulation*, 3(1), 58-59.
- Frantseva, M., Cui, J., Farzan, F., Chinta, L. V., Velazquez, J. L. P., & Daskalakis, Z. J. (2014). Disrupted Cortical Conductivity in Schizophrenia: TMS-EEG Study. *Cerebral Cortex*, 24(1), 211-221.
- Frisoni, G. B., Pievani, M., Testa, C., Sabbatoli, F., Bresciani, L., Bonetti, M., . . . Thompson, P. M. (2007). The topography of grey matter involvement in early and late onset alzheimer's disease. *Brain*, 130(3), 720-730.
- Friston, K., Harrison, L., Daunizeau, J., Kiebel, S., Phillips, C., Trujillo-Barreto, N., ... & Mattout, J. (2008). Multiple sparse priors for the M/EEG inverse problem. *NeuroImage*, 39(3), 1104-1120.
- Fuchs A (2002) Combining Technologies: The Use of Brain Surfaces. In: Biomag 2002, Proc. 13th Int. Conf. on Biomagnetism, Nowak H, Haueisen J, Geißler F, Huonker R, eds., VDE Verlag Berlin pp. 878–880
- Fujiyama, H., Hyde, J., Hinder, M. R., Kim, S. J., McCormack, G. H., Vickers, J. C., & Summers, J. J. (2014). Delayed plastic responses to anodal tDCS in older adults. *Frontiers in aging neuroscience*, 6, 115.
- Gabriel, C., Gabriel, S., & Corthout, E. (1996a). The dielectric properties of biological tissues: I. Literature survey. *Physics in Medicine & Biology*, 41(11), 2231.
- Gabriel, C., Gabriel, S., & Corthout, E. (1996b). The dielectric properties of biological tissues: I. Literature survey. *Physics in Medicine & Biology*, 41(11), 2231.
- Gagan, J. R., Tholpady, S. S., & Ogle, R. C. (2007). Cellular dynamics and tissue interactions of the dura mater during head development. *Birth Defects Research Part C: Embryo Today: Reviews*, 81(4), 297-304.
- Garey, L. J. (1999). Brodmann's localisation in the cerebral cortex. *World Scientific*.
- Gattellaro, G., Minati, L., Grisoli, M., Mariani, C., Carella, F., Osio, M., . . . Bruzzone, M. (2009). White matter involvement in idiopathic Parkinson disease: a diffusion tensor imaging study. *American Journal of Neuroradiology*, 30(6), 1222-1226.
- Ge, Y., Grossman, R. I., Babb, J. S., Rabin, M. L., Mannon, L. J., & Kolson, D. L. (2002). Age-related total gray matter and white matter changes in normal adult brain. Part I:

- volumetric MR imaging analysis. *American journal of neuroradiology*, 23(8), 1327-1333.
- Geddes, A., L., & Baker, L. E. (1967). The specific resistance of biological material—a compendium of data for the biomedical engineer and physiologist. *Medical and biological engineering*, 5(3), 271-293.
- Gençer, N. G., & Acar, C. E. (2004). Sensitivity of EEG and MEG measurements to tissue conductivity. *Physics in Medicine & Biology*, 49(5), 701.
- Georgopoulos, A. P., Karageorgiou, E., Leuthold, A. C., Lewis, S. M., Lynch, J. K., Alonso, A. A., ... & Koutlas, I. G. (2007). Synchronous neural interactions assessed by magnetoencephalography: a functional biomarker for brain disorders. *Journal of neural engineering*, 4(4), 349.
- Geurts, J. J., & Barkhof, F. (2008). Grey matter pathology in multiple sclerosis. *The Lancet Neurology*, 7(9), 841-851.
- Geuzaine, C., & Remacle, J. F. (2009). Gmsh: A 3-D finite element mesh generator with built-in pre-and post-processing facilities. *International journal for numerical methods in engineering*, 79(11), 1309-1331.
- Gibson, A., Bayford, R., & Holder, D. S. (2000). Two-dimensional finite element modelling of the neonatal head. *Physiological measurement*, 21(1), 45.
- Gillick, B. T., Kirton, A., Carmel, J. B., Minhas, P., & Bikson, M. (2014). Pediatric stroke and transcranial direct current stimulation: methods for rational individualized dose optimization. *Frontiers in human neuroscience*, 8, 739.
- Giorgio, A., Santelli, L., Tomassini, V., Bosnell, R., Smith, S., De Stefano, N., & Johansen-Berg, H. (2010). Age-related changes in grey and white matter structure throughout adulthood. *Neuroimage*, 51(3), 943-951.
- Gonçalves, S. I., de Munck, J. C., Verbunt, J. P. A., Bijma, F., Heethaar, R. M., & da Silva, F. L. (2003a). In vivo measurement of the brain and skull resistivities using an EIT-based method and realistic models for the head. *Ieee Transactions on Biomedical Engineering*, 50(6), 754-767.
- Goncalves, S., de Munck, J. C., Verbunt, J. P. A., Heethaar, R. M., & da Silva, F. H. L. (2003b). In vivo measurement of the brain and skull resistivities using an EIT-based method and the combined analysis of SEF/SEP data. *Ieee Transactions on Biomedical Engineering*, 50(9), 1124-1128.

- Gonçalves, S., De Munck, J.C., Heethaar, R.M., Da Silva, F.L. and Van Dijk, B.W. (2000). The application of electrical impedance tomography to reduce systematic errors in the EEG inverse problem—a simulation study. *Physiological measurement*, 21(3), p.379.
- Good, C. D., Johnsrude, I. S., Ashburner, J., Henson, R. N., Friston, K. J., & Frackowiak, R. S. (2001). A voxel-based morphometric study of ageing in 465 normal adult human brains. *Neuroimage*, 14(1), 21-36.
- Gorodnitsky, I. F., & Rao, B. D. (1997). Sparse signal reconstruction from limited data using FOCUSS: A re-weighted minimum norm algorithm. *IEEE Transactions on signal processing*, 45(3), 600-616.
- Gorodnitsky, I. F., George, J. S., & Rao, B. D. (1995). Neuromagnetic source imaging with FOCUSS: a recursive weighted minimum norm algorithm. *Electroencephalography and clinical Neurophysiology*, 95(4), 231-251.
- Gray, H. (1878). *Anatomy of the human body* (Vol. 8). Lea & Febiger.
- Grech, R., Cassar, T., Muscat, J., Camilleri, K. P., Fabri, S. G., Zervakis, M., ... & Vanrumste, B. (2008). Review on solving the inverse problem in EEG source analysis. *Journal of neuroengineering and rehabilitation*, 5(1), 1-33.
- Greimel, E., Nehr Korn, B., Schulte-Rüther, M., Fink, G. R., Nickl-Jockschat, T., Herpertz-Dahlmann, B., . . . Eickhoff, S. B. (2013). Changes in grey matter development in autism spectrum disorder. *Brain Structure and Function*, 218(4), 929-942.
- Groeschel, S., Vollmer, B., King, M. D., & Connelly, A. (2010). Developmental changes in cerebral grey and white matter volume from infancy to adulthood. *International Journal of Developmental Neuroscience*, 28(6), 481-489.
- Groppe, D. M., Bickel, S., Keller, C. J., Jain, S. K., Hwang, S. T., Harden, C., & Mehta, A. D. (2013). Dominant frequencies of resting human brain activity as measured by the electrocorticogram. *Neuroimage*, 79, 223-233.
- Güllmar, D., Haueisen, J., & Reichenbach, J. R. (2010). Influence of anisotropic electrical conductivity in white matter tissue on the EEG/MEG forward and inverse solution. A high-resolution whole head simulation study. *Neuroimage*, 51(1), 145-163.
- Gunning-Dixon, F. M., Brickman, A. M., Cheng, J. C., & Alexopoulos, G. S. (2009). Aging of cerebral white matter: a review of MRI findings. *International journal of geriatric psychiatry*, 24(2), 109-117.
- Gur, R. C., Gunning-Dixon, F. M., Turetsky, B. I., Bilker, W. B., & Gur, R. E. (2002). Brain region and sex differences in age association with brain volume: a quantitative MRI

- study of healthy young adults. *The American journal of geriatric psychiatry*, 10(1), 72-80.
- Gutiérrez, D., Nehorai, A., & Muravchik, C. H. (2004). Estimating brain conductivities and dipole source signals with EEG arrays. *Ieee Transactions on Biomedical Engineering*, 51(12), 2113-2122.
- Guttman, C. R., Jolesz, F. A., Kikinis, R., Killiany, R. J., Moss, M. B., Sandor, T., & Albert, M. S. (1998). White matter changes with normal aging. *Neurology*, 50(4), 972-978.
- Gylys-Colwell, F. (1996). An inverse problem for the Helmholtz equation. *Inverse Problems*, 12(2), 139.
- Håkansson, B., Brandt, A., Carlsson, P., & Tjellström, A. (1994). Resonance frequencies of the human skull in vivo. *The Journal of the Acoustical Society of America*, 95(3), 1474-1481.
- Hallett, M. (2007). Transcranial magnetic stimulation: a primer. *Neuron*, 55(2), 187-199.
- Hallez, H., Vanrumste, B., Grech, R., Muscat, J., De Clercq, W., Vergult, A., ... & Lemahieu, I. (2007). Review on solving the forward problem in EEG source analysis. *Journal of neuroengineering and rehabilitation*, 4(1), 1-29.
- Hallez, H., Vanrumste, B., Van Hese, P., D'Asseler, Y., Lemahieu, I., & Van de Walle, R. (2005). A finite difference method with reciprocity used to incorporate anisotropy in electroencephalogram dipole source localization. *Physics in Medicine and Biology*, 50(16), 3787-3806.
- Hämäläinen, M. S., & Ilmoniemi, R. J. (1994). Interpreting magnetic fields of the brain: minimum norm estimates. *Medical & biological engineering & computing*, 32(1), 35-42.
- Hämäläinen, M., Hari, R., Ilmoniemi, R. J., Knuutila, J., & Lounasmaa, O. V. (1993). Magnetoencephalography—theory, instrumentation, and applications to noninvasive studies of the working human brain. *Reviews of modern Physics*, 65(2), 413.
- Hanley, C. J., Singh, K. D., & McGonigle, D. J. (2016). Transcranial modulation of brain oscillatory responses: A concurrent tDCS–MEG investigation. *Neuroimage*, 140, 20-32.
- Hansman, C. F. (1966). Growth of interorbital distance and skull thickness as observed in roentgenographic measurements. *Radiology*, 86(1), 87-96.
- Hari, R., & Puce, A. (2017). MEG-EEG Primer. *Oxford University Press*.

- Hatipoglu, H. G., Ozcan, H. N., Hatipoglu, U. S., & Yuksel, E. (2008). Age, sex and body mass index in relation to calvarial diploe thickness and craniometric data on MRI. *Forensic science international*, 182(1-3), 46-51.
- Haueisen, J., Büttner, A., Nowak, H., Brauer, H., & Weiller, C. (1999). The Influence of Conductivity Changes in Boundary Element Compartments on the Forward and Inverse Problem in Electroencephalography and Magnetoencephalography. *Biomedical Engineering*, 44(6), 150-157.
- Haueisen, J., Funke, M., Güllmar, D., & Eichardt, R. (2012). Tangential and radial epileptic spike activity: different sensitivity in EEG and MEG. *Journal of Clinical Neurophysiology*, 29(4), 327-332.
- Haueisen, J., Ramon, C., Brauer, H., & Nowak, H. (1996). Comparison of Finite Element Method and Boundary Element Method in Neuromagnetic Field Calculation.
- Haueisen, J., Ramon, C., Czapski, P., & Eiselt, M. (1995). On the influence of volume currents and extended sources on neuromagnetic fields - a simulation study. *Annals of Biomedical Engineering*, 23(6), 728-739.
- Haueisen, J., Ramon, C., Eiselt, M., Brauer, H., & Nowak, H. (1997). Influence of tissue resistivities on neuromagnetic fields and electric potentials studied with a finite element model of the head. *Ieee Transactions on Biomedical Engineering*, 44(8), 727-735.
- Haueisen, J., Tuch, D. S., Ramon, C., Schimpf, P. H., Wedeen, V. J., George, J. S., & Belliveau, J. W. (2002). The influence of brain tissue anisotropy on human EEG and MEG. *Neuroimage*, 15(1), 159-166.
- Heise, K. F., Niehoff, M., Feldheim, J. F., Liuzzi, G., Gerloff, C., & Hummel, F. C. (2014). Differential behavioral and physiological effects of anodal transcranial direct current stimulation in healthy adults of younger and older age. *Frontiers in aging neuroscience*, 6, 146.
- Henderson, R. P., & Webster, J. G. (1978). An impedance camera for spatially specific measurements of the thorax. *IEEE Transactions on Biomedical Engineering*, 3(20), 250-254.
- Henry, J. C. (2006). Electroencephalography: basic principles, clinical applications, and related fields. *Neurology*, 67(11), 2092-2092.
- Hillebrand, A., & Barnes, G. R. (2003). The use of anatomical constraints with MEG beamformers. *Neuroimage*, 20(4), 2302-2313.

- Hirsch, B. E. (2009). Gray's anatomy: the anatomical basis of clinical practice. *JAMA*, *301*(17), 1825-1831.
- Hoekema, R., Wieneke, G. H., Leijten, F. S. S., van Veelen, C. W. M., van Rijen, P. C., Huiskamp, G. J. M., . . . van Huffelen, A. C. (2003). Measurement of the conductivity of skull, temporarily removed during epilepsy surgery. *Brain Topography*, *16*(1), 29-38.
- Holder, D. S. (2004). Electrical impedance tomography: methods, history and applications. *CRC Press*.
- Hosseini, B., Nigam, N., & Stockie, J. M. (2016). On regularizations of the Dirac delta distribution. *Journal of Computational Physics*, *305*, 423-447.
- Hsu, W. Y., Ku, Y., Zanto, T. P., & Gazzaley, A. (2015). Effects of noninvasive brain stimulation on cognitive function in healthy aging and Alzheimer's disease: a systematic review and meta-analysis. *Neurobiology of aging*, *36*(8), 2348-2359.
- Huang, Y., Datta, A., Bikson, M., & Parra, L. C. (2019). Realistic volumetric-approach to simulate transcranial electric stimulation—ROAST—a fully automated open-source pipeline. *Journal of neural engineering*, *16*(5), 056006.
- Huang, Y., Liu, A. A., Lafon, B., Friedman, D., Dayan, M., Wang, X. Y., . . . Parra, L. C. (2017). Measurements and models of electric fields in the in vivo human brain during transcranial electric stimulation. *Elife*, *6*.
- Ibáñez, A., Petroni, A., Urquina, H., Torrente, F., Torralva, T., Hurtado, E., ... & Manes, F. (2011). Cortical deficits of emotional face processing in adults with ADHD: its relation to social cognition and executive function. *Social neuroscience*, *6*(5-6), 464-481.
- Idriz, S., Patel, J. H., Ameli Renani, S., Allan, R., & Vlahos, I. (2015). CT of normal developmental and variant anatomy of the pediatric skull: distinguishing trauma from normality. *Radiographics*, *35*(5), 1585-1601.
- Ilmoniemi, R. (1985). *Neuromagnetism: theory, techniques, and measurements*. Helsinki University of Technology.
- Im, C. H., Jung, H. H., Choi, J. D., Lee, S. Y., & Jung, K. Y. (2008). Determination of optimal electrode positions for transcranial direct current stimulation (tDCS). *Physics in Medicine & Biology*, *53*(11), N219.
- Iriarte, I. G., & George, M. S. (2018). Transcranial magnetic stimulation (TMS) in the elderly. *Current psychiatry reports*, *20*(1), 1-7.

- Ishida, H., & Dodo, Y. (1990). Cranial thickness of modern and Neolithic populations in Japan. *Human biology*, 389-401.
- Jangjetriew, B., Thamtakerngkit, S., Wongchanapai, W., & Sangvichien, S. (2007). Cranial suture closure and age determination in the Thai population. *Siriraj Medical Journal*, 59(5), 226-231.
- Jenkinson, M., Beckmann, C. F., Behrens, T. E., Woolrich, M. W., & Smith, S. M. (2012). Fsl. *Neuroimage*, 62(2), 782-790.
- Jiang, J., Truong, D. Q., Esmailpour, Z., Huang, Y., Badran, B. W., & Bikson, M. (2020). Enhanced tES and tDCS computational models by meninges emulation. *Journal of neural engineering*, 17(1), 016027.
- Job, D. E., Whalley, H. C., Johnstone, E. C., & Lawrie, S. M. (2005). Grey matter changes over time in high risk subjects developing schizophrenia. *Neuroimage*, 25(4), 1023-1030.
- Johansen-Berg, H., & Behrens, T. E. (2013). *Diffusion MRI: from quantitative measurement to in vivo neuroanatomy*: Academic Press.
- Jones, D. K., Alexander, D. C., Bowtell, R., Cercignani, M., Dell'Acqua, F., McHugh, D. J., ... & Tax, C. M. W. (2018). Microstructural imaging of the human brain with a 'super-scanner': 10 key advantages of ultra-strong gradients for diffusion MRI. *NeuroImage*, 182, 8-38.
- Josephson, B. D. (1962). Possible new effects in superconductive tunnelling. *Phys. Lett. 1 (7): 251–253*.
- Kaipio, J., & Somersalo, E. (2006). Statistical and computational inverse problems (Vol. 160). *Springer Science & Business Media*.
- Kalu, U., Sexton, C., Loo, C., & Ebmeier, K. (2012). Transcranial direct current stimulation in the treatment of major depression: a meta-analysis. *Psychological medicine*, 42(9), 1791-1800.
- Kariotou, F. (2004). Electroencephalography in ellipsoidal geometry. *Journal of Mathematical Analysis and Applications*, 290(1), 324-342.
- Keller, J. B. (1976). Inverse Problems. *The American Mathematical Monthly*, 83(2), 107–118.
- Kessler, S. K., Minhas, P., Woods, A. J., Rosen, A., Gorman, C., & Bikson, M. (2013). Dosage considerations for transcranial direct current stimulation in children: a computational modeling study. *PloS one*, 8(9), e76112.

- Khan, S., Manwaring, P., Borsic, A., & Halter, R. (2014). FPGA-based voltage and current dual drive system for high frame rate electrical impedance tomography. *IEEE transactions on medical imaging*, 34(4), 888-901.
- Kimiwada, T., Juhász, C., Makki, M., Muzik, O., Chugani, D. C., Asano, E., & Chugani, H. T. (2006). Hippocampal and thalamic diffusion abnormalities in children with temporal lobe epilepsy. *Epilepsia*, 47(1), 167-175.
- Kirschstein, T., & Köhling, R. (2009). What is the source of the EEG?. *Clinical EEG and neuroscience*, 40(3), 146-149.
- Knickmeyer, R. C., Gouttard, S., Kang, C., Evans, D., Wilber, K., Smith, J. K., . . . Gilmore, J. H. (2008). A structural MRI study of human brain development from birth to 2 years. *Journal of Neuroscience*, 28(47), 12176-12182.
- Knotkova, H., & Rasche, D. (Eds.). (2014). *Textbook of neuromodulation: principles, methods and clinical applications*. Springer.
- Kobayashi, M., & Pascual-Leone, A. (2003). Transcranial magnetic stimulation in neurology. *The Lancet Neurology*, 2(3), 145-156.
- Koessler, L., Colnat-Coulbois, S., Cecchin, T., Hofmanis, J., Dmochowski, J. P., Norcia, A. M., & Maillard, L. G. (2017). In-vivo measurements of human brain tissue conductivity using focal electrical current injection through intracerebral multicontact electrodes. *Human Brain Mapping*, 38(2), 974-986.
- Kosterich, J. D., Foster, K. R., & Pollack, S. R. (1983). Dielectric permittivity and electrical conductivity of fluid saturated bone. *IEEE Transactions on Biomedical Engineering*(2), 81-86.
- Kosterich, J. D., Foster, K. R., & Pollack, S. R. (1984). Dielectric properties of fluid-saturated bone-The effect of variation in conductivity of immersion fluid. *IEEE Transactions on Biomedical Engineering*(4), 369-374.
- Koulouri, A. (2014). Reconstruction of electric fields and source distributions in EEG brain imaging.
- Kubicki, M., Park, H., Westin, C.-F., Nestor, P. G., Mulkern, R. V., Maier, S. E., . . . Frumin, M. (2005). DTI and MTR abnormalities in schizophrenia: analysis of white matter integrity. *Neuroimage*, 26(4), 1109-1118.
- Kumar, A., Ghosh, S. K., & Pareek, V. (2018). Establishing identity from the skeletal remains: in reference of Alum Bheg a martyr from 1857 Indian Freedom Struggle.

- Kutzelnigg, A., Lucchinetti, C. F., Stadelmann, C., Brück, W., Rauschka, H., Bergmann, M., . . . Lassmann, H. (2005). Cortical demyelination and diffuse white matter injury in multiple sclerosis. *Brain*, *128*(11), 2705-2712.
- Kybic, J., Clerc, M., Abboud, T., Faugeras, O., Keriven, R., & Papadopoulo, T. (2005). A common formalism for the integral formulations of the forward EEG problem. *IEEE transactions on medical imaging*, *24*(1), 12-28.
- Laakso, I., Tanaka, S., Koyama, S., De Santis, V., & Hirata, A. (2015). Inter-subject variability in electric fields of motor cortical tDCS. *Brain stimulation*, *8*(5), 906-913.
- Lai, Y., van Drongelen, W., Ding, L., Hecox, K. E., Towle, V. L., Frim, D. M., & He, B. (2005). Estimation of in vivo human brain-to-skull conductivity ratio from simultaneous extra- and intra-cranial electrical potential recordings. *Clinical Neurophysiology*, *116*(2), 456-465.
- Lanfer, B., Scherg, M., Dannhauer, M., Knösche, T. R., Burger, M., & Wolters, C. H. (2012). Influences of skull segmentation inaccuracies on EEG source analysis. *NeuroImage*, *62*(1), 418-431.
- Lapenta, O. M., Marques, L. M., Rego, G. G., Comfort, W. E., & Boggio, P. S. (2018). tDCS in addiction and impulse control disorders. *The journal of ECT*, *34*(3), 182-192.
- Latif, N. A. i. A., Mahmood Dollah, M. K. K., & Ibrahim, S. (2010) A study of frequency effects on conductivity measurements. In: RnD Seminar 2010: Research and Development Seminar 2010, Malaysia.
- Lau, S., Güllmar, D., Flemming, L., Grayden, D. B., Cook, M. J., Wolters, C. H., & Haueisen, J. (2016). Skull defects in finite element head models for source reconstruction from magnetoencephalography signals. *Frontiers in neuroscience*, *10*, 141.
- Law, S. K. (1993). Thickness and resistivity variations over the upper surface of the human skull. *Brain topography*, *6*(2), 99-109.
- Lefaucheur, J. P. (2009). Treatment of Parkinson's disease by cortical stimulation. *Expert review of neurotherapeutics*, *9*(12), 1755-1771.
- Lefaucheur, J. P., André-Obadia, N., Antal, A., Ayache, S. S., Baeken, C., Benninger, D. H., ... & Devanne, H. (2014). Evidence-based guidelines on the therapeutic use of repetitive transcranial magnetic stimulation (rTMS). *Clinical Neurophysiology*, *125*(11), 2150-2206.

- Lew, S., Sliva, D. D., Choe, M. S., Grant, P. E., Okada, Y., Wolters, C. H., & Hämäläinen, M. S. (2013). Effects of sutures and fontanels on MEG and EEG source analysis in a realistic infant head model. *Neuroimage*, *76*, 282-293.
- Li, Z., Park, B.-K., Liu, W., Zhang, J., Reed, M. P., Rupp, J. D., . . . Hu, J. (2015). A statistical skull geometry model for children 0-3 years old. *PloS one*, *10*(5), e0127322.
- Liebetanz, D., Klinker, F., Hering, D., Koch, R., Nitsche, M. A., Pöschka, H., . . . Tergau, F. (2006). Anticonvulsant effects of transcranial direct-current stimulation (tDCS) in the rat cortical ramp model of focal epilepsy. *Epilepsia*, *47*(7), 1216-1224.
- Liebetanz, D., Nitsche, M. A., Tergau, F., & Paulus, W. (2002). Pharmacological approach to the mechanisms of transcranial DC-stimulation-induced after-effects of human motor cortex excitability. *Brain*, *125*(10), 2238-2247.
- Lillie, E. M., Urban, J. E., Lynch, S. K., Weaver, A. A., & Stitzel, J. D. (2016). Evaluation of skull cortical thickness changes with age and sex from computed tomography scans. *Journal of Bone and Mineral Research*, *31*(2), 299-307.
- Lin, F. H., Witzel, T., Ahlfors, S. P., Stufflebeam, S. M., Belliveau, J. W., & Hämäläinen, M. S. (2006). Assessing and improving the spatial accuracy in MEG source localization by depth-weighted minimum-norm estimates. *Neuroimage*, *31*(1), 160-171.
- Lionheart, W. R. (2004). EIT reconstruction algorithms: pitfalls, challenges and recent developments. *Physiological measurement*, *25*(1), 125.
- Lipsett, B. J., Reddy, V., & Steanson, K. (2019). Anatomy, head and neck, fontanelles.
- Liu, G. R., & Quek, S. S. (2013). *The finite element method: a practical course*. Butterworth-Heinemann.
- Liu, H., & Schimpf, P. H. (2006). Efficient localization of synchronous EEG source activities using a modified RAP-MUSIC algorithm. *IEEE transactions on biomedical engineering*, *53*(4), 652-661.
- Lochy, A., Van Belle, G., & Rossion, B. (2015). A robust index of lexical representation in the left occipito-temporal cortex as evidenced by EEG responses to fast periodic visual stimulation. *Neuropsychologia*, *66*, 18-31.
- Lucas, K. (1909). The “all or none” contraction of the amphibian skeletal muscle fibre. *The Journal of physiology*, *38*(2-3), 113.
- Lynnerup, N. (2001). Cranial thickness in relation to age, sex and general body build in a Danish forensic sample. *Forensic science international*, *117*(1-2), 45-51.

- Lynnerup, N., Astrup, J. G., & Sejrsen, B. (2005). Thickness of the human cranial diploe in relation to age, sex and general body build. *Head & face medicine*, 1(1), 13.
- Madeline, L. A., & Elster, A. D. (1995). Suture closure in the human chondrocranium: CT assessment. *Radiology*, 196(3), 747-756.
- Maksymenko, K., Giusiano, B., Roehri, N., Bénar, C. G., & Badier, J. M. (2017). Strategies for statistical thresholding of source localization maps in magnetoencephalography and estimating source extent. *Journal of Neuroscience Methods*, 290, 95-104.
- Malmivuo, J., & Plonsey, R. (1995). *Bioelectromagnetism: principles and applications of bioelectric and biomagnetic fields*. Oxford University Press, USA.
- Mamatjan, Y., Ahn, S., Oh, T., & Adler, A. (2012). Optimized electrode positions and stimulation patterns in head EIT. *CMBES Proceedings*, 35.
- Marin, G., Guerin, C., Baillet, S., Garnero, L., & Meunier, G. (1998). Influence of skull anisotropy for the forward and inverse problem in EEG: simulation studies using FEM on realistic head models. *Human brain mapping*, 6(4), 250-269.
- Mathern, G. W., Giza, C. C., Yudovin, S., Vinters, H. V., Peacock, W. J., Shewmon, D. A., & Shields, W. D. (1999). Postoperative seizure control and antiepileptic drug use in pediatric epilepsy surgery patients: the UCLA experience, 1986–1997. *Epilepsia*, 40(12), 1740-1749.
- Matsuura, K., & Okabe, Y. (1995). Selective minimum-norm solution of the biomagnetic inverse problem. *IEEE Transactions on Biomedical Engineering*, 42(6), 608-615.
- McAlonan, G. M., Cheung, V., Cheung, C., Chua, S. E., Murphy, D. G., Suckling, J., . . . Ho, T. P. (2007). Mapping brain structure in attention deficit-hyperactivity disorder: a voxel-based MRI study of regional grey and white matter volume. *Psychiatry Research: Neuroimaging*, 154(2), 171-180.
- McCann, H., Ahsan, S. T., Davidson, J. L., Robinson, R. L., Wright, P., & Pomfrett, C. J. (2011, August). A portable instrument for high-speed brain function imaging: FEITER. In *2011 Annual International Conference of the IEEE Engineering in Medicine and Biology Society* (pp. 7029-7032). IEEE.
- McGale, E., Pye, I., Stonier, C., Hutchinson, E., & Aber, G. (1977). Studies of the inter-relationship between cerebrospinal fluid and plasma amino acid concentrations in normal individuals. *Journal of neurochemistry*, 29(2), 291-297.
- McGonigle, D., Singh, K., & Hanley, C. (2015). tES-MEG: Simultaneous Combined Transcranial Electrical Stimulation and Magnetoencephalography. *Brain Stimulation: Basic, Translational, and Clinical Research in Neuromodulation*, 8(2), 339.

- McIntyre, C. C., Mori, S., Sherman, D. L., Thakor, N. V., & Vitek, J. L. (2004). Electric field and stimulating influence generated by deep brain stimulation of the subthalamic nucleus. *Clinical Neurophysiology*, *115*(3), 589-595.
- Meijs, J. W., & Peters, M. J. (1987). The EEG and MEG, using a model of eccentric spheres to describe the head. *IEEE Transactions on Biomedical Engineering*, (12), 913-920.
- Michel, C. M., Murray, M. M., Lantz, G., Gonzalez, S., Spinelli, L., & de Peralta, R. G. (2004). EEG source imaging. *Clinical neurophysiology*, *115*(10), 2195-2222.
- Mikkonen, M., Laakso, I., Tanaka, S., & Hirata, A. (2020). Cost of focality in TDCS: Interindividual variability in electric fields. *Brain stimulation*, *13*(1), 117-124.
- Miller, A., Alston, R., & Corsellis, J. (1980). Variation with age in the volumes of grey and white matter in the cerebral hemispheres of man: measurements with an image analyser. *Neuropathology and applied neurobiology*, *6*(2), 119-132.
- Miller, S. L., & Yeh, H. H. (2017). Neurotransmitters and Neurotransmission in the Developing and Adult Nervous System. *Conn's Translational Neuroscience*, 49-84.
- Miura, T., Perlyn, C. A., Kinboshi, M., Ogihara, N., Kobayashi-Miura, M., Morriss-Kay, G. M., & Shiota, K. (2009). Mechanism of skull suture maintenance and interdigitation. *Journal of anatomy*, *215*(6), 642-655.
- Moher, D., Jadad, A. R., & Tugwell, P. (1996). Assessing the quality of randomized controlled trials: current issues and future directions. *International journal of technology assessment in health care*, *12*(2), 195-208.
- Moher, D., Liberati, A., Tetzlaff, J., Altman, D. G., & Group, P. (2009). Preferred reporting items for systematic reviews and meta-analyses: the PRISMA statement. *PLoS medicine*, *6*(7).
- Moliadze, V., Antal, A., & Paulus, W. (2010). Electrode-distance dependent after-effects of transcranial direct and random noise stimulation with extracephalic reference electrodes. *Clinical Neurophysiology*, *121*(12), 2165-2171.
- Moliadze, V., Schmanke, T., Andreas, S., Lyzhko, E., Freitag, C. M., & Siniatchkin, M. (2015). Stimulation intensities of transcranial direct current stimulation have to be adjusted in children and adolescents. *Clinical Neurophysiology*, *126*(7), 1392-1399.
- Monai, H., Ohkura, M., Tanaka, M., Oe, Y., Konno, A., Hirai, H., ... & Hirase, H. (2016). Calcium imaging reveals glial involvement in transcranial direct current stimulation-induced plasticity in mouse brain. *Nature communications*, *7*(1), 1-10.

- Montes-Restrepo, V., van Mierlo, P., Strobbe, G., Staelens, S., Vandenberghe, S., & Hallez, H. (2014). Influence of skull modeling approaches on EEG source localization. *Brain topography*, 27(1), 95-111.
- Montes, V., Hallez, H., & Staelens, S. (2011). Influence of skull inhomogeneities on EEG source localization. In *2011 8th International Symposium on Noninvasive Functional Source Imaging of the Brain and Heart and the 2011 8th International Conference on Bioelectromagnetism* (pp. 72-76). IEEE.
- Mosher, J. C., & Leahy, R. M. (1998). Recursive MUSIC: a framework for EEG and MEG source localization. *IEEE Transactions on Biomedical Engineering*, 45(11), 1342-1354.
- Mosher, J. C., Leahy, R. M., & Lewis, P. S. (1999). EEG and MEG: forward solutions for inverse methods. *IEEE Transactions on biomedical engineering*, 46(3), 245-259.
- Mosher, J. C., Lewis, P. S., & Leahy, R. M. (1992). Multiple dipole modeling and localization from spatio-temporal MEG data. *IEEE transactions on biomedical engineering*, 39(6), 541-557.
- Muffel, T., Kirsch, F., Shih, P. C., Kalloch, B., Schaumberg, S., Villringer, A., & Sehm, B. (2019). Anodal transcranial direct current stimulation over S1 differentially modulates proprioceptive accuracy in young and old adults. *Frontiers in aging neuroscience*, 11, 264.
- Murakami, S., & Okada, Y. (2006). Contributions of principal neocortical neurons to magnetoencephalography and electroencephalography signals. *The Journal of physiology*, 575(3), 925-936.
- Nakahara, K., Utsuki, S., Shimizu, S., Iida, H., Miyasaka, Y., Takagi, H., ... & Fujii, K. (2006). Age dependence of fusion of primary occipital sutures: a radiographic study. *Child's Nervous System*, 22(11), 1457-1459.
- Nielsen, J. D., Madsen, K. H., Puonti, O., Siebner, H. R., Bauer, C., Madsen, C. G., ... & Thielscher, A. (2018). Automatic skull segmentation from MR images for realistic volume conductor models of the head: Assessment of the state-of-the-art. *Neuroimage*, 174, 587-598.
- Nitsche, M. A., & Paulus, W. (2011). Transcranial direct current stimulation—update 2011. *Restorative neurology and neuroscience*, 29(6), 463-492.
- Nitsche, M. A., Boggio, P. S., Fregni, F., & Pascual-Leone, A. (2009). Treatment of depression with transcranial direct current stimulation (tDCS): a review. *Experimental neurology*, 219(1), 14-19.

- Nitsche, M. A., Cohen, L. G., Wassermann, E. M., Priori, A., Lang, N., Antal, A., ... & Pascual-Leone, A. (2008). Transcranial direct current stimulation: state of the art 2008. *Brain stimulation*, *1*(3), 206-223.
- Nunez, P. L., & Pilgreen, K. L. (1991). The spline-Laplacian in clinical neurophysiology: a method to improve EEG spatial resolution. *Journal of clinical neurophysiology: official publication of the American Electroencephalographic Society*, *8*(4), 397-413.
- Nunez, P. L., & Srinivasan, R. (2006). *Electric fields of the brain: the neurophysics of EEG*. Oxford University Press, USA.
- O'Reilly, C., Larson, E., Richards, J. E., & Elsabbagh, M. (2021). Structural templates for imaging EEG cortical sources in infants. *NeuroImage*, *227*, 117682.
- Oberman, L. M., Enticott, P. G., Casanova, M. F., Rotenberg, A., Pascual-Leone, A., McCracken, J. T., & TMS in ASD Consensus Group. (2016). Transcranial magnetic stimulation in autism spectrum disorder: challenges, promise, and roadmap for future research. *Autism Research*, *9*(2), 184-203.
- Oberman, L. M., Rotenberg, A., & Pascual-Leone, A. (2015). Use of transcranial magnetic stimulation in autism spectrum disorders. *Journal of autism and developmental disorders*, *45*(2), 524-536.
- Odabae, M., Tokariev, A., Layeghy, S., Mesbah, M., Colditz, P. B., Ramon, C., & Vanhatalo, S. (2014). Neonatal EEG at scalp is focal and implies high skull conductivity in realistic neonatal head models. *Neuroimage*, *96*, 73-80.
- Oh, S., Lee, S., Cho, M., Kim, T., & Kim, I. (2006). *Electrical conductivity estimation from diffusion tensor and T2: a silk yarn phantom study*. Paper presented at the Proc Intl Soc Mag Reson Med.
- Oh, T., Gilad, O., Ghosh, A., Schuettler, M., & Holder, D. S. (2011). A novel method for recording neuronal depolarization with recording at 125–825 Hz: implications for imaging fast neural activity in the brain with electrical impedance tomography. *Medical & biological engineering & computing*, *49*(5), 593-604.
- Okada, Y. C., Lahtenmaki, A., & Xu, C. B. (1999). Experimental analysis of distortion of magnetoencephalography signals by the skull. *Clinical Neurophysiology*, *110*(2), 230-238.
- Ollikainen, J. O., Vauhkonen, M., Karjalainen, P. A., & Kaipio, J. P. (1999). Effects of local skull inhomogeneities on EEG source estimation. *Medical engineering and physics*, *21*(3), 143-154.

- Oostendorp, T. F., Delbeke, J., & Stegeman, D. F. (2000). The conductivity of the human skull: Results of in vivo and in vitro measurements. *Ieee Transactions on Biomedical Engineering*, 47(11), 1487-1492.
- Oostendorp, T., & van Oosterom, A. (1991). The potential distribution generated by surface electrodes in inhomogeneous volume conductors of arbitrary shape. *IEEE Transactions on Biomedical Engineering*, 38(5), 409-417.
- Oostenfeld, R., & Praamstra, P. (2001). The five percent electrode system for high-resolution EEG and ERP measurements. *Clinical neurophysiology*, 112(4), 713-719.
- Oostenfeld, R., Fries, P., Maris, E., & Schoffelen, J. M. (2011). FieldTrip: open source software for advanced analysis of MEG, EEG, and invasive electrophysiological data. *Computational intelligence and neuroscience*.
- Opitz, A., Falchier, A., Linn, G. S., Milham, M. P., & Schroeder, C. E. (2017). Limitations of ex vivo measurements for in vivo neuroscience. *Proceedings of the National Academy of Sciences*, 201617024.
- Opitz, A., Paulus, W., Will, S., Antunes, A., & Thielscher, A. (2015). Determinants of the electric field during transcranial direct current stimulation. *Neuroimage*, 109, 140-150.
- Opitz, A., Windhoff, M., Heidemann, R. M., Turner, R., & Thielscher, A. (2011). How the brain tissue shapes the electric field induced by transcranial magnetic stimulation. *Neuroimage*, 58(3), 849-859.
- Ou, W., Hämäläinen, M. S., & Golland, P. (2009). A distributed spatio-temporal EEG/MEG inverse solver. *NeuroImage*, 44(3), 932-946.
- Ouypornkochagorn, T., Polydorides, N., & McCann, H. (2014). In Vivo Estimation of the Scalp and Skull Conductivity. *EIT2015*, 10-10.
- Pal, D., Trivedi, R., Saksena, S., Yadav, A., Kumar, M., Pandey, C. M., . . . Gupta, R. K. (2011). Quantification of age-and gender-related changes in diffusion tensor imaging indices in deep grey matter of the normal human brain. *Journal of Clinical Neuroscience*, 18(2), 193-196.
- Pant, S., Te, T., Tucker, A., & Sadleir, R. J. (2011). The conductivity of neonatal piglet skulls. *Physiological measurement*, 32(8), 1275.
- Park, H. J., Kwon, J. S., Youn, T., Pae, J. S., Kim, J. J., Kim, M. S., & Ha, K. S. (2002). Statistical parametric mapping of LORETA using high density EEG and individual MRI: Application to mismatch negativities in schizophrenia. *Human Brain Mapping*, 17(3), 168-178.

- Pascual-Marqui, R. D. (2002). Standardized low-resolution brain electromagnetic tomography (sLORETA): technical details. *Methods Find Exp Clin Pharmacol*, 24(Suppl D), 5-12.
- Penny, W. D., Friston, K. J., Ashburner, J. T., Kiebel, S. J., & Nichols, T. E. (Eds.). (2011). *Statistical parametric mapping: the analysis of functional brain images*. Elsevier.
- Pensler, J., & McCarthy, J. G. (1985). The calvarial donor site: an anatomic study in cadavers. *Plastic and reconstructive surgery*, 75(5), 648-651.
- Pernet, C. R., Wilcox, R. R., & Rousselet, G. A. (2013). Robust correlation analyses: false positive and power validation using a new open source matlab toolbox. *Frontiers in psychology*, 3, 606.
- Peterchev, A. V., Wagner, T. A., Miranda, P. C., Nitsche, M. A., Paulus, W., Lisanby, S. H., ... & Bikson, M. (2012). Fundamentals of transcranial electric and magnetic stimulation dose: definition, selection, and reporting practices. *Brain stimulation*, 5(4), 435-453.
- Peterson, B. S., Anderson, A. W., Ehrenkranz, R., Staib, L. H., Tageldin, M., Colson, E., . . . Ment, L. R. (2003). Regional brain volumes and their later neurodevelopmental correlates in term and preterm infants. *Pediatrics*, 111(5), 939-948.
- Peyman, A., Holden, S. J., Watts, S., Perrott, R., & Gabriel, C. (2007). Dielectric properties of porcine cerebrospinal tissues at microwave frequencies: in vivo, in vitro and systematic variation with age. *Physics in Medicine & Biology*, 52(8), 2229.
- Peyman, A., Rezazadeh, A. A., & Gabriel, C. (2001). Changes in the dielectric properties of rat tissue as a function of age at microwave frequencies. *Physics in Medicine & Biology*, 46(6), 1617.
- Pickel, V. M., & Segal, M. (Eds.). (2013). *The synapse: structure and function*. Elsevier.
- Pierpaoli, C., Jezzard, P., Basser, P. J., Barnett, A., & Di Chiro, G. (1996). Diffusion tensor MR imaging of the human brain. *Radiology*, 201(3), 637-648.
- Plonsey, R., & Barr, R. C., (2007). *Bioelectricity: A Quantitative Approach*. New York, NY: Springer.
- Pohlmeier, R., Buchner, H., Knoll, G., Rienacker, A., Beckmann, R., & Pesch, J. (1997). The influence of skull-conductivity misspecification on inverse source localization in realistically shaped finite element head models. *Brain Topography*, 9(3), 157-162.

- Poreisz, C., Boros, K., Antal, A., & Paulus, W. (2007). Safety aspects of transcranial direct current stimulation concerning healthy subjects and patients. *Brain research bulletin*, 72(4-6), 208-214.
- Purcell, E. M., & Morin, D. J. (2013). *Electricity and magnetism*. Cambridge University Press.
- Rakic, P. (2006). A century of progress in corticoneurogenesis: from silver impregnation to genetic engineering. *Cerebral Cortex*, 16(suppl_1), i3-i17.
- Ramon, C., Garguilo, P., Fridgerisson, E. A., & Haueisen, J. (2014). Changes in scalp potentials and spatial smoothing effects of inclusion of dura layer in human head models for EEG simulations. *Frontiers in neuroengineering*, 7(32).
- Ramon, C., Schimpf, P. H., & Haueisen, J. (2006). Influence of head models on EEG simulations and inverse source localizations. *BioMedical Engineering Online*, 5(1), 10.
- Rezaee, Z., & Dutta, A. (2020). Lobule-specific dosage considerations for cerebellar transcranial direct current stimulation during healthy aging: A computational modeling study using age-specific magnetic resonance imaging templates. *Neuromodulation: Technology at the Neural Interface*, 23(3), 341-365.
- Richards, J. E., & Xie, W. (2015). Brains for all the ages: structural neurodevelopment in infants and children from a life-span perspective. *Advances in child development and behavior*, 48, 1-52.
- Richards, J. E., Sanchez, C., Phillips-Meek, M., & Xie, W. (2016). A database of age-appropriate average MRI templates. *Neuroimage*, 124, 1254-1259.
- Ridding, M. C., & Ziemann, U. (2010). Determinants of the induction of cortical plasticity by non-invasive brain stimulation in healthy subjects. *The Journal of physiology*, 588(13), 2291-2304.
- Robinson, S. E., & Vrba, V. J. (1999). Functional neuroimaging by synthetic aperture magnetometry (SAM). *Recent advances in biomagnetism*.
- Rosenthal, R. (1991). Quality-weighting of studies in meta-analytic research. *Psychotherapy Research*, 1(1), 25-28.
- Rosenthal, R. L., & Tobias, C. W. (1948). Measurement of the electric resistance of human blood; use in coagulation studies and cell volume determinations. *The Journal of laboratory and clinical medicine*, 33(9), 1110-1122.
- Ross, A. H., Jantz, R. L., & McCormick, W. F. (1998). Cranial thickness in American females and males. *Journal of Forensic Science*, 43(2), 267-272.

- Roth, B. J., & Basser, P. J. (1990). A model of the stimulation of a nerve fiber by electromagnetic induction. *IEEE Transactions on Biomedical Engineering*, 37(6), 588-597.
- Rowley, H. A., & Roberts, T. P. (1995). Functional localization by magnetoencephalography. *Neuroimaging Clinics of North America*, 5(4), 695-710.
- Ruengdit, S., Case, D. T., & Mahakkanukrauh, P. (2020). Cranial suture closure as an age indicator: A review. *Forensic science international*, 307, 110111.
- Rullmann, M., Anwander, A., Dannhauer, M., Warfield, S. K., Duffy, F. H., & Wolters, C. H. (2009). EEG source analysis of epileptiform activity using a 1 mm anisotropic hexahedra finite element head model. *Neuroimage*, 44(2), 399-410.
- Ruohonen, J., & Ilmoniemi R. J. (2002) Handbook of Transcranial Magnetic Stimulation. Oxford University Press; New York, 18–30.
- Rush, S., & Driscoll, D. A. (1968). Current distribution in the brain from surface electrodes. *Anesthesia & Analgesia*, 47(6), 717-723.
- Rush, S., & Driscoll, D. A. (1969). EEG electrode sensitivity-an application of reciprocity. *IEEE transactions on biomedical engineering*(1), 15-22.
- Russell, W. P., & Russell, M. R. (2018). Anatomy, Head and Neck, Coronal Suture. *StatPearls Publishing*.
- Rutecki, P. A. (1992). Neuronal excitability: voltage-dependent currents and synaptic transmission. *Journal of clinical neurophysiology: official publication of the American Electroencephalographic Society*, 9(2), 195-211.
- Ryynänen, O. R. M., Hyttinen, J. A., Laarne, P. H., & Malmivuo, J. A. (2004). Effect of electrode density and measurement noise on the spatial resolution of cortical potential distribution. *IEEE transactions on biomedical engineering*, 51(9), 1547-1554.
- Sabancıoğulları, V., Koşar, M. İ., Şalk, İ., Erdil, F. H., Öztoprak, İ., & Çimen, M. (2012). Diploe thickness and cranial dimensions in males and females in mid-Anatolian population: an MRI study. *Forensic science international*, 219(1-3), 289. e281-289. e287.
- Sadleir, R. J., & Argibay, A. (2007). Modeling skull electrical properties. *Annals of Biomedical engineering*, 35(10), 1699-1712.
- Sadleir, R. J., Vannorsdall, T. D., Schretlen, D. J., & Gordon, B. (2010). Transcranial direct current stimulation (tDCS) in a realistic head model. *Neuroimage*, 51(4), 1310-1318.
- Sadler, T. W. (2018). Langman's medical embryology. *Lippincott Williams & Wilkins*.

- Salat, D. H., Kaye, J. A., & Janowsky, J. S. (1999). Prefrontal gray and white matter volumes in healthy aging and Alzheimer disease. *Archives of neurology*, *56*(3), 338-344.
- Saldanha, J. S., Zortea, M., Deliberali, C. B., Nitsche, M. A., Kuo, M. F., Torres, I. L. D. S., ... & Caumo, W. (2020). Impact of age on tDCS effects on pain threshold and working memory: results of a proof of concept cross-over randomized controlled study. *Frontiers in aging neuroscience*, *12*, 189.
- Salehinejad, M. A., Nejati, V., Mosayebi-Samani, M., Mohammadi, A., Wischnewski, M., Kuo, M. F., ... & Nitsche, M. A. (2020). Transcranial direct current stimulation in ADHD: a systematic review of efficacy, safety, and protocol-induced electrical field modeling results. *Neuroscience bulletin*, *36*, 1191-1212.
- Salinas, F. S., Lancaster, J. L., & Fox, P. T. (2009). 3D modeling of the total electric field induced by transcranial magnetic stimulation using the boundary element method. *Physics in Medicine and Biology*, *54*(12), 3631-3647.
- Salman, A., Malony, A., Turovets, S., Volkov, V., Ozog, D., & Tucker, D. (2016). Concurrency in electrical neuroinformatics: parallel computation for studying the volume conduction of brain electrical fields in human head tissues. *Concurrency and Computation: Practice and Experience*, *28*(7), 2213-2236.
- Salvador, R., Silva, S., Basser, P. J., & Miranda, P. C. (2011). Determining which mechanisms lead to activation in the motor cortex: a modeling study of transcranial magnetic stimulation using realistic stimulus waveforms and sulcal geometry. *Clinical neurophysiology*, *122*(4), 748-758.
- Sanchez, C. E., Richards, J. E., & Almlí, C. R. (2012). Age-specific MRI templates for pediatric neuroimaging. *Developmental neuropsychology*, *37*(5), 379-399.
- Sanei, S., & Chambers, J. A. (2013). EEG signal processing. *John Wiley & Sons*.
- Santos, L., Martinho, M., Salvador, R., Wenger, C., Fernandes, S. R., Ripolles, O., . . . Miranda, P. C. (2016). *Evaluation of the electric field in the brain during transcranial direct current stimulation: A sensitivity analysis*. Paper presented at the Engineering in Medicine and Biology Society (EMBC), 2016 IEEE 38th Annual International Conference of the.
- Sastre-Garriga, J., Ingle, G. T., Chard, D. T., Cercignani, M., Ramió-Torrentà, L., Miller, D. H., & Thompson, A. J. (2005). Grey and white matter volume changes in early primary progressive multiple sclerosis: a longitudinal study. *Brain*, *128*(6), 1454-1460.

- Saturnino, G. B., Puonti, O., Nielsen, J. D., Antonenko, D., Madsen, K. H., & Thielscher, A. (2019). SimNIBS 2.1: a comprehensive pipeline for individualized electric field modelling for transcranial brain stimulation. *Brain and Human Body Modeling*, 3-25.
- Saturnino, G. B., Siebner, H. R., Thielscher, A., & Madsen, K. H. (2019). Accessibility of cortical regions to focal TES: Dependence on spatial position, safety, and practical constraints. *NeuroImage*, 203, 116183.
- Saturnino, G. B., Thielscher, A., Madsen, K. H., Knösche, T. R., & Weise, K. (2019). A principled approach to conductivity uncertainty analysis in electric field calculations. *Neuroimage*, 188, 821-834.
- Scherg, M., & Ebersole, J. S. (1993). Models of brain sources. *Brain topography*, 5(4), 419-423.
- Schimpf, P. H., Ramon, C., & Haueisen, J. (2002). Dipole models for the EEG and MEG. *IEEE Transactions on Biomedical Engineering*, 49(5), 409-418.
- Schlosser, R. G. M., Nenadic, I., Wagner, G., Güllmar, D., von Consbruch, K., Kohler, S., . . . Sauer, H. (2007). White matter abnormalities and brain activation in schizophrenia: A combined DTI and fMRI study. *Schizophrenia Research*, 89(1-3), 1-11.
- Schmid, G., & Überbacher, R. (2005). Age dependence of dielectric properties of bovine brain and ocular tissues in the frequency range of 400 MHz to 18 GHz. *Physics in Medicine & Biology*, 50(19), 4711.
- Schmidt, C., Wagner, S., Burger, M., van Rienen, U., & Wolters, C. H. (2015). Impact of uncertain head tissue conductivity in the optimization of transcranial direct current stimulation for an auditory target. *Journal of neural engineering*, 12(4), 046028.
- Schmidt, R. (1979). Multiple signal classification (MUSIC). *ESL Technical Memo TM 1098*.
- Schmithorst, V. J., Wilke, M., Dardzinski, B. J., & Holland, S. K. (2002). Correlation of white matter diffusivity and anisotropy with age during childhood and adolescence: a cross-sectional diffusion-tensor MR imaging study. *Radiology*, 222(1), 212-218.
- Schönborn, F., Burkhardt, M., & Kuster, N. (1998). Differences in energy absorption between heads of adults and children in the near field of sources. *Health Physics*, 74(2), 160-168.
- Secco, A., Tonin, A., Rana, A., Jaramillo-Gonzalez, A., Khalili-Ardali, M., Birbaumer, N., & Chaudhary, U. (2021). EEG power spectral density in locked-in and completely locked-in state patients: a longitudinal study. *Cognitive neurodynamics*, 15(3), 473-480.

- Sekihara, K., & Nagarajan, S. S. (2008). *Adaptive spatial filters for electromagnetic brain imaging*. Springer Science & Business Media.
- Sekihara, K., & Nagarajan, S. S. (2015). *Electromagnetic brain imaging: a bayesian perspective*. Springer.
- Sekino, M., Inoue, Y., & Ueno, S. (2005). Magnetic resonance imaging of electrical conductivity in the human brain. *Ieee Transactions on Magnetism*, 41(10), 4203-4205.
- Shoeb, A. H. (2009). *Application of machine learning to epileptic seizure onset detection and treatment* (Doctoral dissertation, Massachusetts Institute of Technology).
- Silau, A. M., Fischer, B. H., & Kjaer, I. (1995). Normal prenatal development of the human parietal bone and interparietal suture. *Journal of craniofacial genetics and developmental biology*, 15(2), 81-86.
- Singh, P., Oberoi, S. S., Gorea, R. K., & Kapila, A. K. (2004). Age estimation in old individuals by CT scan of skull. *JIAFM*, 26(1), 0971-0973.
- Skrzat, J., Brzegowy, P., Walocha, J., & Wojciechowski, W. (2004). Age dependent changes of the diploe in the human skull. *Folia morphologica*, 63(1), 67-70.
- Smith, C. D., Chebrolu, H., Wekstein, D. R., Schmitt, F. A., & Markesbery, W. R. (2007). Age and gender effects on human brain anatomy: a voxel-based morphometric study in healthy elderly. *Neurobiology of aging*, 28(7), 1075-1087.
- Song, J., Turovets, S., Govyadinov, P., Mattson, C., Luu, P., Smith, K., . . . Tucker, D. M. (2013). *Anatomically accurate infant head models for EEG source localization*. Paper presented at the Journal of Physics: Conference Series.
- Sorensen, A. G., Wu, O., Copen, W. A., Davis, T. L., Gonzalez, R. G., Koroshetz, W. J., . . . Weisskoff, R. M. (1999). Human acute cerebral ischemia: detection of changes in water diffusion anisotropy by using MR imaging. *Radiology*, 212(3), 785-792.
- Sowell, E. R., Peterson, B. S., Thompson, P. M., Welcome, S. E., Henkenius, A. L., & Toga, A. W. (2003). Mapping cortical change across the human life span. *Nature neuroscience*, 6(3), 309-315.
- Spence, A. P. (1986). *Basic human anatomy*. Benjamin-Cummings Publishing Company.
- Srinivasan, R. (1999). Methods to improve the spatial resolution of EEG. *International journal of bioelectromagnetism*, 1(1), 102-111.
- Stagg, C. J., & Nitsche, M. A. (2011). Physiological basis of transcranial direct current stimulation. *The Neuroscientist*, 17(1), 37-53.
- Stenroos, M., & Nenonen, J. (2012). On the accuracy of collocation and Galerkin BEM in the EEG/MEG forward problem. *Int J Bioelectromagn*, 14(11), 29-33.

- Stenroos, M., & Nummenmaa, A. (2016). Incorporating and compensating cerebrospinal fluid in surface-based forward models of magneto-and electroencephalography. *PLoS One*, *11*(7), e0159595.
- Stenroos, M., Hunold, A., & Haueisen, J. (2014). Comparison of three-shell and simplified volume conductor models in magnetoencephalography. *Neuroimage*, *94*, 337-348.
- Stewart-Wallace, A. (1939). A biochemical study of cerebral tissue, and of the changes in cerebral *Æ*dema. *Brain*, *62*(4), 426-438.
- Suh, H. S., Lee, W. H., & Kim, T. S. (2012). Influence of anisotropic conductivity in the skull and white matter on transcranial direct current stimulation via an anatomically realistic finite element head model. *Physics in Medicine and Biology*, *57*(21), 6961-6980.
- Sullivan, W. G., & Smith, A. A. (1989). The split calvarial graft donor site in the elderly: a study in cadavers. *Plastic and reconstructive surgery*, *84*(1), 29-31.
- Tadel, F., Baillet, S., Mosher, J. C., Pantazis, D., & Leahy, R. M. (2011). Brainstorm: a user-friendly application for MEG/EEG analysis. *Computational intelligence and neuroscience*, 2011.
- Tang, C., You, F. S., Cheng, G., Gao, D. K., Fu, F., Yang, G. S., & Dong, X. Z. (2008). Correlation between structure and resistivity variations of the live human skull. *Ieee Transactions on Biomedical Engineering*, *55*(9), 2286-2292.
- Tatum IV, W. O. (2021). *Handbook of EEG interpretation*. Springer Publishing Company.
- Thair, H., Holloway, A. L., Newport, R., & Smith, A. D. (2017). Transcranial direct current stimulation (tDCS): a beginner's guide for design and implementation. *Frontiers in neuroscience*, *11*, 641.
- Thielscher, A., Antunes, A., & Saturnino, G. B. (2015, August). Field modeling for transcranial magnetic stimulation: a useful tool to understand the physiological effects of TMS?. In *2015 37th annual international conference of the IEEE engineering in medicine and biology society (EMBC)* (pp. 222-225). IEEE.
- Todd, T. W. (1924). Thickness of the male white cranium. *The Anatomical Record*, *27*(5), 245-256.
- Todd, T. W., & Lyon, D. W. (1925). Cranial suture closure. *Am. J. Phys. Anthropol*, *8*, 23.
- Torquato, S., & Hyun, S. (2001). Effective-medium approximation for composite media: Realizable single-scale dispersions. *Journal of Applied Physics*, *89*(3), 1725-1729.
- Towle, V. L., Bolaños, J., Suarez, D., Tan, K., Grzeszczuk, R., Levin, D. N., ... & Spire, J. P. (1993). The spatial location of EEG electrodes: locating the best-fitting sphere

- relative to cortical anatomy. *Electroencephalography and clinical neurophysiology*, 86(1), 1-6.
- Tuch, D. S., Wedeen, v. J., Dale, A. M., George, J. S., & Belliveau, J. W. (1999). Conductivity mapping of biological tissue using diffusion MRI. *Annals of the New York Academy of Sciences*, 888(1), 314-316.
- Tuch, D. S., Wedeen, V. J., Dale, A. M., George, J. S., & Belliveau, J. W. (2001). Conductivity tensor mapping of the human brain using diffusion tensor MRI. *Proceedings of the National Academy of Sciences*, 98(20), 11697-11701.
- Tukey, J. W. (1949). Comparing individual means in the analysis of variance. *Biometrics*, 99-114.
- Uluğ, A. M., & Van Zijl, P. C. (1999). Orientation-independent diffusion imaging without tensor diagonalization: anisotropy definitions based on physical attributes of the diffusion ellipsoid. *Journal of Magnetic Resonance Imaging: An Official Journal of the International Society for Magnetic Resonance in Medicine*, 9(6), 804-813.
- Usakli, A. B. (2010). Improvement of EEG signal acquisition: An electrical aspect for state of the art of front end. *Computational intelligence and neuroscience*, 2010.
- Valdés-Hernández, P. A., Von Ellenrieder, N., Ojeda-Gonzalez, A., Kochen, S., Alemán-Gómez, Y., Muravchik, C., & Valdés-Sosa, P. A. (2009). Approximate average head models for EEG source imaging. *Journal of neuroscience methods*, 185(1), 125-132.
- Vallaghé, S., & Clerc, M. (2008). A global sensitivity analysis of three-and four-layer EEG conductivity models. *IEEE Transactions on Biomedical Engineering*, 56(4), 988-995.
- Van den Broek, S. P., Reinders, F., Donderwinkel, M., & Peters, M. (1998). Volume conduction effects in EEG and MEG. *Electroencephalography and clinical neurophysiology*, 106(6), 522-534.
- Van Uitert, R., Johnson, C., & Zhukov, L. (2004). Influence of head tissue conductivity in forward and inverse magnetoencephalographic simulations using realistic head models. *IEEE Transactions on Biomedical Engineering*, 51(12), 2129-2137.
- Van Veen, B. D., Van Drongelen, W., Yuchtman, M., & Suzuki, A. (1997). Localization of brain electrical activity via linearly constrained minimum variance spatial filtering. *IEEE Transactions on biomedical engineering*, 44(9), 867-880.
- Vanrumste, B., Van Hoey, G., Van de Walle, R., D'havé, M., Lemahieu, I., & Boon, P. (2000). Dipole location errors in electroencephalogram source analysis due to volume conductor model errors. *Medical and Biological Engineering and Computing*, 38(5), 528-534.

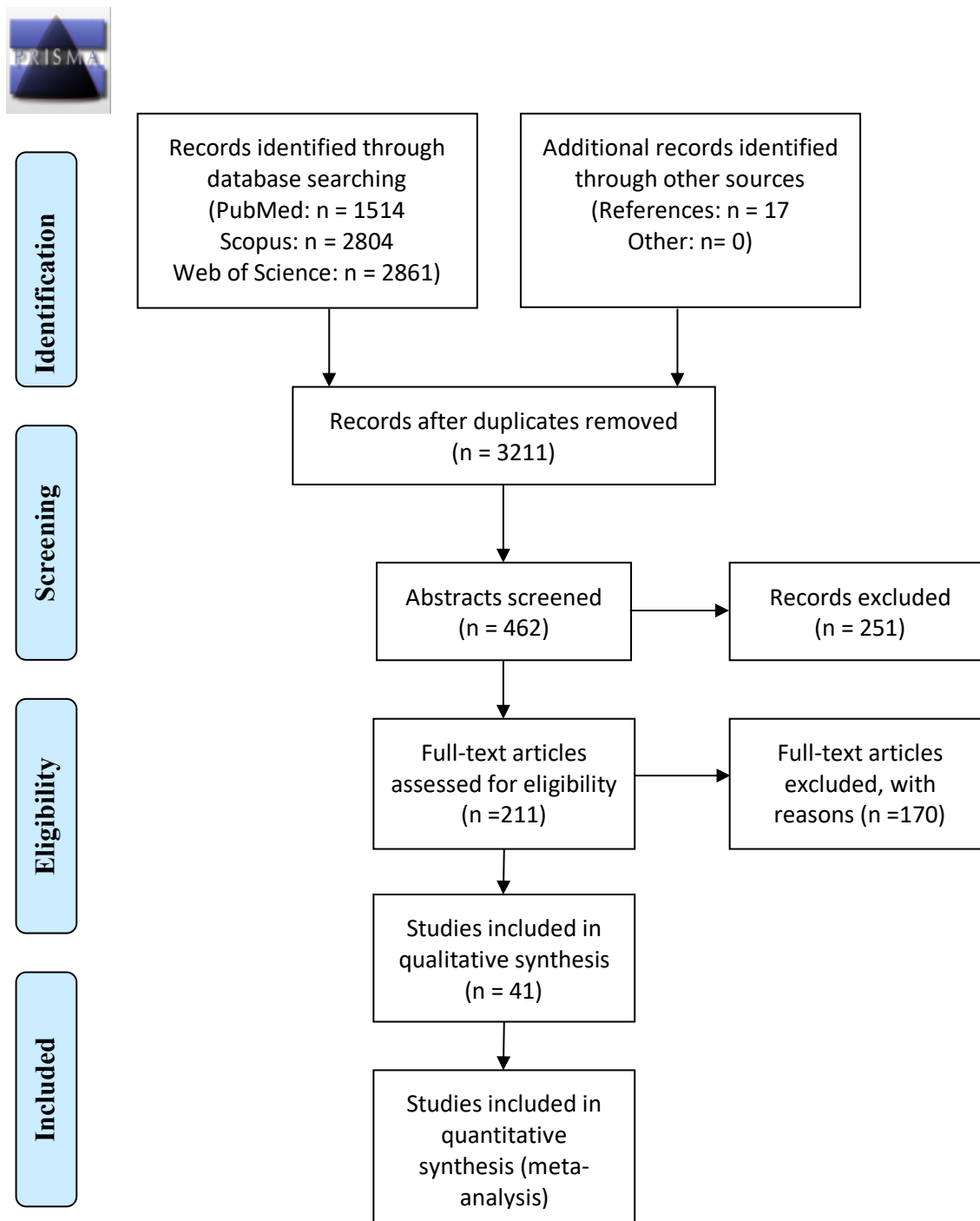
- Vatta, F., Bruno, P., & Inchingolo, P. (2002). Improving lesion conductivity estimate by means of EEG source localization sensitivity to model parameter. *Journal of Clinical Neurophysiology*, *19*(1), 1-15.
- Vatta, F., Bruno, P., & Inchingolo, P. (2005). Multiregion bicentric-spheres models of the head for the simulation of bioelectric phenomena. *IEEE transactions on biomedical engineering*, *52*(3), 384-389.
- Verhagen, A. P., de Vet, H. C., de Bie, R. A., Boers, M., & van den Brandt, P. A. (2001). The art of quality assessment of RCTs included in systematic reviews. *Journal of clinical epidemiology*, *54*(7), 651-654.
- Von Ellenrieder, N., Beltrachini, L., Muravchik, C. H., & Gotman, J. (2014). Extent of cortical generators visible on the scalp: effect of a subdural grid. *Neuroimage*, *101*, 787-795.
- Vorwerk, J., Aydin, Ü., Wolters, C. H., & Butson, C. R. (2019). Influence of head tissue conductivity uncertainties on EEG dipole reconstruction. *Frontiers in neuroscience*, *13*, 531.
- Vorwerk, J., Cho, J. H., Rampp, S., Hamer, H., Knosche, T. R., & Wolters, C. H. (2014). A guideline for head volume conductor modeling in EEG and MEG. *Neuroimage*, *100*, 590-607.
- Vorwerk, J., Clerc, M., Burger, M., & Wolters, C. H. (2012). Comparison of boundary element and finite element approaches to the EEG forward problem. *Biomedical Engineering/Biomedizinische Technik*, *57*(SI-1-Track-O), 795-798.
- Vrba, J. (1996). SQUID gradiometers in real environments. In *SQUID sensors: Fundamentals, fabrication and applications*(pp. 117-178). Springer.
- Vu, H. L., Panchal, J., Parker, E. E., Levine, N. S., & Francel, P. (2001). The timing of physiologic closure of the metopic suture: a review of 159 patients using reconstructed 3D CT scans of the craniofacial region. *Journal of Craniofacial Surgery*, *12*(6), 527-532.
- Wagner, S., Lucka, F., Vorwerk, J., Herrmann, C. S., Nolte, G., Burger, M., & Wolters, C. H. (2016). Using reciprocity for relating the simulation of transcranial current stimulation to the EEG forward problem. *Neuroimage*, *140*, 163-173.
- Wagner, S., Rampersad, S. M., Aydin, Ü., Vorwerk, J., Oostendorp, T. F., Neuling, T., ... & Wolters, C. H. (2013). Investigation of tDCS volume conduction effects in a highly realistic head model. *Journal of neural engineering*, *11*(1), 016002.

- Wagner, T., Fregni, F., Fecteau, S., Grodzinsky, A., Zahn, M., & Pascual-Leone, A. (2007). Transcranial direct current stimulation: a computer-based human model study. *Neuroimage*, 35(3), 1113-1124.
- Wang, K., Zhu, S., Mueller, B. A., Lim, K. O., Liu, Z., & He, B. (2008). A new method to derive white matter conductivity from diffusion tensor MRI. *IEEE Transactions on biomedical engineering*, 55(10), 2481-2486.
- Wang, Q., Xu, X., & Zhang, M. (2010). Normal aging in the basal ganglia evaluated by eigenvalues of diffusion tensor imaging. *American journal of neuroradiology*, 31(3), 516-520.
- Weaver, L., Rostain, A. L., Mace, W., Akhtar, U., Moss, E., & O'Reardon, J. P. (2012). Transcranial magnetic stimulation (TMS) in the treatment of attention-deficit/hyperactivity disorder in adolescents and young adults: a pilot study. *The journal of ECT*, 28(2), 98-103.
- Wendel, K., Malmivuo, J., & Ieee. (2006). *Correlation between live and post mortem skull conductivity measurements*.
- Wendel, K., Väisänen, J., Seemann, G., Hyttinen, J., & Malmivuo, J. (2010). The influence of age and skull conductivity on surface and subdermal bipolar EEG leads. *Computational intelligence and neuroscience*, 2010.
- Wenger, C., Salvador, R., Basser, P. J., & Miranda, P. C. (2015). The electric field distribution in the brain during TTFIELDS therapy and its dependence on tissue dielectric properties and anatomy: a computational study. *Physics in Medicine & Biology*, 60(18), 7339.
- Whiting, P., Rutjes, A. W., Reitsma, J. B., Bossuyt, P. M., & Kleijnen, J. (2003). The development of QUADAS: a tool for the quality assessment of studies of diagnostic accuracy included in systematic reviews. *BMC medical research methodology*, 3(1), 25.
- Wise, T., Radua, J., Via, E., Cardoner, N., Abe, O., Adams, T., . . . Perico, C. d. A. M. (2017). Common and distinct patterns of grey-matter volume alteration in major depression and bipolar disorder: evidence from voxel-based meta-analysis. *Molecular psychiatry*, 22(10), 1455.
- Wolters, C. (2018). Age-related skull conductivity estimated by a calibration
- Wolters, C. H. (2003). Influence of tissue conductivity inhomogeneity and anisotropy on EEG/MEG based source localization in the human brain (Doctoral dissertation, Max Planck Institute of Cognitive Neuroscience Leipzig).

- Wolters, C. H., Anwander, A., Tricoche, X., Weinstein, D., Koch, M. A., & Macleod, R. S. (2006). Influence of tissue conductivity anisotropy on EEG/MEG field and return current computation in a realistic head model: a simulation and visualization study using high-resolution finite element modeling. *NeuroImage*, 30(3), 813-826.
- Wolters, C. H., Grasedyck, L., & Hackbusch, W. (2004). Efficient computation of lead field bases and influence matrix for the FEM-based EEG and MEG inverse problem. *Inverse problems*, 20(4), 1099.
- Wolters, C. H., Köstler, H., Möller, C., Härdtlein, J., & Anwander, A. (2007). Numerical approaches for dipole modeling in finite element method based source analysis. In *International Congress Series* (Vol. 1300, pp. 189-192). Elsevier.
- Wolters, C. H., Köstler, H., Möller, C., Härdtlein, J., Grasedyck, L., & Hackbusch, W. (2008). Numerical mathematics of the subtraction method for the modeling of a current dipole in EEG source reconstruction using finite element head models. *SIAM Journal on Scientific Computing*, 30(1), 24-45.
- Wu, Y., Koch, W., & Pratt, K. (1991). Proposed new electrolytic conductivity primary standards for KCl solutions. *Journal of research of the National Institute of Standards and Technology*, 96(2), 191.
- Youn, T., Park, H.-J., Kim, J.-J., Kim, M. S., & Kwon, J. S. (2003). Altered hemispheric asymmetry and positive symptoms in schizophrenia: equivalent current dipole of auditory mismatch negativity. *Schizophrenia research*, 59(2), 253-260.
- Yuan, Y., Cassano, P., Pias, M., & Fang, Q. (2020). Transcranial photobiomodulation with near-infrared light from childhood to elderliness: simulation of dosimetry. *Neurophotonics*, 7(1), 015009.
- Yvert, B., Bertrand, O., Thevenet, M., Echallier, J. F., & Pernier, J. (1997). A systematic evaluation of the spherical model accuracy in EEG dipole localization. *Electroencephalography and clinical neurophysiology*, 102(5), 452-459.
- Zhang, Y. C., van Drongelen, W., & He, B. (2006). Estimation of in vivo brain-to-skull conductivity ratio in humans. *Applied Physics Letters*, 89(22).

APPENDIX

Appendix A: Prisma Flow Diagram



From Moher D, Liberati A, Tetzlaff J, Altman DG, The PRISMA Group (2009). Preferred Reporting Items for Systematic Reviews and Meta-Analyses: The PRISMA Statement. PLoS Med 6(7): e1000097. doi:10.1371/journal.pmed1000097

For more information, visit www.prisma-statement.org.

Appendix B: Keywords for Literature Search

The inclusion criteria considered Articles, Books, Book Chapters, Corrections, Data Paper, Early Access or Reprints presented or translatable to English. The keyword search was conducted for titles only. Keywords included any variation and combination of “conductivity” (i.e. resistance, impedance, dielectric, electric/current field, electric properties) AND “head tissue” (i.e. head, brain, scalp, skull, cerebral, CSF, dura, white matter, grey matter, brain-skull, brain-scalp, BSCR, lesion). To reduce the amount of retrieved papers, those including unrelated keywords in their titles (i.e. insulin, diabetes, drug, DNA, blight, ship, sea, flower, Kawasaki, train) and non-human animals (i.e. rat, pig sheep, cow, swine, mice, mouse) were excluded from the keyword search.

Appendix C: Quality Assessment Protocol for All Studies

| Item 1: Were participants appropriately recruited and described? | |
|---|---|
| Pre-specified protocol | No participant demographics or pathology were excluded in order to explore how variations affect conductivity values. However, both should be considered when analysing results to accurately determine their impact. Therefore, an accurate description of participants should be provided in order to appropriately group them for analysis. In the case no information is provided, it should be made clear participants are assumed to be healthy adults. |
| Yes - 1 | At minimum, participant pathology was provided. Age is further included in the current meta-analysis if available. |
| No - 0 | No information on participant pathology or demographics were provided, or sufficient to assume participants were healthy adults. |
| Unclear – 0.5 | When no detailed description was available, it is still sufficient to assume participants were healthy adults. |
| Item 2: Does the measurement method appropriately determine the desired value? | |
| Pre-specified protocol | The study measures what they set out to measure (i.e. conductivity/resistivity) and reports the values appropriately. |

| | |
|--|--|
| Yes - 1 | Results were reported in accordance to the study aims and methodology. |
| No – 0 | Reported values were inconsistent with the study aims and what they claimed to report. |
| Unclear – 0.5 | It is unclear whether or not reported results were in line with the studies aim, therefore an average of 0.5 for this item is assigned. |
| Item 3: Is the methodology accurately described such that it can be replicated? | |
| Pre-specified protocol | Employed methodology should be sufficiently described in order to accurately assess variation in conductivity values due to methodological differences. Enough information should therefore, at minimum, be provided to assign methodology. In order to further validate the chosen method, a sufficient description should allow replication of the method. |
| Yes - 1 | Sufficient information was provided to assign a methodology and replicate their chosen method. |
| No - 0 | No information was provided, and the review is unable to appropriately assign chosen methodology. |
| Unclear 0.5 | It is unclear whether enough information is provided for replication, but methodology can be assigned appropriately. |
| Item 4: Is the chosen methodology justified? | |
| Pre-specified protocol | As there are many different methods measuring conductivity, it would be expected each study would justify their chosen methodology, potentially based on the previous literature. |
| Yes - 1 | Justification for the chosen method was provided. |
| No - 0 | No justification for the employed methodology was provided. |
| Unclear – 0.5 | It is unclear whether or not justification was provided, therefore an average of 0.5 for this item is assigned. |
| Item 5: Was the measurement protocol verified for accuracy? | |
| Pre-specified protocol | Tests measuring conductivity do not come without errors, in order to improve validity of the method, measurement errors should be provided to further verify their results. This may be through simulation or phantom experiments, or as standard deviations within each participant. |

| | |
|---|--|
| Yes - 1 | The error associated with the chosen methodology was reported – from simulation, phantom or participant data. |
| No - 0 | No protocol errors were reported. |
| Unclear - 0.5 | It is unclear whether errors were reported or not – i.e. unclear whether reported errors were due to simulation, phantom or participant data errors. |
| Item 6: Did the measurement and verification method remain unchanged throughout the study? | |
| Pre-specified protocol | Methodology should remain constant throughout the measurement process, with any deviations described and justified. |
| Yes - 1 | All measurements were obtained using the same methodology. |
| No - 0 | Methodology did not remain constant. |
| Unclear - 0.5 | It is unclear whether or not the methodology was consistent for each measurement, therefore an average of 0.5 for this item is assigned. |
| Item 7: Were the measurement errors within an acceptable range? Higher weight? | |
| Pre-specified protocol | Errors should be of an acceptable value otherwise use of the chosen method is not justified. Where errors are considerably large, a discussion should be made as to why and ramifications implemented. |
| Yes - 1 | Errors were relatively low and within an acceptable range. |
| No - 0 | Errors were considerably large, and no justifications/ramifications were made. |
| Unclear - 0.5 | No clear error values were provided, or justification/ramification are absent/arbitrary, therefore an average of 0.5 for this item is assigned. |

Direct Measurement

| | |
|---|---|
| Item 8: Were measurements obtained immediately after tissue was excised? If no, how much time elapsed between excision and test? | |
| Pre-specified protocol | For conductivity values that reflect the most natural circumstances, measurements should be made immediately after tissue has been excised, or immediately after death. Time- |

| | |
|--|--|
| <p>Yes - 1</p> <p>No:</p> <p>< 24 hours – 0.8</p> <p>1 - 7 days – 0.6</p> <p>1 - 8 weeks – 0.4</p> <p>>2 months – 0.2</p> <p>Unclear – 0.5</p> | <p>elapsed from excision and measurements may affect the relative conductivity of the tissue.</p> <p>No time elapsed from excision and test.</p> <p>Time elapsed between excision and test within the range described and an item score was assigned accordingly.</p> <p>It was unclear how much time elapsed, therefore an average of 0.5 for this item is assigned.</p> |
| <p>Item 9: Were excised tissue samples kept in 100% saline? If no, what liquid (and concentration) were tissue samples kept in?</p> | |
| <p>Pre-specified protocol</p> <p>Yes - 1</p> <p>No:</p> <p>>90% saline – 0.8</p> <p>50-90% saline – 0.6</p> <p><50% saline – 0.4</p> <p>Dry – 0.2</p> <p>Unclear – 0.5</p> | <p>To ensure conditions are kept as natural as possible, excised tissue should be contained within 100% saline, where conductivity is 1 S/m.</p> <p>Excised tissue samples were contained in 100% saline of 1 S/m conductivity.</p> <p>Tissue samples were kept in varying concentrations of saline and quality scores were assigned accordingly.</p> <p>It is unclear what concentration of saline tissues were kept in, hence they were assigned an average score of 0.5</p> |
| <p>Item 10: Was the tissue kept at body temperature (~37 degrees Celsius)?</p> | |
| <p>Pre-specified protocol</p> <p>Yes - 1</p> <p>No - 0</p> <p>Unclear – 0.5</p> | <p>For conductivity values that reflect the most natural circumstances, excised tissue should be maintained at body temperature.</p> <p>Tissue kept at approximately body temperature (34-39°C)</p> <p>Tissue not at body temperature.</p> |

| | |
|--|--|
| | The temperature of the tissue during conductivity measurements was unclear or ambiguous, therefore an average of 0.5 for this item was assigned. |
|--|--|

Model-dependent Measurements

| | |
|--|--|
| Item 11: Is an individualised head model considered for each participant? | |
| Pre-specified protocol | Head shape and tissue thickness varies considerably between individuals; therefore, head models should be personalised for each individual – i.e. from MRI/DTI data. If not, realistic head models should be employed as opposed to a spherical model, as the head is not a simplistic sphere. |
| Yes, individualistic - 1 | Individualistic head models were considered. |
| No, realistic – 0.75 | A realistic head model was employed. |
| No, spherical – 0.25 | A spherical head model was employed. |
| Unclear – 0.5 | The head model used was unclear, hence an average quality score of 0.5 is given. |
| Item 12: Has the head been maximally segmented into appropriate layers depending on the tissue type being measured? | |
| Pre-specified protocol | As specified by sub-sections: |
| 12a: Scalp | |
| Yes: muscle, fat skin- 1 | The scalp was segmented into the 3 tissue layers of muscle, fat, skin |
| Yes: 2 layers - 0.5 | |
| No - 0 | The scalp is considered as 2 layers (i.e. muscle + fat) |
| N/A | Scalp is considered one homogenous layer. |
| | If the study did not measure scalp conductivity, item 12a is not included in the Quality Assessment score. |
| 12b: Skull | |
| Yes: 4 layers – 1 | The skull was segmented into spongiform, inner and outer compact bone with sutures. |
| Yes: 3 layers – 0.66 | Skull considered tri-layered; spongiform, inner and outer compact bone without sutures. |
| Yes: 2 layers – 0.33 | Skull segmented into spongiform and compact bone. |

| | |
|---|--|
| <p>No: 1 layer – 0 N/A</p> <p>12c: Brain</p> <p>Yes: GM + WM – 1 No: homogenous – 0.5 No: scalp = brain – 0</p> <p>N/A</p> <p>12d: WM anisotropy</p> <p>Yes: anisotropic – 1 No- isotropic – 0</p> <p>N/A</p> | <p>The skull was considered as one homogenous head layer. If the study did not measure scalp conductivity, item 12b is not included in the Quality Assessment score.</p> <p>The brain was compartmented into grey and white matter. The brain was considered as a homogenous tissue. The brain was assumed to have the same conductivity as the scalp. If the study did not measure brain conductivity, item 12c is not included in the Quality Assessment score.</p> <p>WM was modelled as anisotropic WM was modelled as isotropic, or this was not mentioned in the study, therefore WM was assumed to be modelled as isotropic If the study did not measure WM conductivity, item 12d is not included in the Quality Assessment score.</p> |
| <p>Item 13: Were no assumptions made for the conductivity value of any tissue type?</p> | |
| <p>Pre-specified protocol</p> <p>Yes - 1 No – 0</p> | <p>Conductivity values for all reported tissue types were empirically measured rather than assumed from prior literature (i.e. CSF is often assumed to model the remaining tissues).</p> <p>No assumptions were made Conductivity was assumed for one or more tissue types.</p> |

Model-independent Measurements

| | |
|--|---|
| <p>Item 14: Was the magnetic resonance resolution high?</p> | |
| <p>Pre-specified protocol</p> <p>Yes: <1mm - 1</p> | <p>High resolution magnetic resonance imaging data with small voxel sizes should be acquired in order to most accurately segment head tissue and improve spatial resolution.</p> <p>MR resolution is 1mm³ or less.</p> |

| | |
|-----------------|---|
| No: 1-2mm – 0.8 | Resolution between 1-2mm ³ . |
| No: 2-3mm – 0.6 | Resolution between 2-3mm ³ . |
| No: 3-4mm – 0.4 | Resolution between 3-4mm ³ . |
| No: >4mm – 0.2 | Resolution above 4mm ³ . |
| Unclear – 0.5 | The resolution used was unclear or unprovided, hence an average quality score of 0.5 is given. |
| N/A | If the study did not employ a magnetic resonance method, item 14 is not included in the Quality Assessment score. |

Example 1 & 2: Direct Measurements

Baumann *et al.* (1997)

| | | | | | | | | | | | | | | | | | |
|-------|---|---|---|---|---|---|-----|-----|-----|----|-----|-----|-----|-----|-----|-----|-----|
| Item | 1 | 2 | 3 | 4 | 5 | 6 | 7 | 8 | 9 | 10 | 11 | 12a | 12b | 12c | 12d | 13 | 14 |
| Score | 1 | 1 | 1 | 1 | 0 | 1 | 0.5 | 0.4 | 0.5 | 1 | N/A | N/A | N/A | N/A | N/A | N/A | N/A |
| Total | 7.4 | | | | | | | | | | | | | | | | |
| QAS | 0.74 (Score total divided by number of relevant items, in this case 10) | | | | | | | | | | | | | | | | |

Acktari *et al.* (2000)

| | | | | | | | | | | | | | | | | | |
|-------|--|---|---|---|---|---|---|-----|-----|----|-----|-----|-----|-----|-----|-----|-----|
| Item | 1 | 2 | 3 | 4 | 5 | 6 | 7 | 8 | 9 | 10 | 11 | 12a | 12b | 12c | 12d | 13 | 14 |
| Score | 1 | 1 | 1 | 1 | 1 | 1 | 1 | 0.2 | 0.8 | 1 | N/A | N/A | N/A | N/A | N/A | N/A | N/A |
| Total | 9 | | | | | | | | | | | | | | | | |
| QAS | 0.9 (Score total divided by number of relevant items, in this case 10) | | | | | | | | | | | | | | | | |

Example 3 & 4: Model Dependent Measurements

Dannhauer *et al.* (2011) – E/MEG

| | | | | | | | | | | | | | | | | | |
|-------|---|---|---|---|---|---|-----|-----|-----|-----|----|-----|------|-----|-----|----|-----|
| Item | 1 | 2 | 3 | 4 | 5 | 6 | 7 | 8 | 9 | 10 | 11 | 12a | 12b | 12c | 12d | 13 | 14 |
| Score | 1 | 1 | 1 | 1 | 0 | 1 | 0.5 | N/A | N/A | N/A | 1 | 0 | 0.66 | 1 | N/A | 0 | N/A |
| Total | 8.16 | | | | | | | | | | | | | | | | |
| QAS | 0.68 (Score total divided by number of relevant items, in this case 12) | | | | | | | | | | | | | | | | |

Fernández-Corazza *et al.* (2017) – EIT

| | | | | | | | | | | | | | | | | | |
|-------|---|---|---|---|---|---|---|-----|-----|-----|----|-----|------|-----|-----|----|-----|
| Item | 1 | 2 | 3 | 4 | 5 | 6 | 7 | 8 | 9 | 10 | 11 | 12a | 12b | 12c | 12d | 13 | 14 |
| Score | 1 | 1 | 1 | 1 | 1 | 1 | 1 | N/A | N/A | N/A | 1 | 0 | 0.33 | 1 | N/A | 0 | N/A |
| Total | 9.33 | | | | | | | | | | | | | | | | |
| QAS | 0.7775 (Score total divided by number of relevant items, in this case 12) | | | | | | | | | | | | | | | | |

Example 5: Model Independent Measurements

Rullmann *et al.* (2009) – DTI

| | | | | | | | | | | | | | | | | | |
|-------|---|---|---|---|---|---|---|-----|-----|-----|-----|-----|-----|-----|-----|-----|----|
| Item | 1 | 2 | 3 | 4 | 5 | 6 | 7 | 8 | 9 | 10 | 11 | 12a | 12b | 12c | 12d | 13 | 14 |
| Score | 1 | 1 | 1 | 1 | 1 | 1 | 1 | N/A | N/A | N/A | N/A | N/A | N/A | N/A | N/A | N/A | 1 |
| Total | 8 | | | | | | | | | | | | | | | | |
| QAS | 1 (Score total divided by number of relevant items, in this case 8) | | | | | | | | | | | | | | | | |